



AFRL-RX-WP-TR-2008-4380

**SELF-LUBRICATING COATINGS FOR ELEVATED
TEMPERATURE APPLICATIONS USING A HIGH-
VELOCITY-PARTICLE-CONSOLIDATION (HVPC)
PROCESS**

A.E. Segall, I. Smid, P. Walia, and T.J. Eden

The Pennsylvania State University

DECEMBER 2008

Final Report

Approved for public release; distribution unlimited.

See additional restrictions described on inside pages

STINFO COPY

**AIR FORCE RESEARCH LABORATORY
MATERIALS AND MANUFACTURING DIRECTORATE
WRIGHT-PATTERSON AIR FORCE BASE, OH 45433-7750
AIR FORCE MATERIEL COMMAND
UNITED STATES AIR FORCE**

NOTICE AND SIGNATURE PAGE

Using Government drawings, specifications, or other data included in this document for any purpose other than Government procurement does not in any way obligate the U.S. Government. The fact that the Government formulated or supplied the drawings, specifications, or other data does not license the holder or any other person or corporation; or convey any rights or permission to manufacture, use, or sell any patented invention that may relate to them.

This report was cleared for public release by the Air Force Research Laboratory [88 ABW-2009-2852] Public Affairs Office (PAO) and is available to the general public, including foreign nationals. Copies may be obtained from the Defense Technical Information Center (DTIC) (<http://www.dtic.mil>).

AFRL-RX-WP-TR-2008-4380 HAS BEEN REVIEWED AND IS APPROVED FOR PUBLICATION IN ACCORDANCE WITH ASSIGNED DISTRIBUTION STATEMENT.

**//Signature//*

BENJAMIN S. PHILLIPS, Project Engineer
Thermal Sciences and Materials Branch
Nonmetallic Materials Division

//Signature//

NADER HENDIZADEH, Chief
Thermal Sciences and Materials Branch
Nonmetallic Materials Division

//Signature//

SHASHI K. SHARMA, Deputy Chief
Nonmetallic Materials Division
Materials and Manufacturing Directorate

This report is published in the interest of scientific and technical information exchange and its publication does not constitute the Government's approval or disapproval of its ideas or findings.

*Disseminated copies will show “//Signature//” stamped or typed above the signature blocks.

REPORT DOCUMENTATION PAGE				Form Approved OMB No. 0704-0188	
<p>The public reporting burden for this collection of information is estimated to average 1 hour per response, including the time for reviewing instructions, searching existing data sources, gathering and maintaining the data needed, and completing and reviewing the collection of information. Send comments regarding this burden estimate or any other aspect of this collection of information, including suggestions for reducing this burden, to Department of Defense, Washington Headquarters Services, Directorate for Information Operations and Reports (0704-0188), 1215 Jefferson Davis Highway, Suite 1204, Arlington, VA 22202-4302. Respondents should be aware that notwithstanding any other provision of law, no person shall be subject to any penalty for failing to comply with a collection of information if it does not display a currently valid OMB control number. PLEASE DO NOT RETURN YOUR FORM TO THE ABOVE ADDRESS.</p>					
1. REPORT DATE (DD-MM-YY) December 2008		2. REPORT TYPE Final		3. DATES COVERED (From - To) 01 May 2004 – 12 August 2008	
4. TITLE AND SUBTITLE SELF-LUBRICATING COATINGS FOR ELEVATED TEMPERATURE APPLICATIONS USING A HIGH-VELOCITY-PARTICLE-CONSOLIDATION (HVPC) PROCESS				5a. CONTRACT NUMBER FA8650-04-C-5042	
				5b. GRANT NUMBER	
				5c. PROGRAM ELEMENT NUMBER 61102F	
6. AUTHOR(S) A.E. Segall, I. Smid, P. Walia, and T.J. Eden				5d. PROJECT NUMBER 2303	
				5e. TASK NUMBER D1	
				5f. WORK UNIT NUMBER 62400001	
7. PERFORMING ORGANIZATION NAME(S) AND ADDRESS(ES) The Pennsylvania State University 408 Old Main University Park, PA 16802				8. PERFORMING ORGANIZATION REPORT NUMBER	
9. SPONSORING/MONITORING AGENCY NAME(S) AND ADDRESS(ES) Air Force Research Laboratory Materials and Manufacturing Directorate Wright-Patterson Air Force Base, OH 45433-7750 Air Force Materiel Command United States Air Force				10. SPONSORING/MONITORING AGENCY ACRONYM(S) AFRL/RXBT	
				11. SPONSORING/MONITORING AGENCY REPORT NUMBER(S) AFRL-RX-WP-TR-2008-4380	
12. DISTRIBUTION/AVAILABILITY STATEMENT Approved for public release; distribution unlimited.					
13. SUPPLEMENTARY NOTES PAO Case Number: 88 ABW-2009-2852; Clearance Date: 24 Jun 2009. Report contains color.					
14. ABSTRACT The research program developed and demonstrated the ability of the High-Velocity-Particle-Consolidations (HVPC) process to directly and economically create self-lubricating coatings and alloys for elevated temperature. Composite coatings with a low oxide content combining Ni and MoS ₂ and/or other solid lubricants were developed and evaluated for HVPC processing. <p style="text-align: right;"><i>See alternate abstract on reverse →</i></p>					
15. SUBJECT TERMS Coatings, Tribology, HVPC, MoS ₂ , Solid Lubricants, High Temperature					
16. SECURITY CLASSIFICATION OF:			17. LIMITATION OF ABSTRACT: SAR	18. NUMBER OF PAGES 334	19a. NAME OF RESPONSIBLE PERSON (Monitor) Benjamin S. Phillips 19b. TELEPHONE NUMBER (Include Area Code) N/A
a. REPORT Unclassified	b. ABSTRACT Unclassified	c. THIS PAGE Unclassified			

ABSTRACT

Cold Spray or High-Velocity-Particle-Consolidation (HVPC) is a relatively new coating method for the deposition of metals, alloys, polymers, and composite powder-materials onto various substrates without significant heating of the spray powders or substrates. Due to the use of low temperatures and absence of in-flight oxidation and other chemical reactions, thermally vulnerable materials can be deposited without significant material degradation. Given these clear advantages, the objectives of the research detailed herein was to develop self-lubricating composite coatings by using HVPC. For the matrix phase, Nickel was selected due to its success against Ti, as well as its relatively high hardness and wear resistance. Molybdenum-disulfide (MoS_2) and Boron Nitride (BN) were employed as the lubricants because of their excellent solid lubricating properties. Admixed, mechanically milled, and pre-coated lube particles were all studied as feedstock powders. The developed coatings were characterized for the distribution of lubricant and presence of porosity using microscopy; coatings with the highest and most homogeneous lubricant distributions were also analyzed for micro-hardness, wear, and bond-strength. Based on the above analysis, it was concluded that the HVPC process can be used for the development of Ni-BN composite coatings with comparable hardness and adhesive strengths relative to Ni coatings. Results indicated a slight reduction of friction that suggest greater amounts of lubricant are required in the coatings. This in turn suggests that, improved coatings may be best achieved by shrinking the size of the lubricant particle and increasing the thickness of the Ni coating. This was the major directive of the research detailed in Part II of this report.

TABLE OF CONTENTS

LIST OF FIGURES	vi
LIST OF TABLES	xiv

MAIN BODY

Preface	xvi
Summary	xvii

INTRODUCTION

Chapter 1 Introduction	1
1.1 Gas Turbines	1
1.2 Turbine Blade Materials	2
1.3 Fretting Damage	4
1.4 Purpose of this study	5
1.5 Thesis Outline	6
Chapter 2 Literature Survey	7
2.1 Fretting Wear	7
2.1.1 Introduction to Fretting Wear	7
2.1.2 Relation between Fretting Fatigue and Fretting Wear	10
2.1.3 Fretting Wear at Dovetail Joints of Turbine Blades	10
2.2 Cold Spray Process	13
2.2.1 Introduction to Cold Spray Process	13
2.2.2 Cold Gas Dynamic Spray- Background	18
2.2.3 Process Details	19
2.2.4 Bonding in Cold Spray	21
2.2.5 Cold Spray: Process Parameters	24
2.2.6 Cold Spray of Composite Powders	31
2.3 Self-Lubricating Coatings	32
2.3.1 Introduction	32
2.3.2 Self Lubricating Coatings based on Molybdenum-disulfide	34
2.3.3 Self-Lubricating Coatings based on Boron-Nitride	36

METHODS, ASSUMPTIONS, & PROCEDURES

Chapter 3	Experimental Procedures.....	40
3.1	Powders.....	40
3.2	Powder Characterization.....	40
3.2.1	Particle Shape and Microstructure.....	41
3.2.2	Particle Size Analysis	46
3.2.3	Pycnometer Density.....	46
3.2.4	Micro Hardness Measurement of Powders.....	47
3.3	Feedstock Preparation.....	48
3.3.1	Admixed Powders	48
3.3.2	Milled Powders.....	49
3.4	Cold Spray Process and Equipment Detail.....	49
3.4.1	Process Parameters	53
3.5	Characterization and evaluation of cold-sprayed coatings	55
3.5.1	Microstructural analysis	55
3.5.2	X Ray Diffraction	56
3.5.3	Micro-hardness of coating.....	56
3.5.4	Adhesion Testing.....	57
3.5.5	Fretting Wear Testing.....	59

RESULTS AND DISCUSSION

Chapter 4	Feedstock Powders for Cold Spray	62
4.1	Ni-MoS ₂ and Ni-BN Admixed Powders.....	62
4.2	Milled Powders	65
4.2.1	Milled Ni-MoS ₂ Powders.....	65
4.2.2	Milled Ni-BN Powders.....	69
4.2.3	Ni-Ni coated BN admixed Powder.....	79
4.2.4	Micro Hardness	81
4.2.5	Pycnometer Density of Ni coated BN powders.....	82
Chapter 5	Coatings Developed using Cold Spray.....	83
5.1	Cold Spray coatings using Nitrogen as the Process Gas	83
5.1.1	Ni-MoS ₂ Coatings.....	83
5.1.2	Ni-BN Coatings	86
5.2	Cold Spray Coatings using Helium as the Process Gas.....	88
5.2.1	Pure Ni coatings	88

5.2.2 Coatings with Admixed Ni-MoS ₂ Feedstock Powder	89
5.2.3 Coatings with admixed Ni-BN feedstock powder	93
5.2.4 Coatings with milled Ni-MoS ₂ feedstock powder	95
5.2.5 Coatings with milled Ni-BN feedstock powder	97
5.2.6 Coatings with admixed Ni-Ni coated BN powders	100
5.3 Testing of coatings produced with admixed Ni-Ni coated BN.....	107
5.3.1 X-Ray Diffraction (XRD).....	107
5.3.2 Hardness Testing	109
5.3.3 Bond Testing	111
5.3.4 Fretting Wear Testing.....	117

CONCLUSIONS

Chapter 6 Conclusions and Future Recommendations	125
6.1 Summary.....	125
6.2 Conclusions.....	126
6.3 Future Recommendations	129
Bibliography	131
Appendix A Optical and SEM Images of Powders	145
Appendix B Additional SEM images of Ni-MoS ₂ and Ni-BN coatings	151
B.1 Optical images of pure Ni coating sprayed with helium.....	151
B.2 SEM images of (admixed) Ni-MoS ₂ coatings sprayed with helium	153
B.3 SEM images of (admixed) Ni-BN coatings sprayed with helium.....	153
B.4 SEM images of (milled) Ni-MoS ₂ coatings sprayed with helium.....	154
B.5 SEM images of (milled) Ni-BN coatings sprayed with helium	155
B.6 Optical and SEM images of (admixed) Ni-Ni coated BN coatings sprayed with helium.....	156
Appendix C Effect of Particle Diameter and Process Parameters on Particle Velocity.....	160
Appendix D Non-Technical Abstract	164

LIST OF FIGURES

Figure 2.1: Illustration of the wear kinetics of Ti-6Al-V4 under gross slip fretting wear conditions through a debris flow chart approach [11].	8
Figure 2.2: Creation and evolution of the third body debris through the contact interface [25].	9
Figure 2.3: Dovetail joint at the blade/disk interface [39].	11
Figure 2.4: Microstructure of Ti-6Al-4V alloy [42]	13
Figure 2.5: Temperature / velocity regimes for common thermal spray process compared to temperature and velocity in the Cold Spray [46].	15
Figure 2.6: Schematized particle diameter/velocity regimes for various solid particle impact based deposition processes [46].	16
Figure 2.7: Conceptual drawing of the cold spray equipment and process [18].	20
Figure 2.8: Schematic of deformation processes in different combinations of particles and substrate in cold spray coatings [116]	24
Figure 2.9: Typical course of a) velocity and b) temperature of the gas and particles in nozzle [64].	27
Figure 2.10: Deposition efficiency as a function of particle velocity for four typical powders on copper substrate at ambient jet temperature [45]	31
Figure 2.11: Comparison of friction coefficients of various solid lubricants using the Falex Coefficient of Friction Test developed at Falex Corporation [154]	37
Figure 2.12: Coefficient of friction of MoS ₂ , and (h) BN at various temperatures [154].	38
Figure 3.1: SEM image of as-received Ni powder	42
Figure 3.2: SEM image of as-received MoS ₂ powder	43
Figure 3.3: SEM image of as received BN powder	43
Figure 3.4: SEM images of as-received Ni coated BN powders	44
Figure 3.5: Optical Image of Ni-coated BN.	45

Figure 3.6: Schematic of K-tech Cold Spray Equipment used for experiments	50
Figure 3.7: Pressure profiles during cold spray deposition.....	54
Figure 3.8: Change in gas flow rates during cold spray deposition.....	54
Figure 3.9: Temperature control during cold spray deposition.....	55
Figure 3.10: Micro-hardness study pattern	57
Figure 3.11: Samples tested for adhesion	58
Figure 3.12: Samples used for fretting wear testing	60
Figure 3.13: Ellipsoid contact geometry	60
Figure 3.14: Fretting wear tribometer	61
Figure 4.1: SEM image of admixed Ni-3 wt. % MoS ₂ powder	64
Figure 4.2: SEM image of admixed Ni-2 wt. % BN powder	64
Figure 4.3: SEM image of Ni (12 µm)-2wt % MoS ₂ (30 µm) milled for 30 minutes.....	66
Figure 4.4: SEM images of Ni (12 µm)-2 wt. % MoS ₂ (3 µm) milled for 20 minutes.....	66
Figure 4.5: SEM images of Ni (12 µm)-2 wt % MoS ₂ (3 µm) milled for 40 minutes.....	67
Figure 4.6: SEM images of Ni (12 µm)-2 wt. % MoS ₂ (3 µm) milled for 90 minutes.....	67
Figure 4.7: SEM images of Ni (12 µm)-7 wt % MoS ₂ (3 µm) milled for 1 hour	68
Figure 4.8: SEM images of Ni (12 µm)-7 wt % MoS ₂ (3 µm) milled for 4 hours.....	68
Figure 4.9: Particle Size Distribution for Ni-7 wt. % MoS ₂ milled for 4 hours	69
Figure 4.10: SEM images of Ni (12 µm)-2 wt % BN (10 µm) milled for 20 minutes.....	71
Figure 4.11: Particle Size Distribution for Ni (12 µm)-2 wt % BN (10 µm) milled for 20 minutes	71
Figure 4.12: SEM images of Ni (12 µm)-2 wt % BN (10 µm) milled for 40 minutes.....	72

Figure 4.13: Particle Size Distribution for Ni (12 μm)-2 wt % BN (10 μm) milled for 40 minutes	72
Figure 4.14: SEM images of Ni (12 μm)-2 wt % BN (10 μm) milled for 1 hour	73
Figure 4.15: Particle Size Distribution for Ni (12 μm)-2 wt % BN (10 μm) milled for 1 hour	73
Figure 4.16: SEM images of Ni (12 μm)-2 wt % BN (10 μm) milled for 1.5 hour	74
Figure 4.17: Particle Size Distribution for Ni (12 μm)-2 wt % BN (10 μm) milled for 1.5 hour	74
Figure 4.18: SEM images of Ni (12 μm)-2 wt % BN (10 μm) milled for 2 hours	75
Figure 4.19: Particle Size Distribution for Ni (12 μm)-2 wt % BN (10 μm) milled for 2 hours	75
Figure 4.20: SEM images of Ni (12 μm)-2 wt % BN (10 μm) milled for 10 hours	76
Figure 4.21: Particle Size Distribution for Ni (12 μm)-2 wt % BN (10 μm) milled for 10 hours	76
Figure 4.22: SEM images of Ni (12 μm)-2 wt % BN (10 μm) milled for 18 hours	77
Figure 4.23: Particle Size Distribution for Ni (12 μm)-2 wt % BN (10 μm) milled for 18 hours	77
Figure 4.24: SEM images of Ni (12 μm)-2 wt % BN (10 μm) milled for 32 hours	78
Figure 4.25: Particle Size Distribution for Ni (12 μm)-2 wt % BN (10 μm) milled for 32 hours	78
Figure 4.26: SEM image of admixed Ni (12 μm)-30 wt % Ni coated BN (103 μm) ..	80
Figure 4.27: SEM image of admixed Ni (12 μm)-30 wt % Ni coated BN (103 μm) ..	80
Figure 5.1: SEM images of as-sprayed Ni-MoS ₂ coatings using admixed powders with nitrogen	84
Figure 5.2: Energy Dispersive X-ray Spectroscopy of Ni-3 wt % MoS ₂ coating	85
Figure 5.3: Coating thickness versus number of passes at various MoS ₂ wt % in feedstock powder	86
Figure 5.4: SEM images of as-sprayed Ni-BN coatings using admixed powders and nitrogen	87

Figure 5.5: Optical micrograph of etched deposits of as-sprayed Ni (75 μm) coatings depicting particle deformation and absence of grain boundaries	89
Figure 5.6: Top view of an as-sprayed Ni-7 wt% MoS ₂ coating using admixed feedstock.....	90
Figure 5.7: SEM image of unpolished cross section of the Ni-7 wt% MoS ₂ coating sprayed helium, showing weak metallurgical bonding at side away from jet stream.....	91
Figure 5.8: SEM images of as-sprayed Ni-7 wt % MoS ₂ coatings using admixed powders and helium.....	92
Figure 5.9: Top-view of an as-sprayed Ni-5 wt% BN coating using admixed feedstock, showing segregation of BN	93
Figure 5.10: SEM images of as-sprayed Ni-5wt % BN coatings using admixed powders and helium.....	94
Figure 5.11: Top view of an as-sprayed Ni-7 wt% MoS ₂ coating using milled feedstock showing erosion of coating by subsequent passes.....	95
Figure 5.12: SEM images of as-sprayed Ni-7 wt % MoS ₂ coatings using milled powders and helium.....	96
Figure 5.13: Close-up of as-sprayed Ni-2 wt% BN coating using milled feedstock...	97
Figure 5.14: SEM images of as-sprayed Ni-5 wt % BN coatings using milled powders and helium.....	98
Figure 5.15: Low magnification images of Ni- BN coating-substrate interface. Top: Optical image of polished and etched sample; Below: SEM image of cut sample	100
Figure 5.16: Optical image of etched Ni-BN coating	101
Figure 5.17: SEM image of the top surface of the coating	102
Figure 5.18: SEM images of Ni-BN coating	103
Figure 5.19: SEM images of Ni-BN coating	104
Figure 5.20: Energy Dispersive X-ray Spectroscopy of the Ni-Ni coated BN coating.....	105
Figure 5.21: Coating thickness versus number of passes at various BN wt % in feedstock powder	105

Figure 5.22: XRD results for admixed Ni-Ni coated BN powder	107
Figure 5.23: XRD results for coating developed with admixed Ni-Ni coated BN powder	107
Figure 5.24: Magnified view of XRD peak of admixed Ni-Ni coated BN powder.....	108
Figure 5.25: Hardness profiles of pure Ni and Ni-BN coatings	109
Figure 5.26: Top view of Ni coating surface after fracture showing failure at the epoxy.....	111
Figure 5.27: Top view of Ni-20 wt. % Ni coated BN (75 μ m) coating surface after fracture showing cohesive failure within the coating	111
Figure 5.28: Top view of Ni-20 wt. % Ni coated BN (103 μ m) coating surface after fracture showing cohesive failure within the coating.....	112
Figure 5.29: Top view of Ni-25 wt. % Ni coated BN (103 μ m) coating surface after fracture showing cohesive failure within the coating.....	112
Figure 5.30: Top and side views of Ni-30 wt. % Ni coated BN (75 μ m) coating surface after fracture showing adhesive failure at coating-substrate interface.....	113
Figure 5.31: Top and side views of Ni-30 wt. % Ni coated BN (103 μ m) coating surface after fracture showing adhesive failure at coating-substrate interface.....	113
Figure 5.32: Load-Displacement curves for cold sprayed Ni-BN coatings.....	115
Figure 5.33: Bond Strength at maximum load as a function of amount of BN in feedstock powders	116
Figure 5.34: Surface roughness of the Ni-BN coatings as a function of percentage of BN	117
Figure 5.35: Coefficients of friction of various Ni-BN coatings	118
Figure 5.36: Maximum depth of wear track on coating surfaces and mating-surfaces for various Ni-BN coatings.....	118
Figure 5.37: 2D Wear profile of the machined Ni-30 wt. % Ni coated BN sample	119
Figure 5.38: Wear trace of the machined Ni-30 wt. % Ni coated BN sample along the major-axis	119
Figure 5.39: Wear trace of the machined Ni-30 wt. % Ni coated BN sample along the minor axis	120

Figure 5.40: 3D Wear profile of the machined Ni-30 wt. % Ni coated BN sample ...	120
Figure 5.41: 2D wear profile of the uncoated Ti-6Al-4V ellipse worn against the machined Ni-30 wt. % Ni coated BN coating	121
Figure 5.42: Wear trace of the uncoated Ti-6Al-4V ellipse worn against the machined Ni-30 wt. % Ni coated BN coating along the major axis.....	121
Figure 5.43: Wear trace of the uncoated Ti-6Al-4V ellipse worn against the machined Ni-30 wt. % Ni coated BN coating along the minor axis.....	122
Figure 5.44: 3D wear profile of the uncoated Ti-6Al-4V ellipse worn against the machined Ni-30 wt. % Ni coated BN coating	122
Figure 5.45: Modified 2D wear profiles showing the cylindrical portion out of the scan for wear profile of the uncoated Ti-6Al-4V ellipse worn against the machined Ni-30 wt. % Ni coated BN coating so that the wear appears flat for measurements	123
Figure 5.46: Major axis profile of the modified 2D wear trace showing the cylindrical portion out of the scan for wear profile of the uncoated Ti-6Al-4V ellipse worn against the machined Ni-30 wt. % Ni coated BN coating so that the wear appears flat for measurements.....	123
Figure 5.47: Minor axis profile of the modified 2D wear trace showing the cylindrical portion out of the scan for wear profile of the uncoated Ti-6Al-4V ellipse worn against the machined Ni-30 wt. % Ni coated BN coating so that the wear appears flat for measurements.....	124
Figure 5.48: Modified 3D wear scars showing the cylindrical portion out of the scan for wear profile of the uncoated Ti-6Al-4V ellipse worn against the machined Ni-30 wt. % Ni coated BN coating so that the wear appears flat for measurements	124
Figure 6.1: Top view of Ni-Ni coated BN (left) and Ni coating (right).	128
Figure 6.2: Suggested stratified coating for improvement in cohesion strength	129
Figure 6.3: Suggested stratified coating for improvement in adhesion strength	129
Figure A.1: Optical image of Ni coated BN powder	145
Figure A.2: Optical image of Ni coated BN powder	146
Figure A.3: Optical image of Ni coated BN powder	146
Figure A.4: SEM image of Ni coated BN powder.....	147

Figure A.5: SEM image of Ni coated BN powder.....	147
Figure A.6: SEM image of Ni coated BN powder.....	148
Figure A.7: SEM image of Ni coated BN powder.....	148
Figure A.8: SEM image of Ni coated BN powder.....	148
Figure A.9: SEM image of Ni coated BN powder.....	149
Figure A.10: SEM image of admixed Ni-BN powders.....	149
Figure A.11: SEM image of admixed Ni-Ni coated BN powders	149
Figure A.12: SEM image of admixed Ni-Ni coated BN powders	150
Figure A.13: SEM image of admixed Ni-Ni coated BN powders	150
Figure B.1: Optical image of pure Ni coating.....	151
Figure B.2: Optical image of etched pure Ni coating	151
Figure B.3: Optical images of etched pure Ni coating.....	152
Figure B.4: Optical image of etched pure Ni coating	152
Figure B.5: SEM images of (admixed) Ni-MoS ₂ coating.....	153
Figure B.6: SEM images of (admixed) Ni-BN coating.....	153
Figure B.7: SEM image of (admixed) Ni-BN coating	154
Figure B.8: SEM images of (milled) Ni-MoS ₂ coating	154
Figure B.9: SEM image of (milled) Ni-MoS ₂ coating.....	155
Figure B.10: SEM images of (milled) Ni-BN coating.....	155
Figure B.11: SEM images of (milled) Ni-B N coating.....	156
Figure B.12: Optical images of etched (admixed) Ni-Ni coated BN coating	156
Figure B.13 Optical images of (admixed) Ni-Ni coated BN coating	157
Figure B.14: Optical image of (admixed) Ni-Ni coated BN coating.....	157
Figure B.15: SEM images of (admixed) Ni-Ni coated BN coating.....	157

Figure B.16 SEM images of (admixed) Ni-Ni coated BN coating	158
Figure B.17 : SEM images of (admixed) Ni-Ni coated BN coating.....	158
Figure B.18 : SEM images of (admixed) Ni-Ni coated BN coating.....	158
Figure B.19 : SEM image of (admixed) Ni-Ni coated BN coating	159
Figure B.20 : EDX of a BN rich region in the (admixed) Ni-Ni coated BN coating ...	159
Figure C.1 : Particle velocity and critical velocity of Ni as a function of particle diameter, using nitrogen gas at 2.1 MPa.....	160
Figure C.2 : Particle velocity and critical velocity of Ni as a function of particle diameter, using helium gas at 2.1 MPa.....	161
Figure C.3 : Particle velocity and critical velocity of Ni as a function of particle diameter, using argon gas at 2.1 MPa.....	161
Figure C.4 : Particle velocity and critical velocity of Ni as a function of particle diameter, using a mixture of 70% Nitrogen -30% Helium gas at 2.1 MPa	162
Figure C.5 : Particle velocity and critical velocity of Ni as a function of particle diameter, using a mixture of 50% Nitrogen -50% Helium gas at 2.1 MPa	162
Figure C.6 : Particle velocity and critical velocity of Ni as a function of particle diameter, using nitrogen gas at 3.45 MPa.....	163
Figure C.7 : Particle velocity and critical velocity of Ni as a function of particle diameter, using helium gas at 3.45 MPa.....	163

LIST OF TABLES

Table 2.1: Mechanical Properties of Ti-6Al-4V (sheet form)	12
Table 2.2: Comparison of helium and nitrogen as process gas [119]	26
Table 2.3: Applications of Solid-Film Lubricants[131]	33
Table 2.4: Micro-hardness and wear resistance of nickel and nickel-boron nitride composite coatings [131]	38
Table 2.5: Taber Wear Index of Ni-BN Composites (Load: 1Kg, CS-10 Calibrase Wheel) [131]	39
Table 3.1: Summary of the as-received powders	41
Table 3.2: Process Parameters used for cold spraying	53
Table 3.3: Coatings tested for adhesion	58
Table 3.4: Coatings tested for fretting wear	60
Table 4.1: Details of admixed Ni-MoS ₂ and Ni-BN feedstock powders	63
Table 4.2: Details of milled Ni-MoS ₂ and Ni-BN feedstock powders	65
Table 4.3: Statistics for Particle Size Distribution for Ni-7 wt. % MoS ₂ milled for 4 hours	69
Table 4.4: Statistics for Particle Size Distribution of Ni (12 μm)-2 wt % BN (10 μm) milled for 20 minutes	71
Table 4.5: Statistics for Particle Size Distribution of Ni (12 μm)-2 wt % BN (10 μm) milled for 40 minutes	72
Table 4.6: Statistics for Particle Size Distribution of Ni (12 μm)-2 wt % BN (10 μm) milled for 1 hour	73
Table 4.7: Statistics for Particle Size Distribution of Ni (12 μm)-2 wt % BN (10 μm) milled for 1.5 hours	74
Table 4.8: Statistics for Particle Size Distribution of Ni (12 μm)-2 wt % BN (10 μm) milled for 2 hours	75
Table 4.9: Statistics for Particle Size Distribution for Ni (12 μm)-2 wt % BN (10 μm) milled for 10 hours	76

Table 4.10: Statistics for Particle Size Distribution of Ni (12 μm)-2 wt % BN (10 μm) milled for 18 hours	77
Table 4.11: Statistics for Particle Size Distribution for Ni (12 μm)-2 wt % BN (10 μm) milled for 32 hours.....	78
Table 4.12: Details of admixed Ni-Ni coated BN feedstock powders.....	79
Table 4.13: Micro-hardness results for pure-Ni and Ni coated BN powders	81
Table 4.14: Pycnometer density results for Ni coated BN powders	82
Table 5.1: Details of admixed Ni-MoS ₂ feedstock powders sprayed with nitrogen....	84
Table 5.2: Experiments with admixed Ni-BN feedstock sprayed with nitrogen	87
Table 5.3: Experiments with admixed Ni-MoS ₂ feedstock sprayed with helium	90
Table 5.4: Experiments with admixed Ni-BN feedstock sprayed with helium.....	93
Table 5.5: Experiments with admixed Ni-MoS ₂ feedstock sprayed with helium	95
Table 5.6: Experiments with admixed Ni-MoS ₂ feedstock sprayed with helium	100
Table 5.7: Bond Strengths Ni-Ni coated BN coatings.....	115
Table 6.1: Conclusions about coatings sprayed with admixed powders.	127

PREFACE

This report represents the first component of research conducted over a number of years by a multiple graduate students and supervising faculty at the Pennsylvania State University. Accordingly, the main body of this report is the Masters thesis of Parul Walia who studied the development of composite, self-lubricating coatings for the application to Ti dovetail joints commonly encountered in aircraft engines. As detailed in the thesis, the research has clearly established the foundation for a new system of self-lubricating coatings that has the potential for both reducing friction, as well as the relatively high costs of fretting damage and the schedule-based maintenance required to avoid catastrophic failures in the engine. The work conducted by Ms Walia also established the groundwork for the next study where further optimized coatings were the result.

SUMMARY

Clearly, fretting and all associated wear is detrimental for the performance and fatigue life of turbine blade-disk dovetail joints. However, because of the temperature limitations of most solid film lubricants, as well as the relatively high temperatures experienced by dovetail joints, currently used coatings and MoS₂ lubricants do not adequately protect against fretting damage. On the other hand, higher temperature coating methods are not useful due to the thermal vulnerability of solid lubricants. Given these needs and difficulties, Ni-based self-lubricating coatings have been developed using a lower temperature coating process commonly known as cold-spray or High Velocity Particle Consolidation (HVPC).

Using the Cold-Spray or HVPC process, unique Ni-MoS₂ and Ni-BN composite coatings were developed for the first time. For the HVPC process to work, the solid particles must deform and form metallurgical bonds when impacting at supersonic velocities typical for the process. Therefore, particle composition and ductility played an important role in the coating development. By virtue of its high ductility, Ni powder can undergoes relatively high plastic deformation and therefore, tends to adhere to the Ti-6Al-4V substrates under study. However, the likely absence of plasticity of the lubricant powders inhibits it from forming a good bond with the substrate as well as from building up on itself. In order to overcome this difficulty, the roles of feedstock preparation techniques, particle size of Ni,

lube, and pre-coated powders, and amount of lube powders in feedstock were all systematically studied.

Clearly, the most important and useful finding of this research is that the lubricious properties of solid lubricants can indeed be retained in HVPC coatings without significant materials degradation. The success of the research is largely due to the use of low temperatures and absence of in-flight oxidation and other chemical reactions typically encountered when using traditional high temperature coatings processes. As always, there are caveats that have directed the later research as detailed in the other reports. For instance, except for pure Ni and (admixed) Ni-MoS₂ coatings, all other coatings require helium to be used as the process gas; since the Ni coated BN powders and mechanically milled powders are relatively large, they required higher kinetic energy and exit velocities only possible with helium. Even in case of (admixed) Ni-MoS₂ coatings, it was possible to double the amount of lubricant entrapped in the coating by spraying with helium instead of nitrogen.

It was also observed that the deposition improved with a corresponding decrease in the variation of particle size of the agglomerates. Contrary to expectation, the coatings formed with larger Ni coated BN powder (103 μm) exhibited better lubricant incorporation as well as adhesion strengths relative to coating fabricated with smaller Ni coated BN powders. However, it may be assumed that the coating build-up was more dependent on the amount of Ni coating instead of the amount of BN in the feedstock powders. *Hence, improved coatings may be best achieved by shrinking the size of the*

lubricant particle and increasing the thickness of the Ni coating. This was the major directive of the research detailed in Part II of this report.

Chapter 1

Introduction

1.1 Gas Turbines

Most modern passenger and military aircraft are powered by gas turbine engines, which are also called jet engines. Jet turbine engines generate a great amount of energy for their size and weight [1]. A turbine is basically a spinning device that uses the action of a fluid to produce work. Typical fluids are: air, wind, water, steam and helium. In all modern gas turbine engines, the engine produces its own pressurized gas to serve as the fluid, by combusting fuels such as propane, natural gas, kerosene, and jet fuel. The heat that comes from burning the fuel expands air, and the high-speed rush of this hot air spins the turbine. There is enough energy in the hot gases blowing through the blades of the turbine to develop 1,500 horsepower or more as commonly required by modern jet engines [2].

Aero Engine development has been steady since the first “Wright Flyer” flew at Kittyhawk, North Carolina on the 17th December, 1903. The first Aero Engine was a single 12hp, 4 cylinder, water-cooled petrol engine, driving two pusher props each of 2.6 meters diameter at a maximum air speed of approximately 48.3 kph. Since then, everything in terms of Aero Engine development has been dedicated to achieving greater horsepower, to lift increasing aircraft weights at ever-increasing airspeeds [3].

Improved aero engine technology has always been the key element in enabling advances in operational effectiveness. The desire to achieve improvements in engine thrust to weight ratio, air speed performance, reductions in cost of production, and specific fuel consumption led to the independent British and German Ram Jet and Turbo jet developments. It was a British pilot, Frank Whittle, who designed the first turbo jet engine in 1930. The first Whittle engine successfully flew in April, 1937. This engine featured a multistage compressor, a combustion chamber, a single stage turbine, and a nozzle. The first jet airplane to successfully use this type of engine was the German Heinkel He 178 invented by Hans Von Ohain. It was the world's first turbojet powered flight [4]. Since then, the jet engine has revolutionised the way in which we fly. More and more, technology is being used as a means of reducing operating costs through increased component lives and improvements in reliability and maintainability.

1.2 Turbine Blade Materials

Designing and manufacturing of gas turbines has faced several seemingly insurmountable problems from both the engineering and materials standpoints, because of the higher spin speeds and operating temperatures encountered; component materials tend to become weaker with time due to various destructive phenomena such as time-dependent plastic strains (creep), thermally induced stresses, microstructural instabilities, environmental degradation, and the deterioration of moving components caused by fretting wear. In case there is excessive wear of the components, the costly replacement

of component becomes inevitable. This problem in turn necessitates the need to find new materials and measures to increase component reliability and engine life [5, 6].

Development of light-alloys that maintain strength at high temperatures has always preceded advances in turbine engine design. Initially, in order to save weight, the components of turbines were made of pure aluminum. With an increase in the operating temperatures, there was a switch to steel alloys owing to their greater resistance to high temperature creep. Later, due to advances in mining and refining techniques, Titanium (Ti) and its alloys became prevalent. Nowadays, approximately one third of the structural weight of modern turbine engines is made up of titanium [5, 6]. As higher temperature titanium alloys are developed and produced, they are progressively replacing the nickel-alloys for disc and blades at the rear of the jet engine [7]. In-fact, ASTM figure of merit for materials have ranked titanium alloys ahead of conventional bearing steels in tribological applications [8].

Due to the above mentioned merits, high strength titanium based alloys are used in critical rotating components in gas turbine engines. Examples include fan and compressor sections of many jet turbine engines in which dovetail joints are used to attach the titanium fan and compressor blades to the titanium disks within the engine. The blades of a jet engine operating at full throttle can spin at upwards of 10,000 rpm. As such, the centrifugal force acting on these blades is tremendous so they must be able to resist expansion due to the stress. In addition, the temperatures inside the jet engine at operating speed can reach 1027 °C, at these temperatures, thermal creep (expansion due to heat and stress) is significant for most materials. Since parts must be manufactured to

strict tolerances to maintain engine efficiency, thermal creep must be minimized throughout the temperature range. The materials for the turbine blades not only must resist thermal creep (requiring strength in the radial direction of the fan), but also demonstrate strength in the axial direction of the fan. Jet engines draw in tremendous amounts of air through its front intake, and occasionally, debris such as dirt, snow, water, birds etc. The blades must therefore be strong enough to withstand the impact of such objects. Such a combination of strength and resistance to high temperatures can be found in titanium alloys, which have found their way into nearly every industry, from medical implants to submarine pressure hulls [5,6]. Titanium alloys also exhibit good resistance to compressive failures and to most common forms of corrosion. All these properties render titanium alloys as a material of choice for rotor and blades of turbines instead of other candidate materials like nickel based super-alloys and ferritic and martensitic stainless steels [7]. However, Ti alloys have rather poor surface properties in other respects. In fact, Ti alloys generally have high coefficients of friction and low resistance to wear. The situation is further complicated by the fact that Ti alloys are not effectively lubricated by conventional liquid lubricants, greases, and solid coatings [8].

1.3 Fretting Damage

Fretting is a small amplitude oscillatory motion, which occurs when components in contact rub against each other and, eventually, wear away parts of the contacting surfaces. During fretting, repeated loading and unloading causes cyclic stresses which induce surface or subsurface break-up and loss of material [9, 10].

The detrimental effects of fretting on fatigue life of the fan and compressor blade-disk dovetail joints have been recognized for many years. Since the blade and disk experience a wide range of vibrations, gross and partial slip conditions occur in the dovetail contact with both wear and crack nucleation being generated. In critical situations, cracks can propagate, mainly driven by fatigue loading. Application of surface modification methods to mitigate the fretting damage at the dovetail is therefore required [11-13].

1.4 Purpose of this study

Investigations of the fretting failure of Ti dovetails at high temperatures have shown the threat of fretting and the protective benefit of the solid film lubricants. In fact, there appears to be virtually no damage to the coatings as long as the lubricant remains intact. However, given the temperature limitation of most solid film lubricants, and the relatively high temperatures experienced by the dovetail joints, the benefits are clearly short lived [14].

Several types of surface treatments and thin films, including shot-peening, ion-beam-enhanced deposition (IBED), ion implantation of carbon and nitrogen, laser gas nitriding, surface lubrication and various combinations thereof have been investigated in the past to improve the hardness and lubricity of contacting surfaces. Despite broad research efforts on the protection of dovetail contact from fretting wear, there are still significant points of contention about the application of the above mentioned measures [15-17].

Cold Spray is a relatively new coating method for deposition of metal, alloy, polymer, and/or composite powder materials onto various substrates without significant heating of the spray powder or substrate. Due to the use of low temperatures and absence of in-flight oxidation and other chemical reactions, thermally vulnerable materials can be deposited without significant material degradation [18]. In the present study, cold spray has been chosen as a method of choice for the development of self lubricating coatings for dovetail joints of turbine blades. For the matrix phase, Nickel has been selected since it has high hardness and wear resistance. Molybdenum-disulfide (MoS_2) and Boron Nitride (BN) have been chosen as the solid lubricating phases because of their excellent lubricating properties. Admixed, mechanically milled, and pre-coated lube particles have been used as feedstock powders. The developed coatings have been tested for microstructural homogeneity, fretting and wear resistance, and mechanical durability.

1.5 Thesis Outline

Chapter 2 presents an overview of fretting wear of the dovetail joints of turbine blades, as well as background information about the cold spray method including prior studies done on self lubricating coatings developed using other methods. Chapter 3 gives the details of experimental procedures used in this study. Chapter 4 discusses the results obtained by various feedstock development techniques, followed by results for coating characterization and testing in Chapter 5. The findings are summarized and firm conclusions are made in Chapter 6.

Chapter 2

Literature Survey

2.1 Fretting Wear

2.1.1 Introduction to Fretting Wear

Wear is defined by the American Society for Testing and Materials (ASTM) as “damage to a solid surface, generally involving the progressive loss of material, due to relative motion between that surface and a contacting substance or substances”[19]. One of the consequences of wear between two contacting surfaces in normal atmospheric conditions is production of oxide debris thus the term “fretting wear” or “fretting corrosion”. Fretting occurs between contacting components which experience a tangential displacement relative to each other due to a small amplitude cyclic-type loading occurring at high frequencies. Oxide debris produced by fretting gets trapped inside the small amplitude displacements, thus causing further erosion of the surface known as fretting wear [20]. The specific transformed structure from which debris is made is called the tribologically transformed structure (TTS). Research indicates that the TTS is formed in the first accommodation stage within a very few initial fretting cycles [23]. Figure 2.1 illustrates the fretting wear mechanism of Ti-6Al-4V [11].

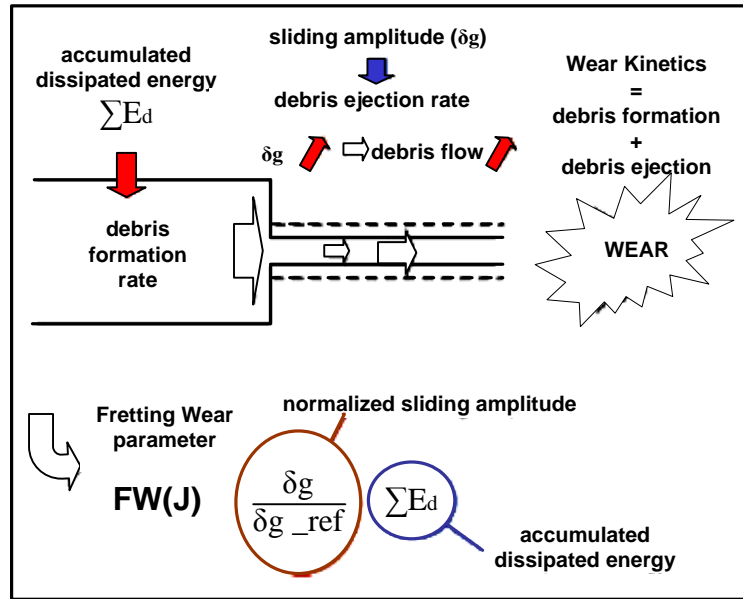


Figure 2.1: Illustration of the wear kinetics of Ti-6Al-V4 under gross slip fretting wear conditions through a debris flow chart approach [11].

The role of particles in the fretting process has been studied by using an apparatus consisting of a short cylinder oscillating in a V-groove. It was established that fretting is proceeded by a series of stages involving plastic flow, the formation and breaking of junctions, the production of loose particles, and finally, the scoring and tearing of the surfaces. In addition, the magnitude of the wear volume, the electrical contact resistance of the system, and the friction coefficient during fretting are all greatly dependent on the amplitude of vibration [21].

Additional research on the fretting of various steel samples, whose hardness varied by almost a factor of three revealed that hardness had much less effect on fretting behavior than did the presence of third-bodies (wear debris) [22]. Furthermore, others experimentally verified the importance of wear debris by using transparent substrates [23]. Generation and motions of debris particles within fretting contacts were captured on video tape and analyzed, leading to the development of the third body approach to

wear modeling. Researchers developed fretting maps which display the synergistic interactions of fretting variables such as frequency and amplitude of slip in fretting wear [24]. Figure 2.2 illustrates the mechanism of creation and evolution of third body debris at the contact interface [25].

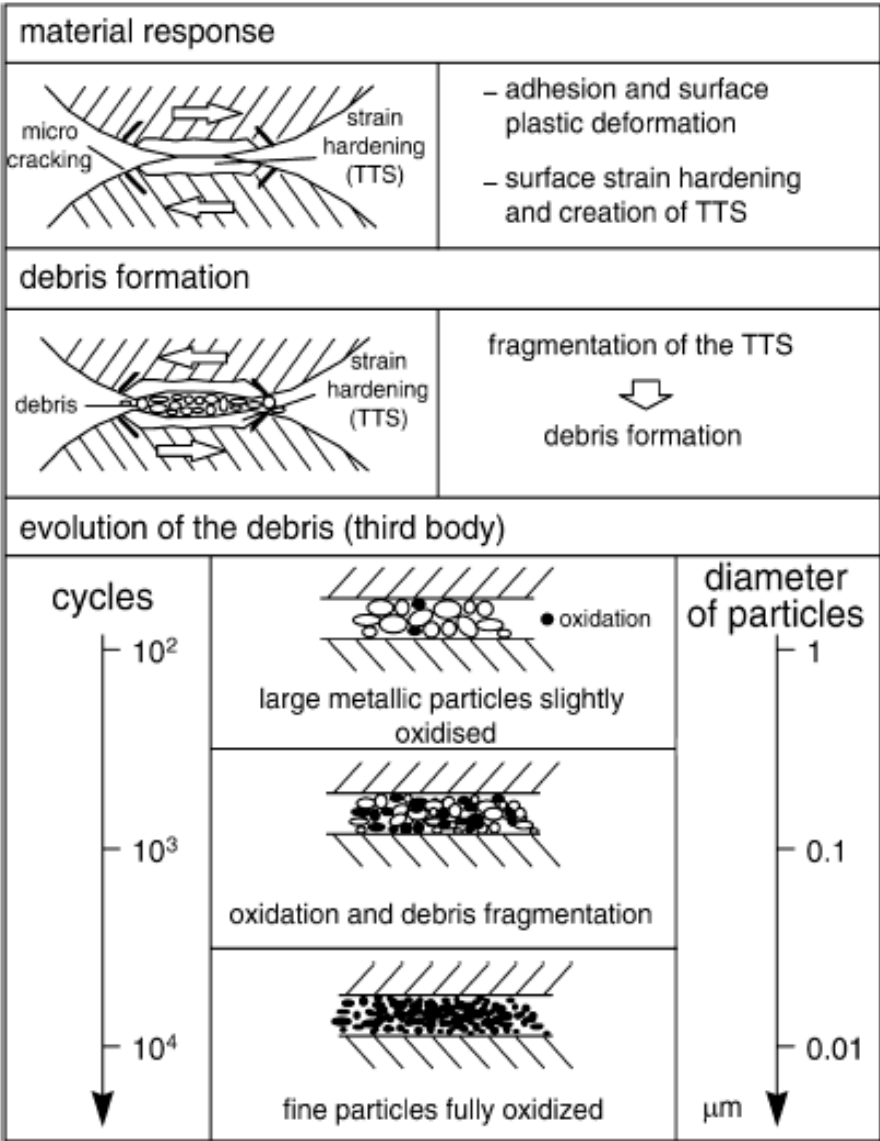


Figure 2.2: Creation and evolution of the third body debris through the contact interface [25]

2.1.2 Relation between Fretting Fatigue and Fretting Wear

Fretting wear occurs when minute surface tangential motion arises between components pressed together by normal forces [26] that cause surface deterioration and dimensional changes in the component [27-29]. The transition from fretting wear to fretting fatigue is evidenced by the nucleation and propagation of one or more surface micro-cracks into the bulk material. As the crack propagates several hundred microns away from the fretting surface, the influence of the contact stresses becomes less important [30-33]. In such a scenario, any bulk or global stresses then begin to dominate the propagation of the crack. Fretting leads to a decrease in fatigue performance, thus the name fretting fatigue [34]. Typically, fretting fatigue leads to a shorter life cycle of the components, or smaller maximum stress range possible for a given life cycle [20, 35, 36]. In some cases, fretting can reduce the expected fatigue life by 40% to 60% [35]. As per the data of the USAF, fretting fatigue is responsible for about one out of six in-service accidents in gas turbine engines for which high cycle fatigue is itself the largest single cause of failure [26].

2.1.3 Fretting Wear at Dovetail Joints of Turbine Blades

As illustrated in Figure 2.3 , the dovetail joint represents the junction of a turbine blade and its outer annulus. Due to the small amplitude, relative motion at the dovetail joint, the turbine blade and the rotor disk rub and slip against each other, resulting in fretting wear [38].

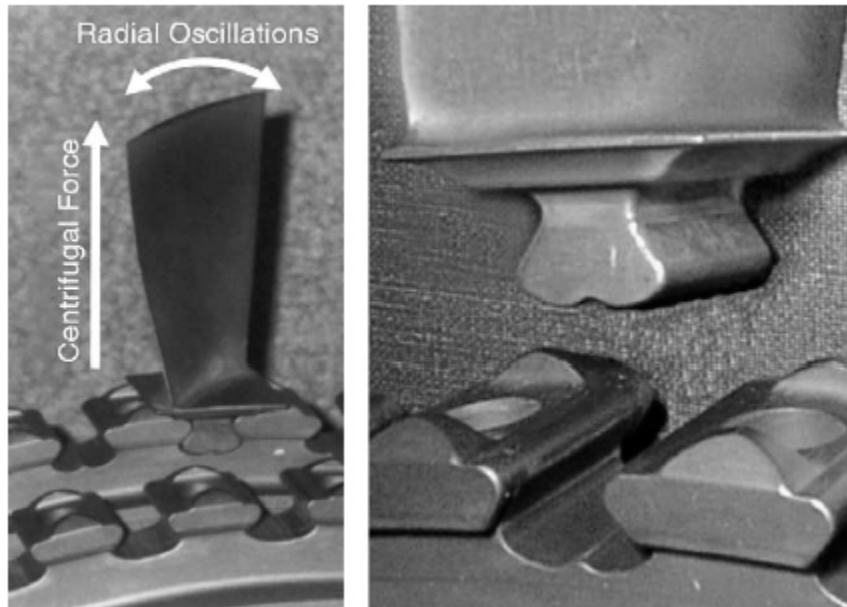


Figure 2.3: Dovetail joint at the blade/disk interface [39]

Turbine engine-blade roots typically experience fretting via a flat-on-flat contact with rather large radii at the edges of contact [12]. There are essentially three types of fretting that can occur in at the dovetail contact: stick regime, partial slip, and gross slip regime. In the stick regime, high contact forces and low fretting amplitudes lead to perfect locking or cold welding between blade and disk components. During partial slip, the dovetail contacts exhibit a central welded area surrounded by a slip annulus where there may be crack formation, fretting fatigue and wear debris. No stable welding occurs in the gross slip regime. However, the adhesive welds are formed and broken during each half phase of a fretting cycle. The contact surfaces can be in full sliding across their surfaces during a portion of the cyclic loading. This is referred to as gross slip, and the damage caused by this condition leads to fretting wear. The high-frequency, low-amplitude vibrations occurring at the dovetail contact result in gross and partial slip conditions. Both wear and crack nucleation can be generated by this contact [11].

Typical dovetail components are made of high strength titanium based alloys such as Ti-6Al-4V. Table 2.1 shows the mechanical properties of a Ti-6Al-4V alloy.

Table 2.1: Mechanical Properties of Ti-6Al-4V (sheet form)

0.2% proof stress MPa	Tensile strength MPa	Elongation %	Tensile modulus GPa	Fatigue limit % of TS	Density g/cm ³
980	1035	12	105-120	55-60	4.42

As already stated, titanium alloys are particularly susceptible to fretting wear and fatigue [40, 41]. In fact, it has been illustrated that fretting can reduce the fatigue strength limit of a Titanium alloy from 700MPa to 200MPa. The susceptibility of the alloy to fretting initiated fatigue has been related to the reactivity of the alloy once the protective surface oxide is damaged. Since the oxide formed is thin (approx 30 nm), it may be expected that any action which disrupts the oxide film may have an effect on the fretting fatigue behavior. It is believed that microstructural transformations also contribute towards the fretting fatigue of the Ti-6Al-4V alloy. The alloy has a duplex microstructure consisting of primary α -phase in a transformed matrix of lamellar α platelets in β , as seen in Figure 2.4 [42]. During a deformation or temperature induced transformation, the microstructure of the titanium alloy transforms from a two-phase α (hexagonal close packed or h.c.p.) plus β (body-centered cubic or b.c.c.), to a single phase α (h.c.p.) microstructure which is more brittle. Deformation due to fretting of a two phase $\alpha + \beta$ structure results in the formation of a superficial layer consisting of 20-50 nm crystallites exclusively of the α phase. The transformed phase is susceptible to crack formation and fretting damage [7].

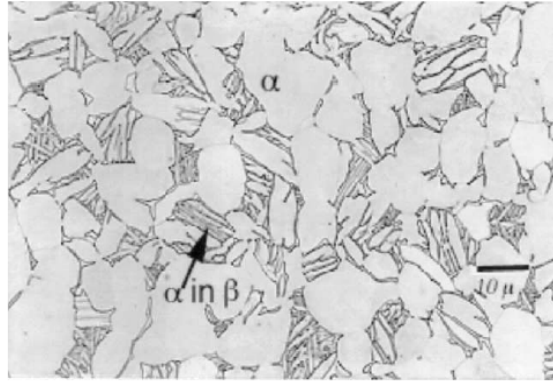


Figure 2.4: Microstructure of Ti-6Al-4V alloy [42]

The titanium alloy dovetails experience temperatures upto 450 °C in the compressor. It has been experimentally verified that the transition from mixed to gross slip fretting wear occurs at higher loads at room temperature. This may be caused by the strain hardening of the surface, which leads to brittle fracture of the surface and create large amounts of debris at the interface. However, at elevated temperatures, the softened surface is unable to strain harden resulting in a gradual transition from mixed to gross slip fretting. Therefore, elevating the temperature promotes the transition from mixed to gross slip fretting wear [39, 43].

2.2 Cold Spray Process

2.2.1 Introduction to Cold Spray Process

Thermal spray processes are widely used to apply protective coatings and to repair worn components such as large-diameter shafts in turbines and pumps [44]. These processes may be broadly classified into two regimes. The first category consists of the

processes in which the feedstock material is rendered molten by its introduction into a region of intense heat such as flame, plasma or arc prior to propulsion onto the substrate [45]. Consequently, the high heat input to the part being coated accompanying these processes can be detrimental if the material of the part degrades when subjected to high temperatures. This problem is generally avoided by using the second category of thermal spray processes which are based on the principle of particle impact and deformation. These methods exploit high particle velocities, have shorter transit times, and experience overall low temperatures of the feed stock material. These include Aerosol Deposition method (ADM), Gas Deposition Method (GDM), Electrostatic Particle-Impact Deposition Method (EPID), Supersonic Cluster Beam Deposition Method (SCBD), Hypersonic Plasma Particle Deposition Method (HIPPD), and the Cold Gas Dynamic Spraying Method (CGSM or simply cold spray) [45, 46].

The Cold Spray method is a relatively new coating method for deposition of metal, alloy, polymer, and/or composite powder material onto various substrates without significant heating of the spray powder or substrate [46]. Cold Spray is based on the selection of a combination of particle temperature, velocity, and size allowing spray coatings at the lowest temperature possible [47]. In the cold spray process, solid phase particles of size 1-110 μm are accelerated to velocities between 300 and 1200 m/s by the supersonic gas flow at low temperatures so as to provide the coating formation from particles in solid state [18, 48-50]. Figure 2.5 shows the specific temperature and velocity ranges of particles for various thermal spray methods. As shown in the figure, the jet temperature range for cold spray lies between 0 °C and 700°C, which is usually lower than the melting or softening temperature of the candidate powder and substrate

materials [51]. As a consequence, the deleterious effects of oxidation, evaporation, melting, crystallization, residual stresses, de-bonding, gas release, and other common problems in traditional thermal spray methods can be avoided [52].

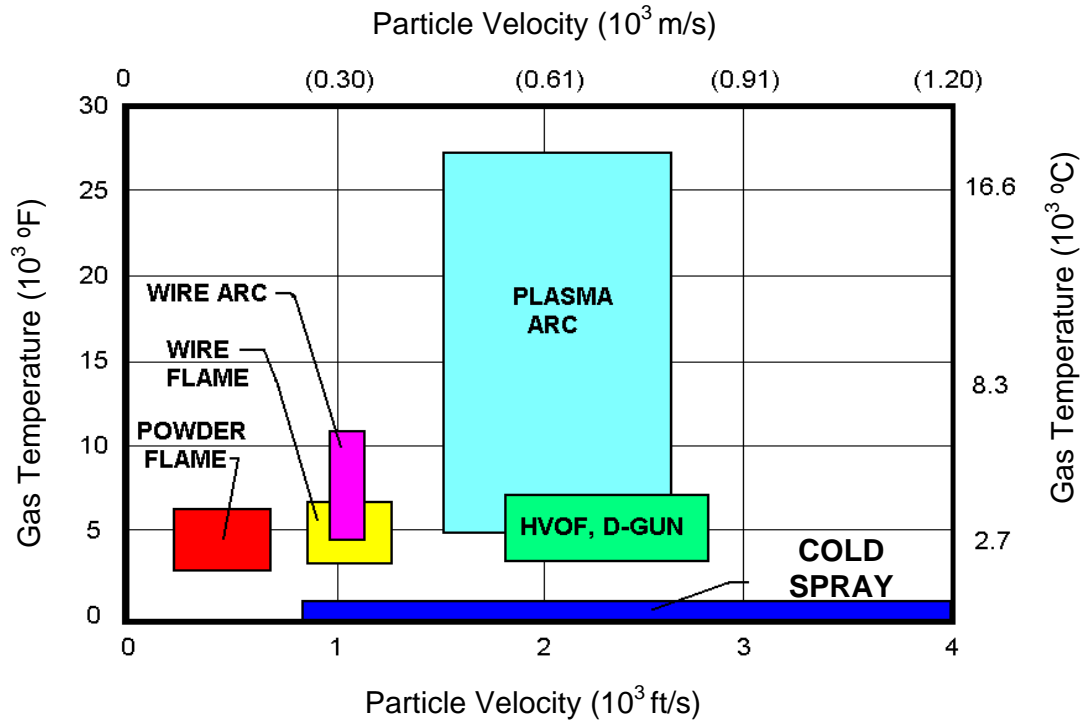


Figure 2.5: Temperature / velocity regimes for common thermal spray process compared to temperature and velocity in the Cold Spray [46]

Moreover, because of relatively larger particle sizes used, the deposition rate of the cold spray method is higher than that of other methods based on the principle of particle impacting. This is evident from Figure 2.6, which shows the particle diameter/velocity regimes for various dry particle impact based deposition processes [46].

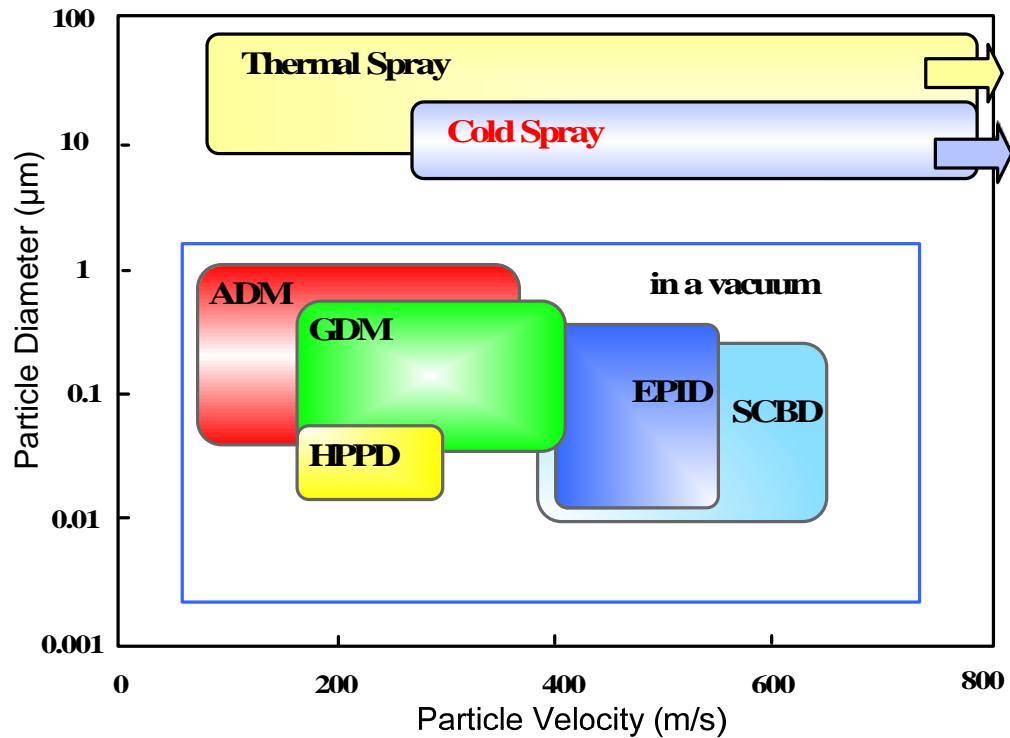


Figure 2.6: Schematized particle diameter/velocity regimes for various solid particle impact based deposition processes [46].

The cold spray process offers several advantages over the conventional thermal-spray material deposition technologies. Since the amount of heat delivered to the coated part is relatively small, the microstructural changes in the substrate material are minimal or nonexistent and the formation of brittle oxide phases is generally avoided. In addition, the macro- and micro-segregations of the alloying elements during solidification does not occur during cold spraying. Consequently, attractive properties of the powder material are retained in cold-sprayed bulk materials. The ‘peening’ effect of the impinging solid particles can also give rise to potentially beneficial compressive residual-stresses in cold-spray deposited materials in contrast to the highly detrimental tensile residual stresses

induced by solidification shrinkage accompanying traditional thermal-spray processes. A precise control over the process is possible due to the use of small size nozzle and resulting small spray beams. [53, 54]. Additionally, it may be possible to collect and reuse the powders which have not been incorporated in the coating with the help of dust collectors [55]. As such, the cold spray process is very versatile in its applications. Due to the absence of in-flight oxidation and other chemical reactions, thermally and oxygen-sensitive depositing materials (e.g. copper or titanium) can be cold sprayed without significant material degradation. The nano-phase, intermetallic and amorphous materials, which are not amenable to conventional thermal spray processes due to degradation of the depositing material, can be cold sprayed as well [56-61]. Cold spray of materials like copper, solder, and polymeric coatings offers exciting new possibilities for cost-effective and environmentally friendly alternatives to the technologies such as electroplating, soldering and painting [62-66].

The above mentioned advantages enable the use of cold spray process for a wide range of industrial products, such as turbine blades, pistons, cylinders, valves, bearing components, pump components, sleeves, shafts, seals etc. Several types of coatings including those used for strengthening, hardening, wear-resistance, corrosion-resistance, electro-magneto conductive and thermo-conductive applications can be successfully applied using the cold spray process. It is expected that sundry industries such as aerospace, petrochemicals, automotives, paper and printing, electronics, computers, biomedical, military and many others will benefit from this technology [51].

However, cold spray is usually limited to ductile materials like aluminum, nickel, stainless steel, copper, and titanium alloys [67-74]. Hard and brittle materials like ceramics can not be generally sprayed in pure form, but may be applied as composites with a ductile matrix phase [75]. Substrate materials are also limited to those that can withstand the aggressive action of the spray particles. Soft substrates will erode rather than be coated [18, 76, 77]. Lastly, post spray heat treatments may be required in order to improve mechanical properties of the coatings [78-79].

2.2.2 Cold Gas Dynamic Spray- Background

The cold spray method was developed at the Institute of Theoretical and Applied Mechanics of the Siberian Division of the Russian Academy of Science in Novosibirsk. Interestingly, the process principle was accidentally demonstrated during experiments designed to test high-speed re-entry vehicles in a supersonic wind tunnel using metal tracer particles. It was discovered that above a particular minimum particle velocity, the abrasion caused by the particles changes to adhesion, i.e., a coating was formed on the object. This effect was enhanced by an increase in gas temperature. Alkhimov, Papyrin, and coworkers successfully developed the process to produce coatings [80]. They successfully deposited a wide range of pure metals, metallic alloys, polymers and composites onto a variety of substrate materials. In addition, they demonstrated that very high coating deposition rates on the order of $3 \text{ m}^2/\text{min}$ ($300 \text{ ft}^2/\text{min}$) are attainable using the cold-spray process [81-83]

The process was named “cold gas-dynamic spraying” because of the relatively low temperatures (0 °C to 700°C) of the expanded gas and particle stream that emanates from the nozzle. A U.S. patent on the cold spray technology was issued in 1994 [18], and a European one in 1995 [48]. In the USA, a consortium was formed under the auspices of the National Center for Manufacturing Sciences (NCMS) of Ann Arbor, MI in 1994-1995. Presently, a wide spectrum of research on the cold spray process is being conducted at several research centers including the Institute of Theoretical and Applied Mechanics of the Russian Academy of Science, Sandia National Laboratories, the Pennsylvania State University, ASB Industries, Inc., Ford Motor Company, Thayer School of Engineering, Dartmouth College, Rutgers University, University of Bundeswehr, Germany, European Aeronautic Defense and Space Company, Germany, Shinshu University, Japan, and others [84-88]. Likewise, several companies including Flame Spray Industries, Ford Motor Company, General Electric-Aircraft Engines, General Motors Corporation, the Naval Aviation Depot, TubalCain Company and the Pratt and Whitney Division of United Technologies Corporation participated in the consortium [45].

2.2.3 Process Details

Cold spray is a material deposition process by which coatings of ductile materials, or composite materials with significant ductile phase content, can be applied to metallic or dielectric substrates by exposing their surfaces to a high-velocity jet of 1 to 110 μm particles accelerated by a supersonic jet of compressed gas. A conceptual drawing of the

cold spray equipment is shown in Figure 2.7 . Initially, the cold spray process was used to develop coatings with powder of size 1-50 μm [18]. Later, the process was modified and parameters were optimized so as to spray powders of relatively larger size, upto 110 μm [89-98].

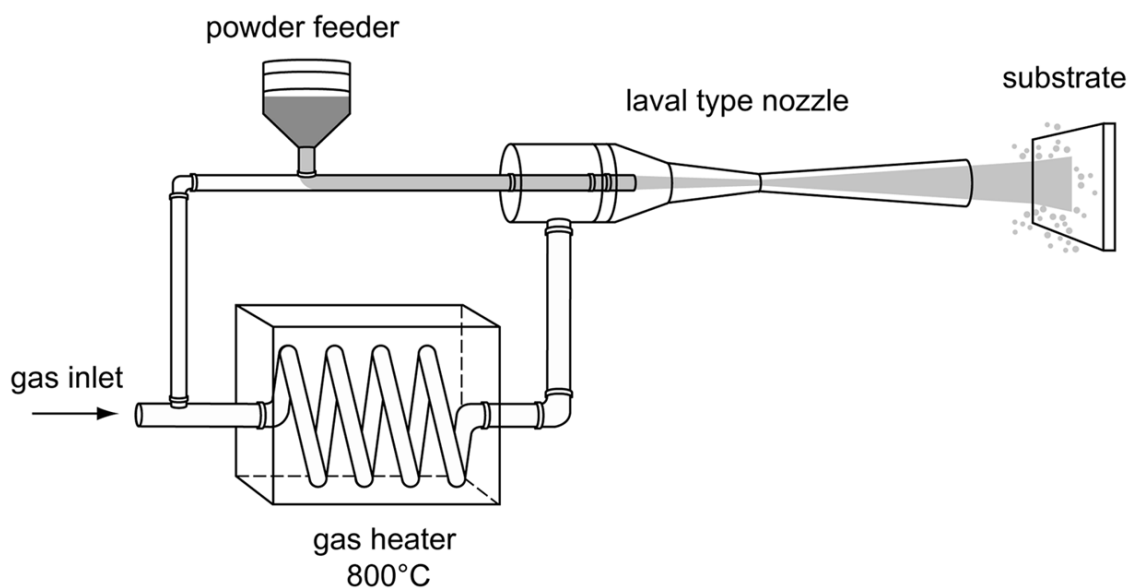


Figure 2.7: Conceptual drawing of the cold spray equipment and process [18]

Compressed gas, usually nitrogen, helium, or air, is introduced in a heater and a powder feeder. The pressurized gas is heated in a gas heater. Feedstock powder is injected axially into the gas flow at the gun nozzle intake. The spray gun is fitted with a convergent-divergent nozzle (de Laval nozzle) designed to produce a supersonic gas jet. The energy stored in the high pressure compressed gas moderately heats up the fine powder particles and accelerates them to very high velocities of 300-1200m/sec. On impact with a substrate, the powder particles deform and bond to form a coating [18]. In addition to coating deposition, cold spray process can also be used for net-shaping [88, 99, 100]

As with the other processes, a fine balance between particle size, density, temperature, and velocity are important criteria to achieve the desired coating [101-103]. The particles remain in the solid state and are relatively cold, so the bulk reaction on impact is solid state only. The process imparts little to no oxidation to the spray material, so surfaces stay clean which aids bonding. No melting and relatively low temperatures result in very low shrinkage on cooling, plus with the high strain induced on impact, the coatings tend to be stressed in compression and not in tension as with liquid/solid state reactions of most of the other thermal spray processes. Low temperatures also aid in retaining the original powder chemistry and phases in the coating with only changes due deformation and cold working. Deposited metals that can be used with this process include iron, stainless steel, nickel, copper, aluminum, molybdenum, titanium, and many alloys [104].

2.2.4 Bonding in Cold Spray

The actual mechanism by which the solid particles deform and bond during cold spray is still not well understood. However, it is well established that the powder particles and the substrate undergo an extensive localized deformation during impact. Such a severe contact causes disruption of the thin oxide surface films and enables an intimate conformal contact between the particles and substrate. The intimate conformal contact of clean surfaces combined with high contact pressures are believed to be necessary conditions for particles/substrate and particles/deposited material bonding. Due to very short particle/substrate contact times, atomic diffusion is not expected to play

a significant role in particle/substrate bonding [105-108]. However, local heating during impact may augment the bonding by a process akin to friction or explosive welding [109-111]. In some cases, an intermetallic phase from the sprayed powder and substrate material may form at the interface [70].

Some researchers have worked out a hypothesis for the bonding of particles in cold gas spraying, by using the numerical modeling of the deformation during particle impact. The results of modeling suggest that cold spray bonding mechanism can be attributed to adiabatic shear instability which occurs at the particle/substrate or particle/deposited material interfaces at high impact particle velocities. On the basis of this criterion, critical velocities can be predicted and used to optimize process parameters for various materials [112].

Further investigations on the susceptibility of metallic materials to adiabatic shear instability during cold spray were carried out. It was concluded that the localization of the plastic strain to the interfacial region combined with the thermal-softening effects leads to adiabatic shear instability in this region. This causes the injection of an interfacial jet consisting of the highly deformed material. The interfacial jet removes the oxide films from the surfaces of the particle and the substrate enabling an intimate contact of clean metallic surfaces and hence promoting particle/substrate bonding. Experimental investigations have shown that successful bonding is achieved only above a critical particle velocity, whose value depends on the temperature and the thermo-mechanical properties of the sprayed material and substrate. Results obtained after investigating a one-dimensional thermo-mechanical model for adiabatic strain softening and the accompanying adiabatic shear localization show that the minimal impact particles

velocity needed to produce shear localization at the particles/substrate interface correlates with the critical velocity for particles deposition by the cold-gas dynamic-spray process in a number of metallic materials. This finding suggests that the onset of adiabatic shear instability in the particles/substrate interfacial region plays an important role in promoting particle/substrate adhesion and, thus, particles/substrate bonding during the cold-gas dynamic-spray process [44, 105-107].

Debonding may occur due to the accumulation of compressive residual stress resulting from high level of cold work in the coating. An increase in the coating thickness aggravates the debonding as the stress due to strain energy release exceeds the bond strength of the coating. In order to overcome the problem of debonding and improve adhesion, higher gas temperatures and pressures can be used for recrystallization and stress-relief of the deposited coating [113]. Additionally, it has been observed that an incompatibility of plastic flow evolution in the coating and substrate causes the local bending of specimen which is the major cause of nucleation of the stress concentrator at the interface. The propagation of transverse cohesive crack in the coating as well as adhesive crack along the interface are the result of its relaxation [114, 115].

Researchers have investigated the adhesion mechanisms for different combinations of particles and substrates. It was concluded that the adhesion produced by cold spray processes appeared to be dependent on the combination of hardness of powder and substrate metals. Soft and ductile substrates produced stronger adhesion in comparison to hard and rigid substrates. In addition, it was concluded that soft metal deposits can be easily formed on any metals whether soft or hard. Figure 2.8 illustrates the deformation processes for different combination of substrates and powders [116].

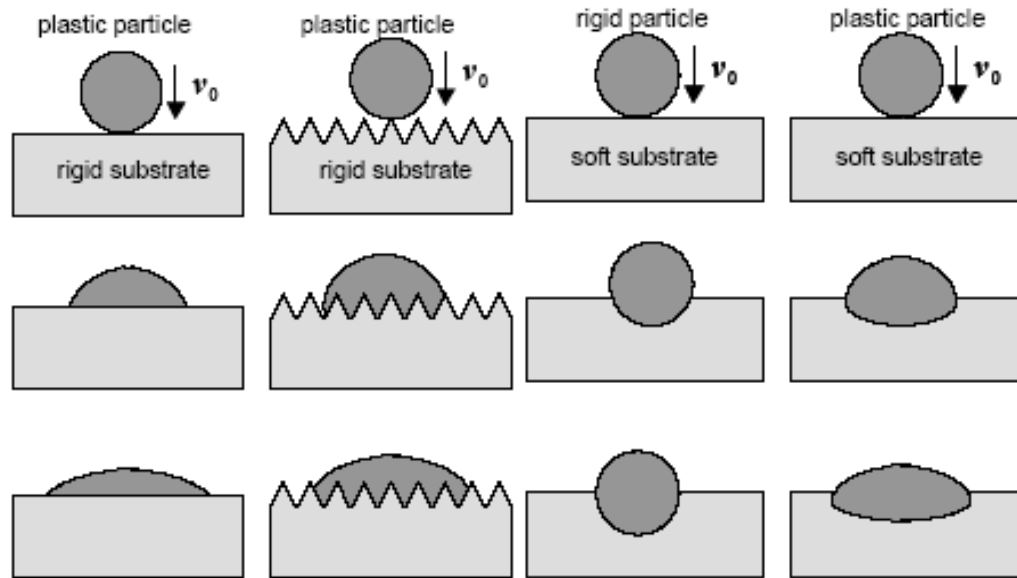


Figure 2.8: Schematic of deformation processes in different combinations of particles and substrate in cold spray coatings [116]

2.2.5 Cold Spray: Process Parameters

Cold spray is based on the selection of a combination of parameters such as particle temperature, velocity, and size allowing spray coatings at the lowest possible temperature [47].

Particle Velocity and Critical Particle Velocity

The particle velocity reflects the amount of acceleration of the powder particles injected into the gas stream before the throat of the nozzle. The particle velocity may vary from 500 m/s to 1000 m/s, depending upon the nozzle geometry, process gas, gas inlet pressure, gas inlet temperature, and size and density of the particles [64].

Below a critical particle velocity, successful bonding between the impacting particles and the substrate does not take place. Instead, the impacting particles only cause densification and abrasion of the substrate, in a way similar to that in grit blasting or shot peening [112]. The value of the critical velocity depends most significantly on the thermo-mechanical properties of the spray and the substrate materials. As such, the critical particle velocity changes with spray material. It has been reported that the critical particle velocities of Cu, Fe, Ni and Al are approximately 560–580, 620–640, 620–640 and 680–700 m/s, respectively. The critical particle velocity may be influenced by the sizes of the particles, the size distribution of particles and substrate materials [87]. Equation 2.1 shows an empirical formula for the determination of critical velocity for Cu. The particle velocity for any material is also determined by the nature, operating pressure, and temperature of the accelerating gas, and nozzle design [117]. The material parameters such as density, particle size and morphology influence the acceleration and subsequent deposition behavior of the particles. It has been reported that a dense coating can be deposited by cold spraying when spray conditions result in a particle velocity larger than the critical particle velocity [112].

$$V_{cr} = 667 - 14\rho + 0.08 T_m + 0.1\sigma_u - 0.4 T_i \quad (2.1)$$

where ρ is the density in g/cm^3 , T_m is the melting temperature in $^{\circ}\text{C}$, σ_u is the ultimate strength in MPa and T_i is the initial particle temperature in $^{\circ}\text{C}$.

Process gas

Higher particle velocities for the same inlet conditions and nozzle geometry are achieved with pure helium, and Helium-Nitrogen mixtures (Table 2.3). Helium has a relatively low density and higher specific heat ratio as compared to nitrogen. Therefore, helium provides higher exit velocities and higher kinetic energy to particles. Hence, it is possible to accelerate larger particles using helium [64, 104]. Because of the prohibitive price of helium, plants with helium recycling capability are being developed. These systems are designed to recover and reuse 95% of the helium used in the process [118].

Table 2.2: Comparison of helium and nitrogen as process gas [119]

	Nitrogen	Helium
Relative Cost	1	21 9.6 (recycled)
Density, kg/m ³	1.170	0.167
Specific heat capacity, J/kg K	1,040	5,190
Thermal conductivity, W/mK	0.0255	0.1536
Heat transfer coefficient, W/(m ² .K),	500	775
Relative heat transfer coefficient	1.00	1.55

Process Gas-Velocity and Temperature

Figure 2.9 illustrates the velocities and temperatures of the process gas with respect to corresponding length scales of the pre-chamber and nozzle. Different Computational Fluid Dynamic (CFD) codes have been used to simulate the particle behavior and the effect of various process parameters on the velocity and temperature of the particle [64].

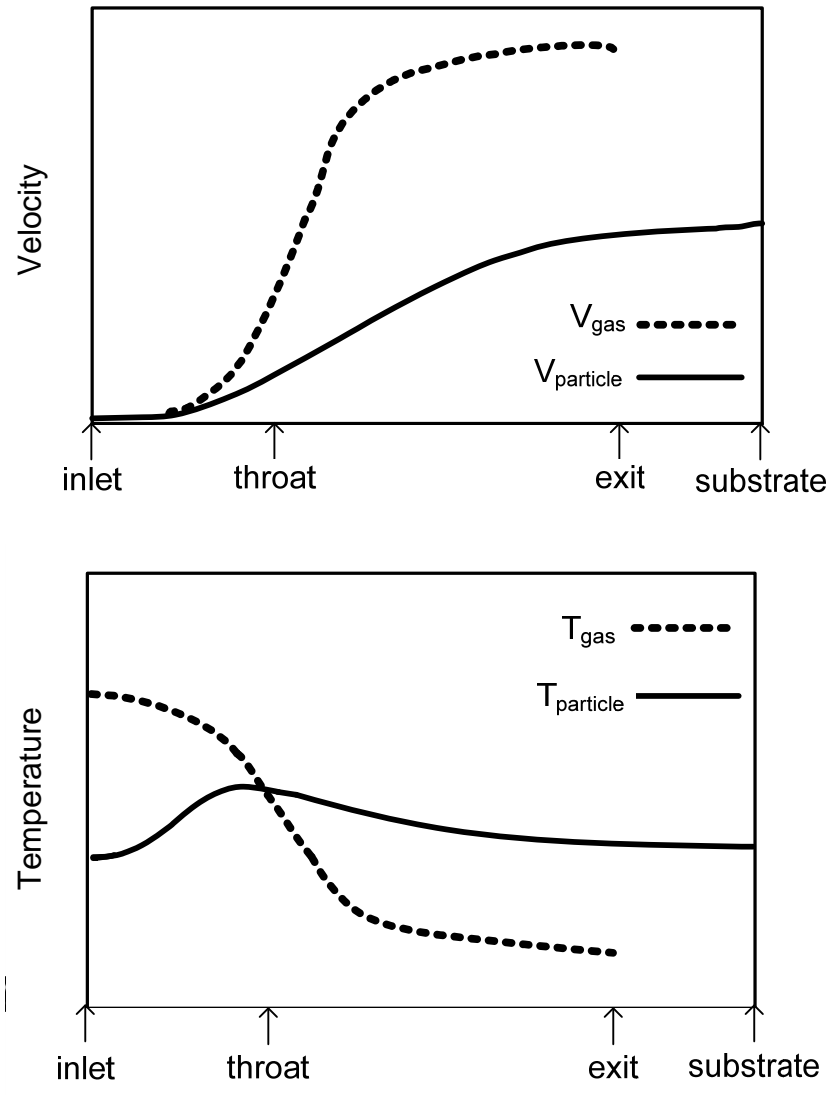


Figure 2.9: Typical course of a) velocity and b) temperature of the gas and particles in nozzle [64]

Some researchers studied the effect of pressure and temperature of gas on the deposition efficiency by cold-spraying copper and titanium powders. It was observed that the deposition efficiency of both copper and titanium coatings increased with the pressure and temperature of gas at the nozzle entrance because of the increase the gas velocity, or the particle impact velocity [120].

Further experiments demonstrated that an increase in gas pressure not only improves the deposition efficiency, it also enhances the substrate deformation, thereby resulting in an increase in micro-hardness of the deposit due to higher levels of work hardening. However, at elevated gas temperatures, any benefits of increasing the gas velocity are counteracted by the decrease in the density of the gas which reduces the drag on entrained particles. Using microstructural observations and micro-hardness measurements, it was inferred that at a constant gas pressure, elevated spraying temperatures result in recrystallization of the coatings. This research also indicated that the tendency for coatings to de-bond from the substrate is greatly reduced at elevated temperatures of spraying due to the phenomenon of recrystallization [113].

During deposition, the incoming compressed gas can be introduced at room temperature, or preheated in order to achieve higher gas flow velocities in the nozzle. Although preheat temperatures as high as 630 °C are sometimes used, the gas rapidly cools as it expands in the diverging section of the nozzle. Hence, the dwell time of the particles in contact with the hot gas is brief, and the temperatures of the solid particles at impact remain substantially below the initial gas preheat temperature [108].

Particle size

Previous research illustrated that at the same inlet condition, the velocity of smaller particles is greater than that of the larger particles at the exit of the divergent section of the nozzle. Additionally, while the particle density has a significant effect on the acceleration of larger particles, this disappears when the particle diameter was below 0.1 μm [121].

Nozzle

The maximum gas velocity at the nozzle exit is realized when a sonic velocity is achieved at the nozzle throat. Such a condition is referred to as choking of the nozzle. For any nozzle, the value of critical throat area for a given set of flow conditions below which the nozzle is choked is given by Equation 2.2

$$A^* = \frac{m_o}{P_o} \left(\frac{RT_o}{\gamma} \right)^{\frac{1}{2}} \left(\frac{2}{\gamma+1} \right)^{\frac{-(\gamma+1)}{2(\gamma-1)}} \quad 2.2$$

where m_o is the gas mass flow rate, P_o is the gas stagnation pressure, T_o is the gas stagnation temperature, R is the gas constant and, γ is the ratio of the constant pressure and constant volume specific heat capacities (C_p/C_v) for the gas [113] .

Nozzle geometries of either a round or a rectangular cross section can be used for the cold spray process. At the same ratio of the exit and critical cross sections, nozzles with a rectangular section can provide, on one hand, a wider spray beam in the direction of smaller size of the section and, on the other hand, a more narrow beam (to 1-2 mm) in the direction of larger size of the section. Such nozzles can also decrease the effect of the particle deceleration in the compressed layer in front of the substrate due to decreasing thickness of the layer [47]

Numerical and experimental research of wedge-shaped nozzles showed that there is a specific nozzle geometry that produce the maximum possible particle velocity at the moment of impact on a target surface [53]. Furthermore, it was found that if the cold-spray nozzle is designed in such a way that at each axial location the acceleration of the particles is maximized, a significant increase in the average velocity of the particles at the

nozzle exit can be obtained. For the optimum design of the nozzle, helium as the carrier gas was found to give rise to a substantially higher exit velocity of the particles than air [44]. A longer nozzle is useful only to the acceleration of micron size particles. In order to achieve a higher particle velocity, it is possible to optimize a nozzle length for different particle sizes [121].

Substrate Condition

A study on the influence of substrate condition on cold sprayed coatings by spraying copper and titanium powders was conducted. It was observed that while the deposition efficiency of copper increases with increasing substrate thickness, that of titanium decreases slightly. However the temperature of the substrates after coating decreases in both cases. An increase in surface roughness from 0.2 μm (polished surface) to 0.7 μm (blasted surface) resulted in slight increase in the deposition efficiency of both coatings. By increasing the substrate preheat temperature, the deposition efficiency of copper decreases slightly, while that of titanium increases slightly [120].

Deposition Efficiency:

The deposition efficiency is the ratio, expressed in percentage, of the weight of spray deposit on substrate to the weight of powder sprayed. Figure 2.10 illustrates the dependence of the deposition efficiency on particle velocities for several metal powders. The two characteristic ranges of deposition efficiency are bounded by the critical velocity. The first range where the particle velocity is below the critical velocity corresponds to the process of substrate erosion. However, with a steady increase in

particle velocity up to the critical value, the coating process begins [121]. Deposition efficiency is improved at higher gas pressures and temperatures since the particle velocities are increased [122].

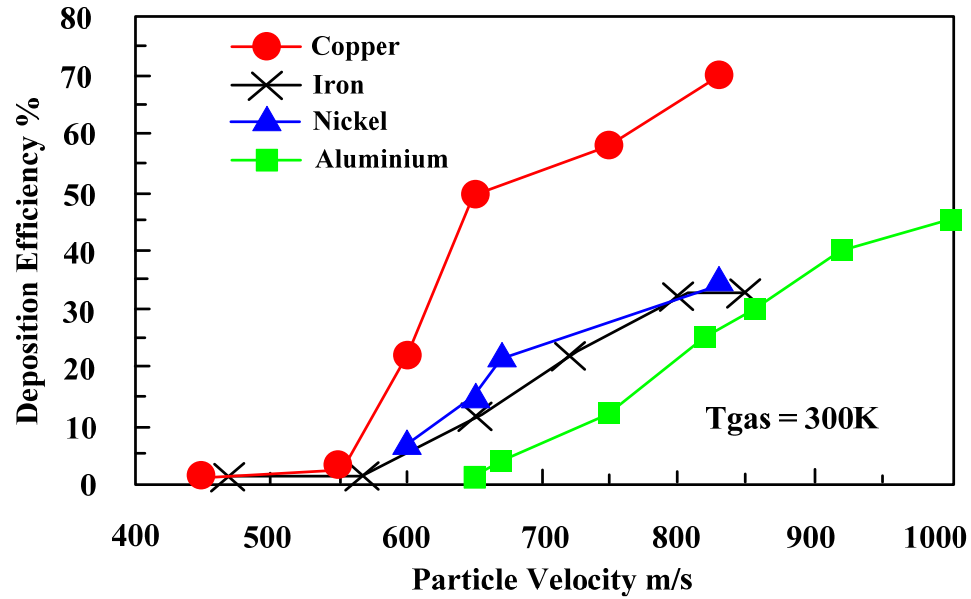


Figure 2.10: Deposition efficiency as a function of particle velocity for four typical powders on copper substrate at ambient jet temperature [45]

2.2.6 Cold Spray of Composite Powders

Recently, the cold spray process has been investigated for several composite coating systems. Composite powders consisting of micrometers sized Ti powder and nano-sized hydroxy-apatite powder have been deposited for biomedical applications [123-125]. Experiments on the deposition of Fe-Si with Si content higher than that achieved with other coating techniques for improved properties of magnetic components have been successful [56]. W-Cu composite materials used in electronic package

applications have been deposited by cold spray. The developed coating offers a potential economic alternative to the infiltration process [126]. W-Co composite coatings for heat sink and contact material applications have been deposited [127-129]. The current research aims at the development of composite coatings with self lubricating properties for the protection of dovetail joints of turbine blades using cold spray process.

2.3 Self-Lubricating Coatings

2.3.1 Introduction

Most of the proposals to protect a material from fretting wear fall into the following three categories: a) Reduce relative slip or vibration, b) Raise the strength by changing the base material or by surface treatment, and c) Lower the coefficient of friction. These palliative methods may be interactive and sometimes contradictory. For instance, lubrication, one of the methods for preventing fretting damage, allows relative movement between the contacting surfaces, but with as low a coefficient of friction as possible [130].

At extreme conditions of temperature and pressure, where conventional organic lubricants cannot survive, it is imperative to apply solid-film lubrication. Table 2.3 lists the different applications of solid-film lubricant composite coatings [131]. In order to protect contacting surfaces from friction and wear, solid-film lubricants must have a low coefficient of friction and provide with low shear strengths. Additionally, they should

provide uniform coverage on the substrate by forming an integral bond with the substrate, which is strong enough to survive severe service conditions.

Table 2.3: Applications of Solid-Film Lubricants[131]

Application	Primary Environment	Operating Requirements
Journal bearing	Nuclear radiation	No deterioration
Conveyor slide rail	Food processing	No contamination
Threaded tubing sliding die core	Liquid oxygen, high-pressure vacuum	No deterioration, no seizing, low torque
Plain spherical bearing	High load	Low torque
Thrust washer	High sliding speed	No abrasion
Gears	Helium coolant	Reduced friction
Self-locking nuts	High temperature	No galling
Turbine blade roof	High temperature	No galling
Wire rope	High load	No scoring
Valve	Cryogenic fluid	No reactivity
Fastener	Water	No corrosion
Press-fit part	High load	Smooth assembly
Spacer	Room temperature	No leakage
Compressor nozzle	High temperature	No evaporation
Rolling contact bearing	Vacuum	Low torque

There has been considerable interest in identifying and developing solid lubricating systems which can survive at higher operating temperatures and offer a superior load-bearing capacity than liquid lubricants. Solid lubricating films, however, tend to be worn away rapidly and thus require some mechanical means for replenishment. Since continuous replenishment is impractical for many hard-to-reach surfaces in motion, self-lubricating materials are being increasingly used for applications such as air flight, space flight, and military equipments [132].

Self-lubricating coatings are essentially composite alloys, comprising of a phase with characteristic lubricating properties. Periodic lubrication during service can be

avoided by using self lubricating coatings for a variety of components operating at a wide range of temperatures, loads, and speeds [131]. The solid lubricants used for self-lubricating coatings are mainly based on molybdenum disulphide (MoS_2) [133-153] and boron nitride (BN) [131, 154-156].

2.3.2 Self Lubricating Coatings based on Molybdenum-disulfide

Molybdenum disulphide (MoS_2) has a highly anisotropic crystal layer structure, which consists of a layer of molybdenum atoms arranged in a hexagonal array with each molybdenum atom surrounded at equal distance by six sulfur atoms placed at the corners of a triangular prism. Within the MoS_2 ‘sandwiches’ there is strong covalent bonding, but between the sandwiches only weak Van der Waals’ forces exist, resulting in low shear strength, and hence low friction in the sliding direction. The basal plane of the crystals in polycrystalline films lies parallel to the sliding direction for good lubrication. Due to its favorable structure, MoS_2 is the most widely used lamellar compound solid lubricant for space applications and is used in release mechanisms, precision bearing applications, main weather sensor bearings and gimbal bearings. Unlike fluid lubricants, MoS_2 is suitable for use in a vacuum environment because of its low out-gassing pressure and lack of migration [148-152].

Investigations of fretting tests with MoS_2 powder showed that low frictional energy is observed during the initial stage of fretting. However, frictional energy eventually increases with the number of fretting cycles and reaches the same value as in non-lubricated tests. Recent developments in the field of new surface modification

techniques have allowed depositing anti-friction film such as MoS₂ on the contact surfaces [130, 145, 146]. The coefficient of friction under magnetron-sputtered MoS₂ film deposition with thickness of 1 mm was only about 0.06 for the first 500 cycles, owing to the protection of the film, and then increased rapidly to 0.48 due to film degradation. Eventually, the coefficient decreased to 0.12 during passage from two to three-body contact, and then rose slowly at 2400 cycles due to MoS₂ debris ejection from the contact, finally reaching a value similar to that of bare contact [130]. The generation of significant film debris is considered undesirable, because long endurance becomes dependent upon the retention or recirculation of the film particles in the contact zone, rather than on the gradual wearing away of the film [147]. MoS₂ properties degrade when in humid air, causing an increase in friction coefficient and a decrease in a lifetime [145-152]. Most importantly, molybdenum disulfide experiences major increase in coefficient of friction as it loses its lubricity at temperatures between 400° C and 500° C [145, 154].

The failure of pure MoS₂ coatings for fretting wear applications motivated the development of self-lubricating composite coatings. These coatings contain a solid lubricating phase along with a hard, ceramic or metallic matrix phase as distinctly segregated crystalline phases. They possess the desired combination of lubricity and structural integrity [132]. Such coatings have very low friction characteristics and high hardness, which results in very low wear rates. The MoS₂ based self-lubricating coatings have ideal properties for a wide range of applications, including dovetail joints [148-152].

2.3.3 Self-Lubricating Coatings based on Boron-Nitride

Boron nitride powder is a soft, white, lubricious refractory material with unique characteristics that make it an attractive, performance-enhancing alternative to molybdenum disulfide, graphite and other frequently used inorganic solid lubricants. With its superior adherence and thermo-chemical stability, boron nitride presents an opportunity to formulate new solid lubricants for applications where conventional solid lubricants break down or fail to deliver the desired performance. The inorganic solid lubricant retains its ability to lubricate in extreme cold or heat and is well suited to extreme pressure applications. In addition, BN is environmentally friendly and inert to most chemicals. BN also displays excellent electrical insulating properties and maintains those properties in vacuum, unlike graphite [154-156].

The two common crystalline structures of BN are cubic and hexagonal. Cubic boron nitride, (c-BN) is like diamond, being hard and abrasive, while hexagonal boron nitride (h-BN) is soft and lubricious like graphite. Hexagonal boron nitride powder exhibits the same characteristics of solid lubricants found in graphite and molybdenum disulfide. These include crystalline structure, low shear strength, adherence of the solid lubricant film, low abrasivity, and thermo-chemical stability. In many instances, h-BN exceeds the performance levels of these conventional solid lubricant characteristics, particularly adherence and thermo-chemical stability. In addition, h-BN yields the lowest coefficient of friction with respect to all the other solid lubricating materials. This is clearly evident from Figure 2.11. Hexagonal BN also exhibits better extreme pressure characteristics and higher weld points as compared to graphite, molybdenum disulfide

and other solid lubricants. It may be noted that the weld point is the amount of applied weight-kilograms of force (kgf), that causes the lubricant to break down, allowing welding or metal-to-metal transfer [154-156].

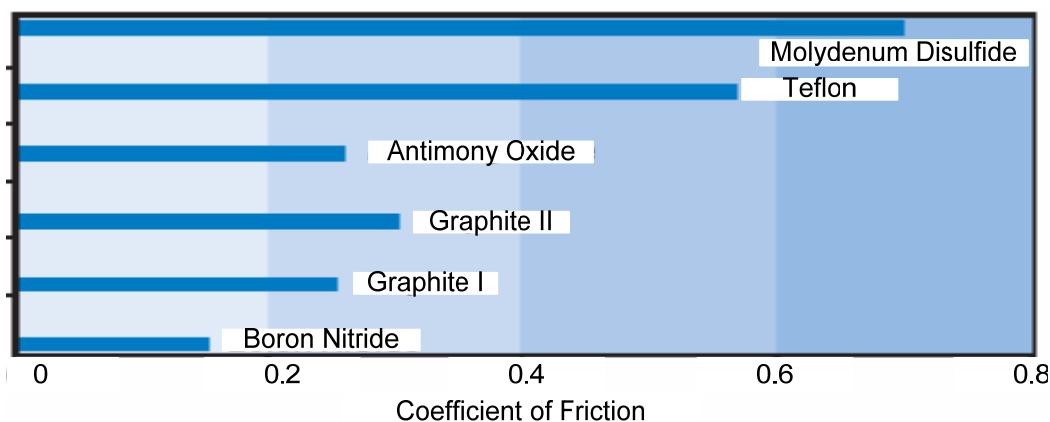


Figure 2.11: Comparison of friction coefficients of various solid lubricants using the Falex Coefficient of Friction Test developed at Falex Corporation [154]

Another important characteristic of (h) BN is its ability to retain lubricity at elevated temperatures. BN has an oxidation threshold of approximately 850° C, and even up to 1000° C, the rate of reaction is negligible. Other inorganic solid lubricants such as graphite and molybdenum disulfide experience major increases in coefficient of friction (lose their lubricity) at between 400° C and 500° C [156]. Figure 2.12 illustrates the changes in coefficient of friction for molybdenum disulfide and (h)BN as the temperature increases in air [154].

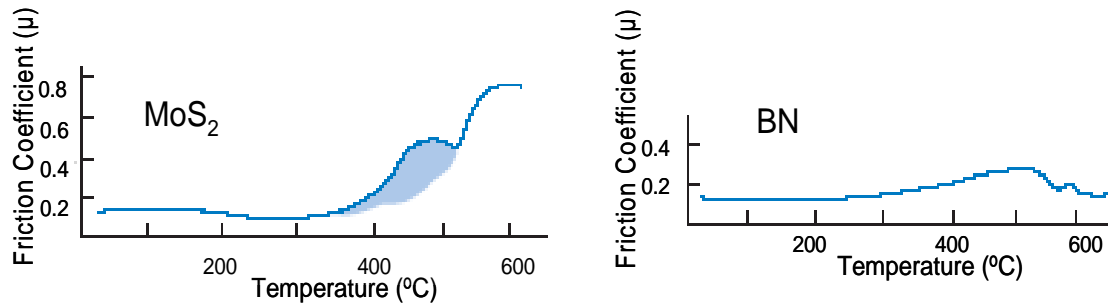


Figure 2.12: Coefficient of friction of MoS₂, and (h) BN at various temperatures [154]

Electro-deposition or electroplating of fine particles of (h) BN with Nickel was investigated for the development of a self-lubricating metal-ceramic coating for metal substrates in engine parts. The anti-friction and anti-corrosion nickel-(h) BN composites exhibited superior friction properties under non-lubricated, high-load conditions [154]. Increased percentages of (h) BN improved hardness and wear, in spite of (h) BN's soft and easy sliding nature, as evident from Tables 2.4 and 2.5. Hardness improvements seem to have resulted from the uniform distribution of (h) BN particles in the nickel matrix. Lower wear was explained by the glazing and adhesion of the (h) BN particles that remain in place after initial wear, providing effective lubrication and separation of the remaining metal surfaces [131].

Table 2.4: Micro-hardness and wear resistance of nickel and nickel-boron nitride composite coatings [131]

Systems	Hardness (KHN)	Wear Index
Nickel	265	45.5
Ni-BN (5-6%)	380	22.1
Ni-BN (7-8%)	350	20.8

Table 2.5: Taber Wear Index of Ni-BN Composites (Load: 1Kg, CS-10 Calibrase Wheel) [131]

Coating	Cycle 1	Cycle 2	Cycle 3
Mild Steel	5.7	4.9	4.8
Ni-BN, 11.8 vol%	5.0	4.5	3.6
Ni-BN, 19.6 vol%	4.5	3.9	3.4
Ni-BN, 28.8 vol%	3.5	2.5	2.4

In the current research, Ni-BN self lubricating coatings have been developed via the cold spray process. The coatings offer the attractive benefits of Ni as a wear resistant material and BN as an effective and stable lubricant. The following chapter details the experimental procedures involved in the research.

Chapter 3

Experimental Procedures

The chapter describes powders used for the project, and the experimental procedures used for powder testing and feedstock preparation via admixing and milling. After that, the cold spray coating technique and specific parameters used for this study have been detailed. Finally, the various techniques used for evaluation of coatings, such as optical and scanning microscopy, micro-hardness testing, adhesion testing, and fretting wear analysis methods have been explained.

3.1 Powders

Commercially available Nickel (Ni), Molybdenum-di-dulfide (MoS_2), Boron Nitride (BN), and Nickel coated Boron Nitride powders were used for this study. Table 3.1 summarizes the as-received powders. The 75 μm and 103 μm Ni coated BN powder had 20 wt % and 10 wt. % BN respectively.

3.2 Powder Characterization

The as received powders were characterized for shape, size distribution, and micro-hardness measurements. These properties provided an insight into the behavior of the powders during cold spraying.

Table 3.1: Summary of the as-received powders

Sr. No.	Material	Powder Size (μm)	Vendor	Designation	Lot No.
1	Ni	12	Novamet	Inco Ni powder	3465211
2	Ni	30	Praxair Surface Technologies	Ni-101	216
3	Ni	75	Atlantic Equipment Engineers	Ni-122	50752
4	MoS ₂	3	Atlantic Equipment Engineers	Mo-801	406508
5	MoS ₂	30	Rosemill Co.	MoS ₂ Powder	CAS01317-33-5
6	BN	10	FJ Brodmann and Company	BN Flomaster	753
7	Ni coated BN (90 wt % Ni)	75	Federal Technology Group	Ni coated BN (90-10)	PTX60
8	Ni coated BN (85 wt % Ni)	103	Federal Technology Group	Ni coated BN(80-20)	-

3.2.1 Particle Shape and Microstructure

In order to study the morphology, the as-received powders were observed under a Scanning Electron Microscope (model: ABT-32, supplier: TOPCON, Pleasanton, CA). Scanning electron microscope (SEM) utilizes the interaction of electrons with the test sample to observe the surface microstructure. An electron beam is emitted from a heated tungsten element. A system of magnetic lenses (condenser and objective lens) is used to focus the electrons into a narrow beam. The magnification of the beam is controlled by adjusting the current through the scanning coils. Electrons are emitted from the sample surface due to excitation of the electron beam. These electrons are then collected by an

electron detector and amplified by the electron amplifiers. The amplified signal reveals the surface topography of the sample, which is displayed on a cathode ray tube (CRT). Vacuum pumps are used to generate vacuum during the operation of an SEM. \

Typical morphologies of the as-received powders are shown in Figure 3.1- 3.4. Ni powder formed by the carbonyl decomposition process is irregular and spiky in shape. Lubricant powders (MoS_2 and BN) which were manufactured by the milling process have a platelet structure. Figure 3.4 shows the SEM images of Ni coated BN powder. The powders are irregular in shape.

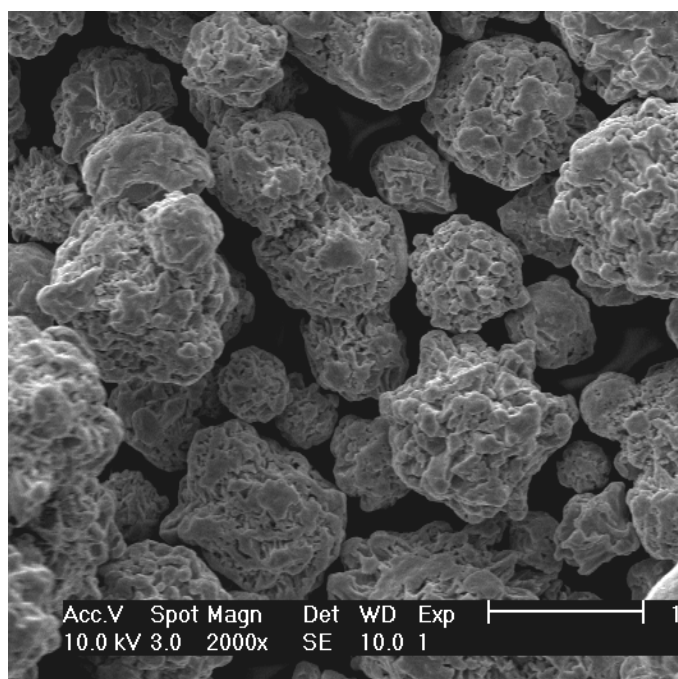


Figure 3.1: SEM image of as-received Ni powder

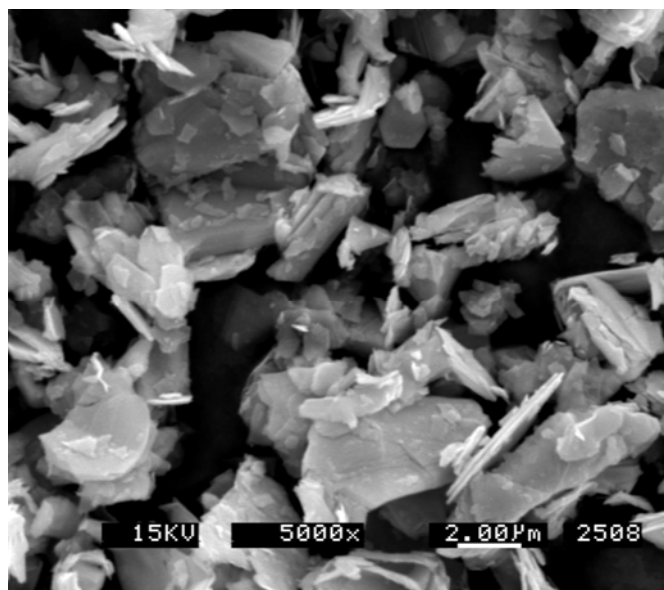


Figure 3.2: SEM image of as-received MoS₂ powder

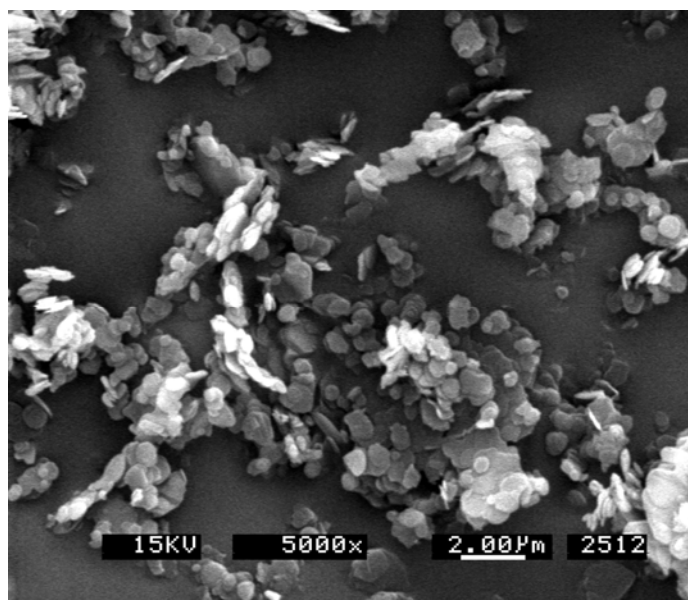


Figure 3.3: SEM image of as received BN powder

Additionally, the internal structure of the cross section of the Ni coated BN powders was studied under the optical microscope. A representative powder sample was mounted in epoxy and was polished on the Rotopol polisher. Figure 3.5 reveals three different phases present in a single coated particle. The interior of the particle consists of

BN. There is a thin outer layer of Ni coating on each particle. However, in most of the particles, there is an intermediate layer between Ni and BN, which has a lamellar structure. In some rare cases, the particle is completely comprised of the lamellar structure.

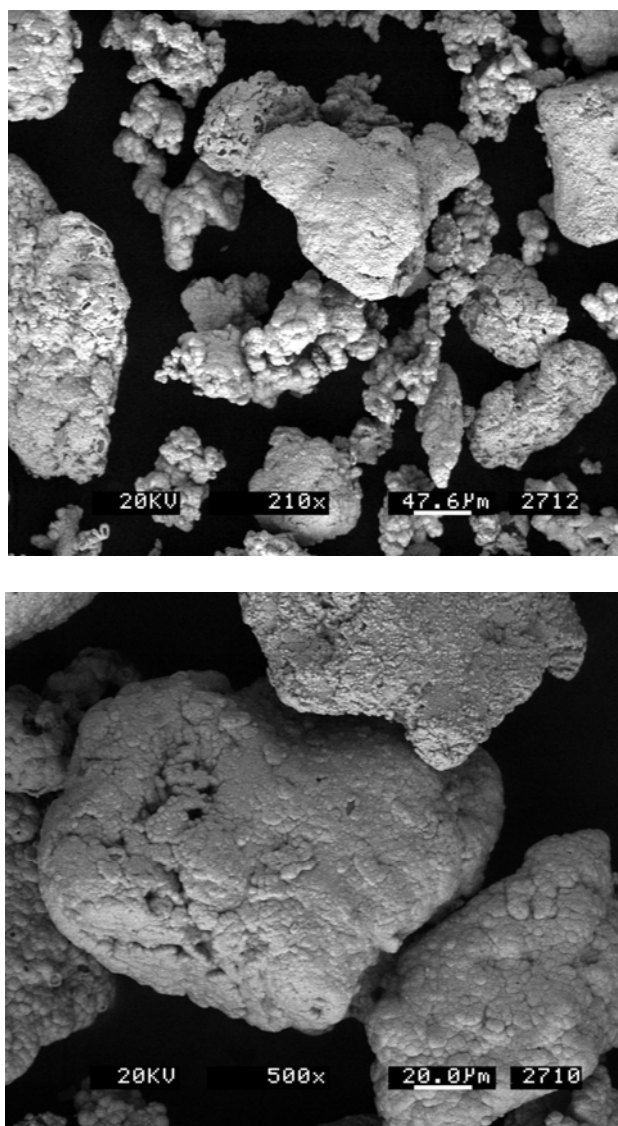


Figure 3.4: SEM images of as-received Ni coated BN powders

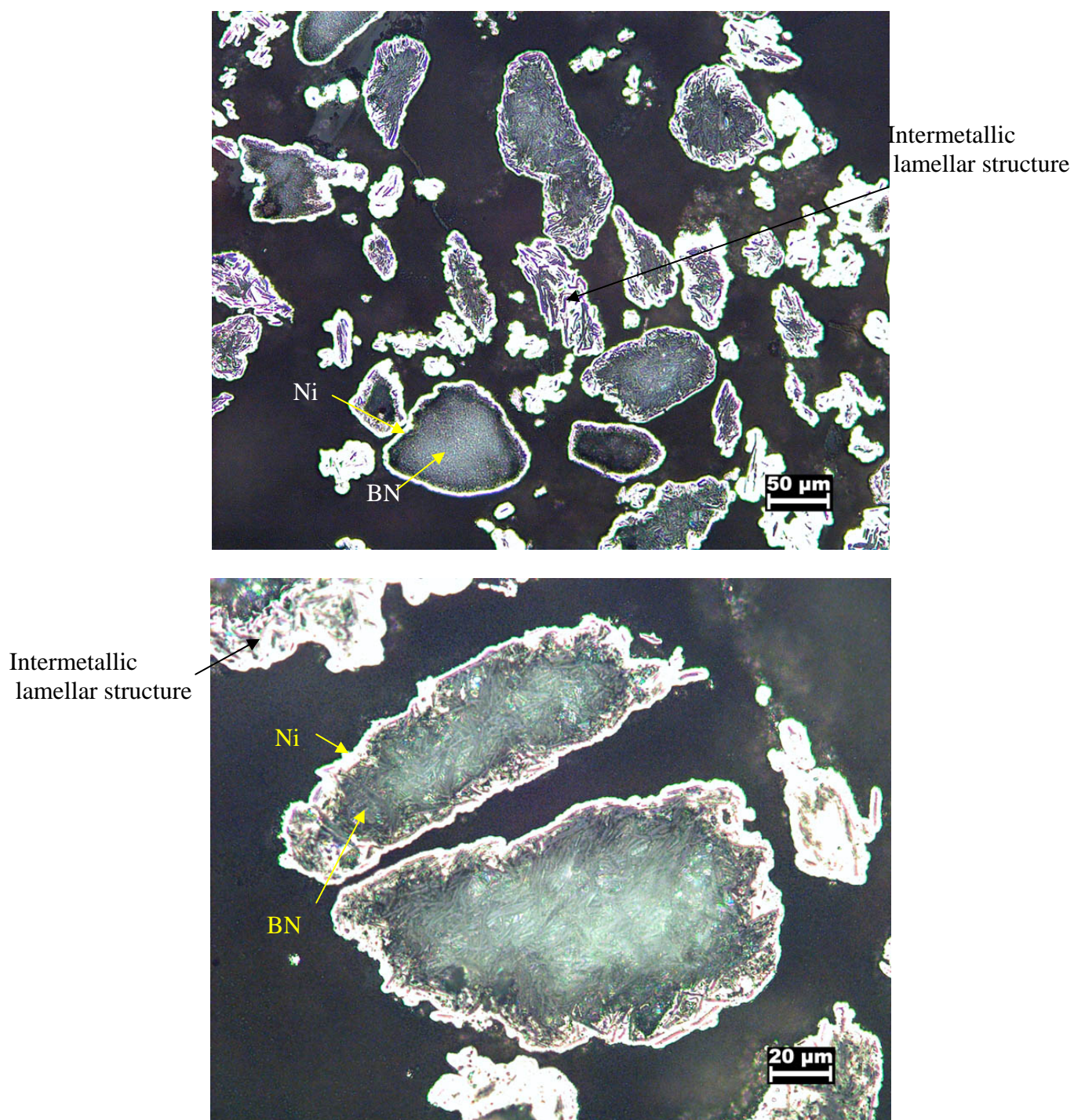


Figure 3.5: Optical Image of Ni-coated BN

3.2.2 Particle Size Analysis

Particle size analysis of the as-received and the milled powders was carried out using a laser scattering particle size analyzer (model: Horiba LA-920, supplier: Horiba Instruments Inc., Irvine, CA). The instrument is capable of measuring particle sizes within the range of 0.02 to 2000 μm . The operation of LA-920 utilizes the light scattering due to the powders dispersed in fluid medium to measure the particle size and distribution. Mie theory [157], which states an inverse relationship between the angle of the scattered light and particle diameter is used as the basic measuring principle. Two light sources (He-Ne laser and tungsten lamp) are used to illuminate the particles dispersed in liquid medium. Particles greater than 3 μm scatter light in the direction of its original travel which further pass through a condenser lens. The output from the condenser lens is a pattern of concentrating rings (Frounhofer dispersion). Smaller particles ($<3 \mu\text{m}$) scatter the light to the sides and back towards to the source. A series of photo diodes measure the angle and intensity of the scattered light. Computer analysis of these data provides the particle size distribution. The instrument is calibrated and checked for repeatability every month using a standard reference material of stainless steel spheres and carbonyl powder of known particle size distribution. A standard deviation of less than 1% of average value was recorded on testing reference materials.

3.2.3 Pycnometer Density

Pycnometer density gives a measure of the actual density of the powder. This value can be less than the theoretical value due to presence of internal porosity or

impurities such as oxides. The true density values of the as received Ni and Ni coated BN powders were measured using a helium pycnometer (Micrometrics Accupyc 1330). The unit was calibrated using stainless steel calibration balls of known volume and density. The calibrated density was within 0.05% of the given value. A known mass of powder is placed in the sample cell of volume V_0 . A reference cell of volume V_c , is pressurized to P_1 . The sample cell is then connected to the reference chamber. There is a drop in chamber pressure to an equilibrium value of P_2 . By applying the ideal gas law the powder volume V_p can be calculated as per Equation 3.1.

$$P_1(V_s - V_p) = P_2(V_s - V_p + V_c) \quad 3.1$$

The actual density of the powder was determined to an accuracy of 0.01 g/cm^3 . Fifteen measurements were performed for each powder. A variation of less than 0.1% was observed in the measured readings.

3.2.4 Micro Hardness Measurement of Powders

Micro-hardness was measured using a Leco hardness testing machine as per the MPIF Standard 51 instructions. The powders were mounted in epoxy and polished on the Rotapol. Auto-polisher. Hardness measurements were conducted by using a vickers diamond pyramid indenter. A load of 10 g was applied for a dwelling time of 10 seconds during the measurement of micro-hardness. A Leco video line micrometer VL-101 was used for measuring the length of the indentation on diagonals. The Vickers hardness number was calculated by dividing the applied load in kilograms force by the measured

projecting area of the resulting indentation (Equation 3.2). The indentation projected area was computed from the mean of the measured diagonals of indentation.

$$HV = \frac{1854.4P}{d^2} \quad 3.2$$

where HV is the Vickers hardness number, P is the force in grams, and d is the mean of the two diagonals in micrometers.

3.3 Feedstock Preparation

Feedstock for the spraying was prepared by either admixing, or mechanical milling.

3.3.1 Admixed Powders

Ni and lubricant powders were weighed accurately and mixed so as to obtain the desired composition. The powders were weighed with an accuracy of 0.001 gram using an electronic balance. The weighed powders were placed in a polypropylene jar and mixed in a turbula mixer (Glen Mills T2C) for 2 hours. Due to the 3D spiral motion of the turbula, the powders were imparted with sufficient energy for the homogenous mixing.

3.3.2 Milled Powders

Ni and lubricant powders were accurately weighed using an electronic balance and placed in a polypropylene jar. The powders were ball milled on a jar milling apparatus (Supplier: Speed Selector Inc., Model 4000) with grade 440 C stainless steel balls (diameter: 4.75 mm) for specified time. The ball to powder ratios for Ni- MoS₂ and Ni-BN mixtures were 3:1 and 3.5:1 respectively. Heptane was added to the mix in order to avoid any oxidation of the powders. As the jar rotated, the powder filled the interstitial voids between the balls. Due to continuous collisions with the balls, the powders undergo a series of fracture and welding to form large size agglomerates. The milled powder was dried and sieved at 53 or 75 µm to achieve constant powder feeding and a homogeneous coating.

3.4 Cold Spray Process and Equipment Detail

Figure 3.6 illustrates a schematic of the cold spray system (Supplier K-Tech Corporation). A compressed and heated gas was accelerated to supersonic velocity in a de-Laval nozzle. Feedstock powder was injected into the gas jet at the nozzle intake and then propelled onto the substrate. During deposition, the spray gun was manipulated by a robot. Plastic deformation of particles upon impact produced high strength bonds between the powder and the substrate.

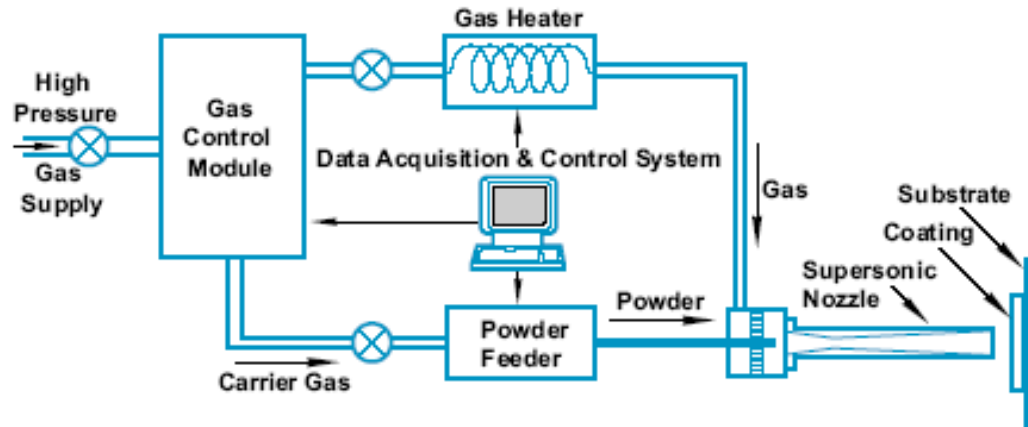


Figure 3.6: Schematic of K-tech Cold Spray Equipment used for experiments

Powder Feeder

A powder feeder (Praxair, Model 1264 HP) is used to provide a consistent, pulse-free feeding of powders. The 1264 is an open-loop pressurized feeder with a high capacity powder canister. Additionally, the 1264 control panel allows for a digital display and toggle switch control for various parameters, such as powder wheel speed control. The powder feed rate is controlled through a powder feed rate control equipment (Praxair Model 1280). A set-temperature heater blanket protects the powder from absorbing moisture. The powder feeder is mounted on a turntable for easy transport and relocation.

Powder Hopper

The powder hopper consists of a large canister so as to deliver a continuous flow of powder during cold spraying. It can be operated up to 500-psi operating backpressure. The hopper has been integrated with the data acquisition and control system. In order to

measure the amount of powder sprayed, a balance scale is incorporated with the powder feeder.

Gas Heater

The gas heater heats the main gas to the operating temperature. It operates a 40 KW heating coil element constructed of RA 330 stainless steel powered by a 480 V , three-phase 63 Ampere electrical current. The tubular heating coil is housed in a thermally insulated aluminum enclosure. Compressed gas at a pressure up to 500 psi can be heated up to 500° C in approximately 2 minutes. Gas flow rate ranging from 0.5-50 standard cubic feet per minute can be achieved. A proportional temperature device and a thermocouple are installed on the pre-chamber. These instruments are used by the data acquisition and control system to control the gas temperature at the nozzle. A graphical user interface on the control console enables to input the desired gas temperature. A cooling system with chilled water flowing at 2.8 gal/min at 30 psi is employed for cooling the transformer.

Gas Control Module

The gas control module offers an accurate gas flow to the nozzle through the main gas line and the carrier gas. The carrier gas is used to drive the powder from the powder hopper to the pre-chamber of the nozzle. The gas flow is controlled by using high-pressure regulators and solenoid valves which are operated by the data acquisition and control system. Pressure transducers and check valves are installed in both the main gas and carrier gas lines. The system is installed in a powder-coated Hoffman enclosure with

a dual inlet connection for helium or nitrogen supply gas and two exits, one for the main gas and one for the carrier gas. The enclosure is configured with a blow-out panel in case of over pressurization, and a fan to eliminate gas buildup inside the enclosure.

Pre-chamber and Nozzle

Powder is fed to the top of pre-chamber by a stainless steel tube (3.175 mm outer diameter X 2.286 mm inner diameter). The powder enters the pre-chamber and is mixed with the accelerating gas at the nozzle aperture entrance. Both, the pre-chamber and the nozzle are light in weight, so that they can be mounted on the robot. The pre-chamber is connected to a supersonic de-laval type nozzle by a conical flange. The inner lining of the nozzle is fabricated from sintered tungsten carbide so as to minimize and plugging. Vertical and horizontal spraying is possible through the spray gun. The nozzle has a length of 211 mm, and a circular cross section with a 7.1 mm diameter at exit.

Computer Control and Data Acquisition

The data acquisition and control system will consist of the 2.2 GHz, Pentium III processor, 17 inch monitor, control and communication hardware, and LabView source software. It is capable of programming for controlling the powder hopper, gas heater, and gas control module. The processor is housed in a NEMA 12 enclosure for use in industrial environment. Overall, the system helps to control and monitor all the cold spray parameters such as gun temperature and gun pressure.

Robot Mounted on Rolling Frame

Since the cold spray gun achieves very high temperatures during operation, an automation for handling the gun is facilitated by the ABB, IRB 2400 robot. The movement of the robot can be accurately controlled by optimizing the acceleration and retardation. Position and movement can be repeated by saving a particular program for robot movement. The entire heater, pre-chamber, and nozzle gun assembly is mounted on the robot arm for spraying powder on the substrate.

3.4.1 Process Parameters

Pure Nickel was sprayed to establish conditions for the build up of dense nickel coatings on Ti-6Al-4V substrates. These conditions (Table 3.2) were later used for experiments with feedstock powders. Figures 3.7 - 3.9 display the variation in parameters during the spray. As shown in Figure 3.7, the actual process gas and powder laden gas pressures are in close proximity of the set values. Additionally, the powder laden gas is pressurized about 0.20 MPa higher than the gas pressure in order to maintain a good flow of powder while spraying. Likewise, the powder laden gas flow rate is also set at higher values in comparison to the process gas flow rate (Figure 3.8). As evident from Figure 3.9, a temperature of up to 500°C was reached during spraying.

Table 3.2: Process Parameters used for cold spraying

Process gas	Helium or Nitrogen
Gas temperature	500°C
Gas pressure	3.45 MPa for Helium and 2.4 MPa for Nitrogen
Spray distance	12.5 mm
Spray gun velocity	20 mm/sec

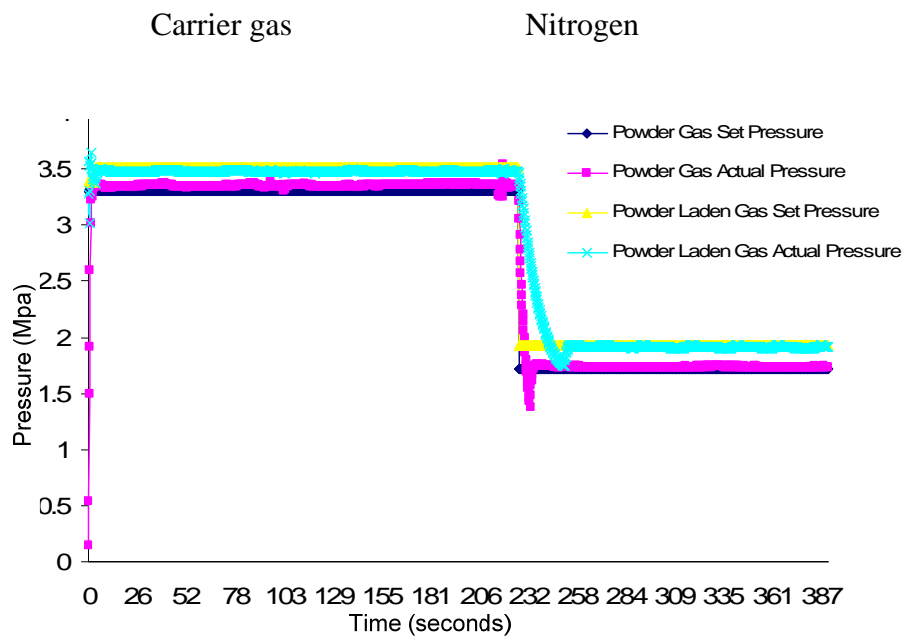


Figure 3.7: Pressure profiles during cold spray deposition

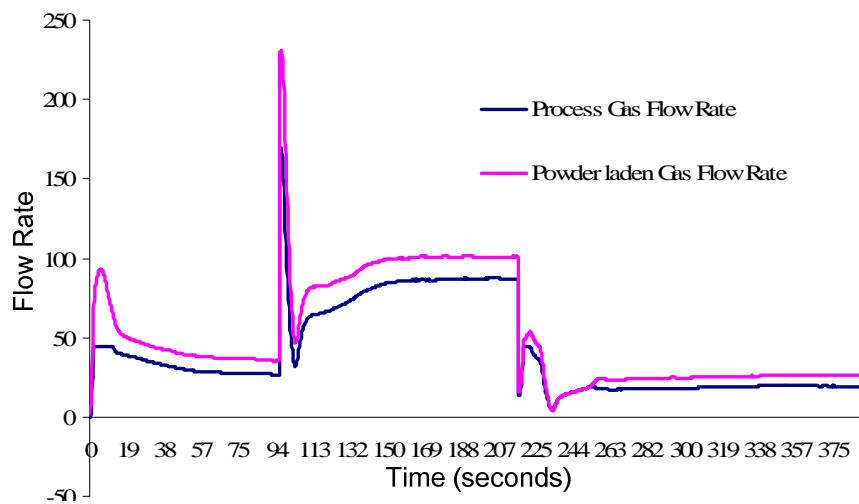


Figure 3.8: Change in gas flow rates during cold spray deposition

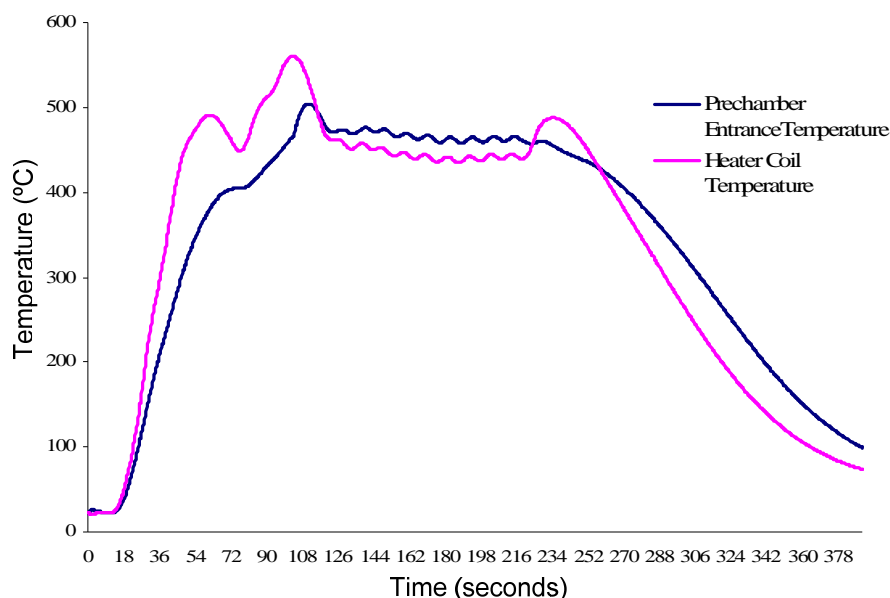


Figure 3.9: Temperature control during cold spray deposition

3.5 Characterization and evaluation of cold-sprayed coatings

Cold Sprayed coatings were characterized for the distribution of lubricant and presence of porosity. Furthermore, coatings with the most homogeneous lubricant distribution were analyzed using X ray diffraction and micro-hardness testing. Finally, the bond strength, mechanical durability and wear behavior of some selected coatings were analyzed using adhesion strength testing and fretting wear evaluations.

3.5.1 Microstructural analysis

Coating coupons were sectioned perpendicular to the coating surface, mounted, and polished using the standard procedures. Polished samples were in turn analyzed on the Nikon Epiphot 300 optical microscope. A Philips XL30 scanning electron

microscope set in secondary electron mode was used to obtain the micrographs for microstructural analysis. In order to reveal the lubricant distribution in the coatings, various magnification levels were used. The presence of lubricant in coatings was verified by the energy dispersive x-ray analysis.

3.5.2 X Ray Diffraction

X-rays of various wavelengths were diffracted from the atomic planes in the samples so as to yield diffraction peaks. The condition for diffraction from planes with spacing, d , is given by Bragg's Law (Equation 3.4)

$$\lambda = 2d \sin(\theta) \quad 3.3$$

where θ is the angle between the atomic planes and the incident x-ray beam. Resultant diffraction pattern were used to identify crystalline phases.

3.5.3 Micro-hardness of coating

Micro-hardness measurements were performed on mounted samples using a conventional Vickers micro-hardness tester with a 300 g load. The measurements were made at increasing distances from the interface of the coating and substrate on the coating cross section, as shown in Figure 3.10. The values presented are the average of 4 measurements.

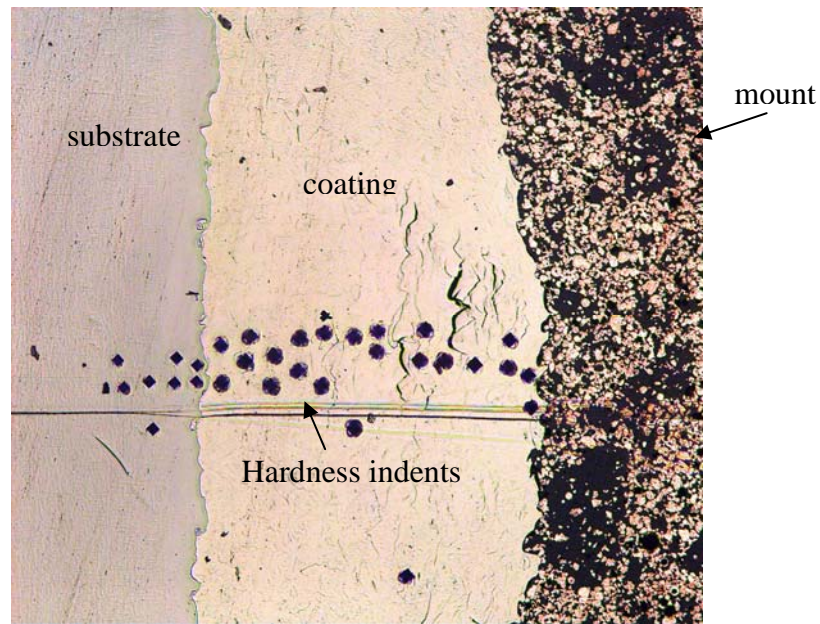


Figure 3.10: Micro-hardness study pattern

3.5.4 Adhesion Testing

Adhesion testing was conducted as per ASTM C633-01 Standard test method for adhesion or cohesion strength of thermal spray coatings. Each test specimen comprised of an assembly of a coated substrate fixture and a loading fixture. These were cylindrical in shape, with a height of 3.8 cm and, diameter of 2.5 cm. One of the faces of the coated substrate fixture was grit blasted. Grit blasting increased the surface roughness of the sample from 0.483 μm to 6.35 μm . Ni-BN coatings were applied at one of the grit blasted faces of the substrate fixture. A rough grinding treatment was performed on the coating so as to decrease the thickness variation across the surface to below 0.025 mm. The coating thickness was measured with a micrometer by measuring the total length of the coating fixture before the coating was applied and after the coating was ground. The

cleaned loading fixtures were attached to the coated substrate fixtures by using about 0.1 cc of epoxy; E-214HP HYSOL. Additionally, a set of uncoated fixtures was prepared for measurement of the adhesion strength of the bonding agent. The bonded fixtures were air cured for 20 minutes, after which the bonded fixtures were cured at 150 °C for two hours. Figure 3.11 shows the coated samples which were tested for adhesion.

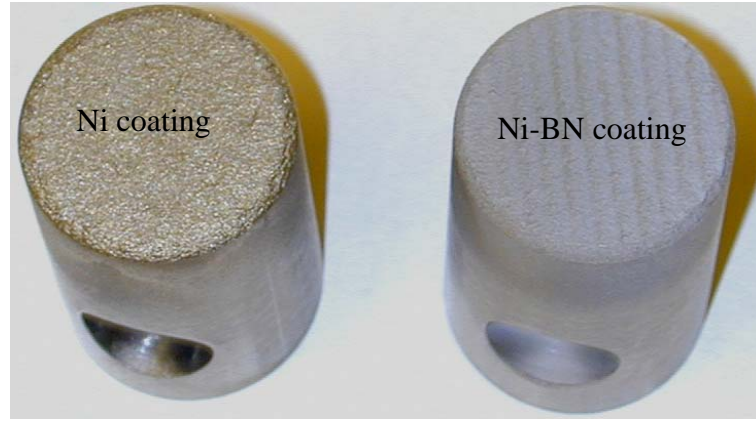


Figure 3.11: Samples tested for adhesion

Once the samples were prepared, they were tested by using the Instron IX automated testing system. An increasing tensile load was applied to each test specimen at a constant rate of cross head travel equal to 0.013 mm/sec. The degree of adhesion strength was calculated as shown in Equation 3.4

$$S_t = \frac{P_{\max}}{A} \quad 3.4$$

where S_t is the adhesion or cohesion strength, P_{\max} is the maximum load applied, and A is the cross-sectional area. Table 3.3 details the coatings which were tested for adhesion.

Table 3.3: Coatings tested for adhesion.

Sr. No.	Mixture Composition	Size of Ni powder (μm)	Size of coated powder (μm)	Amount of BN (wt.%)	Coating thickness in mm (as sprayed)	Coating thickness in mm (after grinding)
1	Epoxy E-214HP HYSOL	--	--	--	--	--
2	Pure Ni	68	--	0	0.95	0.7
3	Ni-20 wt. % Ni coated BN	12	75	2	0.88	0.63
4	Ni-20 wt. % Ni coated BN	12	103	4	1.10	0.57
5	Ni-25 wt. % Ni coated BN	12	103	5	1.23	0.90
6	Ni-30 wt. % Ni coated BN	12	75	3	1.995	1.54
7	N-30 wt. % Ni coated BN	12	103	6	2.195	1.56

3.5.5 Fretting Wear Testing

Table 3.4 details the coatings which were tested for fretting wear. Coated Ti-6Al-4V circular disks with a diameter of 12.7 mm on the test face and 3.175 mm thick were used as test specimens (Figure 3.12). An ellipsoid test geometry on a flat rigid plate, (Figure 3.13) was used so as to eliminate stress concentrations and resulting contact edge effects. Two fretting wear experiments were conducted on each of the coatings at room temperature and 40% relative humidity. Each test was conducted at 30Hz, a 50 N normal load, for 100,000 cycles, and a stroke length of 200 μm . The wear profiles of the scars on coating surface as well as counter-surface were plotted.

Table 3.4: Coatings tested for fretting wear

Sr. No.	Mixture Composition	Size of Ni powder (μm)	Size of coated powder (μm)	Amount of BN (wt.%)
1	Pure Ni	68	--	0
2	Ni-20 wt. % Ni coated BN	12	75	2
3	Ni-20 wt. % Ni coated BN	12	103	4
4	Ni-25 wt. % Ni coated BN	12	103	5
5	Ni-30 wt. % Ni coated BN	12	75	3
6	Ni-30 wt. % Ni coated BN	12	103	6

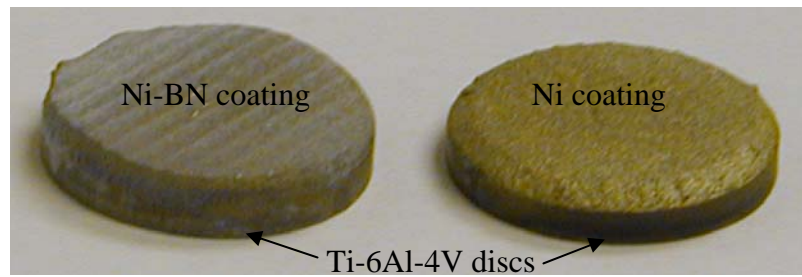


Figure 3.12: Samples used for fretting wear testing

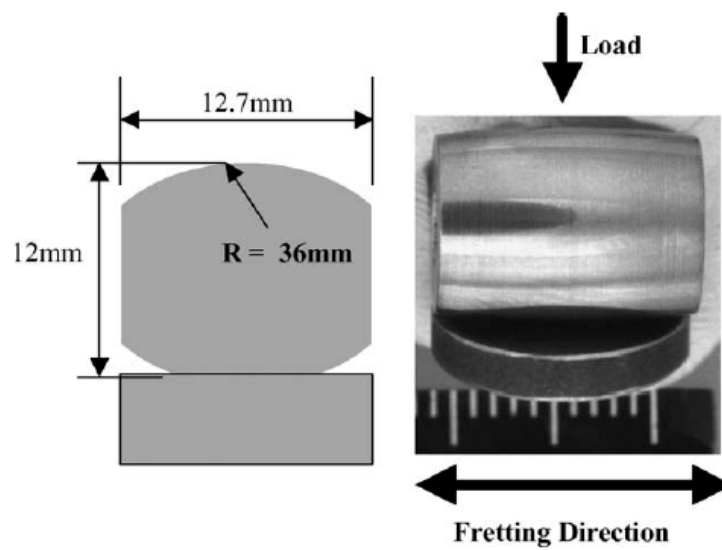


Figure 3.13: Ellipsoid contact geometry

Figure 3.14 illustrates a schematic of the fretting wear tribometer used in this investigation. The instrument utilizes a piezo-electric transducer to measure friction between the mating specimens. A laser measurement device was used to continuously track the position of the oscillating specimen during the test [39, 43, 158].

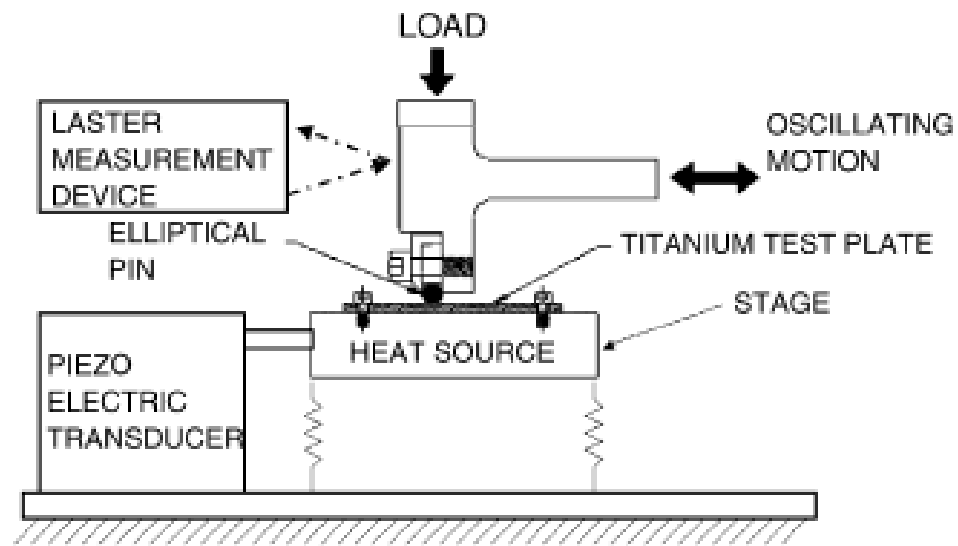


Figure 3.14: Fretting wear tribometer

Chapter 4

Feedstock Powders for Cold Spray

In cold spraying, the powder is not molten before impacting on the substrate. Therefore, the bonding of the coating completely depends on powder characteristics and impact conditions. Moreover, particle morphology also plays an important role in the cold spray process. Due to a higher drag coefficient, angular and irregular particles are accelerated to higher particle velocities relative to spherical particles. In the current study, admixed, milled and pre-coated feedstock powders were used. While admixed powders were easy to prepare and economical, the milled and coated powders provided the advantage of forcing some level of contact between Ni and lubricant powders prior to spraying. In theory, the irregular shaped milled and pre-coated particles should see greater acceleration and be better suited to bond to the roughened substrate, since they possess greater surface area and more irregularities increasing the possibility of mechanical interlocking [60]. Recently, the non-spherical particles have been advocated as most suited for cold spraying because they achieve higher velocities during impact [59].

4.1 Ni-MoS₂ and Ni-BN Admixed Powders

During cold spraying, non-ductile particles can penetrate into a soft substrate and aid mechanical bonding despite the absence of plasticity. However, in case of higher hardness substrate such as Ti-6Al-4V most of the deformation occurs within the

impacting particles. MoS₂ and BN powders are brittle and soft ceramics which do not undergo the required plastic deformation to form a good bond with the substrates. However, this problem was solved by using Ni as the coating matrix. Ni is a ductile metal which undergoes very high plastic deformation during cold spraying. Hence, in theory, Ni powders can entrap the lubricant powders into the coatings. It is also expected that larger Ni powders would aid in better incorporation of the lubricant. However, the advantage of using larger Ni powders was offset by the fact that larger Ni has a mass which is incomparable to that of the lubricant. While Ni powder has a density of 8.8g/cc, MoS₂ and BN powders have very low densities of 4.8 g/cc and 2.7 g/cc respectively. While spraying powders, the particles with lower mass are accelerated to a much higher extent than those with higher mass at the same spray conditions. In order to find out the effect of particle size on coating development, various feedstock powders were prepared by admixing different sizes of Ni and lubricant powders. Table 4.1 details the composition of powder mixtures used.

Table 4.1: Details of admixed Ni-MoS₂ and Ni-BN feedstock powders

Sr. No.	Mixture Composition	Size of Ni powder (μm)	Size of lubricant powder (μm)
1	Ni-2 wt. % MoS ₂	12	30
2	Ni-3 wt. % MoS ₂	12	30
3	Ni-4 wt. % MoS ₂	12	30
4	Ni-2 wt. % MoS ₂	12	3
5	Ni-7 wt. % MoS ₂	12	30
6	Ni-7 wt. % MoS ₂	32	30
7	Ni-4 wt. % BN	12	10
8	Ni-4 wt. % BN	32	10
9	Ni-4 wt. % BN	75	10
10	Ni-5 wt. % BN	12	10
11	Ni-5 wt. % BN	75	10

Figure 4.1 and Figure 4.2 show the morphology of the admixed Ni (12 μm)-MoS₂ (30 μm) and Ni (12 μm)-BN (10 μm) powders. As shown in the figures, the lubricant powders are homogeneously mixed with the nickel powder. Out of the various sizes of Ni powders tested, the 12 μm Ni powder gave the best results because of density values closer to those of the lubricant powders.

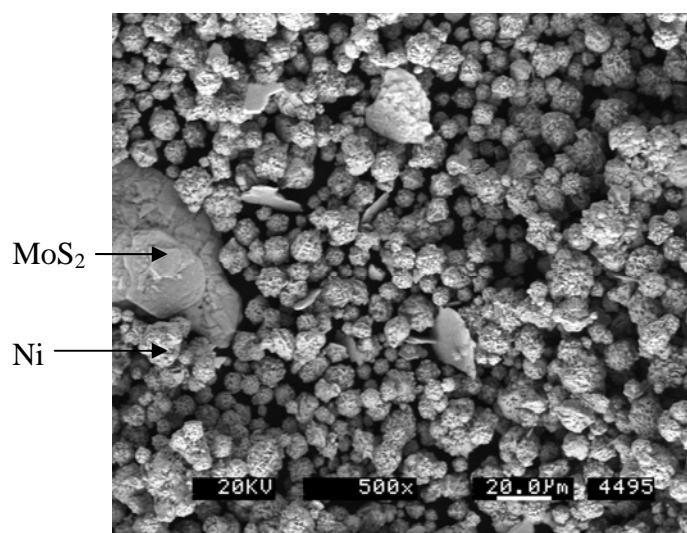


Figure 4.1: SEM image of admixed Ni-3 wt. % MoS₂ powder

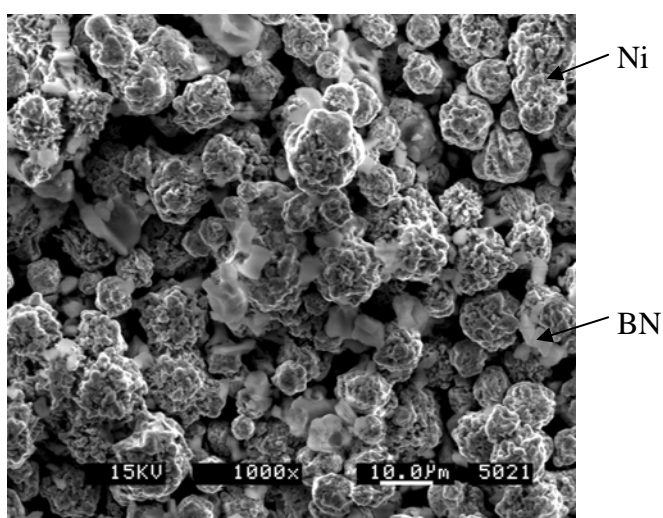


Figure 4.2: SEM image of admixed Ni-2 wt. % BN powder

4.2 Milled Powders

Commercially available Ni and lubricant (MoS_2 and BN) powders were used as starting materials to produce composite powders. Table 4.2 summarizes the details of the various feedstock powders prepared by mechanical milling.

Table 4.2: Details of milled Ni- MoS_2 and Ni-BN feedstock powders

Sr. No.	Mixture Composition	Initial Size of Ni powder (μm)	Initial Size of lubricant powder (μm)	Milling Time (hours)
1	Ni-3 wt. % MoS_2	12	30	.33
2	Ni-3 wt. % MoS_2	12	3	.33
3	Ni-3 wt. % MoS_2	12	3	.66
4	Ni-3 wt. % MoS_2	12	3	1
5	Ni-3 wt. % MoS_2	12	3	1.5
6	Ni-9 wt. % MoS_2	12	3	4
7	Ni-2 wt. % BN	12	10	.33
8	Ni-2 wt. % BN	12	10	.66
9	Ni-2 wt. % BN	12	10	1
10	Ni-2 wt. % BN	12	10	1.5
11	Ni-2 wt. % BN	12	10	2
12	Ni-2 wt. % BN	12	10	6
13	Ni-2 wt. % BN	12	10	12
14	Ni-2 wt. % BN	12	10	18
15	Ni-2 wt. % BN	12	10	32

4.2.1 Milled Ni- MoS_2 Powders

As shown in Figure 4.3, there was no change in morphology of mixed Ni (12 μm) and MoS_2 (30 μm) after milling. However, by using a smaller sized MoS_2 (3 μm), the constituent powders cold welded to form larger agglomerates.

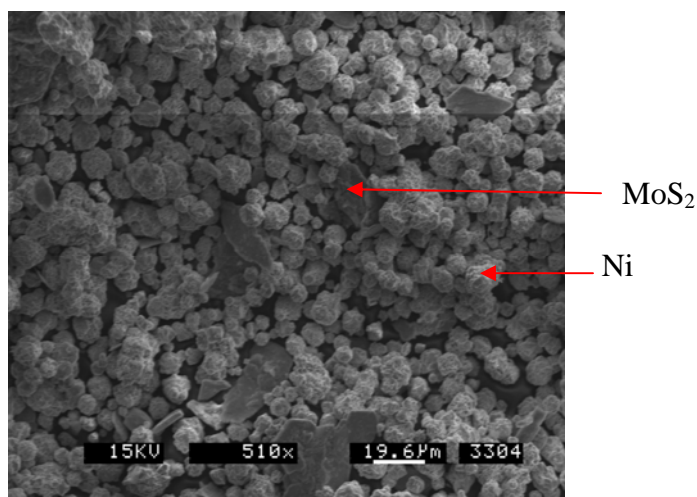


Figure 4.3: SEM image of Ni (12 μm)-2wt % MoS₂ (30 μm) milled for 30 minutes.

Figures 4.4-4.6 illustrate the morphologies of as-milled Ni (12 μm)-2 wt % MoS₂ (3 μm) powders at different milling times. Apparently, the ductile Ni powder has welded together, and trapped the brittle MoS₂ in between the large size agglomerates.

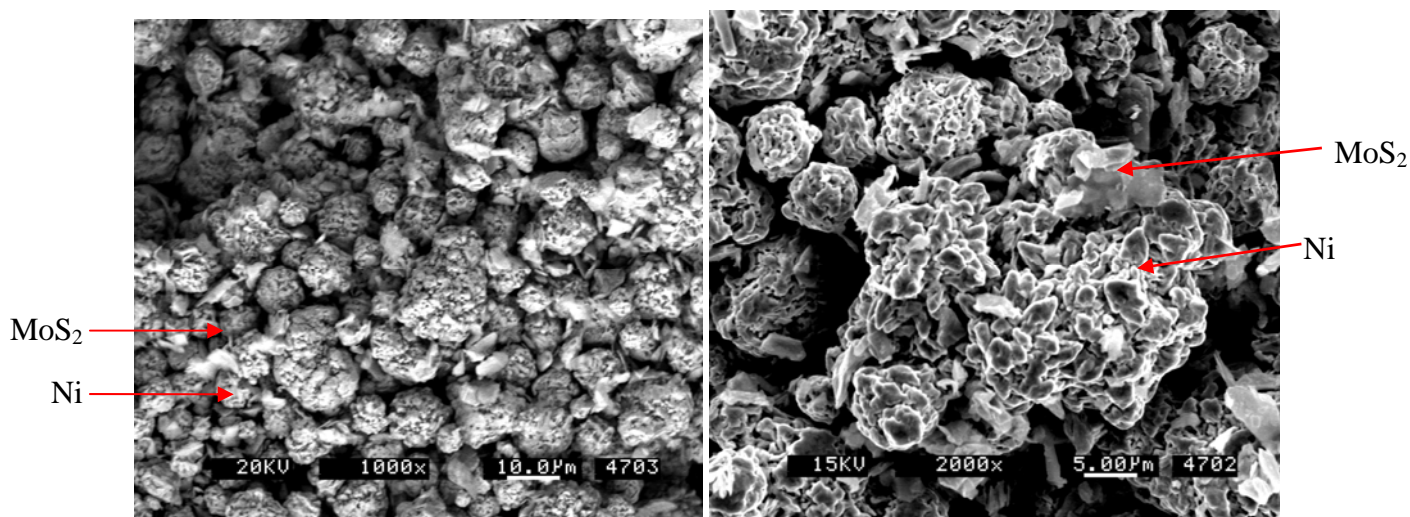


Figure 4.4: SEM images of Ni (12 μm)-2 wt. % MoS₂ (3 μm) milled for 20 minutes.

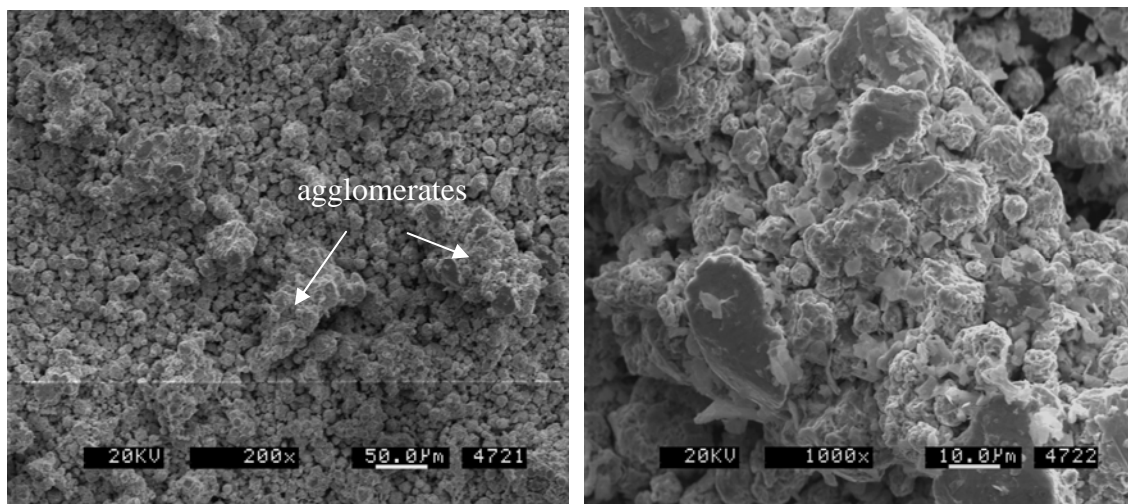


Figure 4.5: SEM images of Ni (12 μm)-2 wt % MoS₂ (3 μm) milled for 40 minutes.

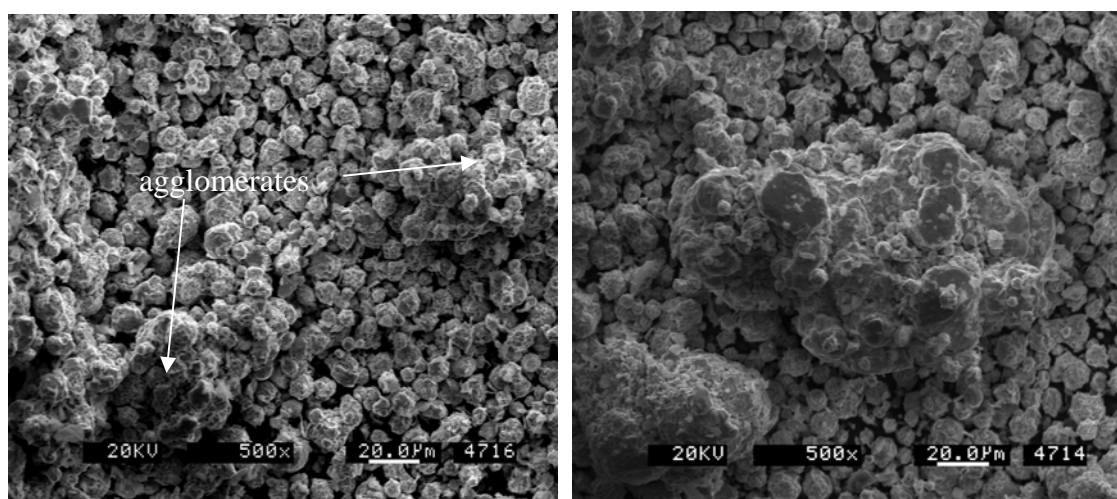


Figure 4.6: SEM images of Ni (12 μm)-2 wt. % MoS₂ (3 μm) milled for 90 minutes.

Figures 4.7-4.8 show the morphologies of Ni (12 μm)-7 wt % MoS₂ (3 μm) milled for one and four hours, respectively. However, the Ni-MoS₂ powders did not agglomerate as much as the Ni-BN powders. This may be due to the small particle size of MoS₂ powders. As shown in Figure 4.7, milling for one hour did not create substantial agglomeration. However, when the milling time was increased to four hours (Figure 4.8), large agglomerates of irregular shapes were formed.

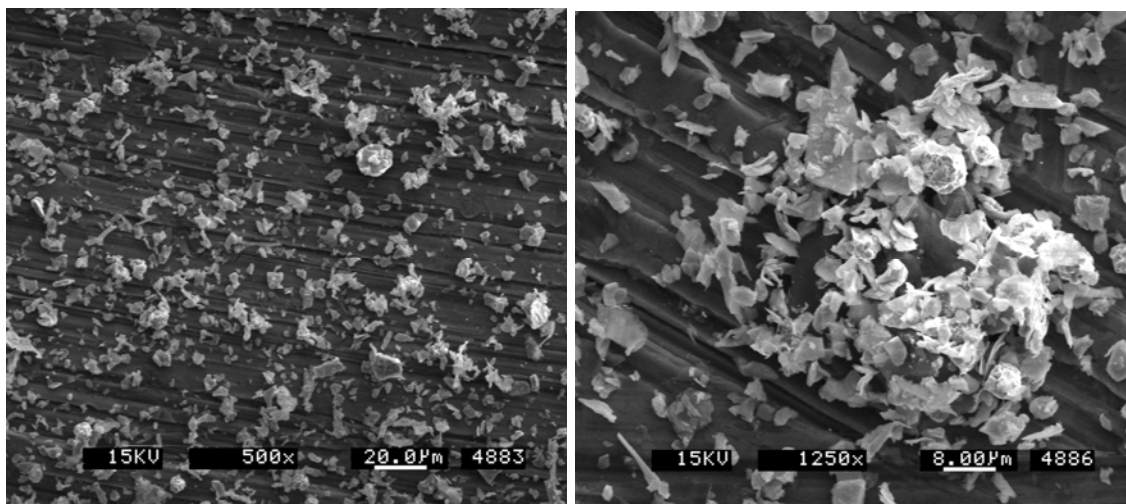


Figure 4.7: SEM images of Ni (12 μm)-7 wt % MoS₂ (3 μm) milled for 1 hour

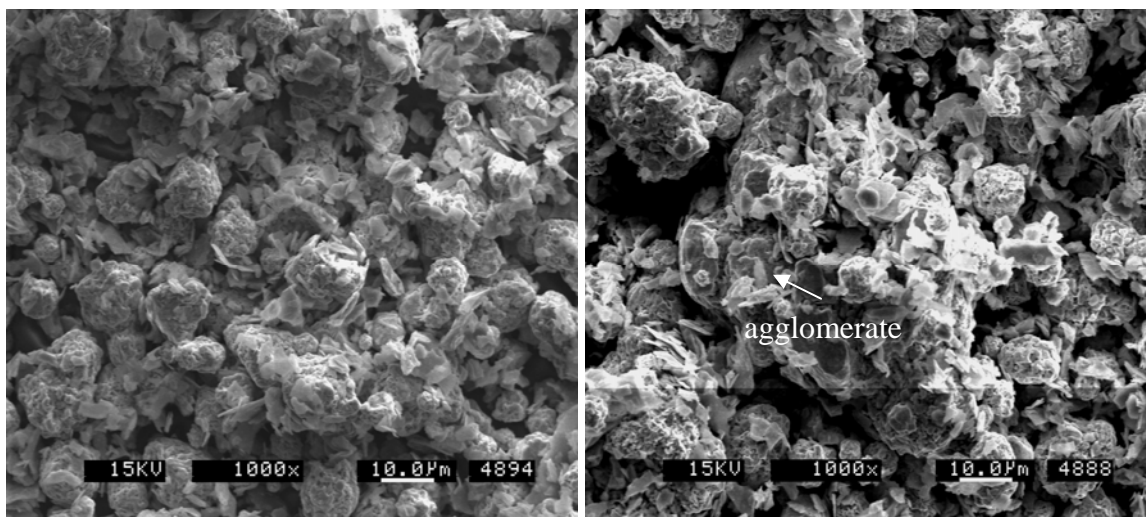


Figure 4.8: SEM images of Ni (12 μm)-7 wt % MoS₂ (3 μm) milled for 4 hours

Figure 4.9 shows a histogram displaying the number of particles in various size increments on a log scale. Clearly, the particle size distribution of the Ni (12 μm)-7 wt % MoS₂ (3 μm) milled powders is bimodal. A cumulative particle size distribution is generated by adding the interval percentages and plotting the cumulative percentages versus the lower incremental particle size. While the first peak shows the non-bonded Ni

particles of size 12 μm , the second peak shows large agglomerates of size 40 μm to 85 μm . Table 4.3 details the statistics of the particle size distribution, which has been described by using seven different sizes. These have been taken directly from the population based cumulative particle size distribution at seven points designated D_5 , D_{10} , D_{20} , D_{50} , D_{80} , D_{90} and D_{95} .

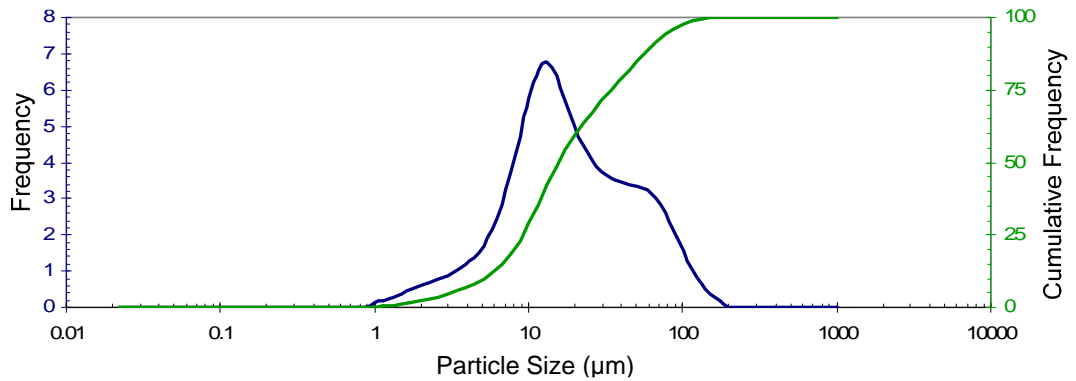


Figure 4.9: Particle Size Distribution for Ni-7 wt. % MoS_2 milled for 4 hours

Table 4.3: Statistics for Particle Size Distribution for Ni-7 wt. % MoS_2 milled for 4 hours

D_5 (μm):	3.217	D_{10} (μm):	5.218	Mean (μm):	26.13
D_{20} (μm):	8.066	D_{50} (μm):	15.713	Variance:	680.6
D_{80} (μm):	41.784	D_{90} (μm):	63.349	S.D. (μm):	26.09
D_{95} (μm):	82.255	S.P.Area (cm^2/cm^3):	573.0	Mode (μm):	12.36

4.2.2 Milled Ni-BN Powders

The SEM images of Ni-BN composite powders (Figure 4.10) clearly show the large degree of mechanical deformation undergone by the milled powders. The morphology of the as-milled powders is completely different from that of the starting powder mixture. Moreover, the size of some particles in the milled powders is up

to about 70 μm , which is much larger than that of the starting powder (12 μm and 10 μm). The large particles were present in the agglomerated condition and have an irregular and angular morphology. During mechanical alloying, welding and fracture are the two major processes. The experiments indicate that cold welding dominates the milling process for an hour. After that, the large agglomerates tend to fracture and reduce in size. The increase in D_{80} from 28 to 41 with an increase in milling time from 20 minutes to 1 hour indicates that the powder particles are cold welding with each other. A similar trend has been observed in the D_{90} and D_{95} of the particle size distribution as well. Obviously, as the size of individual agglomerates increases, there is an improvement in the efficiency as well; the efficiency may be defined as the percentage of powder which bonded into agglomerates of desired size range. As evident from the statistics of powder size distribution, the mode of all feedstock powders is always 12 μm , which is the starting size of the Ni particles. In order to improve the yield, powders were subjected to milling for greater lengths of time.

The D_{80} decreases to 28 at 10 hours of milling time. Further, it is interesting to note that the particle size distribution parameters follow a cyclic trend. For example, at 18 hours of milling, the D_{80} is again increased to 35 (Figure 4.22, Figure 4.23, Table 4.10). The entire sequence of fracturing and cold welding of particles can be replicated by milling between 18 to 32 hours (Figures 4.22-4.25, Tables 4.10-4.11).

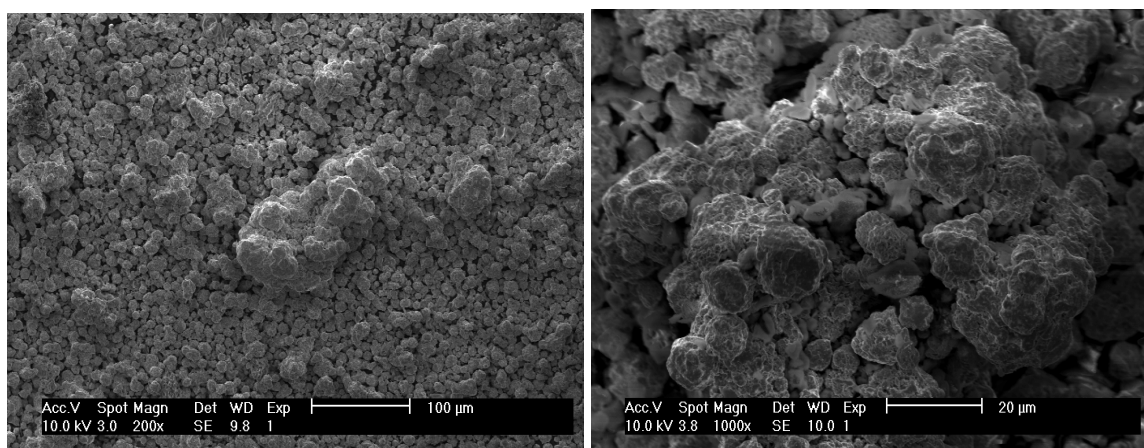


Figure 4.10: SEM images of Ni (12 μm)-2 wt % BN (10 μm) milled for 20 minutes

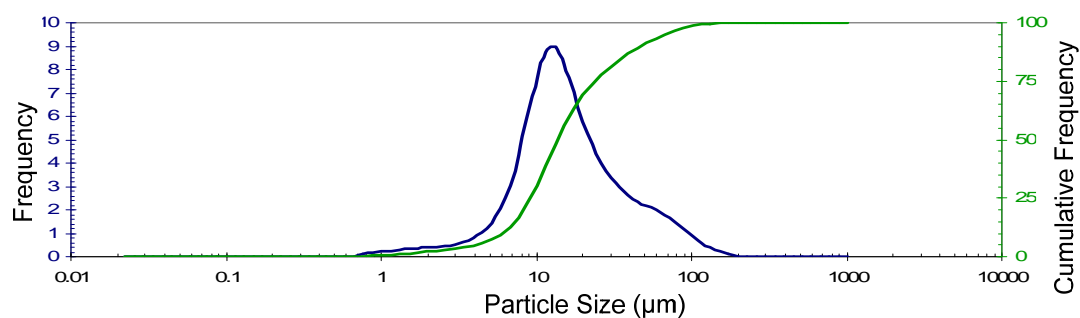


Figure 4.11: Particle Size Distribution for Ni (12 μm)-2 wt % BN (10 μm) milled for 20 minutes

Table 4.4: Statistics for Particle Size Distribution of Ni (12 μm)-2 wt % BN (10 μm) milled for 20 minutes

D₅ (μm):	4.027	D₁₀ (μm):	6.043	Mean (μm):	21.12
D₂₀ (μm):	8.290	D₅₀ (μm):	13.688	Variance:	453.2
D₈₀ (μm):	28.461	D₉₀ (μm):	47.331	S.D. (μm):	21.29
D₉₅ (μm):	67.033	S.P.Area (cm^2/cm^3):	595.0	Mode (μm):	12.33

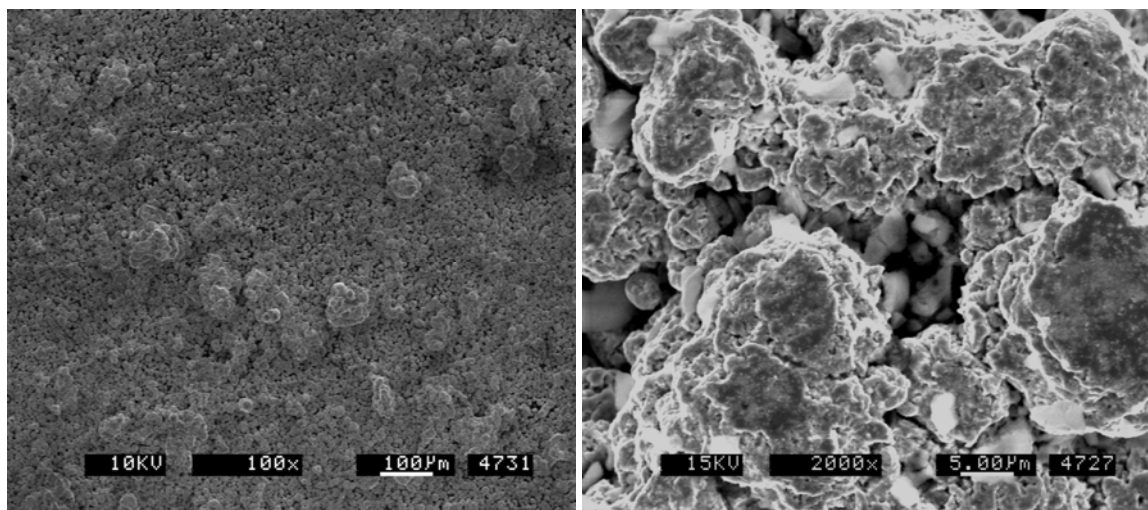


Figure 4.12: SEM images of Ni (12 μm)-2 wt % BN (10 μm) milled for 40 minutes

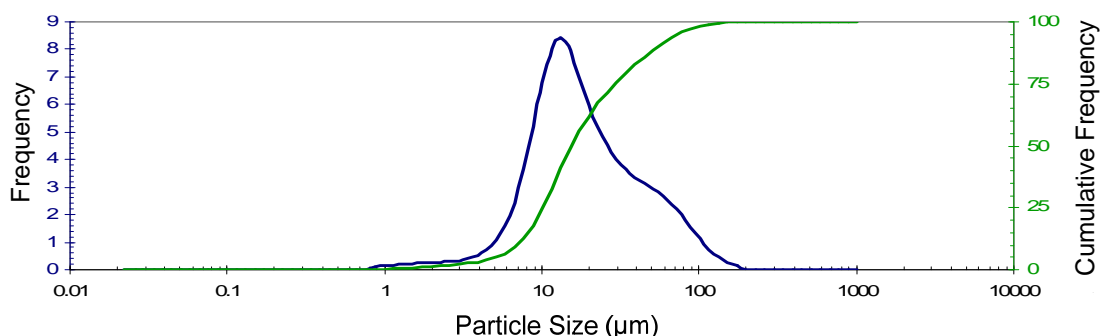


Figure 4.13: Particle Size Distribution for Ni (12 μm)-2 wt % BN (10 μm) milled for 40 minutes

Table 4.5: Statistics for Particle Size Distribution of Ni (12 μm)-2 wt % BN (10 μm) milled for 40 minutes

D₅ (μm):	5.032	D₁₀ (μm):	6.903	Mean (μm):	23.72
D₂₀ (μm):	9.141	D₅₀ (μm):	15.351	Variance:	497.2
D₈₀ (μm):	34.579	D₉₀ (μm):	53.701	S.D. (μm):	22.30
D₉₅ (μm):	71.564	S.P.Area (cm^2/cm^3):	512.0	Mode (μm):	12.37

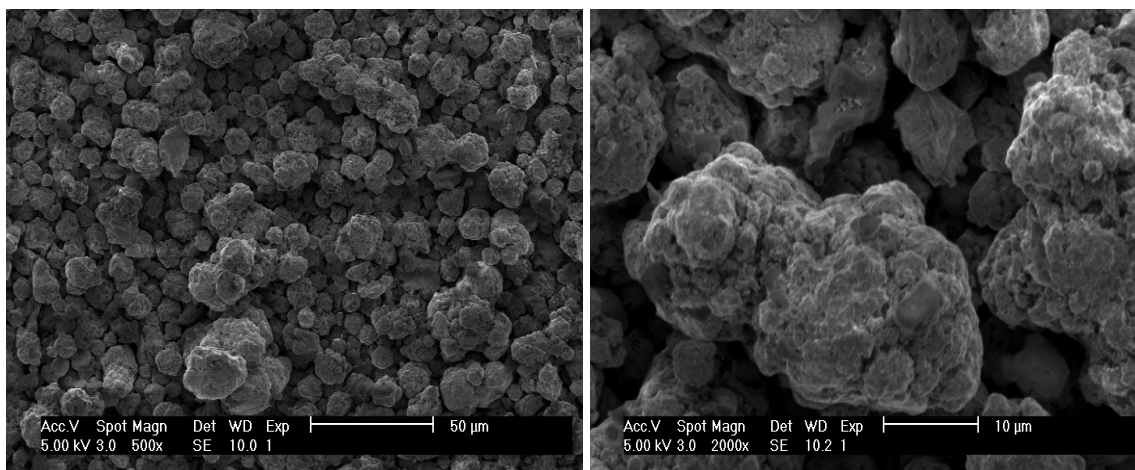


Figure 4.14: SEM images of Ni (12 μm)-2 wt % BN (10 μm) milled for 1 hour

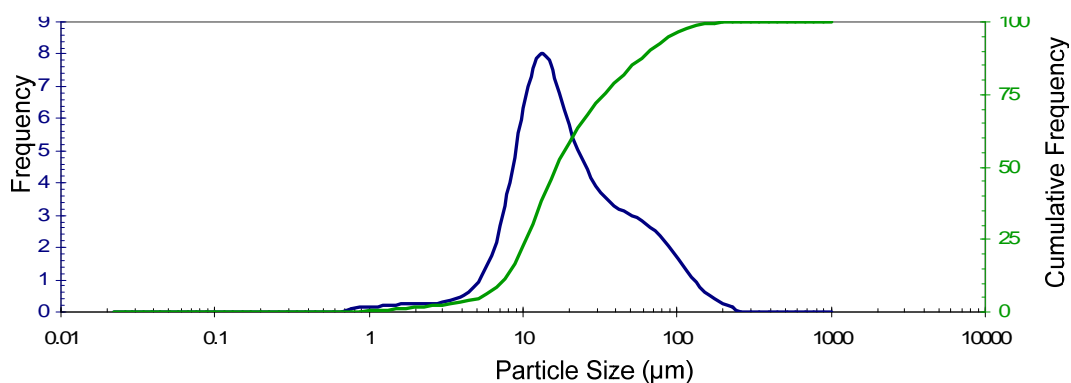


Figure 4.15: Particle Size Distribution for Ni (12 μm)-2 wt % BN (10 μm) milled for 1 hour

Table 4.6: Statistics for Particle Size Distribution of Ni (12 μm)-2 wt % BN (10 μm) milled for 1 hour

D₅ (μm):	5.252	D₁₀ (μm):	7.195	Mean (μm):	28.01
D₂₀ (μm):	9.521	D₅₀ (μm):	16.454	Variance:	867.5
D₈₀ (μm):	41.326	D₉₀ (μm):	66.339	S.D. (μm):	29.45
D₉₅ (μm):	90.456	S.P.Area (cm^2/cm^3):	493.0	Mode (μm):	12.39

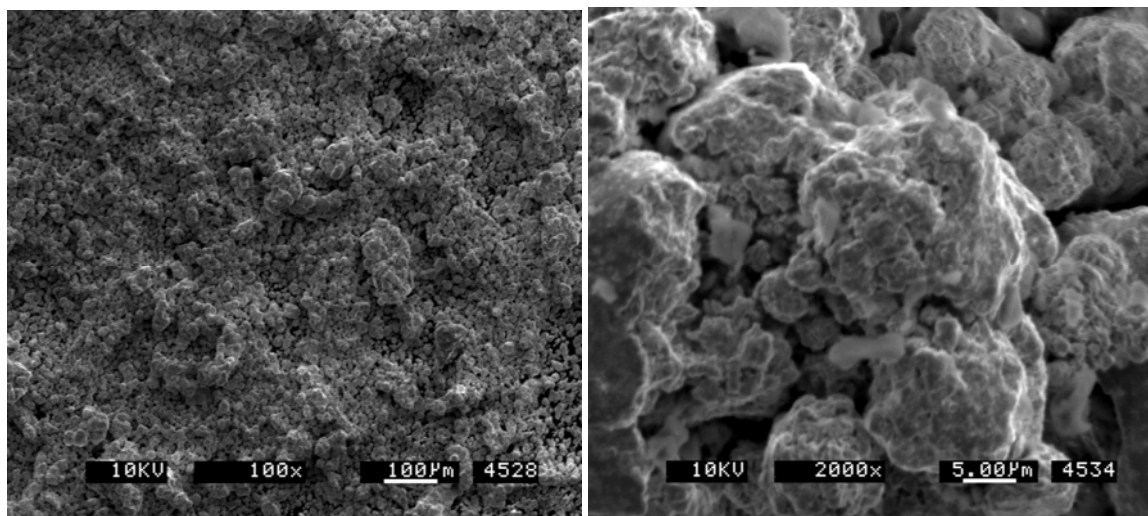


Figure 4.16: SEM images of Ni (12 μm)-2 wt % BN (10 μm) milled for 1.5 hour

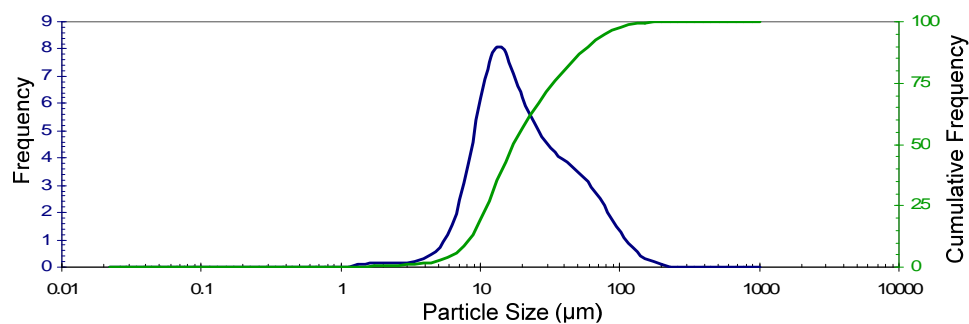


Figure 4.17: Particle Size Distribution for Ni (12 μm)-2 wt % BN (10 μm) milled for 1.5 hour

Table 4.7: Statistics for Particle Size Distribution of Ni (12 μm)-2 wt % BN (10 μm) milled for 1.5 hours

D₅ (μm):	6.368	D₁₀ (μm):	7.971	Mean (μm):	26.73
D₂₀ (μm):	10.174	D₅₀ (μm):	17.328	Variance:	605.3
D₈₀ (μm):	39.699	D₉₀ (μm):	59.229	S.D. (μm):	24.60
D₉₅ (μm):	77.908	S.P.Area (cm^2/cm^3):	418.0	Mode (μm):	12.41

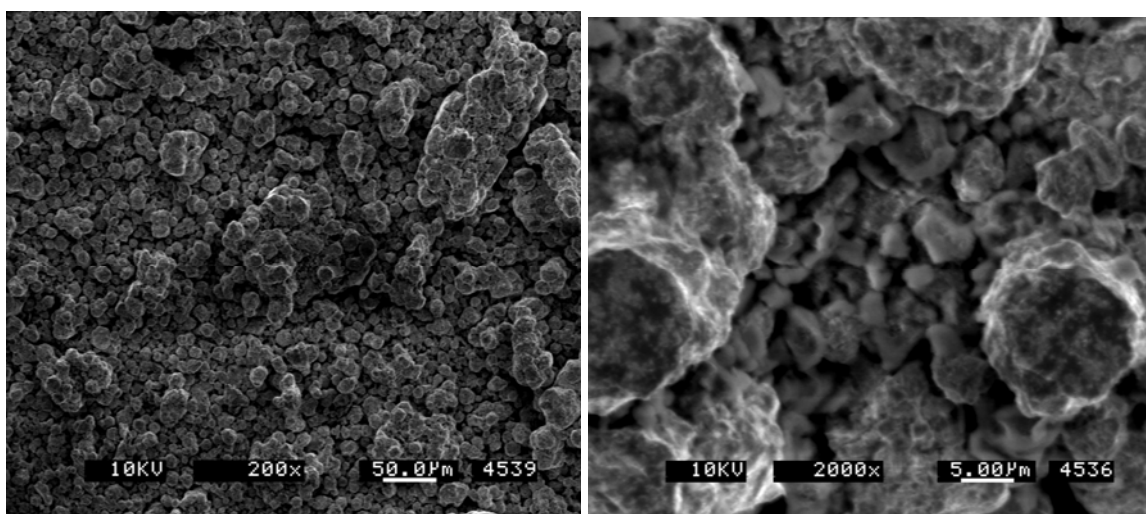


Figure 4.18: SEM images of Ni (12 μm)-2 wt % BN (10 μm) milled for 2 hours

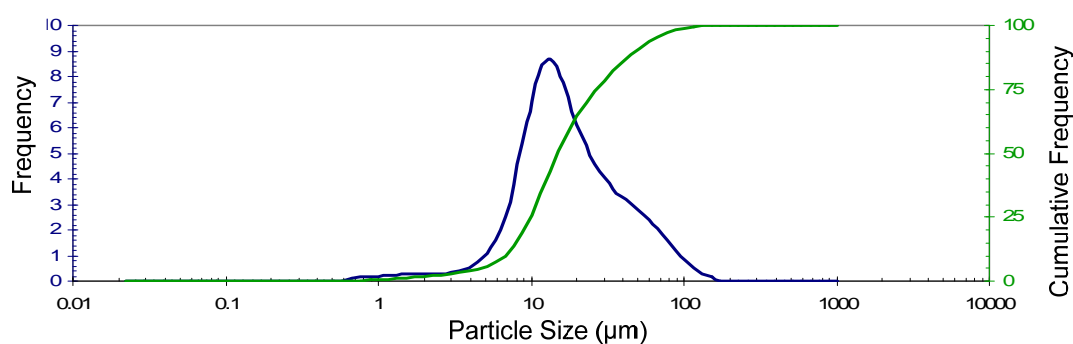


Figure 4.19: Particle Size Distribution for Ni (12 μm)-2 wt % BN (10 μm) milled for 2 hours

Table 4.8: Statistics for Particle Size Distribution of Ni (12 μm)-2 wt % BN (10 μm) milled for 2 hours

D₅ (μm):	4.760	D₁₀ (μm):	6.791	Mean (μm):	22.16
D₂₀ (μm):	9.013	D₅₀ (μm):	14.899	Variance:	405.2
D₈₀ (μm):	31.776	D₉₀ (μm):	48.896	S.D. (μm):	20.13
D₉₅ (μm):	65.384	S.P.Area (cm^2/cm^3):	555.0	Mode (μm):	12.37

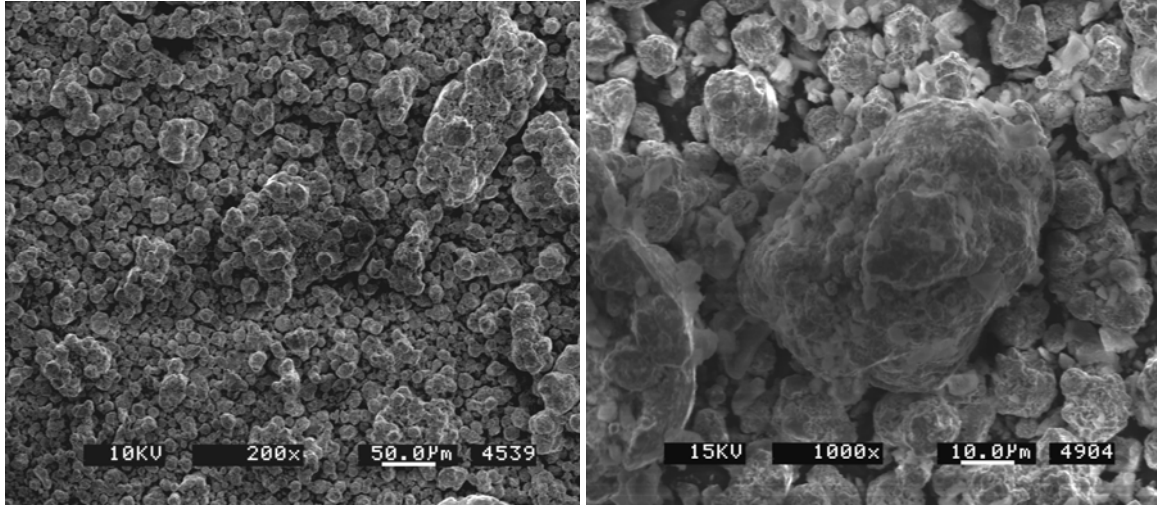


Figure 4.20: SEM images of Ni (12 μm)-2 wt % BN (10 μm) milled for 10 hours

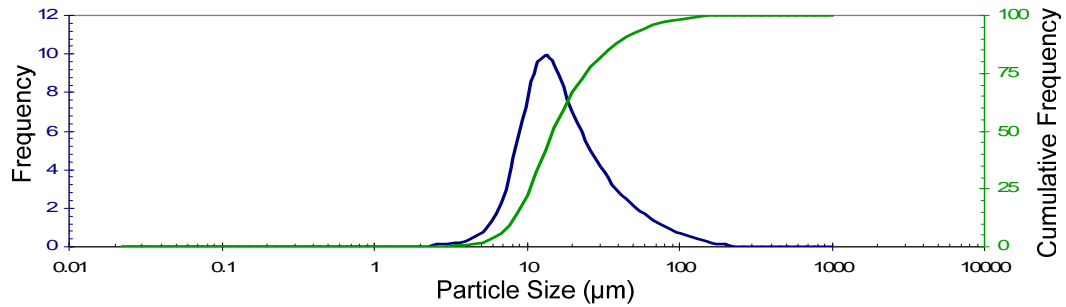


Figure 4.21: Particle Size Distribution for Ni (12 μm)-2 wt % BN (10 μm) milled for 10 hours

Table 4.9: Statistics for Particle Size Distribution for Ni (12 μm)-2 wt % BN (10 μm) milled for 10 hours

D₅ (μm):	6.529	D₁₀ (μm):	7.852	Mean (μm):	21.82
D₂₀ (μm):	9.663	D₅₀ (μm):	14.905	Variance:	432.8
D₈₀ (μm):	28.307	D₉₀ (μm):	43.302	S.D. (μm):	20.80
D₉₅ (μm):	62.353	S.P.Area (cm^2/cm^3):	441.0	Mode (μm):	12.39

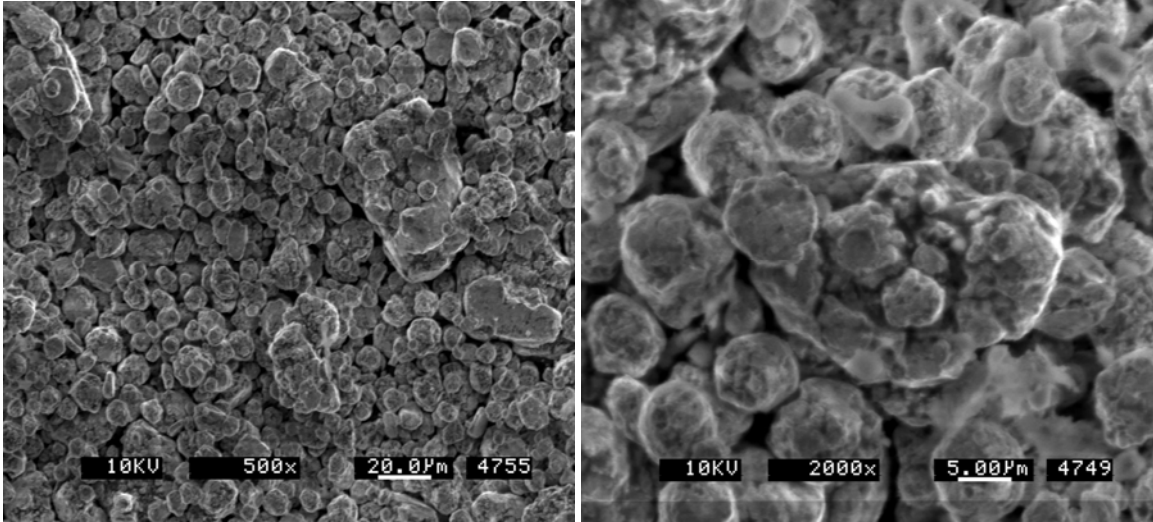


Figure 4.22: SEM images of Ni (12 μm)-2 wt % BN (10 μm) milled for 18 hours

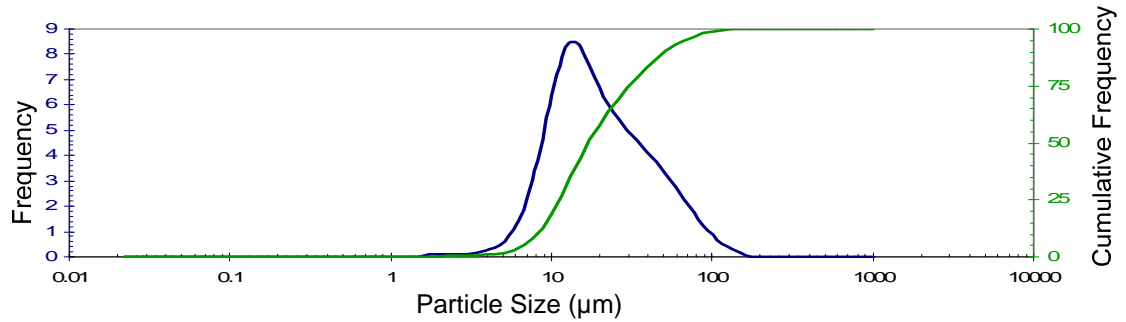


Figure 4.23: Particle Size Distribution for Ni (12 μm)-2 wt % BN (10 μm) milled for 18 hours

Table 4.10: Statistics for Particle Size Distribution of Ni (12 μm)-2 wt % BN (10 μm) milled for 18 hours

D₅ (μm):	6.747	D₁₀ (μm):	8.175	Mean (μm):	24.43
D₂₀ (μm):	10.278	D₅₀ (μm):	17.010	Variance:	416.2
D₈₀ (μm):	35.501	D₉₀ (μm):	51.271	S.D. (μm):	20.40
D₉₅ (μm):	67.027	S.P.Area (cm^2/cm^3):	409.0	Mode (μm):	12.42

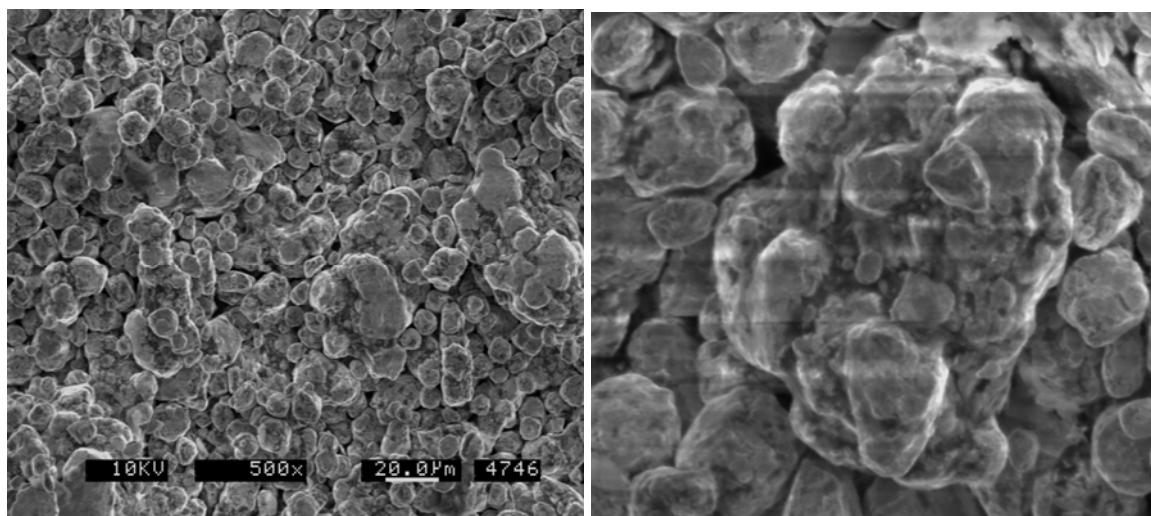


Figure 4.24: SEM images of Ni (12 μm)-2 wt % BN (10 μm) milled for 32 hours

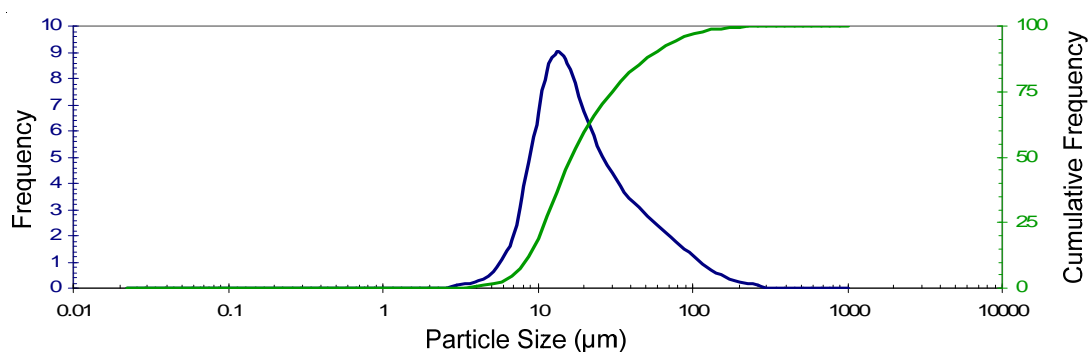


Figure 4.25: Particle Size Distribution for Ni (12 μm)-2 wt % BN (10 μm) milled for 32 hours

Table 4.11: Statistics for Particle Size Distribution for Ni (12 μm)-2 wt % BN (10 μm) milled for 32 hours

D₅ (μm):	6.899	D₁₀ (μm):	8.265	Mean (μm):	26.65
D₂₀ (μm):	10.267	D₅₀ (μm):	16.525	Variance:	789.1
D₈₀ (μm):	35.928	D₉₀ (μm):	57.598	S.D. (μm):	28.09
D₉₅ (μm):	82.374	S.P.Area (cm^2/cm^3):	400.0	Mode (μm):	12.42

4.2.3 Ni-Ni coated BN admixed Powder

Table 4.12 details the set of experiments undertaken with Ni-Ni coated BN admixed powders.

Table 4.12: Details of admixed Ni-Ni coated BN feedstock powders

Sr. No.	Mixture Composition	Size of Ni powder (μm)	Size of lubricant powder (μm)
1	Ni-5 wt. % Ni-coated-BN	12	75
2	Ni-15 wt. % Ni-coated-BN	12	75
3	Ni-20 wt. % Ni-coated-BN	12	75
4	Ni-30 wt. % Ni-coated-BN	12	75
5	Ni-5 wt. % Ni-coated-BN	12	103
6	Ni-15 wt. % Ni-coated-BN	12	103
7	Ni-20 wt. % Ni-coated-BN	12	103
8	Ni-30 wt. % Ni-coated-BN	12	103

Figure 4.26 shows that the Ni (12 μm) and Ni coated BN powders have mixed homogeneously. Although various sizes of Ni powders were tried with the coated powders, the 12 μm powder gave best results. As shown in Figure 4.27, the small Ni particles are sitting in the depressions of the irregularly shaped Ni coated BN powder. From both the SEM images, it is clear that the surface morphology of Ni coated BN powders is similar to those of the pure Ni powders.

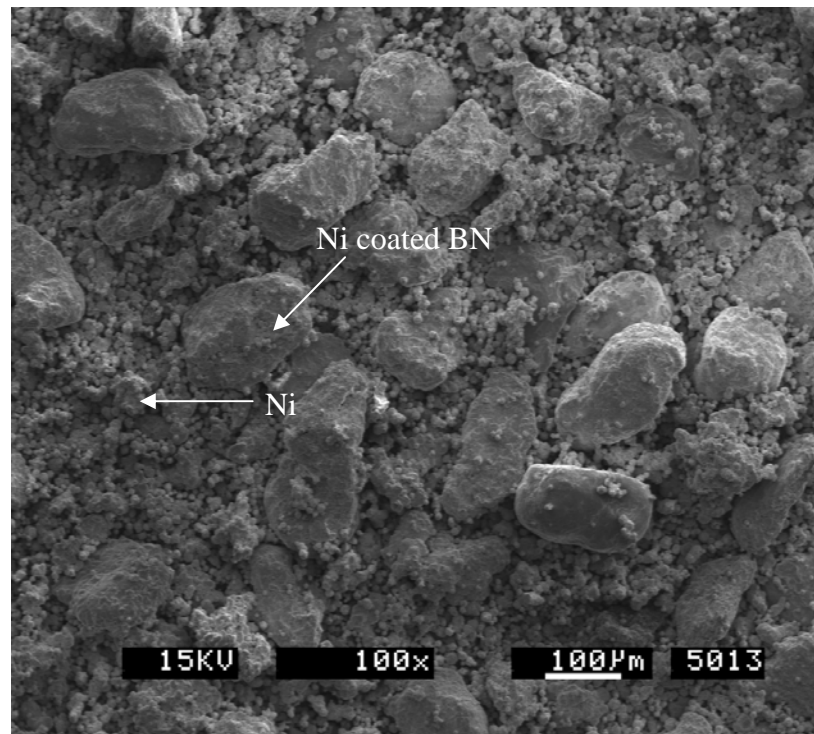


Figure 4.26: SEM image of admixed Ni (12 μm)-30 wt % Ni coated BN (103 μm)

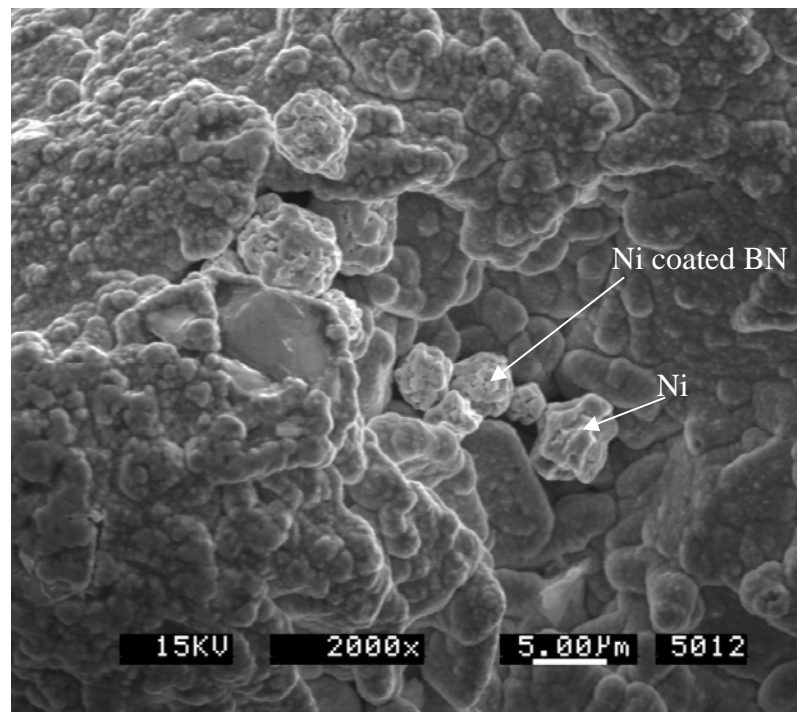


Figure 4.27: SEM image of admixed Ni (12 μm)-30 wt % Ni coated BN (103 μm)

4.2.4 Micro Hardness

It was observed that the pure Ni and Ni coated BN powders behaved very differently during the cold spraying process. In addition to observing the surface morphologies of the two powders, their micro-hardness values were measured using a Vickers hardness tester at a load of 10 grams. Table 4.13 summarizes the hardness results for pure Ni and Ni coated BN powders. As detailed earlier (Figure 3.5), three different hardness regions are present in each Ni coated BN particle. The pure BN core has the minimum hardness, while the outer Ni coating has the maximum hardness. The transition layer between the Ni and BN phases has an intermediate hardness value. These results were later compared to micro-hardness values for the developed coatings, which will be discussed in chapter 5.

Table 4.13: Micro-hardness results for pure-Ni and Ni coated BN powders

Powder	Powder Size (μm)	Powder Structure	Average Hardness (HV₁₀)
Nickel	12	Angular	176.8
		Pure BN core	10.76
Ni coated BN	103	Bright white phase at particle boundary	316.3
		Interface with platelets structure	57.5

All the different types of feedstock powders explained in this chapter were sprayed on Ti-6Al-4V substrates. The results of the cold sprayed coatings formed using these powders are detailed in the next chapter.

4.2.5 Pycnometer Density of Ni coated BN powders

The pycnometer density assesses the pore free density of the powders. It also provides a measure of the closed-off porosity. The pycnometer densities of the 75 μm and 103 μm Ni coated BN powders were measured as 5.651 g/cm³ and 4.35 g/cm³ respectively. The results were expected as the 75 μm and 103 μm Ni coated BN powders contain 10 wt % and 20 wt % BN respectively. Table 4.14 details the results of pycnometer density measurements for the coated powders.

Table 4.14: Pycnometer density results for Ni coated BN powders

Sr. No	Particle Size (μm)	Amount of BN (wt %)	Av.Density (g/cm ³)	Std. Deviation in density (g/cm ³)	Std. Deviation in density (%)
1	75	10	5.651	0.005	0.10
2	103	20	4.345	0.003	0.07

Chapter 5

Coatings Developed using Cold Spray

Coating formation during cold-spray is comprised of two stages. During the initial pass, the adhesion between the coating and substrate that forms the interface is crucial. In the subsequent passes, the build-up of the deposited layers is of primary importance. During this study, several coating strategies were tried. Various feedstock development techniques were used, as described in chapter 4. In addition, two different process gases, namely nitrogen and helium were used.

5.1 Cold Spray coatings using Nitrogen as the Process Gas

Given its economical cost and low reactivity, nitrogen was preferred as the process gas initially. Nitrogen being a heavier gas, with a density of 1.2506 kg/m^3 , cannot provide the high critical velocity required to cold spray large sized milled and pre-coated powders. Therefore, only admixed feedstock powders were sprayed using nitrogen. As such, all other sprays were done with helium.

5.1.1 Ni-MoS₂ Coatings

Table 5.1 details the set of experiments with admixed Ni-MoS₂ feedstock sprayed with nitrogen.

Table 5.1: Details of admixed Ni-MoS₂ feedstock powders sprayed with nitrogen

Sr. No.	Mixture Composition	Size of Ni powder (μm)	Size of lubricant powder (μm)
1	Ni-2 wt. % MoS ₂	12	30
2	Ni-3 wt. % MoS ₂	12	30
3	Ni-4 wt. % MoS ₂	12	30
4	Ni-2 wt. % MoS ₂	12	3

Typical microstructures of cold-sprayed Ni-MoS₂ coating on a Ti-6Al-4V are shown in Figure 5.1. The substrate and coating can be distinguished from each other by the interface. The undulations observed at the interface between the substrate and coating results from the impacts with the Ni and MoS₂ particles during spraying. Figure 5.1 also shows an entrapped MoS₂ particle in the Ni matrix.

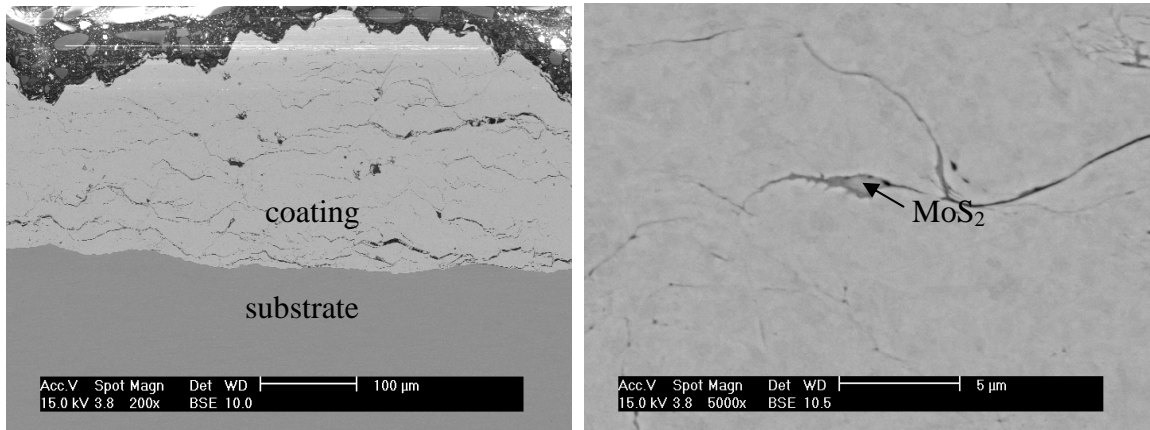
Figure 5.1: SEM images of as-sprayed Ni-MoS₂ coatings using admixed powders with nitrogen

Figure 5.2 shows the results of energy dispersive x-ray spectroscopy, which verify the presence of MoS₂ in the coating.

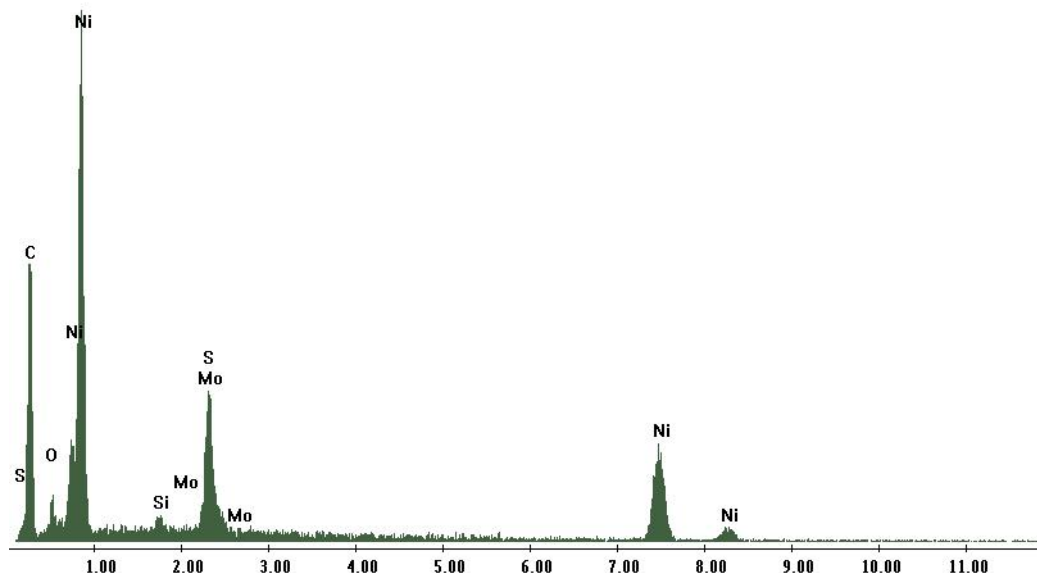


Figure 5.2: Energy Dispersive X-ray Spectroscopy of Ni-3 wt % MoS₂ coating

Based on the current experiments, there appears to be a threshold of coating thickness above which the coating build up slows down. This could also be due to the fact that as the coating builds up on itself, the distance between the nozzle and surface to be coated decreases continuously. As shown in Figure 5.3, irrespective of the number of overlaps, the coating thickness decreases with increasing amount of MoS₂. However, the effect of number of overlaps depends on the composition of the coating. While coatings with 2 and 3 wt % MoS₂ benefit from an increase in number of overlaps, there is a sharp decrease in coating thickness in case of coating with 4 wt% MoS₂.

When spraying with feedstock powder containing smaller size (3 μ m) MoS₂, no coating was formed on the substrate. As mentioned in the previous chapter, there is a large difference in density between the powders which results in varying critical velocity requirements for Ni and MoS₂. In order to compensate for the lower density of MoS₂, it is imperative to employ higher volumes and sizes of the low density lubricant powder. In

addition, aerodynamics also imposes a certain minimum requirement of particle size for enduring the shock observed during the impact of the particle on to the substrate. It is possible that the small sized lubricant particle would decelerate and deflect to a different trajectory on impact instead of deforming and adhering to the substrate.

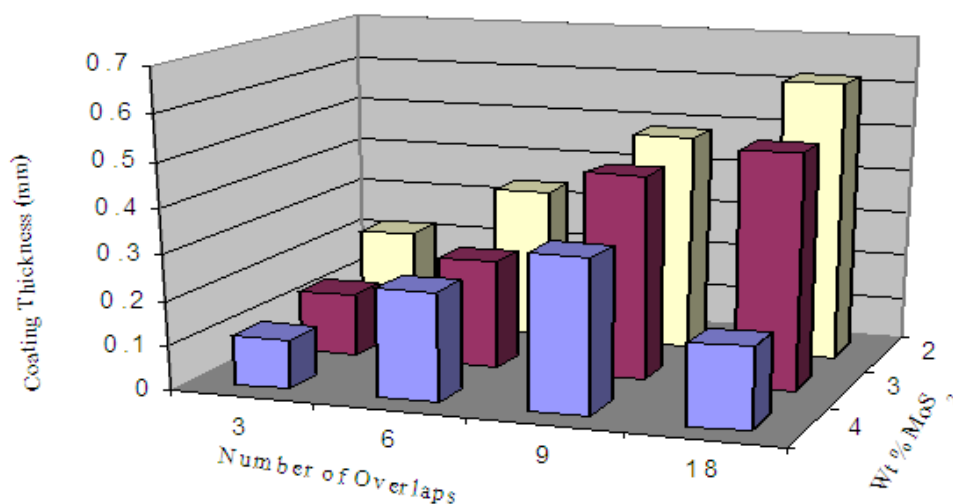


Figure 5.3: Coating thickness versus number of passes at various MoS₂ wt % in feedstock powder

5.1.2 Ni-BN Coatings

Table 5.2 summarizes the cold spray experiment with admixed Ni-BN feedstock sprayed with nitrogen.

Table 5.2: Experiments with admixed Ni-BN feedstock sprayed with nitrogen

Sr. No.	Mixture Composition	Size of Ni powder (μm)	Size of lubricant powder (μm)
1	Ni-1 wt. % BN ₂	12	10
2	Ni-2 wt. % BN ₂	12	10

Figure 5.4 shows an SEM image of an as-sprayed Ni-BN coating. Based on SEM and EDS analysis, it was determined that there was no BN present in the coating. In addition, the BN appeared to have been deflected to the vice holding the substrate during cold spraying. BN is a brittle synthetic ceramic, which does not undergo the required plastic deformation to form a good bond with the substrates. As such, because of its higher density and low specific heat ratio, nitrogen gas could not provide the high critical velocity required for BN powder.

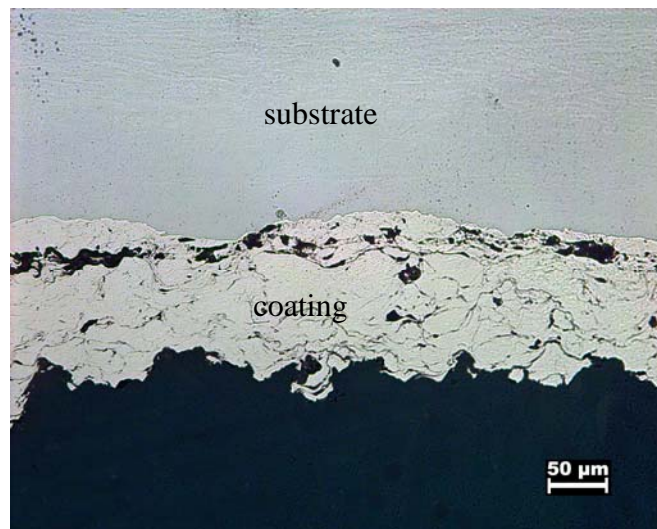


Figure 5.4: SEM images of as-sprayed Ni-BN coatings using admixed powders and nitrogen

5.2 Cold Spray Coatings using Helium as the Process Gas

Powders sprayed with helium resulted in much better coating build-up as compared to those sprayed with nitrogen. It is generally accepted that mechanical bonding is the main mechanism of coating formation in cold sprayed coatings. An

increasing plastic deformation reduces the porosity by enhancing the compression among the particles so much that the voids disperse or are minimized. Higher specific heat ratio and lower mass density of helium aid in generating high degree of plastic deformation, thereby resulting in better build-up of coatings. Particles with diameter greater than 50 μm can be accelerated using helium because of similar reasons. As will be in this section, about 1.25 – 1.5 times more lubricant was incorporated into the coatings when sprayed with helium.

5.2.1 Pure Ni coatings

Due to the tamping of the sprayed Ni powder onto the substrate, a dense structure with minimal porosity was obtained, as endorsed in optical micrograph (Figure 5.5). The boundaries of single particles are not recognizable in the optical photograph because of severe plastic deformation of the particles. Overall, a uniform deposition of the large Ni powder (75 μm) is observed in this figure. The process of plastic deformation and reconsolidation of the impacting particles is distinct in the etched microstructure of the pure Ni coating sprayed with helium. Ni is ductile and therefore can easily undergo plastic deformation when impacting onto the substrate achieving good bonding with the substrate. Even if an impact leaves a pore after deposition, the further impact and easy plastic deformation of Ni successfully closes the pores and voids of the coating. The particle velocity as well as the critical velocity mainly depends on particle size. Research has shown that the critical velocity for Ni is approximately 640 m/s [122, 159]. Good

bonding of the relatively large Ni particle can be explained by a particle velocity clearly higher than the critical one, which has been easily achieved by spraying with helium.

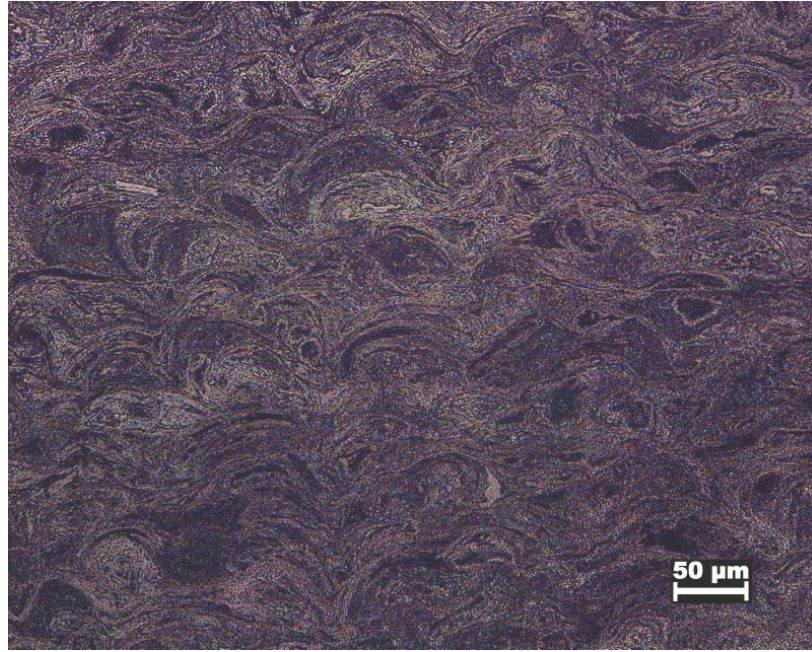


Figure 5.5: Optical micrograph of etched deposits of as-sprayed Ni (75 μm) coatings depicting particle deformation and absence of grain boundaries

5.2.2 Coatings with Admixed Ni-MoS₂ Feedstock Powder

Table 5.3 details the set of cold spray experiments undertaken with admixed Ni-MoS₂ feedstock powders sprayed with helium. Higher amounts of MoS₂ (7 wt %) and better coating build-up were achieved by spraying with helium instead of nitrogen as the process gas.

Table 5.3: Experiments with admixed Ni-MoS₂ feedstock sprayed with helium

Sr. No.	Mixture Composition	Size of Ni powder (μm)	Size of lubricant powder (μm)
1	Ni-3 wt. % MoS ₂	12	30
2	Ni-4 wt. % MoS ₂	12	30
3	Ni-7 wt. % MoS ₂	12	30
4	Ni-7 wt. % MoS ₂	32	30

Figure 5.6 shows a photograph of the top-view of an as sprayed Ni-7 wt% MoS₂ coating. It is evident from the photograph that the Ni and MoS₂ particles have segregated during cold spraying. While the initial sprays are rich in MoS₂, the subsequent passes look depleted of MoS₂. During spraying admixed feedstock, the MoS₂ particles are accelerated to a much higher extent due to their lesser density (4.8g/cc) in comparison to Ni(8.8g/cc). Consequently, the feedstock left for the subsequent passes is depleted of MoS₂.

Figure 5.6: Top view of an as-sprayed Ni-7 wt% MoS₂ coating using admixed feedstock.

Figure 5.7 shows a cross section of the coating. The circled areas on the image illustrate regions which were away from the jet stream during deposition. In these regions, the jet is at an angle with the substrate. Therefore, a relatively lower particle impact velocity was achieved. Kinetic energy transferred during impact was insufficient for a good metallurgical bonding between the deposited layers.

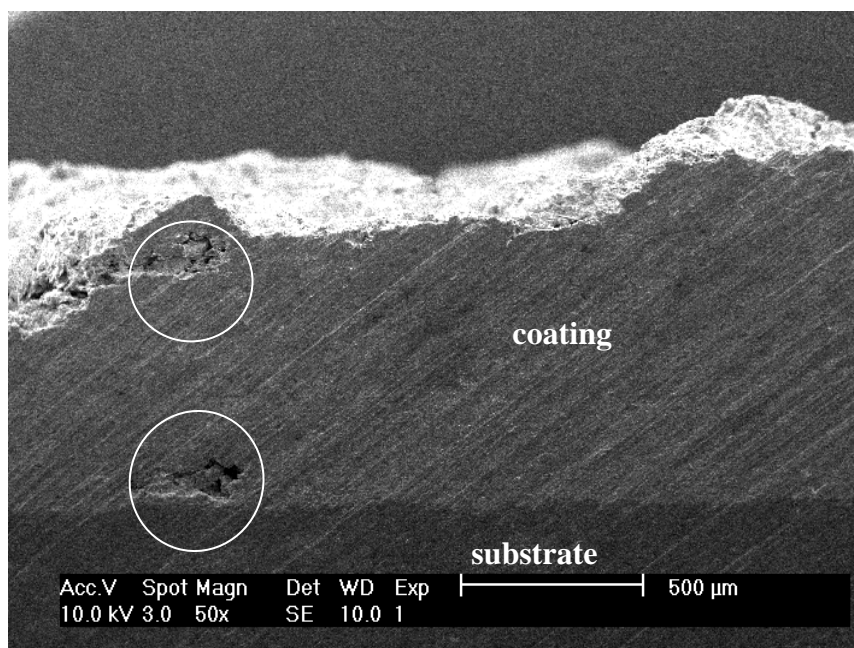


Figure 5.7: SEM image of unpolished cross section of the Ni-7 wt% MoS₂ coating sprayed helium, showing weak metallurgical bonding at side away from jet stream

Figure 5.8 shows that MoS₂ has indeed been embedded into the Ni matrix. However, the distribution of MoS₂ in the coatings is not homogeneous. It is interesting to note that the MoS₂ particles do not appear to be deformed. Moreover, the size of the MoS₂ particles embedded into the coating is much smaller than the initial particle size (30 μm). It may be assumed that while the ductile Ni powders underwent high deformation, the brittle MoS₂ particles fractured during impact and were caught up in the coating by

the incoming and surrounding Ni particles. As such, an increased porosity was observed in the MoS₂ rich regions. It is not clear if this porosity was formed due to pulling out of MoS₂ particles while polishing and sample preparation.

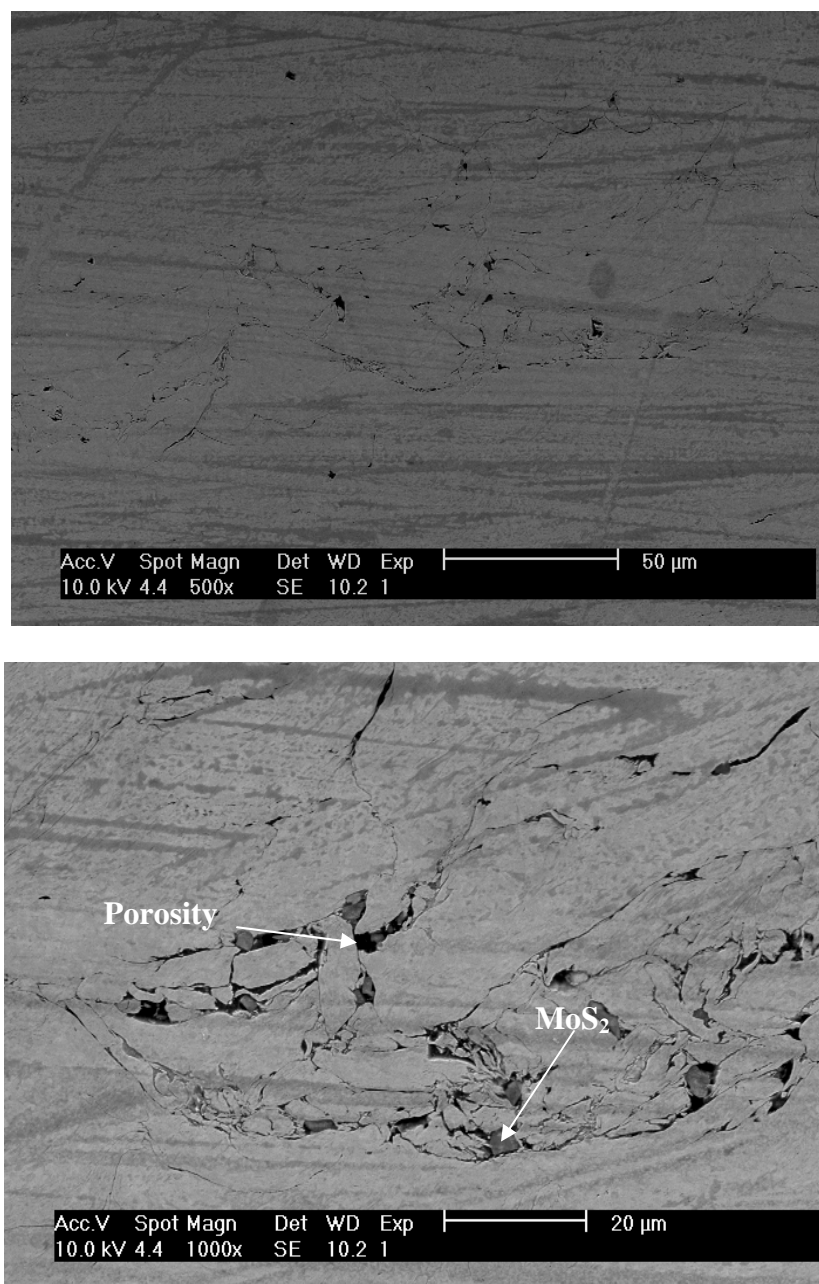


Figure 5.8: SEM images of as-sprayed Ni-7 wt % MoS₂ coatings using admixed powders and helium

5.2.3 Coatings with admixed Ni-BN feedstock powder

Table 5.4 details the admixed Ni-BN feedstock powders which were sprayed with helium.

Table 5.4: Experiments with admixed Ni-BN feedstock sprayed with helium

Sr. No.	Mixture Composition	Size of Ni powder (μm)	Size of lubricant powder (μm)
1	Ni-4 wt. % BN	12	10
2	Ni-4 wt. % BN	32	10
3	Ni-4 wt. % BN	75	10
4	Ni-5 wt. % BN	12	10
5	Ni-5 wt. % BN	75	10

Figure 5.9 shows a photograph of the top-view of an as sprayed Ni-5 wt% BN coating. There is a segregation of Ni and BN powders, akin to what was observed with spraying admixed Ni-MoS₂ coatings. Again, due to the difference in densities of Ni (8.8g/cc) and BN (2.7g/cc) powders, the particles have segregated.

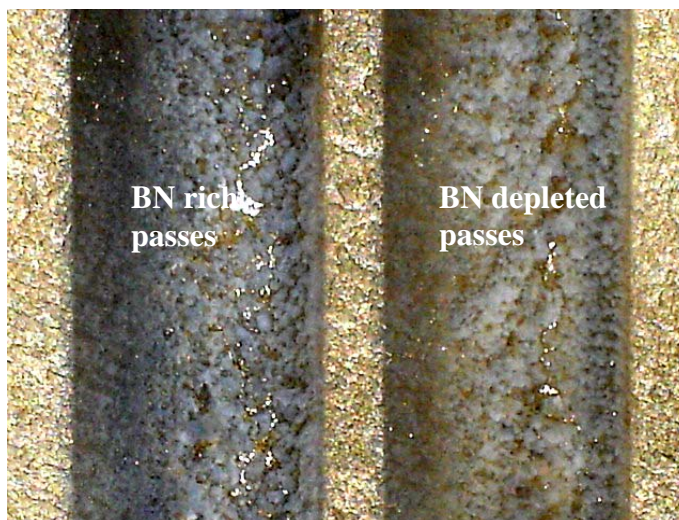


Figure 5.9: Top-view of an as-sprayed Ni-5 wt% BN coating using admixed feedstock, showing segregation of BN

The BN particles appear to deform to a greater extent than the MoS₂ particles, as endorsed in Figure 5.10. However, there is some porosity in the coating, which might be due to pulling out of BN while polishing..

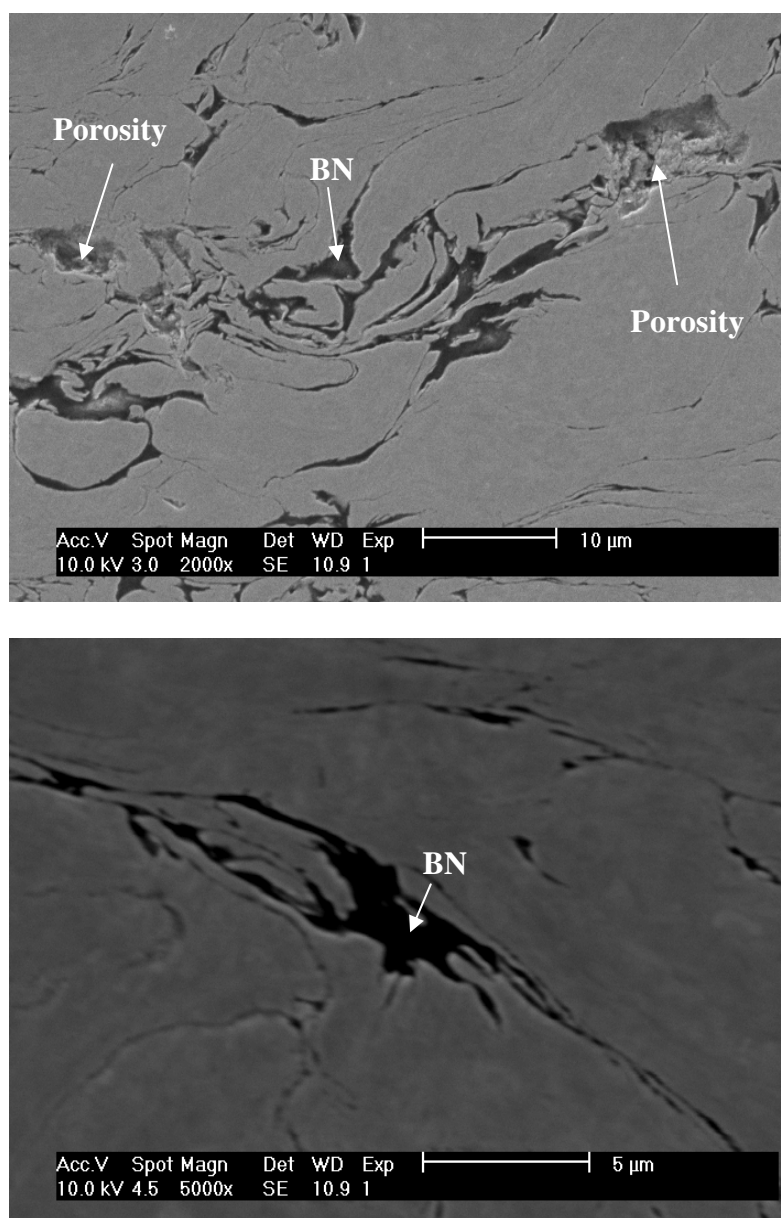


Figure 5.10: SEM images of as-sprayed Ni-5wt % BN coatings using admixed powders and helium

5.2.4 Coatings with milled Ni-MoS₂ feedstock powder

In order to avoid the segregation of admixed feedstock powders during spraying, the raw powders were milled together so as to create metallurgical bonding between the Ni and lubricant powders prior to spraying. Table 5.5 details the admixed Ni-MoS₂ feedstock powders which were sprayed with helium. It was observed that the deposition improved with decrease in the variation of particle size of the agglomerates.

Table 5.5: Experiments with admixed Ni-MoS₂ feedstock sprayed with helium

Sr. No.	Mixture Composition	Initial Size of Ni powder (μm)	Initial Size of lubricant powder (μm)	Size of agglomerates (μm)
1	Ni-3 wt. % MoS ₂	12	30	32-53
2	Ni-7 wt. % MoS ₂	12	3	25-75
3	Ni-7 wt. % MoS ₂	12	3	32-53



Figure 5.11: Top view of an as-sprayed Ni-7 wt% MoS₂ coating using milled feedstock showing erosion of coating by subsequent passes

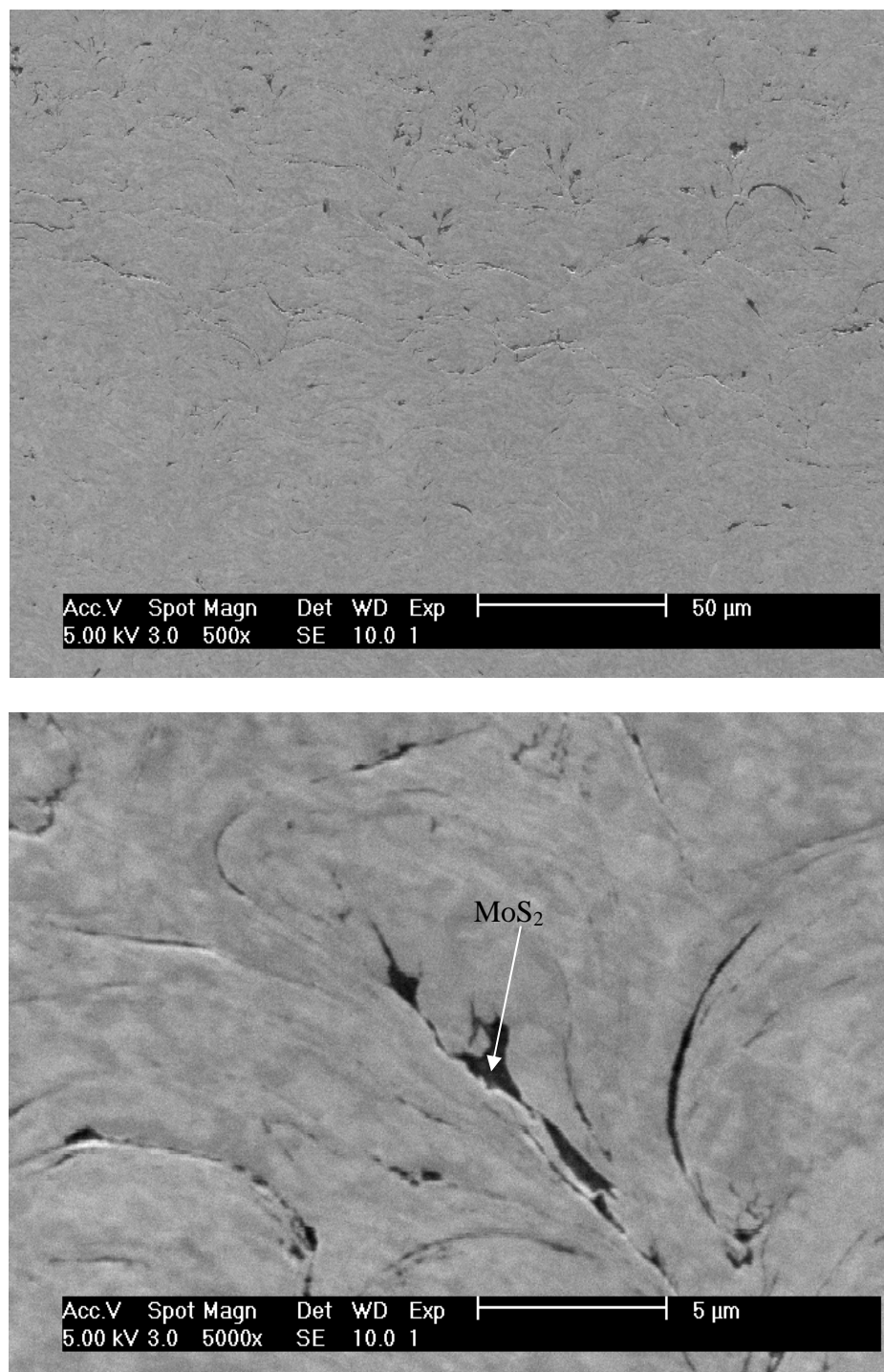


Figure 5.12: SEM images of as-sprayed Ni-7 wt % MoS₂ coatings using milled powders and helium

During spraying of mechanically milled powders, the aggregation of feedstock powder particles of a relatively large size was destroyed upon impact on the substrate, resulting in a highly irregular surface. Figure 5.11 shows that particle bombardment onto the first layer of the coating actually eroded the previously deposited coating layers. During mechanical milling, the powders could have experienced cold-working and strain-hardening. As a result, the milled powders were unable to deform on impacting the substrate while cold-spraying. It appears that most of the MoS_2 in the agglomerates was lost while fracturing. However, there was some MoS_2 incorporation into the coatings, as shown in Figure 5.12.

5.2.5 Coatings with milled Ni-BN feedstock powder

An optimized milled Ni-2 wt. % BN powder was cold sprayed on the Ti-6Al-4V substrate. As shown in Figure 5.13 the problem of segregation in admixed feedstock could not be avoided by mechanically milling the powders. In addition, some erosion of previously deposited coating layers was also observed.

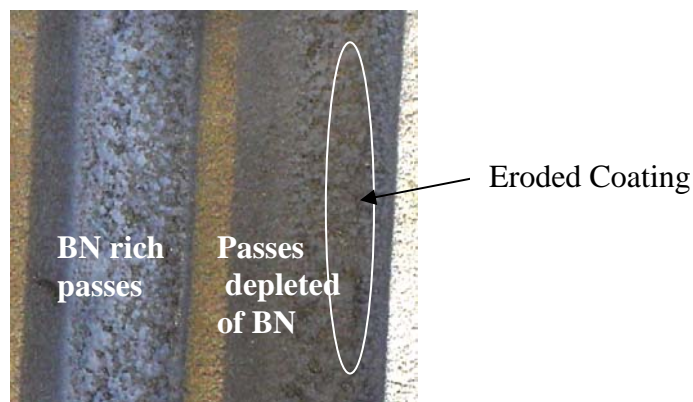


Figure 5.13: Close-up of as-sprayed Ni-2 wt% BN coating using milled feedstock

Figure 5.14 shows images of the coatings developed with milled Ni-5 wt % BN feedstock. In these coatings, the BN was non- uniformly distributed in the coatings.

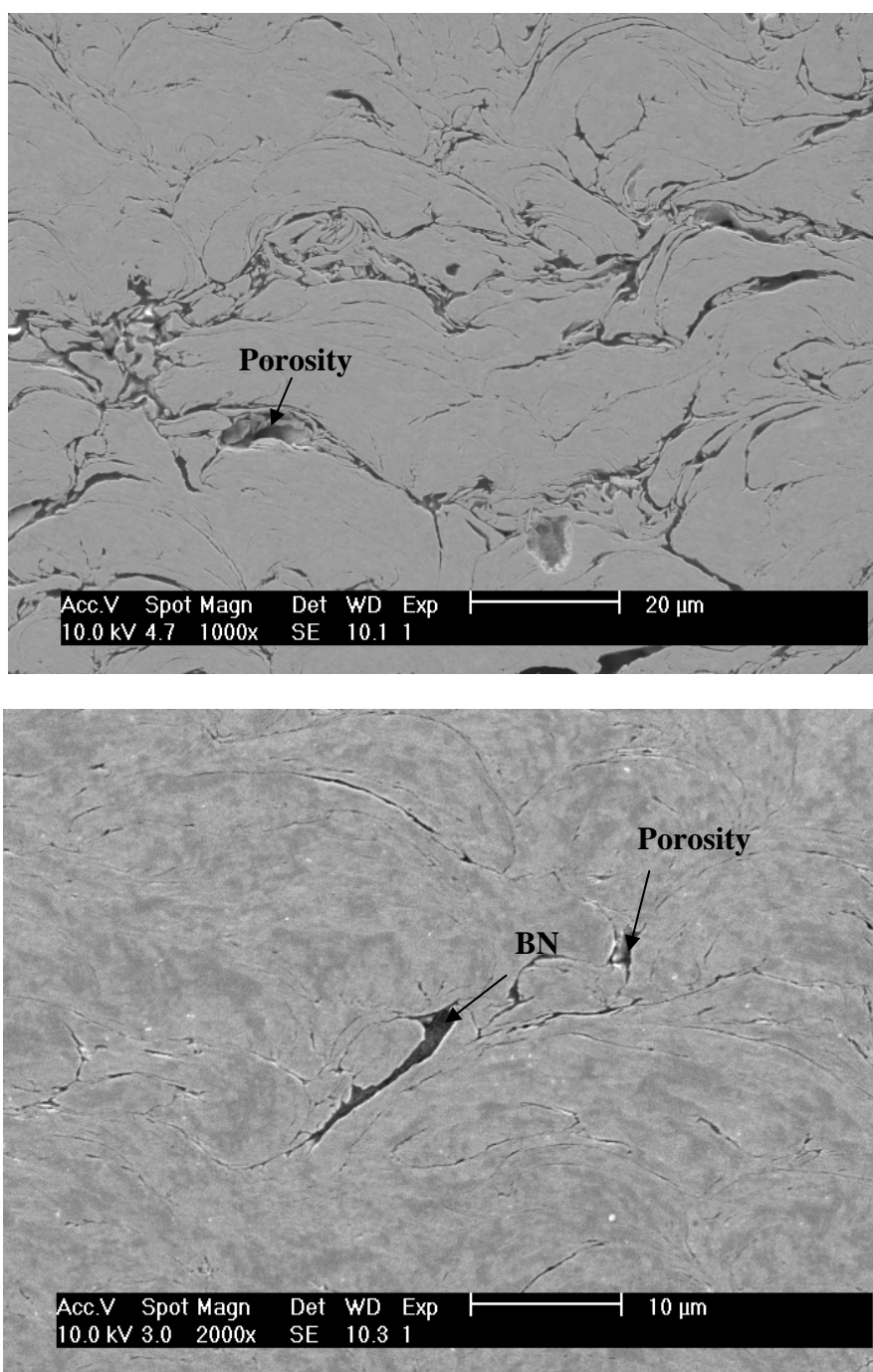


Figure 5.14: SEM images of as-sprayed Ni-5 wt % BN coatings using milled powders and helium

5.2.6 Coatings with admixed Ni-Ni coated BN powders

Table 5.6 lists the various feedstock powders which were sprayed on the Ti-6Al-4V substrates. Figure 5.15 shows the low magnification optical and SEM images of the coatings formed with admixed Ni-Ni coated BN feedstock powders using helium. From the etched optical microstructure of the coating (Figure 5.16), it is clear that the Ni particles have experienced extensive plastic deformation during deposition. There appears to be no evidence of any recrystallized grain structure in the coatings. It may be inferred that no thermal softening or heating of the Ni or BN particles took place at the localized contact region on impact.

Table 5.6: Experiments with admixed Ni-MoS₂ feedstock sprayed with helium

Sr. No.	Mixture Composition	Amount of BN (wt.%)	Size of Ni powder (μm)	Size of lubricant powder (μm)
1	Ni-5 wt. % Ni coated BN	0.5	12	75
2	Ni-15 wt. % Ni coated BN	1.5	12	75
3	Ni-20 wt. % Ni coated BN	2.0	12	75
4	Ni-30 wt. % Ni coated BN	3.0	12	75
5	Ni-30 wt. % Ni coated BN	3.0	75	75
6	Ni-5 wt. % Ni coated BN	1.0	12	103
7	Ni-15 wt. % Ni coated BN	3.0	12	103
8	Ni-20 wt. % Ni coated BN	4.0	12	103
9	Ni-25 wt. % Ni coated BN	5.0	12	103
10	Ni-30 wt. % Ni coated BN	6.0	12	103

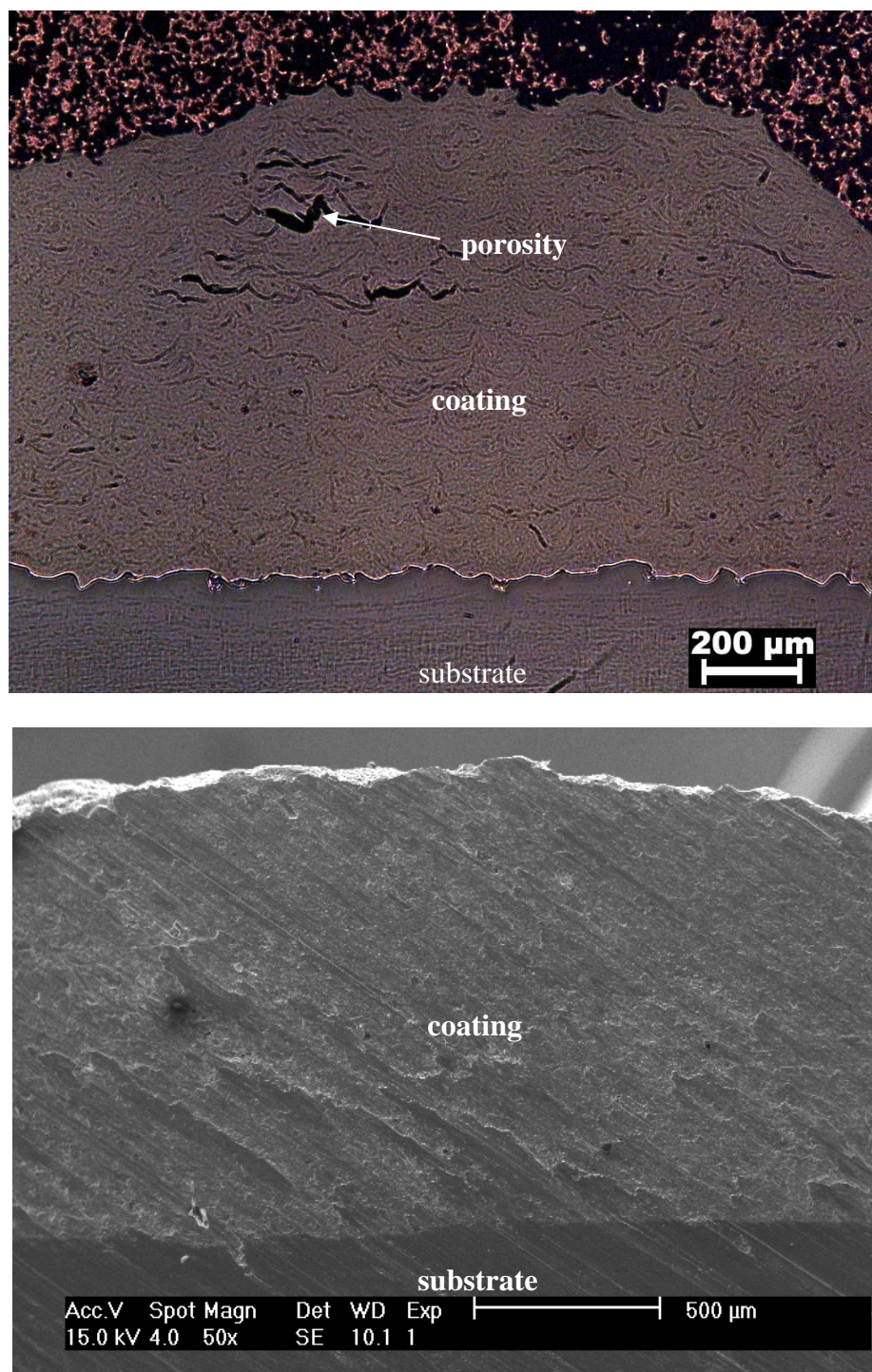


Figure 5.15: Low magnification images of Ni- BN coating-substrate interface. Top: Optical image of polished and etched sample; Below: SEM image of cut sample

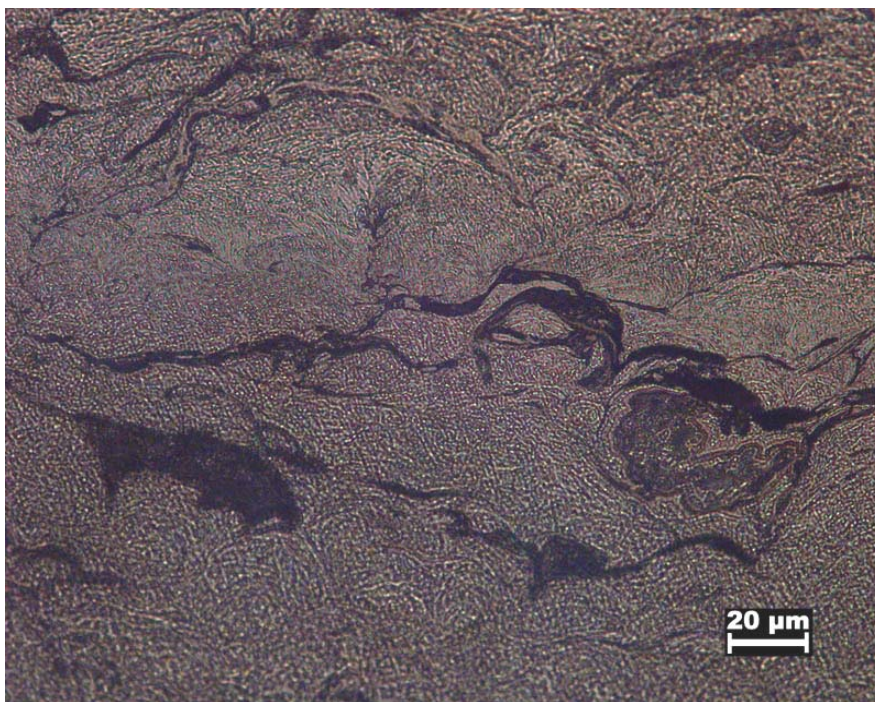


Figure 5.16: Optical image of etched Ni-BN coating

Figure 5.17 shows a high magnification image of the coating surface. The coating has a rough surface morphology, with many humps on the surface formed through the stacking of the deformed powder particles. Detailed examination clearly confirms the presence of BN particles on the surface of the coatings. Since the BN is non conductive, it appears as bright white spots on the SEM image.

In Figure 5.18, the overlaps of deposited layers are delineated. A relatively larger amount of BN was found at the overlaps. However, some porosity and voids were also visible at the overlaps. With increasing distance from the overlaps, the BN concentration decreased. Consequently, the minimum amount of BN was present in the areas between two overlaps.

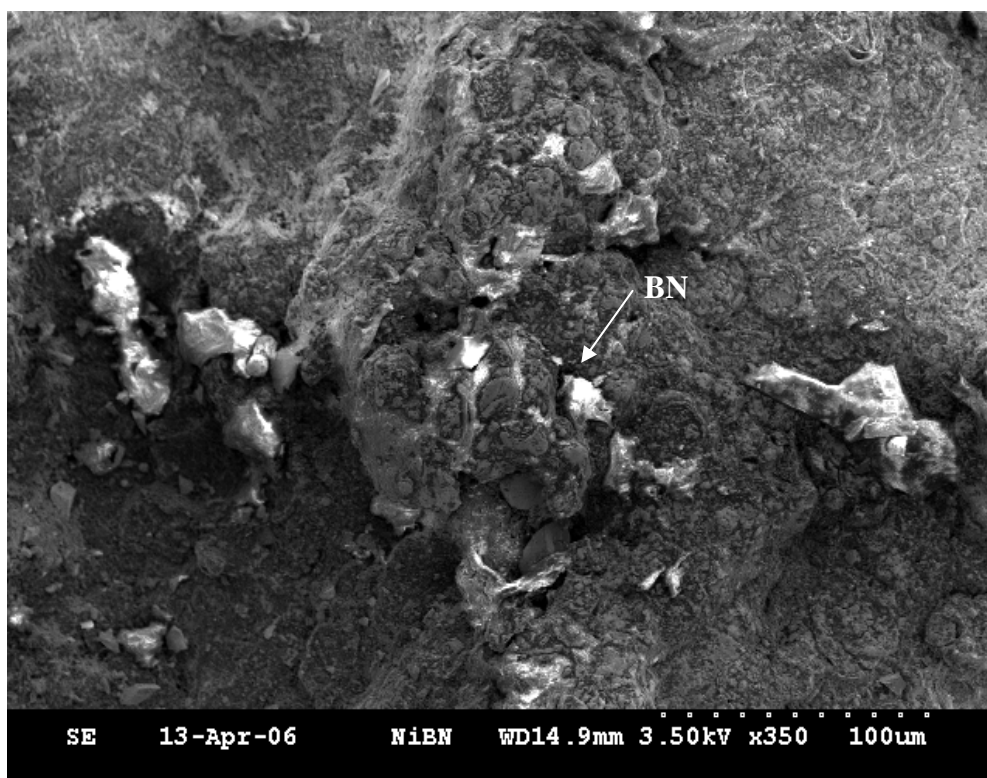


Figure 5.17: SEM image of the top surface of the coating

Figure 5.19 shows high magnification SEM images of the coatings. From the size of BN embedded in the coatings, it is obvious that the large Ni coated BN powders have fractured. As expected, the smaller Ni powder deformed extensively and adhered to the surface. On the other hand, the large size coated powders fractured on impact. These large particles not only provided a tamping effect for improved adhesion, but some of the fragments of the fractured powder got entrapped into the coating because of the surrounding and incoming Ni particles. Consequently, a dense and coherent coating with BN particles embedded in the Ni matrix was formed.

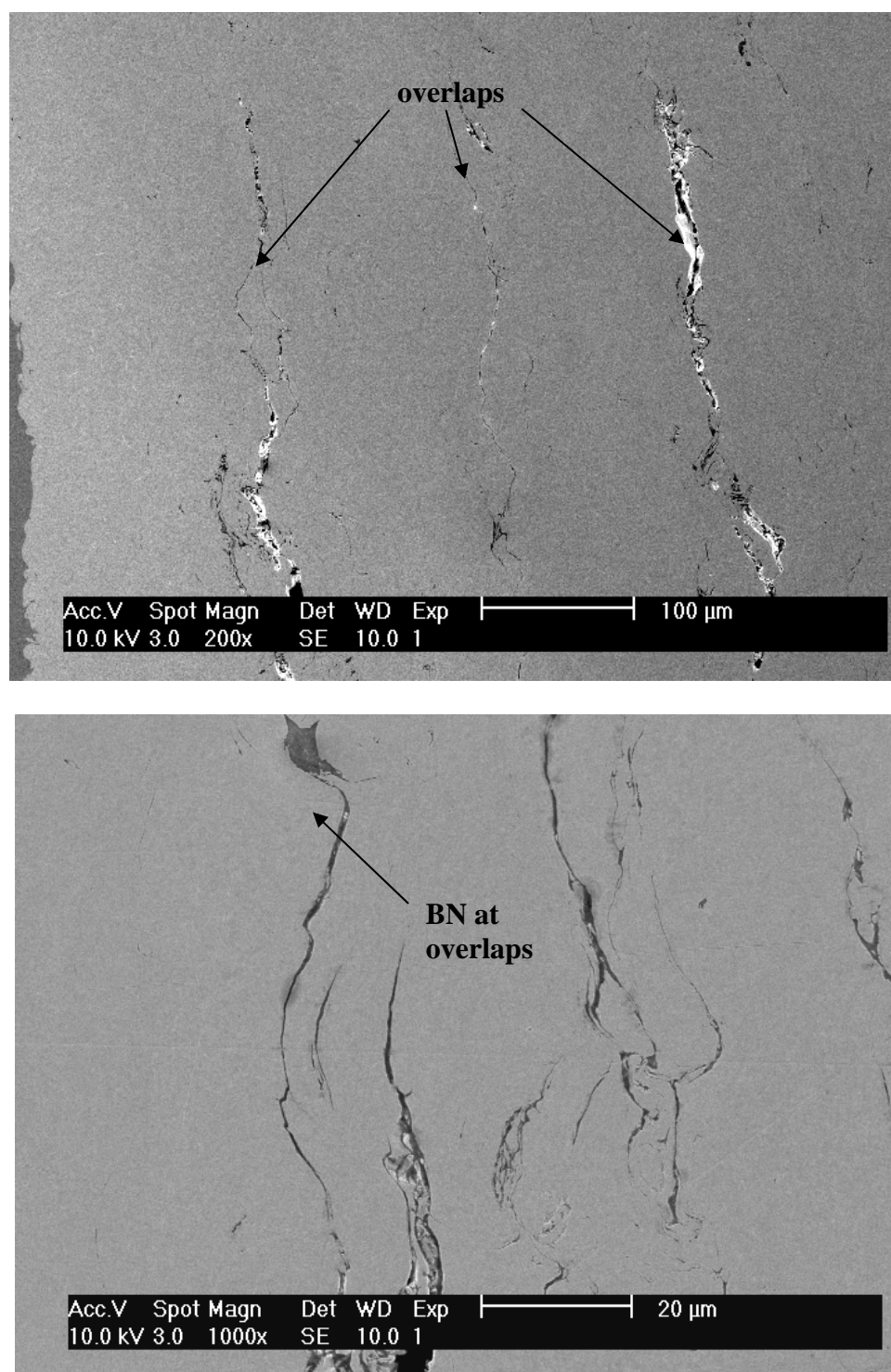


Figure 5.18: SEM images of Ni-BN coating

Figure 5.20 shows Energy Dispersive X-ray results for Ni-Ni coated BN coating.

The peaks of B and N corroborate the presence of BN in the coatings.

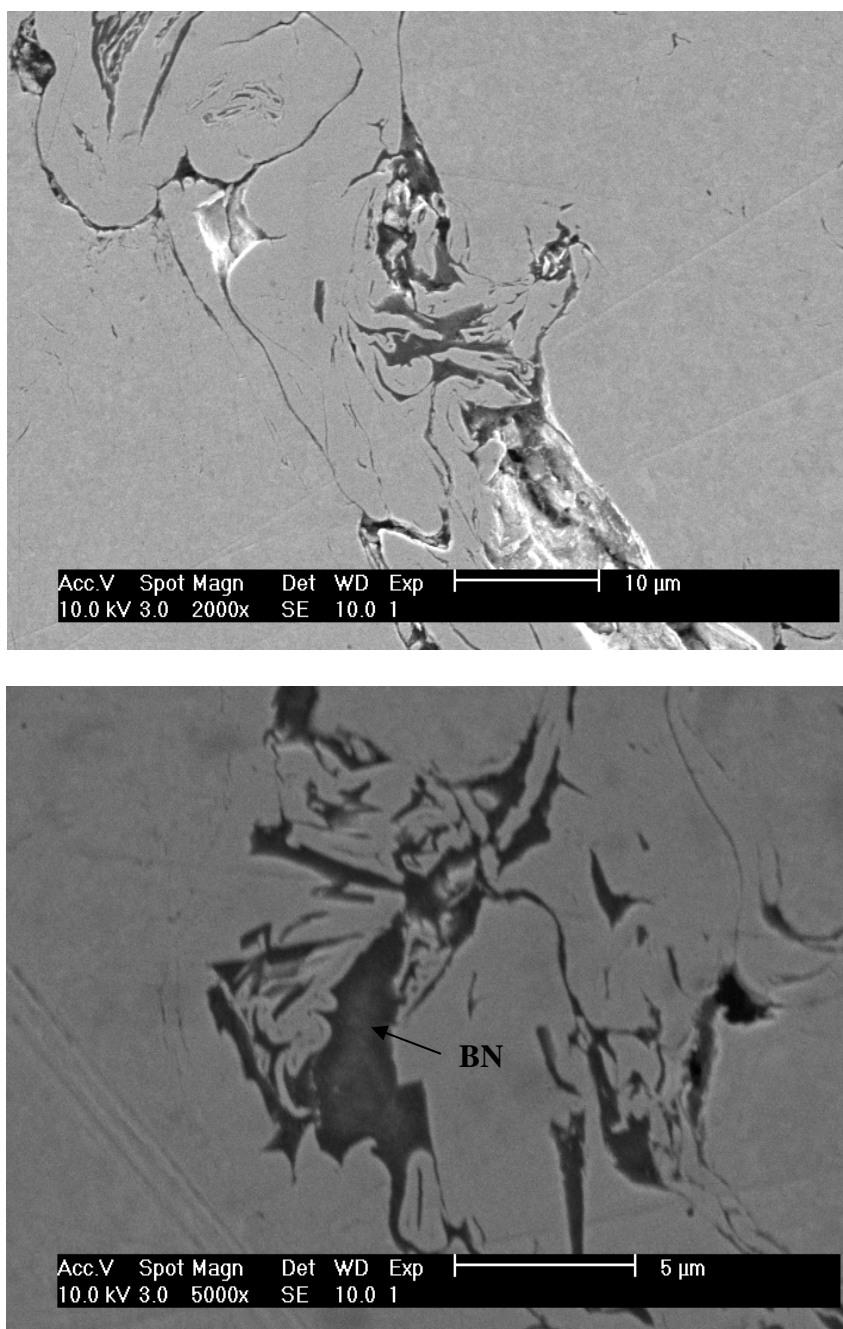


Figure 5.19: SEM images of Ni-BN coating

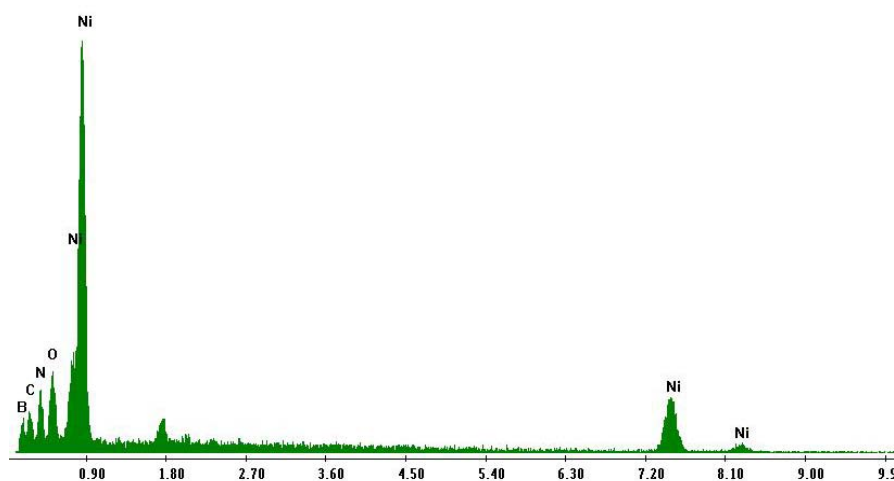


Figure 5.20: Energy Dispersive X-ray Spectroscopy of the Ni-Ni coated BN coating

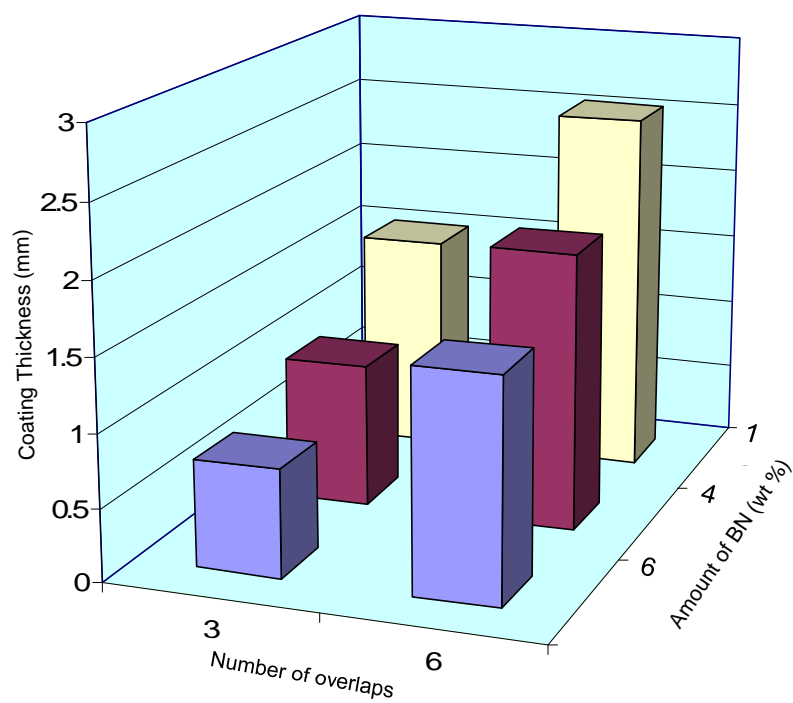


Figure 5.21: Coating thickness versus number of passes at various BN wt % in feedstock powder

Figure 5.21 shows the effect of number of passes and amount of BN on the coating thickness. The results were analogous to those obtained for Ni-MoS₂ coatings sprayed with nitrogen. The decrease in coating thickness with increasing amount of BN confirms that the presence of BN slows down the coating build-up.

5.3 Testing of coatings produced with admixed Ni-Ni coated BN

In addition to optical microscopy, scanning electron microscopy, and energy dispersive X-ray spectroscopy, the coating developed with pre-coated Ni powders was subjected to several other tests. X-ray diffraction patterns of the powder and coating were compared. Micro-hardness of the coating was evaluated throughout the coating cross section. The bond strength of the coating to the substrate was studied using adhesion testing. Finally, the coatings were tested for fretting wear.

5.3.1 X-Ray Diffraction (XRD)

Figure 5.22 and Figure 5.23 show the XRD patterns of feedstock powder and coating developed using admixed Ni-30 wt % Ni coated BN powder. Clearly, the main XRD peaks of the coating are the same as that of the starting feedstock powder. Furthermore, no significant changes in lattice dimension and chemical composition are observed. Therefore, it seems that the cold-sprayed coating of the admixed Ni-Ni coated BN powder on the Ti-6Al-4V substrate was carried out without significant crystallographic and chemical alteration.

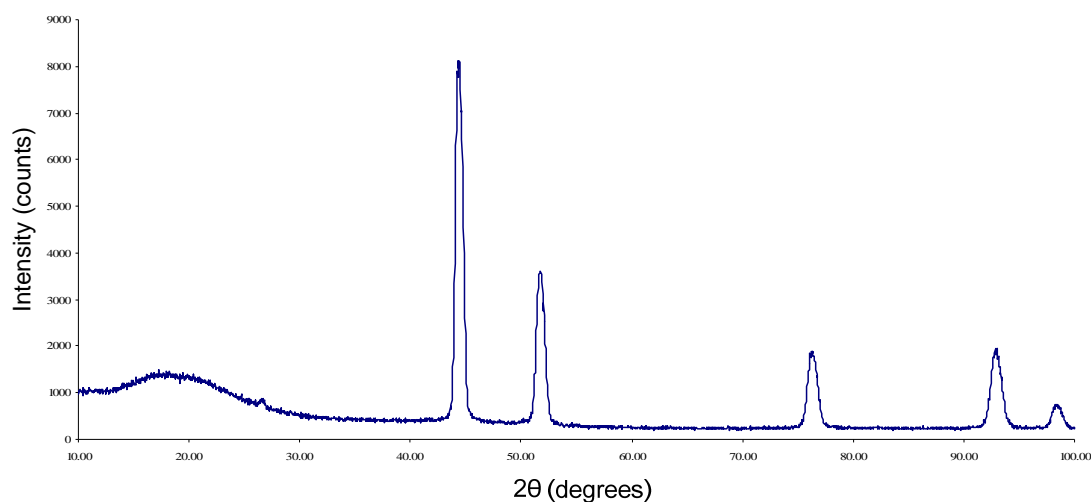


Figure 5.22: XRD results for admixed Ni-Ni coated BN powder

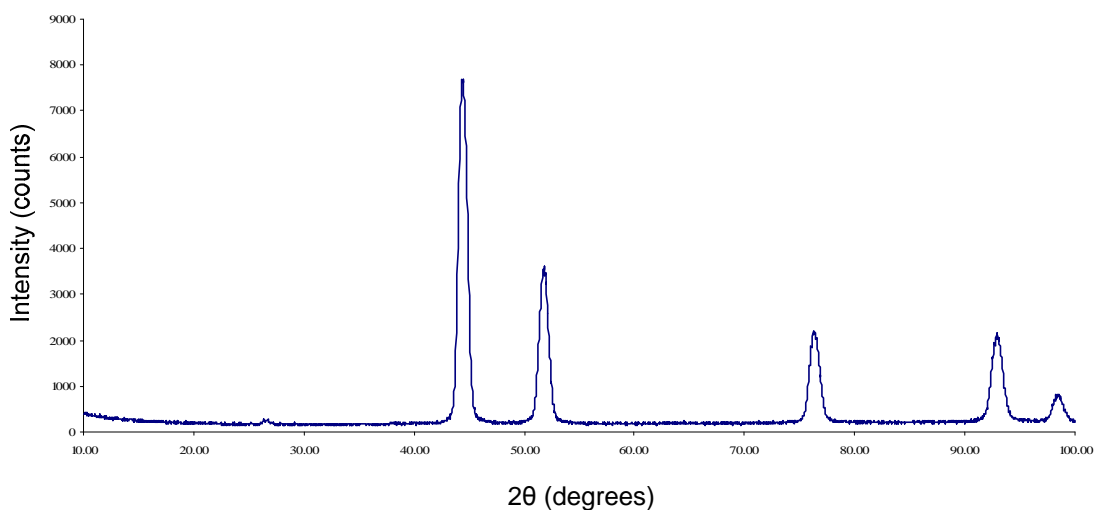


Figure 5.23: XRD results for coating developed with admixed Ni-Ni coated BN powder

As such, it is too difficult to identify BN in the powder as well as the coating. The diffraction pattern shows mostly the nickel phase, but there is a peak around 26.5° (Figure 5.24) that was not identified. It is difficult to conclude if the peak is for C or BN.

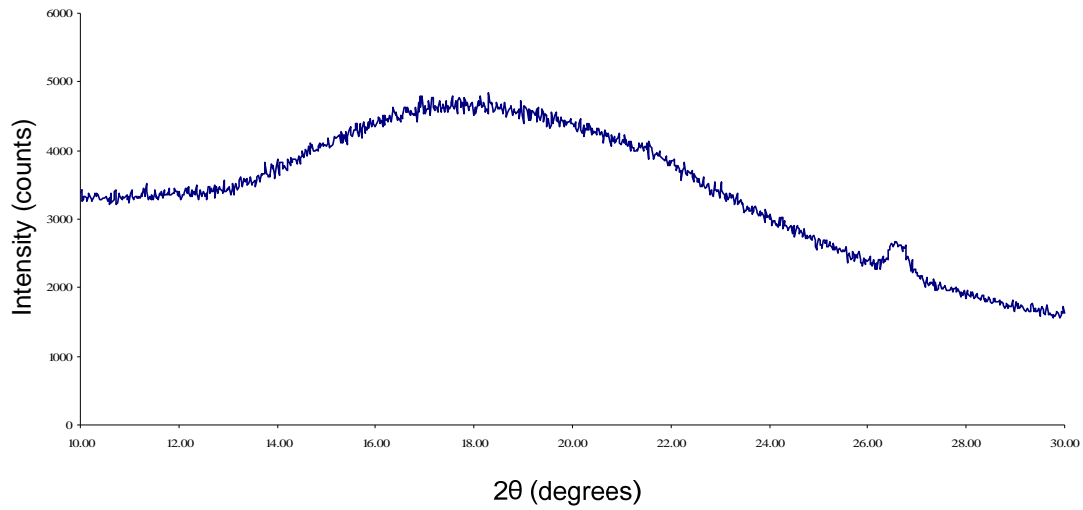


Figure 5.24: Magnified view of XRD peak of admixed Ni-Ni coated BN powder

5.3.2 Hardness Testing

Figure 5.25 shows the hardness profiles of pure Ni and Ni-BN coatings. The cold-sprayed Ni and Ni-BN coatings have a higher micro-hardness as compared to that of the individual Ni and Ni coated BN powders. The coating micro-hardness enhancement is more dependent on the impact velocity than the starting particle micro-hardness itself. The impact of the particles against the substrate at supersonic velocities promotes a densification amongst the feedstock powder particles. In addition, a high plastic deformation of the powder particles during compaction leads to an increase in dislocation density, and strain hardening in the coating, resulting in an increased micro-hardness.

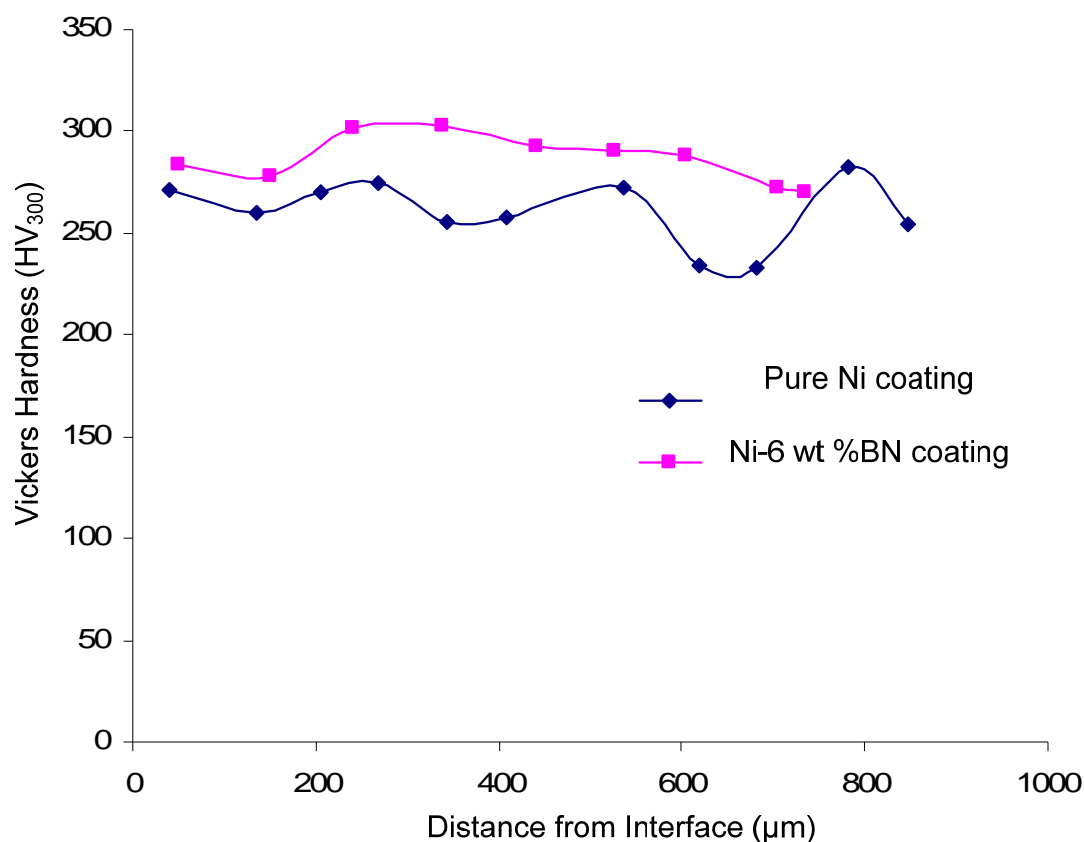


Figure 5.25: Hardness profiles of pure Ni and Ni-BN coatings

The self-lubricating coatings possessed a higher hardness relative to the pure Ni coatings. Despite being soft and lubricious, the interlacing hexagonal structure of the BN improves the hardness by providing effective lubrication between the contacting surfaces. Some BN particles remain embedded into the coating even after initial wear. These particles can enhance the effective lubrication and separation of the remaining metal surfaces. As seen in the SEM images, the BN particles are homogeneously distributed in the nickel matrix; these particles would obstruct the easy movement of dislocations and resist plastic flow during indentation. The experimental observations regarding improved hardness agree with the densification and uniform distribution of BN particles observed

in the microstructures of the powder and coating. It is expected that the improvement in hardness by adding BN to the coating should provide sufficient protection to the substrate against wear and other surface damages.

5.3.3 Bond Testing

Bond testing was performed to determine the degree of adhesion strength of the coatings to the Ti-6Al-4V substrate. Such testing also evaluated the cohesion strength of the coating under tension normal to the surface.

Figures 5.26-5.31 show the fractured surfaces of the bond tested samples. In case of the pure Ni coating (Figure 5.26), the failure occurred at the adhesive at 33.7 MPa. This result is unexpected since the bond strength of the adhesive was measured as 53 MPa. Probably, a fracture from the adhesive may have occurred due to improper bonding between the two slugs. The samples coated with feedstock powders with a Ni coated BN up-to 25 wt. % fractured within the coating resulting in cohesive failures (Figures 5.27–5.29). However, at 30 wt. % Ni coated BN, the failure occurred at the coating-substrate interface resulting in an adhesive failure (Figures 5.30 - 5.31).

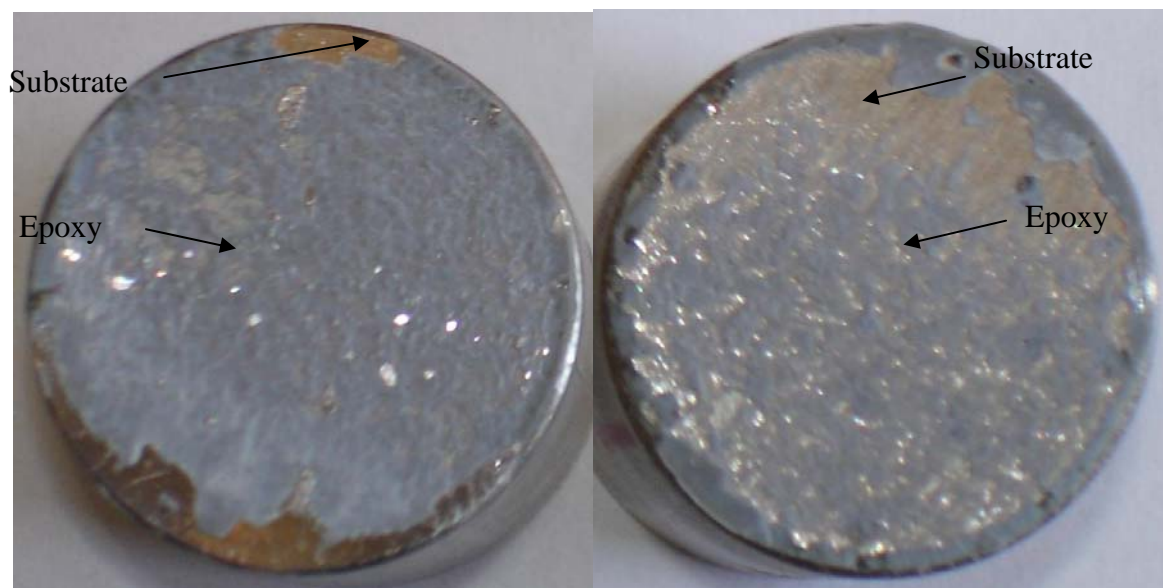


Figure 5.26: Top view of Ni coating surface after fracture showing failure at the epoxy

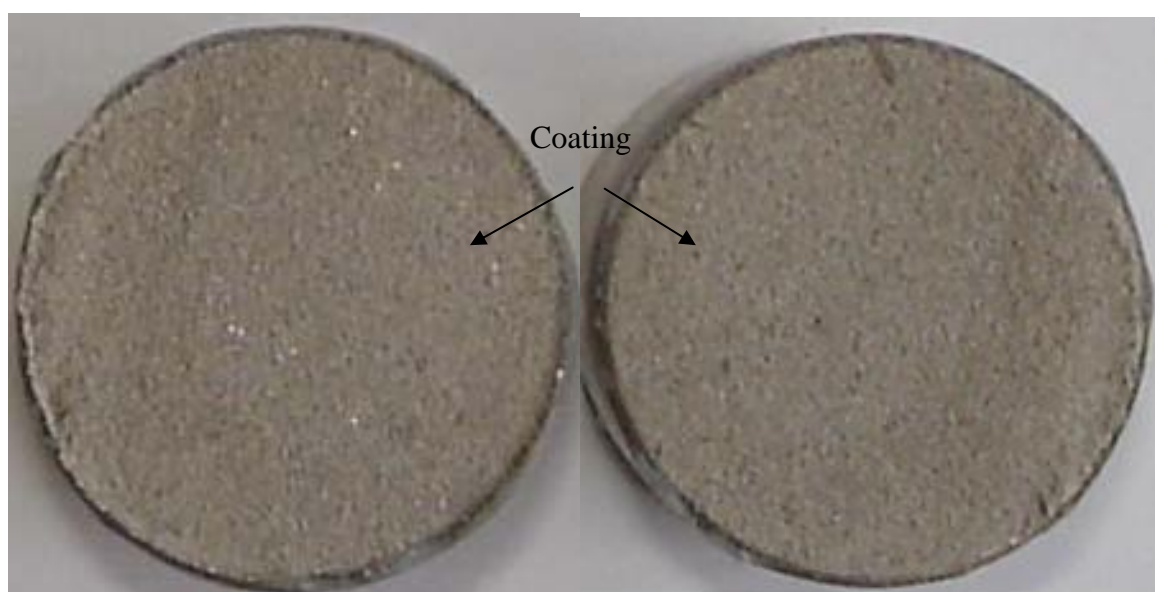


Figure 5.27: Top view of Ni-20 wt. % Ni coated BN (75 μm) coating surface after fracture showing cohesive failure within the coating

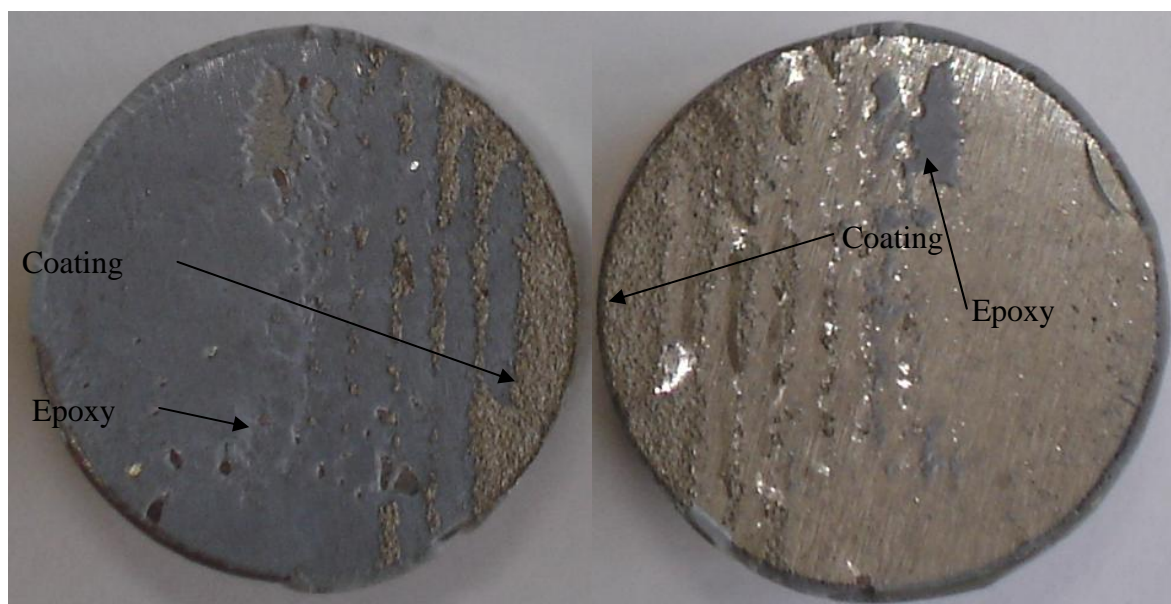


Figure 5.28: Top view of Ni-20 wt. % Ni coated BN (103 μm) coating surface after fracture showing cohesive failure within the coating

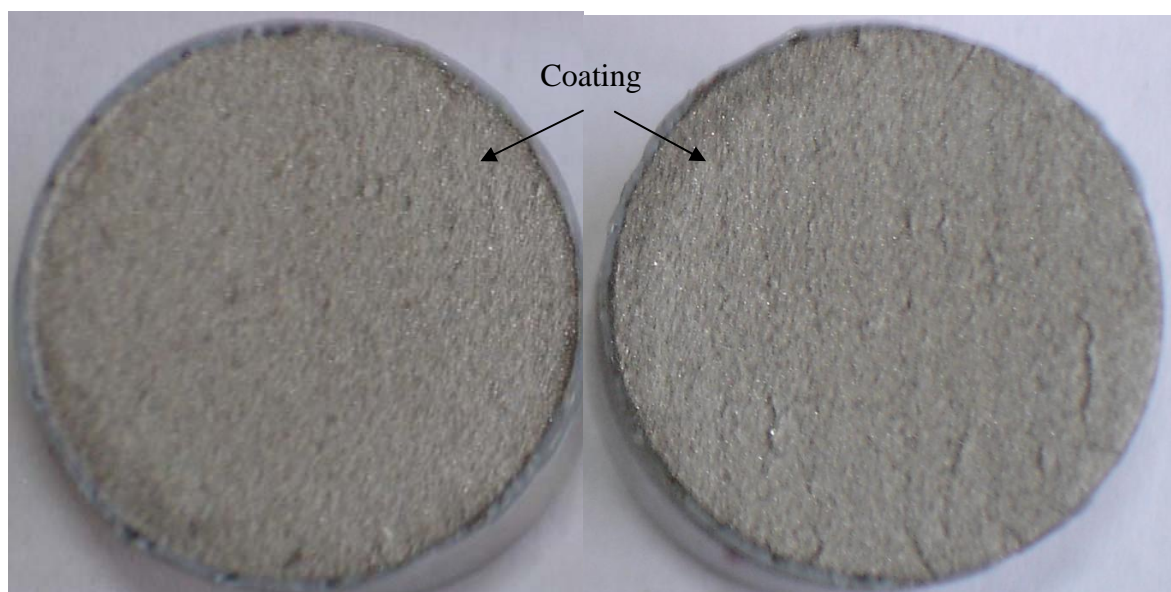


Figure 5.29: Top view of Ni-25 wt. % Ni coated BN (103 μm) coating surface after fracture showing cohesive failure within the coating

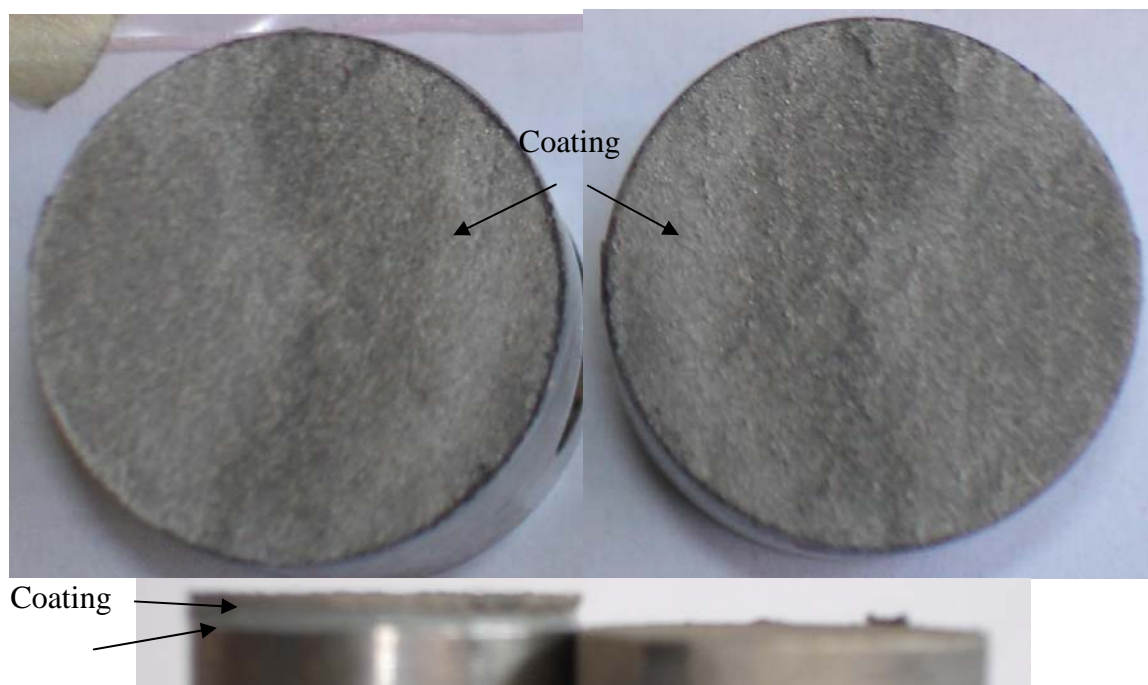


Figure 5.30: Top and side views of Ni-30 wt. % Ni coated BN (75 μm) coating surface after fracture showing adhesive failure at coating-substrate interface

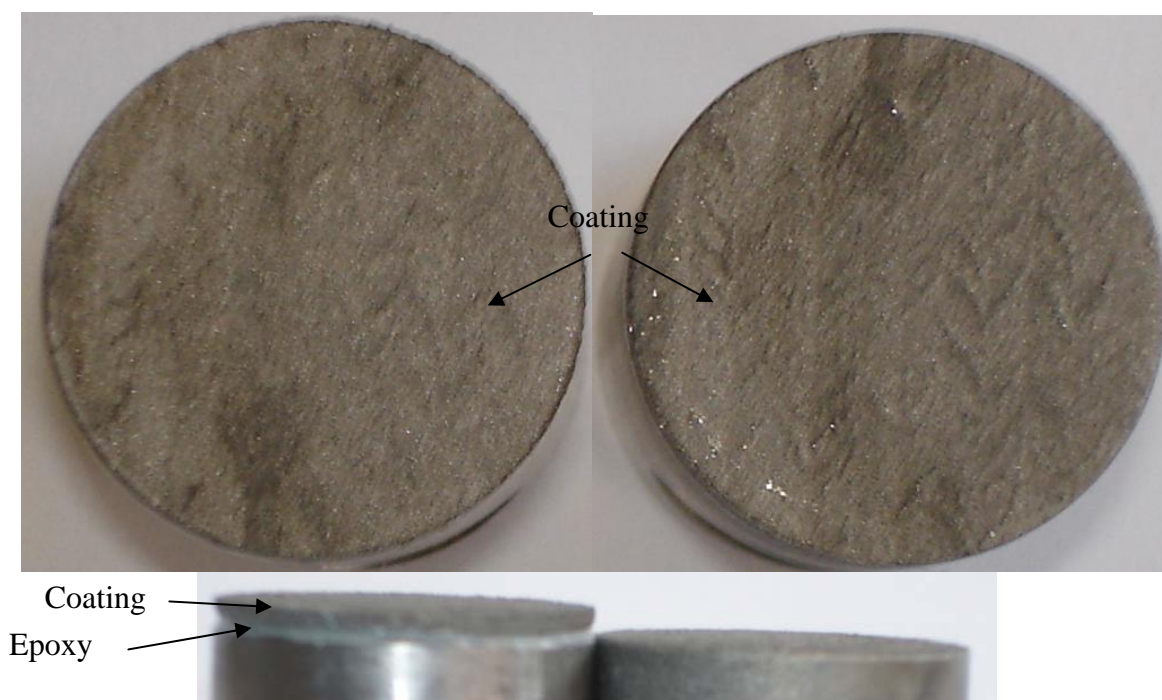


Figure 5.31: Top and side views of Ni-30 wt. % Ni coated BN (103 μm) coating surface after fracture showing adhesive failure at coating-substrate interface

Figure 5.32 shows the load displacement curves for various coatings tested under tensile load. Since the geometry of all the samples was the same, the load displacement curves can be construed as being analogous to the stress-strain curves. The adhesive strength of the bonding agent was measured as 53 MPa. As evident from the plot, the pure Ni coating has the maximum adhesive strength (33.7 MPa). With increasing amount of BN in the coatings, the bond strength decreases. While the cohesive strengths of the Ni-20 wt. % Ni coated BN (75 μm), Ni-20 wt. % Ni coated BN (103 μm), and Ni-25 wt. % Ni coated BN (103 μm) were in the range of 25-30 MPa, The adhesive strengths of coating with Ni-30 wt. % Ni coated BN (75 μm) and Ni-30 wt. % Ni coated BN (103 μm) were below 5.5 MPa. These findings have been detailed in Table 5.7.

Table 5.7: Bond Strengths Ni-Ni coated BN coatings.

Sr. No.	Mixture Composition	Size of Ni powder (μm)	Size of coated powder (μm)	Amount of BN (wt.%)	Type of Failure	Bond Strength (MPa)
1	Epoxy E-214HP HYSOL	--	--	--	At epoxy	53
2	Pure Ni	68	--	0	At epoxy	33.7
3	Ni-20 wt. % Ni coated BN	12	75	2	Cohesive	25
4	Ni-20 wt. % Ni coated BN	12	103	4	Cohesive	29
5	Ni-25 wt. % Ni coated BN	12	103	5	Cohesive	28
6	Ni-30 wt. % Ni coated BN	12	75	3	Adhesive	3.9
	N-30 wt. % Ni coated BN	12	103	6	Adhesive	5.4

Figure 5.33 compares the cohesive/adhesive strengths of various coatings formed with admixed Ni-BN Coated BN powders. Clearly, the strength decreases with increasing amount of BN in the feedstock powders and coatings. The plot also indicates that coatings formed with larger Ni coated BN powder (103 μm) have higher adhesion strengths than those with smaller Ni coated BN powder (75 μm).

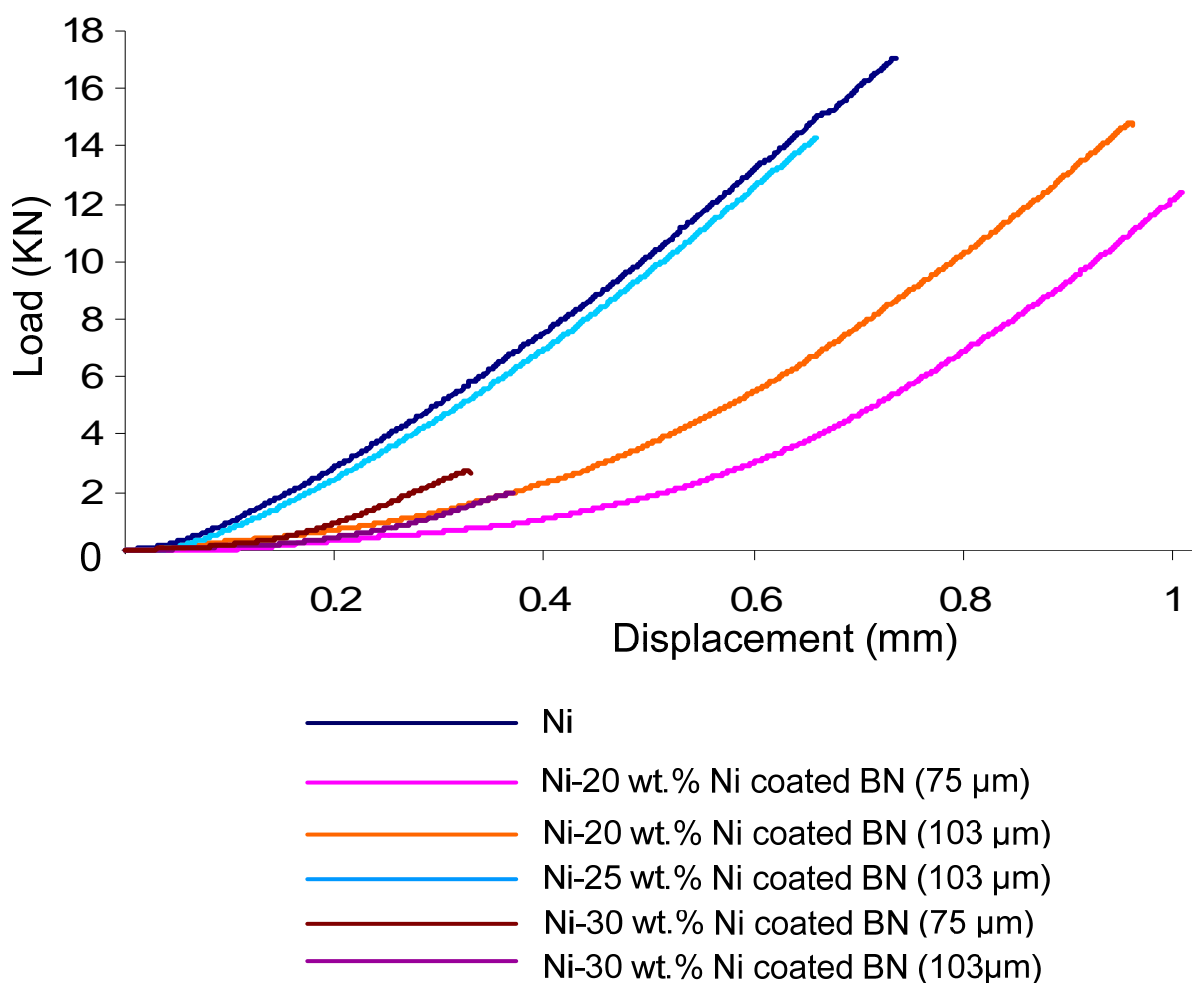


Figure 5.32: Load-Displacement curves for cold sprayed Ni-BN coatings

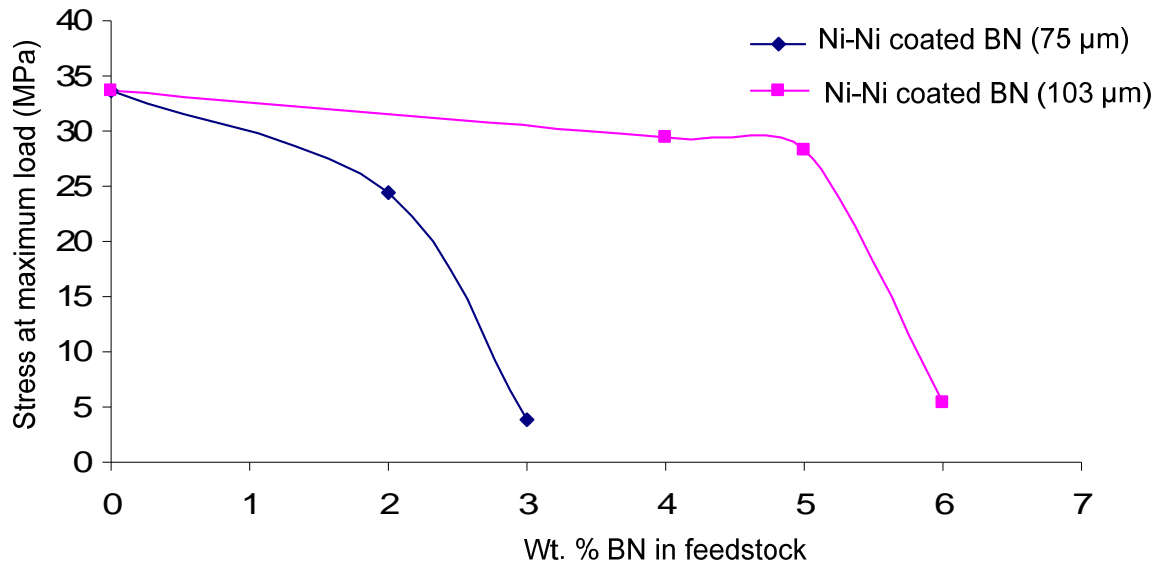


Figure 5.33: Bond Strength at maximum load as a function of amount of BN in feedstock powders

5.3.4 Fretting Wear Testing

Figure 5.34 shows the change of roughness with increasing amounts of BN in the coatings. The roughness of the 4 wt. % BN coatings is less than that of the pure Ni coatings. However, beyond 4 wt. % BN, the coating roughness increases with increasing amount of BN. Figure 5.35 shows the change in the coefficient of friction of the as-sprayed and machined coatings with increasing amounts of BN. On an average, very high coefficients of friction were obtained for all the coatings. The coefficient of friction of the Ni- Ni coated BN (75 μm) coatings increases up-to 4 wt. % BN, followed by a decrease in the coefficient of friction at 5 wt. % BN. In the case of the Ni-Ni coated BN (103 μm), the as-sprayed and machined coatings behave differently as shown in the

graph. However, the minimum coefficient of friction was obtained at the highest lubricant content (6 wt. %) in the as-sprayed and machined coatings.

Figure 5.36 shows that the maximum depth of the wear-track on the coating surfaces as well as the mating surfaces for various Ni-BN coatings. As expected, the depth of wear track is much less on the mating surfaces than on the actual coating. The least deterioration was found to occur at 4 wt. % BN in the case of the Ni-Ni coated BN (75 μm) coatings. However, the Ni-Ni coated BN (75 μm) coatings exhibited the least amount of deterioration at 5 wt. % BN.

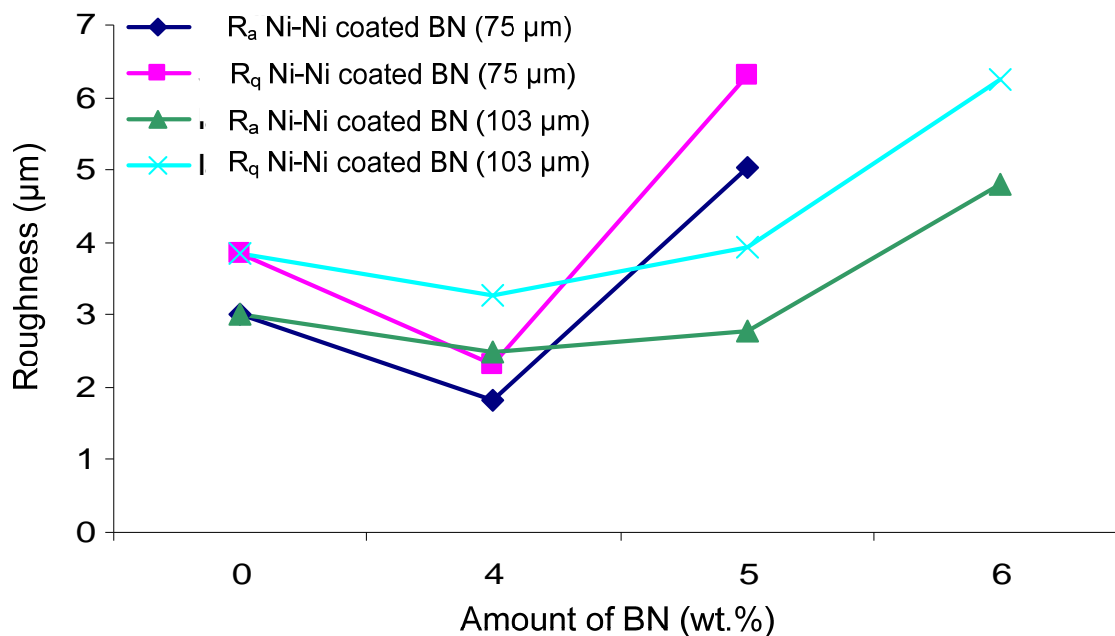


Figure 5.34: Surface roughness of the Ni-BN coatings as a function of percentage of BN

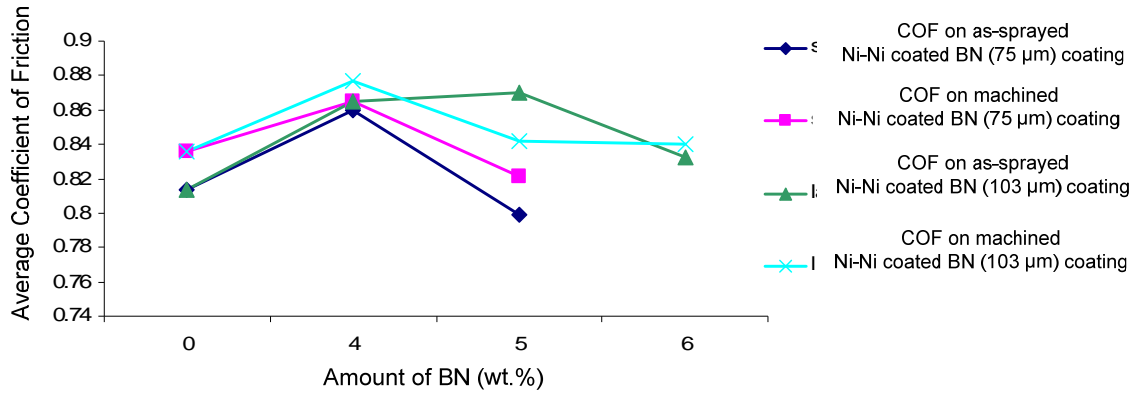


Figure 5.35: Coefficients of friction of various Ni-BN coatings

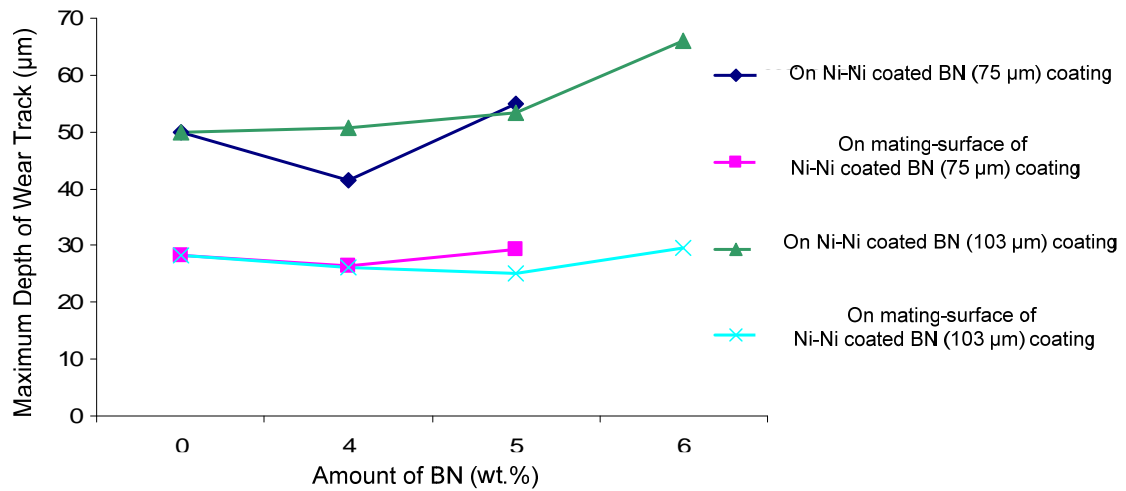


Figure 5.36: Maximum depth of wear track on coating surfaces and mating-surfaces for various Ni-BN coatings

Figures 5.37-5.39 show the 2D wear profile and wear traces of the machined Ni-30 wt. % Ni coated BN sample along the major and minor axes. The 3D image of the wear profile (Figure 5.40) shows the formation of a concave and elliptical wear scar in the machined Ni-30 wt. % Ni coated BN sample. Similarly, Figures 5.41-5.44 show the 2D wear profile, and traces on the major and minor axes, and the 3D wear profiles for the uncoated Ti-6Al-4V ellipse worn against the machined Ni-30 wt. % Ni coated BN coating. The wear profiles of the uncoated Ti-6Al-4V ellipse worn against the machined

Ni-30 wt. % Ni coated BN coating were modified to show the cylindrical portion out of the scan such that the wear appears flat for measurements. These results are shown in Figures 5.45-5.48.

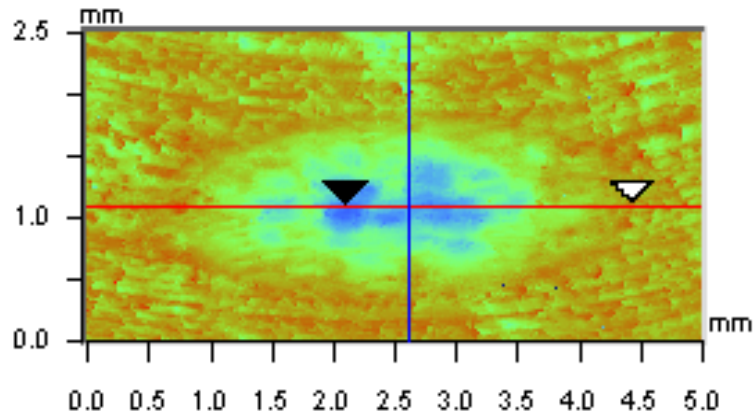


Figure 5.37: 2D Wear profile of the machined Ni-30 wt. % Ni coated BN sample

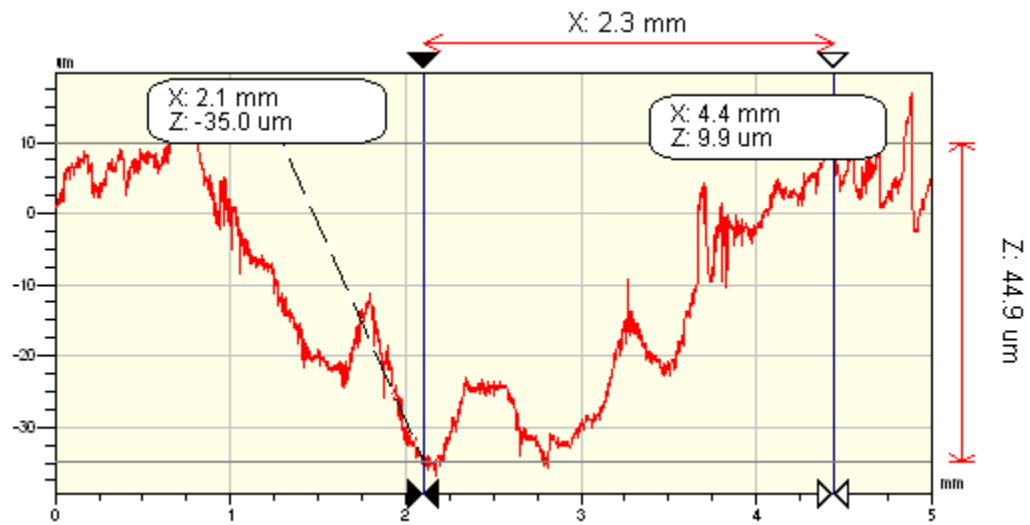


Figure 5.38: Wear trace of the machined Ni-30 wt. % Ni coated BN sample along the major-axis



Figure 5.39: Wear trace of the machined Ni-30 wt. % Ni coated BN sample along the minor axis

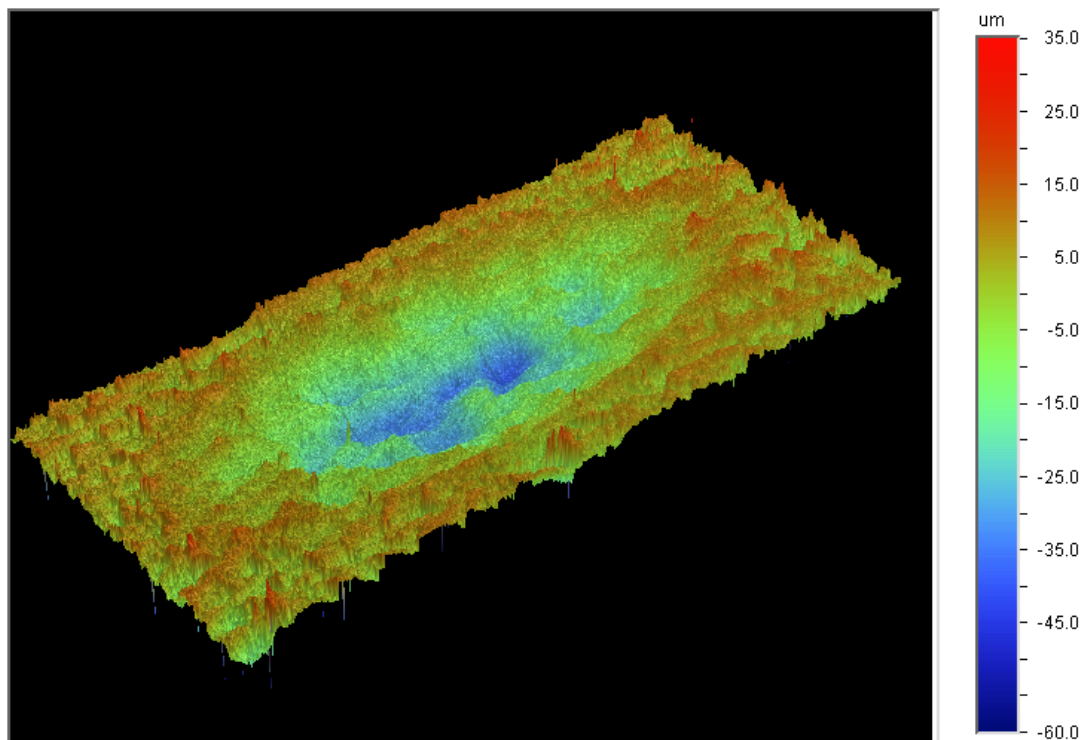


Figure 5.40: 3D Wear profile of the machined Ni-30 wt. % Ni coated BN sample

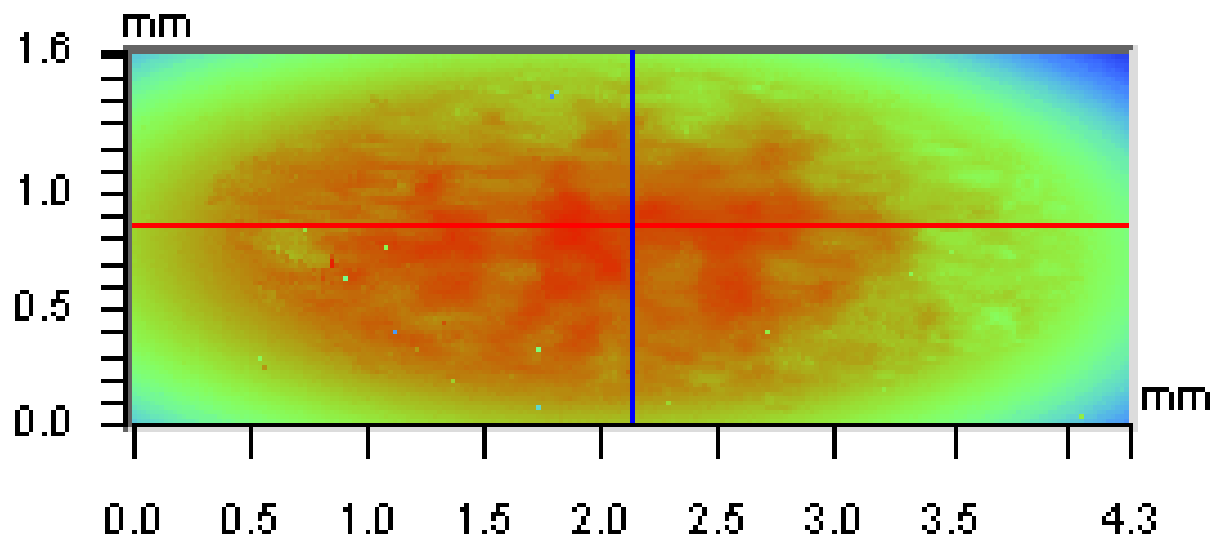


Figure 5.41: 2D wear profile of the uncoated Ti-6Al-4V ellipse worn against the machined Ni-30 wt. % Ni coated BN coating



Figure 5.42: Wear trace of the uncoated Ti-6Al-4V ellipse worn against the machined Ni-30 wt. % Ni coated BN coating along the major axis



Figure 5.43: Wear trace of the uncoated Ti-6Al-4V ellipse worn against the machined Ni-30 wt. % Ni coated BN coating along the minor axis

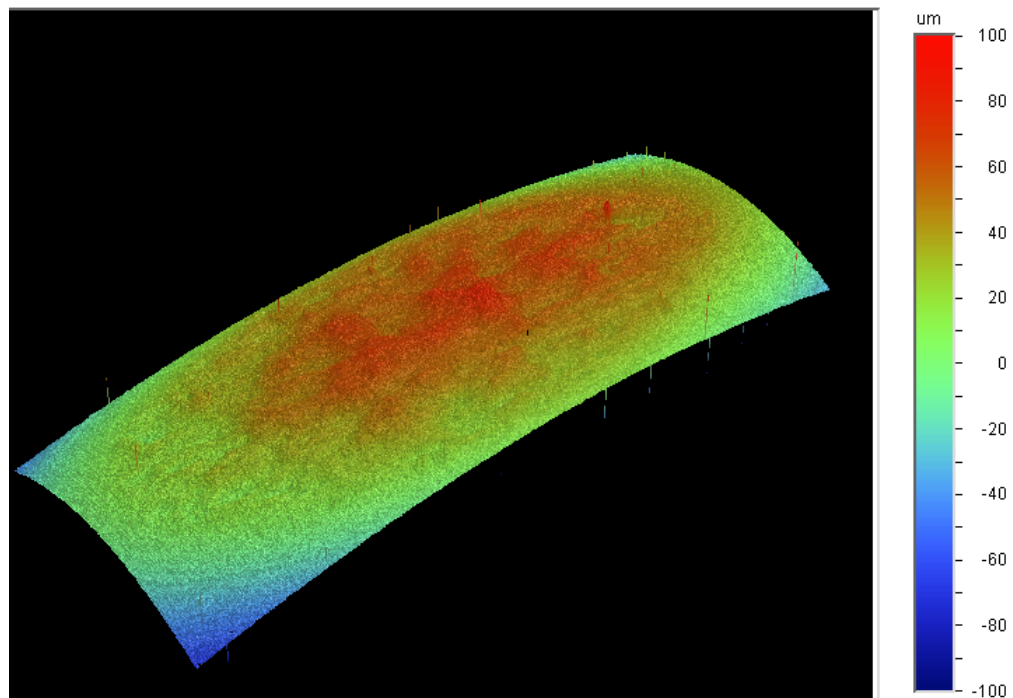


Figure 5.44: 3D wear profile of the uncoated Ti-6Al-4V ellipse worn against the machined Ni-30 wt. % Ni coated BN coating

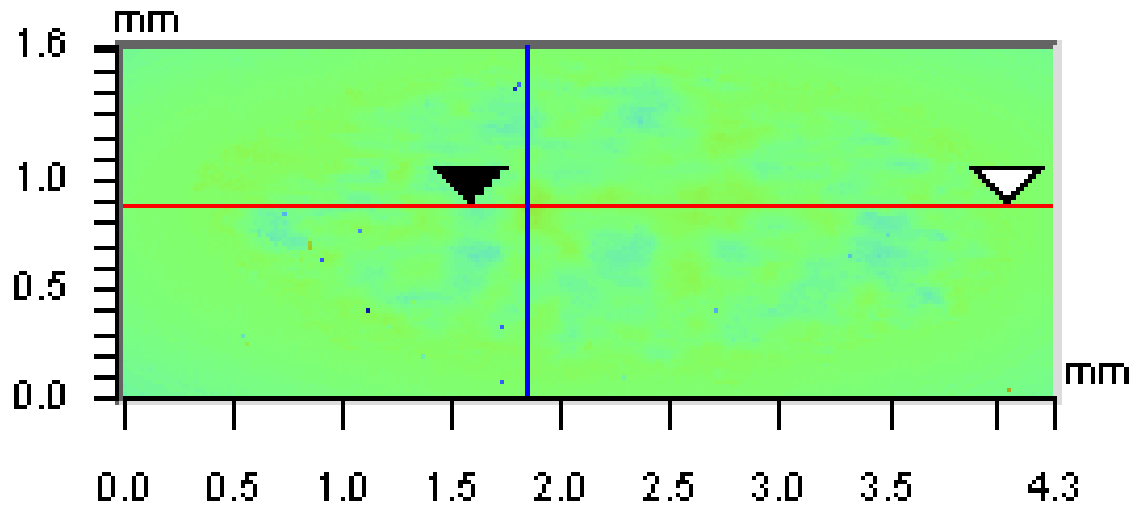


Figure 5.45: Modified 2D wear profiles showing the cylindrical portion out of the scan for wear profile of the uncoated Ti-6Al-4V ellipse worn against the machined Ni-30 wt. % Ni coated BN coating so that the wear appears flat for measurements

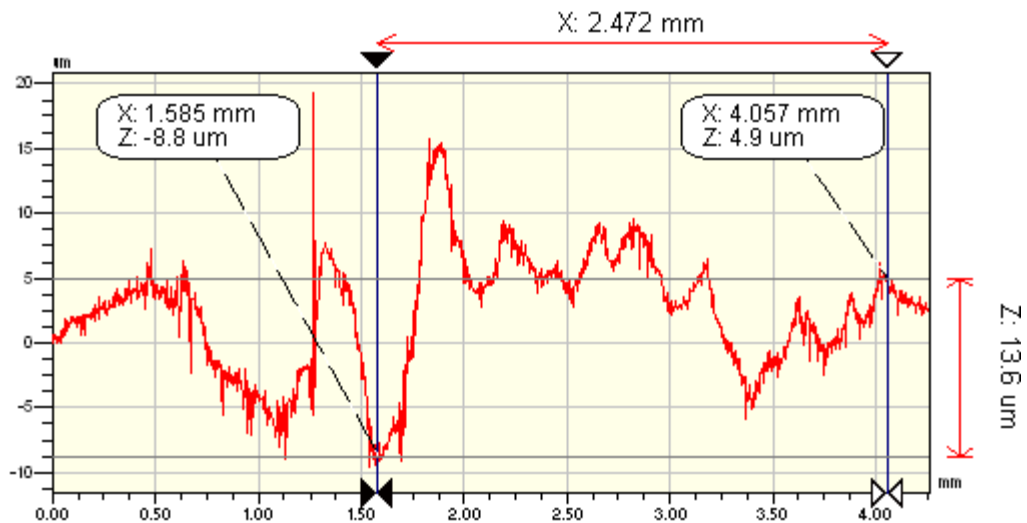


Figure 5.46: Major axis profile of the modified 2D wear trace showing the cylindrical portion out of the scan for wear profile of the uncoated Ti-6Al-4V ellipse worn against the machined Ni-30 wt. % Ni coated BN coating so that the wear appears flat for measurements

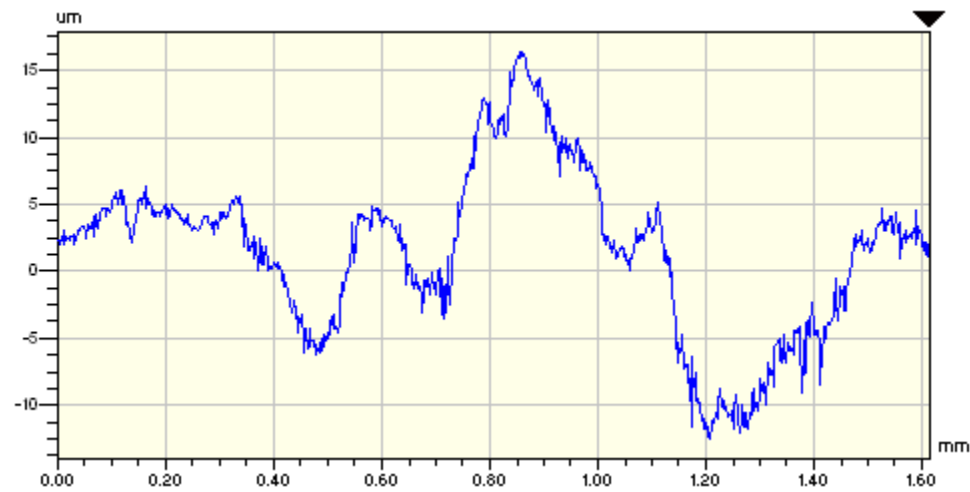


Figure 5.47: Minor axis profile of the modified 2D wear trace showing the cylindrical portion out of the scan for wear profile of the uncoated Ti-6Al-4V ellipse worn against the machined Ni-30 wt. % Ni coated BN coating so that the wear appears flat for measurements

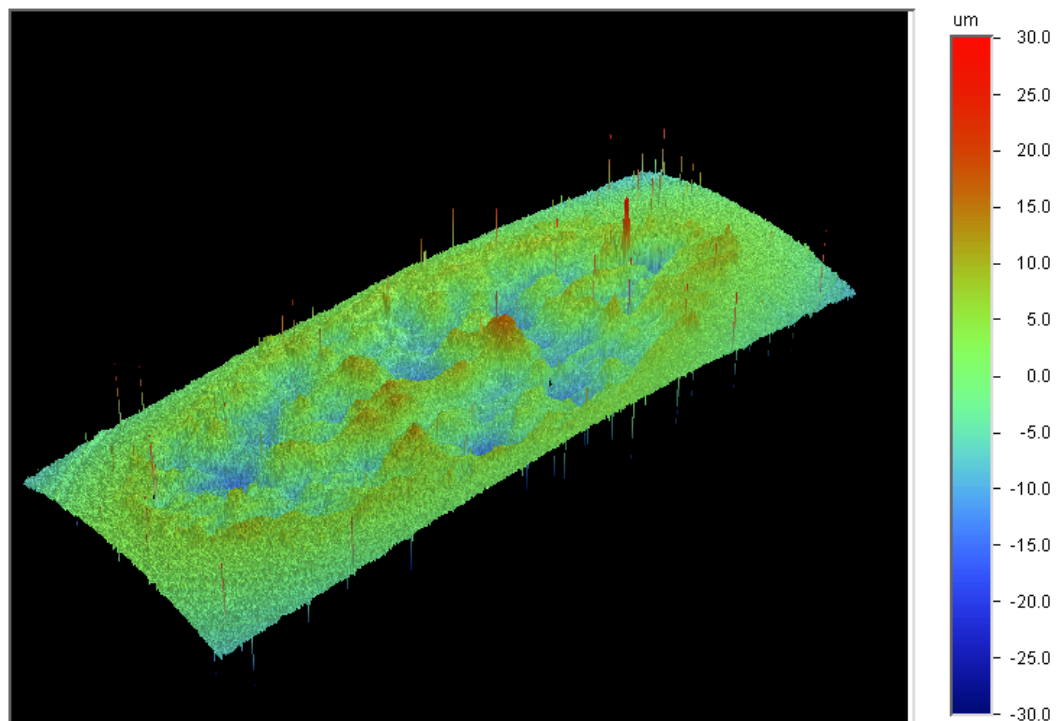


Figure 5.48: Modified 3D wear scars showing the cylindrical portion out of the scan for wear profile of the uncoated Ti-6Al-4V ellipse worn against the machined Ni-30 wt. % Ni coated BN coating so that the wear appears flat for measurements

Chapter 6

Conclusions and Future Recommendations

In the current study, the cold spray process was investigated for the fabrication of self-lubricating coatings.

6.1 Summary

For the first time, Ni-MoS₂ and Ni-BN composite coatings have been developed using a low temperature cold spray process. Some of the most important findings are summarized in this section.

Fretting and wear are detrimental for the fatigue life of turbine blade-disk dovetail joints. Because of the temperature limitation of most solid film lubricants, and the relatively high temperatures experienced by the dovetail joints, the currently used alloy coatings and painted MoS₂ lubricant do not protect against fretting damage completely. High-temperature coating methods are not useful due to the thermal vulnerability of solid lubricants. Ni-based self-lubricating coatings have been invented using the cold spray process. Due to the use of low temperatures and absence of in-flight oxidation and other chemical reactions, lubricating properties of solid lubes can be retained in these coatings without significant material degradation.

In cold spray, solid particles deform and form metallurgical bonds when impacted at supersonic velocities. Therefore, particle composition and ductility play an important

role. By virtue of its high ductility, Ni powder undergoes very high plastic deformation and adheres well to the Ti-6Al-4V substrates during cold spraying. However, the likely absence of plasticity of the lubricant powders inhibits it from forming a good bond with the substrate as well as from building up on itself. In order to overcome this difficulty, the roles of feedstock preparation techniques, particle size of Ni, lube, and pre-coated powders, and amount of lube powders in feedstock were studied.

6.2 Conclusions

Except for pure Ni and (admixed) Ni-MoS₂ coatings, all other coatings require helium to be used as the process gas. Since the Ni coated BN powders and mechanically milled powders are relatively large ($> 50 \mu\text{m}$), they require higher kinetic energy and exit velocity which can only be provided by helium. In addition, higher specific heat ratio and lower mass density of helium should aid in generating high degree of plastic deformation, thereby resulting in better build-up of coatings. Even in case of (admixed) Ni-MoS₂ coatings, it was possible to double the amount of lube entrapped in coating by spraying with helium instead of nitrogen. Other coating parameters were optimized by spraying pure Ni ($75 \mu\text{m}$) with helium. It was concluded that best results were obtained with a gas pressure of 3.1 MPa, gas temperature of 500 °C, and a spray distance of 12.5 mm.

Table 6.1 summarizes the results of Ni-MoS₂ and Ni-BN coatings prepared with admixed feedstocks. More lube and a higher coating build-up were obtained when powders were sprayed using helium. In addition, the smaller Ni ($12 \mu\text{m}$) aided in better

entrapment of lube particles as compared to larger Ni (30 μm and 75 μm). However, due to large difference in densities of Ni and lube powders, the less dense lube powders were accelerated to higher velocities than Ni. As a result, higher amounts of lube were incorporation in initial passes whereas the subsequent passes were depleted of lube.

Table 6.1: Conclusions about coatings sprayed with admixed powders.

Sr. No.	Feedstock Composition	Process Gas	Results
1	Ni-MoS ₂	Nitrogen	Coating thickness decreases with increasing amount of MoS ₂ for same number of overlaps. At 4 wt% MoS ₂ , the coating did not build-up with increasing number of overlaps.
2	Ni-MoS ₂	Helium	It was possible to coat 7 wt.% MoS ₂ , however the Ni and MoS ₂ powders segregated during spraying.
3	Ni-BN	Nitrogen	No lube was incorporated at 1 wt.% BN
4	Ni-BN	Helium	Ni-5 wt.% BN powders were sprayed. Although the coating build up was good, Ni and BN powders were segregated.

Ni-MoS₂ and Ni-BN powders were mechanical milled. The ductile Ni powder welded together, and trapped the lube powders in between the large agglomerates. It was observed that the deposition improved with a corresponding decrease in the variation of particle size of the agglomerates. Although the coatings fabricated with milled feedstock powders were able to incorporate some lube, particle bombardment onto the initial layers of the coating tended to erode the previously deposited coating layers.

Apparently, admixed Ni-Ni coated BN feedstock is best suited for formation of Ni-BN self-lubricating coatings. Figure 6.1 shows Ni and Ni-Ni coated BN coatings. Based on the SEM and EDS analysis, it was concluded that large amounts of BN was embedded into the coatings, with a very homogenous distribution. Although the Ni

coated BN powder fractured during impact, the BN particles were entrapped into the coatings because of the incoming and surrounding Ni particles. Feedstock powders with BN content up-to 6 wt. % were found to adhere to the substrate and build up on itself. These coatings possessed higher hardness than the pure Ni coatings. Tensile testing of these samples resulted in cohesive fracture of coatings with Ni coated BN powder up to 25 wt.%, and adhesive fracture of coatings with 30 wt. % Ni coated BN powder. With increasing amount of BN in the coatings, the bond strength decreases. The cohesive strengths of the Ni-20 wt. % Ni coated BN (75 μm), Ni-20 wt. % Ni coated BN (103 μm), and Ni-25 wt. % Ni coated BN (103 μm) were 25, 29, and 28 MPa respectively. The coating with Ni-30 wt. % Ni coated BN (75 μm) and Ni-30 wt. % Ni coated BN (103 μm) were found to have adhesive strengths of 3.9 and 5.4 MPa. Based on these finding, it seems that Ni-25 wt. % Ni coated BN is the best feedstock composition.

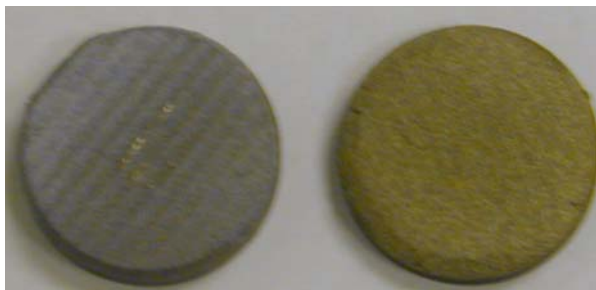


Figure 6.1: Top view of Ni-Ni coated BN (left) and Ni coating (right).

Contrary to expectation, the coatings formed with larger Ni coated BN powder (103 μm) exhibited better lube incorporation as well as adhesion strengths relative to coating fabricated with smaller Ni coated BN powders (75 μm). Additionally, it may be assumed that the coating build up depended on the amount of Ni coated BN instead of the actual amount of BN in the feedstock powders. The larger and smaller Ni coated BN

powders had 20 wt. % and 10 wt. % BN. Hence, much more lube was incorporated by using the larger powder.

6.3 Future Recommendations

In order to improve the cohesion and adhesion strengths, stratified coatings can be formed as shown in Figures 6.2 and 6.3.

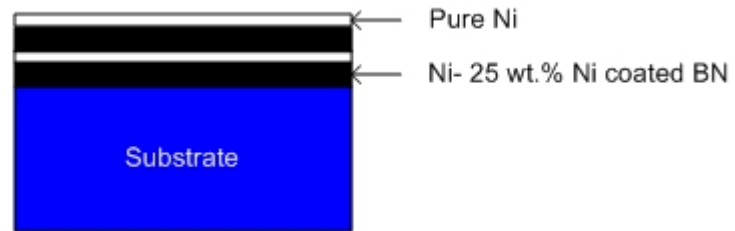


Figure 6.2: Suggested stratified coating for improvement in cohesion strength

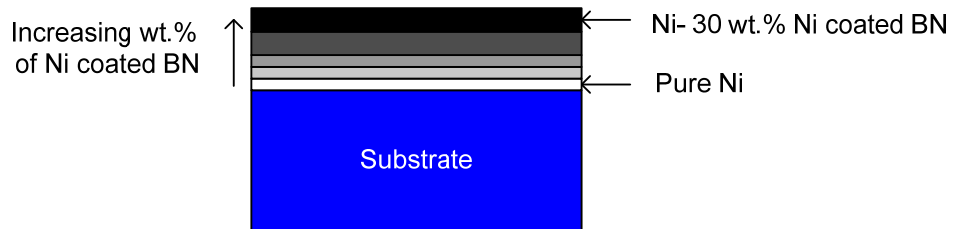


Figure 6.3: Suggested stratified coating for improvement in adhesion strength

Low temperature annealing or cryogenic treatments on the as sprayed coatings may improve the coating strength by relieving residual stresses.

The particle velocity and temperature prior to impact can be estimated using computational fluid dynamics. Additionally, the impacting behavior including particle

deformation and temperature increment can be estimated through the finite element analysis programs.

Research can be done in the direction of fabricating smaller Ni coated BN particles with sufficient Ni coating thickness to avoid the need of admixing with pure Ni powder. From the results of this research, it may be expected that if these particles are in the size range of 80-100 μm , they can be cold sprayed. Spraying these coated particles would result in incorporation of higher amounts of lubricant in the coatings with a homogeneous distribution, which would in turn improve protection against fretting.

Bibliography

1. Meherwan P Boyce, “*Gas Turbine Engineering Handbook*”, Gulf Professional Publishing; 2001
2. Jack D. Mattingly, “*Elements of Gas Turbine Propulsion*,” Mc Graw-Hill, Inc., 1996
3. Joshua Stoff, “*Aviation Firsts: 336 Questions and Answers*,” Dover Publications, 2000
4. Christopher Orlebar, “*The Concorde Story: 21 Years in Service (Civil Aircraft)*” Osprey, 2002
5. G. W. Meetham, “*The Development of Gas Turbine Materials*”, London: Applied Science Publishers, 1981.
6. G. Lucas and J. F. Pollock, “*Gas Turbine Materials*”, London Temple Press Limited, 1957.
7. R. A. Antoniou, T. C. Radtke, Mechanisms of fretting-fatigue of titanium alloys, *Materials Science & Engineering A*, **237** 1997, pp.229-40.
8. L. Wu, B. C. Holloway, D. P. Beesabathina, C. Kalil, D. M. Manos, Analysis of diamond-like carbon and Ti MoS₂ coatings on Ti-6Al-4V substrates for applicability to turbine engine applications, *Surface and Coatings Technology*, **130** (2-3), 2000, pp.207-17.
9. S. Adibnazari, D. W. Hoepfner, Characteristics of the fretting fatigue damage threshold, *Wear*, **159** 1992, pp.43-46.
10. S. Adibnazari, D. W. Hoepfner, Fretting fatigue normal pressure threshold concept, *Wear*, **160** 1993, pp.33-35.
11. S. Fouvry, P. Duo, Ph. Perruchaut, A quantitative approach of Ti-6Al-4V fretting damage: Friction, wear and crack nucleation, *Wear*, **257**, (9-10), pp 916-929
12. A. L. Hutson, T. Nicholas, Rick Goodman, Fretting fatigue of Ti-6Al-4V under flat-on-flat contact, *International Journal of Fatigue*, **21**,(7), 1999, pp 663-669
13. V. Fridrici, S. Fouvry, P.H. Kapsa, Fretting wear behavior of a Cu-Ni-In plasma coating, *Surface and Coatings Technology*, **163-164**, 2003, pp 429-434

14. A. J. Freimanis, A. E. Segall, J.C. Jr. Conway, E. J. Whitney, Elevated temperature evaluation of fretting and metal transfer between coated titanium components, *Tribology Transactions*, **43** (4), 2000, pp 653-658
15. Y. Fu, N. L. Loh, A.W. Batchelor, D. Liu, X. Zhu, J. He, K. Xu, Improvement in fretting wear and fatigue resistance of Ti-6Al-4V by application of several surface treatments and coatings, *Surface & Coatings Technology*, **106**, (2-3), 1998, pp 193-197
16. L. Xue, A. K. Koul, M. Bibby, W. Wallace, M. Islam, Survey of surface treatments to improve the fretting fatigue resistance of Ti-6Al-4V, *Proceedings of the 2nd International Conference on Computer Methods and Experimental Measurements for Surface Treatment Effects* 1995, pp 265
17. Y. Fu, J. Wei, A.W Batchelor, Some considerations on the mitigation of fretting damage by the application of surface-modification technologies, *Journal of Materials Processing Technology*, **99** (1), 2000, pp 231-245
18. A. P. Alkhimov, A. N. Papyrin, V. F. Kosarev, N. I. Nesterovich, M. M. Shushpanov, *Gas-dynamic spraying method for applying a coating*, United States Patent No. 5,302,414, April 12 1994, p. 1-13.
19. P. J. Blau, Fifty years of research on the wear of metals, *Tribology International*, **30** (5), 1997, pp 321-331
20. J.C. Jr. Conway, A. J. Freimanis, A. E. Segall E. J. Whitney, The influence of temperature on the wear mode and deterioration of coatings used for titanium aircraft engine components, *Tribology Transactions*, **45** (2), 2002, pp 193-198
21. J. S. Halliday, W. Hirst, The fretting corrosion of mild steel, *Proceedings of The Royal Society A*, **236**, 1956, pp 411-425
22. T. Kayaba, A. Iwabuchi, Influence of hardness on fretting wear. *Proceeding of the international Conference on Wear of Materials, American Society of Mechanical Engineers*, New York, 1979, pp 371-378
23. M. Godet., The third-body approach: a mechanical view of wear. *Wear*, **100**, 1984, pp 437-452
24. O. Vingsbo, S. Soderberg, On fretting maps, *Proceedings of the. International. Conference on Wear of Materials: American Society of Mechanical Engineers*, New York, 1987, pp 885-894
25. E. Sauger, S. Fouvry, L. Ponsonnet, Ph. Kapsa, J.M. Martin, L. Vincent, Tribologically transformed structure in fretting, *Wear*, **245** (1), 2000, pp 39-52

26. M. Ciavarella, G. Demelio, A review of analytical aspects of fretting fatigue, with extension to damage parameters, and application to dovetail joints, *International Journal of Solids and Structures*, **38** (10-13) , 2001, pp 1791-1811
27. R. B. Waterhouse, “*Fretting corrosion*”, New York: Pergamon Press, 1972.
28. R. B. Waterhouse, *Fretting Fatigue*, Applied Science Publishers, London, 1981.
29. R. B. Waterhouse, D. E. Taylor, The Initiation of Fatigue Cracks in a 0.7% Carbon Steel by Fretting, *Wear*, **17** (2), 1979, pp.139-47.
30. J. Doboromirski, I. O. Smith, Metallographic Aspects of Surface Damage, Surface Temperature and Crack Initiation in Fretting Fatigue, *Wear*, **117** 1987, pp.357-87.
31. K. Endo, H. Gota, Initiation and Propagation of Fretting Fatigue Cracks, *Wear*, **38** 1976, pp.311-24.
32. J. A. Alic, A. L. Hawley, On the early growth of Fretting Fatigue Cracks, *Wear*, **56** 1979, pp.377-89.
33. J. A. Alic, A. L. Hawley, J. M. Urey, Formation of Fretting Fatigue Cracks in 7075-T7351 Aluminum Alloy, *Wear*, **56** (2), 1979, pp.351-61.
34. D. W. Taylor, V. Chandrasekaran, *Fretting Fatigue: Advances in Basic Understanding and Applications*, ASTM International, West Conshohocken, PA, 2003.
35. M. P. Szolwinski, T. N. Farris, Mechanics of fretting fatigue crack formation, *Wear*, **198** (1-2) 1996, pp 93-107
36. R. K. Reeves, D. W. Hoepfner, The effect of fretting on fatigue, *Wear*, **40** 1976, pp.395-97.
37. D. Nowell, D. A. Hills, “*Mechanics of fretting fatigue*” The Netherlands: Kluwer Academic Publishers, 1994.
38. R. S. Magaziner, Examination of Contact Width on Fretting Fatigue, in: AFIT/GAE/ENY/02-8, Wright-Patterson Air Force Base, Ohio, 2002.
39. C.H. Hager Jr., J.H. Sanders , S. Sharma, Effect of high temperature on the characterization of fretting wear regimes at Ti6Al4V interfaces, *Wear*, **260**, 2006, pp 493–508
40. K. Betts, Wear resistant coatings for titanium alloys: Fretting fatigue of uncoated Ti- 6Al-4V, in: AFML-TR-71-212, Wright-Patterson Air Force Base, Ohio, 1971.

41. S. Fayeulle, P. Blanchard, L. Vincent, Fretting behavior of titanium alloys, *Tribological Transaction*, **36** 1993, pp.267-75.
42. W. A. Glaeser, B. H. Lawless, Behavior of alloy Ti-6Al-4V under pre-fretting and subsequent fatigue conditions, *Wear*, **250-251** (1), 2001, pp 621-630
43. C.H. Hager Jr., J.H. Sanders, S. Sharma, Characterization of mixed and gross slip fretting wear regimes in Ti6Al4V interfaces at room temperature, *Wear* **257**, 2004, pp. 167–80
44. M. Grujicic, C. Tong, W. S. DeRosset, D. Helfritch, Flow analysis and nozzle-shape optimization for the cold-gas dynamic-spray process, *Proceedings of the Institution of Mechanical Engineers, Part B:Journal of Engineering Manufacture*, **217** (11), 2003, pp.1603-13.
45. R. C. McCune, A. N. Papyrin, J. N. Hall, W. L. Riggs, P. H. Zajchowski, An exploration of the cold gas-dynamic spray method for several material systems, in: *Proceedings of the 8th National Thermal Spray Conference*, Houston, TX. 1995, 1-5.
46. K. Sakaki, Cold Spray Process-Overview and Application Trends, *Materials Science Forum*, **449-452** 2004, pp.1305-08.
47. V. F. Kosarev, S. V. Klinkov, A. P. Alkhimov, A. N. Papyrin, On some aspects of gas dynamics of the cold spray process, *Journal of Thermal Spray Technology*, **12** (2), 2003, pp.265-81.
48. A. P. Alkhimov, A. N. Papyrin, V. F. Kosarev, N. I. Nesterovich, M. M. Shushpanov, *Method and Device for Coating*, European Patent No. 0484533, 13 May 1995, p. 1-18.
49. A. P. Alkhimov, Gas-Dynamic Spraying. A Study of a Plane Supersonic Two-Phase Jet, *Journal of Applied Mechanics and Technical Physics*, **38** (2), 1997, pp.324-30.
50. A. P. Alkhimov, A. I. Gudilov, V. F. Kosarev, N. I. Nesterovich, Specific features of microparticle deformation upon impact on a rigid barrier, *Journal of Applied Mechanics and Technical Physics*, **41** (1), 2000, pp.188-92.
51. A. N. Papyrin, R. Blose, Cold spray technology: From R and D to commercial applications, *Materials Technology*, **18** (2), 2003, pp.73-78.
52. A. P. Alkhimov, V. F. Kosarev, A. N. Papyrin, A Method of Cold-Gas Dynamic Compaction, *Sov. Phys. Dokl.*, **35** (12), 1991, pp.1047-49.

53. A. P. Alkhimov, V. F. Kosarev, S. V. Klinkov, The features of cold spray nozzle design, *Journal of Thermal Spray Technology*, **10** (2), 2001, pp.375-81.
54. J. Villafuerte, Cold spray: A new technology, *Welding Journal (Miami, Fla)*, **84** (5), 2005, pp.24-29.
55. A. Papyrin, Cold Spray Technology, *Advanced Materials and Processes*, **159** (9), 2001, pp.49-51.
56. C.-J. Li, W.-Y. Li, W.-H. Ma, H. Fukanuma, Characterization of microstructure of nanostructured Fe-Si coating deposited by cold spraying, in: *Proceedings of the International Thermal Spray Conference*, Osaka, Japan. 2004, 371-77.
57. C.-J. Li, G.-J. Yang, X.-C. Huang, W.-Y. Li, A. Ohmori, Formation of TiO₂ photocatalyst through cold spraying, in: *Proceedings of the International Thermal Spray Conference*, Osaka, Japan. 2004, 315-19.
58. C.-J. Li, W.-Y. Li, Y.-Y. Wang, Formation of metastable phases in cold-sprayed soft metallic deposit, *Surface and Coatings Technology*, **198** (1-3), 2005, pp.469-73.
59. J. Mondoux, B. Jodoin, L. Ajdelsztajn, J. M. Schoenung, G. E. Kim, Nanostructured aluminum coatings produced using cold spraying technology, in: *Proceedings of the International Thermal Spray Conference*, Osaka, Japan. 2004, 347-51.
60. L. Ajdelsztajn, B. Jodoin, G. E. Kim, J. M. Schoenung, Cold spray deposition of nanocrystalline aluminum alloys, *Metallurgical and Materials Transactions A: Physical Metallurgy and Materials Science*, **36** (3), 2005, pp.657-66.
61. J. Mondoux, B. Jodoin, L. Ajdelsztajn, J. M. Schoenung, G. E. Kim, Nanostructured aluminum coatings produced using cold spraying technology, in: *Proceedings of the International Thermal Spray Conference*, Osaka, Japan. 2004, 347-51.
62. A. N. Papyrin, Cold Gas Dynamic Spraying: What Is It?, *ASM International Materials Solutions Conference*, Rosemont, Illinois, ASM International, Materials Park, OH, 1998.
63. C. Borchers, F. Gartner, T. Stoltenhoff, H. Assadi, H. Kreye, Microstructural and macroscopic properties of cold sprayed copper coatings, *Journal of Applied Physics*, **93** (12), 2003, pp.10064-70.

64. H. Kreye, T. Stoltenhoff, Cold Spraying- A Study of Process and Coating Characteristics, in: *Proceedings of the International Thermal Spray Conference*, 2000, 419-22.
65. C. Borchers, T. Stoltenhoff, F. Gartner, H. Kreye, H. Assadi, Deformation microstructure of cold gas sprayed coatings, in: *Dislocations and Deformation Mechanics in Thin Films and Small Structures*, San Francisco, CA. 2001, **673**, 7.10.1-7.10.6.
66. H. Kreye, T. Stoltenhoff, Cold Spraying- A Study of Process and Coating Characteristics, in: *Proceedings of the International Thermal Spray Conference*, 2000, 419-22.
67. R. Morgan, P. Fox, J. Pattison, C. Sutcliffe, W. O'Neill, Analysis of cold gas dynamically sprayed aluminium deposits, *Materials Letters*, **58** (7-8), 2004, pp.1317-20.
68. A. O. Tokarev, Structure of Aluminium Powder Coatings Prepared by Cold Gas Dynamic Spraying, *Metal Science and Heat Treatment*, **38** (3-4), 1996, pp.36-39.
69. D. Zhang, P. H. Shipway, D. G. McCartney, Cold gas dynamic spraying of aluminum: The role of substrate characteristics in deposit formation, *Journal of Thermal Spray Technology*, **14** (1), 2005, pp.109-16.
70. A. V. Bolesta, V. M. Fomin, M. R. Sharafutdinov, B. P. Tolochko, Investigation of interface boundary occurring during cold gas-dynamic spraying of metallic particles, *Nuclear Instruments and Methods in Physics Research, Section A: Accelerators, Spectrometers, Detectors and Associated Equipment*, **470** (1-2), 2001, pp.249-52.
71. M. K. Decker, R. A. Neiser, D. Gilmore, H. D. Tran, Microstructure and Properties of Cold Spray Nickel, in: *Proceedings of the International Thermal Spray Conference*, Singapore, Singapore. 2001, 433-39.
72. A. E. Segall, A. N. Papyrin, J. Joseph C. Conway, D. Shapiro, A Cold-Gas Spray Coating Process for Enhancing Titanium, *Journal of Metals*, **50** (9), 1998, pp.52-54.
73. J. Karthikeyan, C. M. Kay, J. Linderman, R. S. Lima, C. C. Berndt, Cold Spray Processing of Titanium Powder, in: *International Thermal Spray Conference*, 2000, 255-62.
74. C.-J. Li, W.-Y. Li, Deposition characteristics of titanium coating in cold spraying, *Surface and Coatings Technology*, **167** (2-3), 2003, pp.278-83.

75. H. Y. Lee, Y. H. Yu, Y. C. Lee, Y. P. Hong, K. H. Ko, Cold spray of SiC and Al₂O₃ with soft metal incorporation: A technical contribution, *Journal of Thermal Spray Technology*, **13** (2), 2004, pp.184-89.
76. J. Intrater, Cold spray technology - Prospects and applications, *Surface Engineering*, **18** (5), 2002, pp.321-23.
77. J. Vlcek, L. Gimeno, H. Huber, E. Lugscheider, A systematic approach to material eligibility for the cold-spray process, *Journal of Thermal Spray Technology*, **14** (1), 2005, pp.125-33.
78. C.-J. Li, W.-Y. Li, Microstructure evolution of cold-sprayed coating during deposition and through post-spraying heat treatment, *Transactions of the Nonferrous Metals Society of China*, **14** (2), 2004, pp.49-54.
79. J. Morimoto, T. Onoda, Y. Sasaki, N. Abe, Improvement of solid cold sprayed TiO₂-Zn coating with direct diode laser, *Vacuum*, **73** (3-4), 2004, pp.527-32.
80. A. Papyrin, Cold Spray Technology, *Advanced Materials and Processes*, **159** (9), 2001, pp.49-51.
81. A. N. Papyrin, V. F. Kosarev, S. V. Klinkov, A. P. Alkhimov, On the interaction of high speed particles with a substrate under the cold spraying, in: *Proceedings of the International Thermal Spray Conference*, Dusseldorf, Germany. 2002, 380-84.
82. A. N. Papyrin, A. P. Alkhimov, V. F. Kosarev, S. V. Klinkov, Experimental Study of Interaction of Supersonic Gas Jet with a Substrate Under Cold Spray Process, in: *Thermal Spray 2001 New Surfaces for a New Millennium: Proceedings of the International Thermal Spray Conferences*, Singapore, Singapore. May 28-30.2001, 423-31.
83. A. N. Papyrin, V. F. Kosarev, S. V. Klinkov, A. P. Alkhimov, On the interaction of high speed particles with a substrate under the cold spraying, in: *Proceedings of the International Thermal Spray Conference*, Dusseldorf, Germany. 2002, 380-84.
84. V. F. Kosarev, S. V. Klinkov, A. P. Alkhimov, A. N. Papyrin, On some aspects of gas dynamics of the cold spray process, *Journal of Thermal Spray Technology*, **12** (2), 2003, pp.265-81.
85. R. C. Dykhuizen, M. F. Smith, Gas dynamic principles of cold spray, *Journal of Thermal Spray Technology*, **7** (2), 1998, pp.205-12

86. R. C. Dykhuizen, M. F. Smith, D. L. Gilmore, R. A. Neiser, X. Jiang, S. Sampath, Impact of high velocity cold spray particles, *Journal of Thermal Spray Technology*, **8** (4), 1999, pp.559-64.
87. D. L. Gilmore, R. C. Dykhuizen, R. A. Neiser, T. J. Roemer, M. F. Smith, Particle velocity and deposition efficiency in the cold spray process, *Journal of Thermal Spray Technology*, **8** (4), 1999, pp.576-82.
88. M. F. Smith, J. E. Brockmann, R. C. Dykhuizen, D. L. Gilmore, R. A. Neiser, T. J. Roemer, Cold spray direct fabrication - high rate, solid state, material consolidation, in: *MRS Fall Meeting - Symposium V, 'Solid Freeform and Additive Fabrication'*, Boston, MA. Nov 30-Dec 3.1998, **542**, 65-76.
89. R. C. McCune, J. L. Bomback, G. Gao, *Method for Selective Control of Corrosion Using Kinetic Spraying*, United States Patent No. 6,592,947, July, 15 2003, p. 1-8.
90. R. C. McCune, W. T. Donlon, E. L. Cartwright, A. N. Papyrin, E. F. Rybicki, J. R. Shadley, Characterization of Copper and Steel Coatings Made by the Cold Gas-Dynamic Spray Method, in: *Thermal Spray: Practical Solutions for Engineering Problems*, 1996, 397-403.
91. R. C. McCune, W. T. Donlon, O. O. Popoola, E. L. Cartwright, Characterization of copper layers produced by cold gas-dynamic spraying, *Journal of Thermal Spray Technology*, **9** (1), 2000, pp.73-82.
92. T. H. V. Steenkiste, J. R. Smith, R. E. Teets, Aluminum coatings via kinetic spray with relatively large powder particles, *Surface and Coatings Technology*, **154** (2-3), 2002, pp.237-52.
93. T. H. V. Steenkiste, J. R. Smith, R. E. Teets, J. J. Moleski, D. W. Gorkiewicz, R. P. Tison, D. R. Marantz, K. A. Kowalsky, W. L. Riggs, P. H. Zajchowski, B. Plisner, R. C. McCune, K. J. Barnett, Kinetic Spray Coatings, *Surface Coatings and Technology*, **111** 1999, pp.62-71.
94. T. V. Steenkiste, *Method of Producing a Coating Using a Kinetic Spray Process with Large Particles and Nozzles for the Same.*, United States Patent No. 6,623,796, September, 23 2003, p. 1-8.
95. T. V. Steenkiste, D. W. Gorkiewicz, Analysis of Tantalum Coatings Produced by the Kinetic Spray Process, *Journal of Thermal Spray Technology*, **13** (2), 2004, pp.265- 73.
96. T. V. Steenkiste, J. R. Smith, Evaluation of coatings produced via kinetic and cold spray processes, *Journal of Thermal Spray Technology*, **13** (2), 2004, pp.274-82.

97. T. V. Steenkiste, J. R. Smith, R. E. Teets, J. J. Moleski, D. W. Gorkiewicz, *Kinetic Spray Coating Method and Apparatus*, United States Patent No. 6,139,913, October, 31 2000, p. 1-6.
98. T. V. Steenkiste, J. R. Smith, R. E. Teets, J. J. Moleski, D. W. Gorkiewicz, *Kinetic Spray Coating Apparatus*, United States Patent No. 6,283,386, September, 4 2001, p. 1-6.
99. J. Karthikeyan, Cold Spray Technology: International Status and USA efforts, *ASB Industries Inc.*
100. R. H. Morgan, C. J. Sutcliffe, J. Pattison, M. Murphy, C. Gallagher, A. Papworth, P. Fox, W. O'Neill, Cold gas dynamic manufacturing - A new approach to near-net shape metal component fabrication, in: *Rapid Prototyping Technologies*, Boston, MA. 2003, **758**, 73-84.
101. T. Stoltenhoff, H. Kreye, H. J. Richter, H. Assadi, Optimization of Cold Spray Process, in: *Thermal Spray 2001: New Surfaces for a New Millennium*, San Francisco, CA, USA. 2001, 409-16.
102. J. Vlcek, H. Huber, H. Voggenreiter, A. Fischer, E. Lugscheider, H. Hallen, G. Pache, Kinetic Powder Compaction Applying the Cold Spray Process- A Study on Parameters, in: *International Thermal Spray Conference*, 2001, 417-22.
103. W.-Y. Li, C.-J. Li, Optimization of spray conditions in cold spraying based on numerical analysis of particle velocity, *Transactions of the Nonferrous Metals Society of China*, **14** (2), 2004, pp.43-48.
104. T. Stoltenhoff, H. Kreye, H. J. Richter, An Analysis of the Cold Spray Process and its Coatings, *Journal of Thermal Spray Technology*, **11** (4), 2002, pp.542-50.
105. M. Grujicic, J. R. Saylor, D. E. Beasley, W. S. DeRosset, D. Helfrich, Computational analysis of the interfacial bonding between feed-powder particles and the substrate in the cold-gas dynamic-spray process, *Applied Surface Science*, **219** (3-4), 2003, pp.211-27.
106. M. Grujicic, C. L. Zhao, W. S. DeRosset, D. Helfrich, Adiabatic shear instability based mechanism for particles/substrate bonding in the cold-gas dynamic-spray process, *Materials and Design*, **25** (8), 2004, pp.681-88.
107. M. Grujicic, C. L. Zhao, C. Tong, W. S. DeRosset, D. Helfrich, Analysis of the impact velocity of powder particles in the cold-gas dynamic-spray process, *Materials Science & Engineering A*, **368** (1-2), 2004, pp.222-30.
108. F. Gartner, C. Borchers, T. Stoltenhoff, H. Kreye, H. Assadi, Numerical and Microstructural Investigations of the Bonding Mechanisms in Cold Spraying, in:

Thermal Spray 2003: Advancing the Science & Applying the Technology, Orlando, FL. 2003, 1-8.

109. C.-J. Li, W.-Y. Li, H. Fukanuma, Impact fusion phenomenon during cold spraying of zinc, in: *Proceedings of the International Thermal Spray Conference*, Osaka, Japan. 2004, 335-40.
110. D. G. Brasher, D. J. Butler, Explosive welding: principles and potentials, *Advanced Materials and Processes*, **147** 1995, pp.37-38.
111. M. Hammerschmidt, H. Kreye, Microstructure and bonding mechanism in explosive welding, in: M. A. Meyers, L. E. Murr (Eds.), *Shock waves and high strain rate phenomena in metals*, Plenum Press, New York, 1981, pp. 961-72.
112. H. Assadi, F. Gartner, T. Stoltenhoff, H. Kreye, Bonding Mechanisms in Cold Gas Spray, *Acta Materialia*, **51** 2003, pp.4379-94.
113. E. Calla, D. G. McCartney, P. H. Shipway, Deposition of copper by cold gas dynamic spraying: An investigation of dependence of microstructure and properties of the deposits on the spraying conditions, in: *Proceedings of the International Thermal Spray Conference*, Osaka, Japan. 2004, 352-57.
114. S. V. Panin, A. P. Alkhimov, V. A. Klimenov, N. N. Korobina, O. N. Nekhoroshkov, Investigation of influence of adhesive strength on plastic flow at mesolevel in low-carbon specimens with gas-dynamic coatings, in: *Proceedings KORUS 2000. The 4th Korea-Russia International Symposium On Science and Technology*, Ulsan, South Korea. 2000, **3**, 229-34.
115. N. N. Korobina, S. V. Panin, A. P. Alkhimov, Investigation of plastic deformation development at mesoscale level in composition with cold-sprayed coatings, *Proceedings of the 7th International Scientific and Practical Conference of Students, Post-graduates and Young Scientists*, Tomsk, Russia, ,2001, pp 71-73
116. H. Fukanuma, N. Ohno, A study of adhesive strength of cold spray coatings, in: *Proceedings of the International Thermal Spray Conference*, Osaka, Japan. 2004, 329-34.
117. L. W. Ya, L. C. Jiu, Optimization of spray conditions in cold spraying based on numerical analysis of particle velocity, in: *Transactions of the Nonferrous Metals Society of China*, Shenzhen, China. 2004, **14**, 43-48.
118. O. Cheng, Equipment engineering and process control for cold spraying, in: *Proceedings of the International Thermal Spray Conference*, Osaka, Japan. 2004, 309-14.

119. P. F. Stratton, Hydrogen Economy: A study of gas quenching costs, *Heat Treating Progress*, 2006, pp. 53-55 *Engineering Congress*, Washington, DC., United States. 2003, **374**, 281-87.
120. K. Sakaki, T. Tajima, H. Li, S. Shinkai, Y. Shimizu, Influence of substrate conditions and traverse speed on cold sprayed coatings, in: *Proceedings of the International Thermal Spray Conference*, Osaka, Japan. 2004, 358-62.
121. T.-C. Jen, L. Li, Q. Chen, W. Cui, X. Zhang, The acceleration of micro-and nanoparticles in supersonic De-Laval-Type nozzle, in: *2003 ASME International Mechanical*
122. F. Raletz, G. Ezo'o, M. Vardelle, M. Ducos, Characterization of cold-sprayed nickel-base coatings, in: *Proceedings of the International Thermal Spray Conference*, Osaka, Japan. 2004, 323-28.
123. V. Shukla, G. S. Elliott, B. H. Kear, L. E. McCandlish, Hyperkinetic deposition of nanopowders by supersonic rectangular jet impingement, *Scripta Materialia*, **44** (8-9), 2001, pp.2179-82.
124. V. Shukla, R. K. Sadangi, B. H. Kear, L. E. McCandlish, Use of a twin powder feeder with the cold gas dynamic spray process, in: *Proceedings of the International Thermal Spray Conference*, Osaka, Japan. 2004, 378-81.
125. P. H. Shipway, C. A. Scotchford, B. Sim, D. G. McCartney, D. Zhang, Improved titanium coatings for biomedical applications using cold gas spraying, in: *Transactions -7th World Biomaterials Congress*, Sydney, Australia. 2004, 787.
126. H. K. Kang, S. B. Kang, Tungsten/copper composite deposits produced by a cold spray, *Scripta Materialia*, **49** (12), 2003, pp.1169-74.
127. H.-J. Kim, C.-H. Lee, S.-Y. Hwang, Superhard nano WC-12%Co coating by cold spray deposition, *Materials Science and Engineering A*, **391** (1-2), 2005, pp.243-48.
128. J. Karthikeyan, C. M. Kay, J. Linderman, R. S. Lima, C. C. Berndt, Cold Sprayed Nanostructured WC-Co, in: *International Thermal Spray Conference*, 2001, 383-87.
129. R. S. Lima, J. Karthikeyan, C. M. Kay, J. Linderman, C. C. Berndt, Microstructural Characteristics of Cold-Sprayed nanostructured WC-Co Coatings, *Thin Solid Films*, **416** 2002, pp.129-35.
130. Z. R. Zhou, L. Vincent, Lubrication in Fretting - A Review, *Wear*, **225-229**(2), 1999, pp. 962-967

131. M. Pushpavanam, S.R. Natrajan, Nickel-boron nitride electrocomposites, *Metal Finishing*, **93** (6), 1995, pp 97-99
132. Y. W. Bae, W. Y. Lee, T. M. Besmann, C. S. Yust, P. J. Blau, Preparation and friction characteristics of self-lubricating TiN- MoS₂ composite coatings, *Materials Science & Engineering A: Structural Materials: Properties, Microstructure and Processing*, **A209** (1-2), 1996, pp 372-376
133. V. A. Al'tman, V. M. Valakina, Y. A. Gluskin, V. L. Memelov, A. N. Moskvichev, Effect of alloying on the physicochemical interaction between the components of the Ni-MoS/sub 2/ system, *Poroshkovaya Metallurgiya*, **17** (8), 1978, pp.59-61.
134. B. W. Buchholtz, F. M. Kustas, Effects of surface pretreatment of Ti-6Al-4V on the adhesion and wear lifetimes of sputtered MoS₂ coatings, *TribologyTransactions*, **39** (2), 1996, pp.330-37.
135. X. Dangsheng, P. Chaoqun, H. Qizhong, Development of MoS₂-containing Ni-Cr based alloys and their high-temperature tribological properties, *Transactions of the Nonferrous Metals Society of China*, **8** (2), 1998, pp.226-29.
136. L. E. Seitzman, R. N. Bolster, I. L. Singer, IBAD MoS₂ lubrication of titanium alloys, *Surface and Coatings Technology*, **78** (1), 1996, pp.10-13.
137. P. Skeldon, H. W. Wang, G. E. Thompson, Formation and characterization of selflubricating MoS₂ precursor films on anodized aluminum, *Wear*, **206** (1-2), 1997, pp.187- 96.
138. L. Xibin, L. Rutie, G. Xuebing, Study of Ni-Cr High Temperature Solid Self-Lubricating Materials Added with Ni Coated MoS₂ Powders, *Rare Metal Materials and Engineering*, **32** (10), 2003, pp.783-84.
139. G.-z. Xu, Z.-r. Zhou, J.-j. Liu, A comparative study on fretting wear-resistant properties of ion-plated TiN and magnetron-sputtered MoS₂ coatings, *Wear*, **224** (2), 1999, pp.211-15.
140. J. Xu, M. H. Zhu, Z. R. Zhou, P. Kapsa, L. Vincent, An investigation on fretting wear life of bonded MoS₂ solid lubricant coatings in complex conditions, *Wear*, **255** (1-6), 2003, pp.253-58.
141. R M. H. Zhu, Z. R. Zhou, The damage mechanisms under different fretting modes of bonded molybdenum disulfide coating, in: *PRICM 5: The Fifth Pacific Rim International Conference on Advanced Materials and Processing*, Beijing, China. 2004, **475-479**, 1545-50.

142. D. Zhuang, J. Liu, B. Zhu, W. Li, A study of the friction and wear performance of MoS₂ thin films produced by ion beam enhanced deposition and magnetron sputtering, *Wear*, **210** (1-2), 1997, pp.45-49.
143. G. Jayaram, L. D. Marks, M. R. Hilton, Nanostructure of Au-20% Pd layers in MoS₂ multilayer solid lubricant films, *Surface and Coatings Technology*, **76-77** (2), 1995, pp.393-99.
144. D. G. Teer, J. Hampshire, V. Fox, V. Bellido-Gonzalez, The tribological properties of MoS₂/metal composite coatings deposited by closed field magnetron sputtering, *Surface and Coatings Technology*, **94-95** 1997, pp.572-77.
145. V. Fox, A. Jones, N. M. Renevier, D. G. Teer, Hard lubricating coatings for cutting and forming tools and mechanical components, *Surface and Coatings Technology*, **125** (1), 2000, pp 347-353
146. V. Fox, J. Hampshire, D. Teer, MoS₂/metal composite coatings deposited by closed field unbalanced magnetron sputtering: tribological properties and industrial uses, *Surface and Coatings Technology*, **112** (1-3), 1999, pp.118-22.
147. M. R. Hilton, G. Jayaram, L.D. Marks, Microstructure of cosputter-deposited metal- and oxide-MoS₂ solid lubricant thin films, *Journal of Materials Research*, **13** (4), 1998, pp 1022-1032
148. N. M. Renevier, J. Hampshire, V. C. Fox, J. Witts, T. Allen, D. G. Teer, Advantages of using self-lubricating, hard, wear-resistant MoS₂-based coatings, *Surface and Coatings Technology*, **142-144**, 2001, pp 67-77
149. N. M. Renevier, V. C. Fox, D. G. Teer, J. Hampshire, Coating characteristics and tribological properties of sputter-deposited MoS₂/metal composite coatings deposited by closed field unbalanced magnetron sputter ion plating, *Surface and Coatings Technology*, **127** (1), 2000, pp 24-37
150. N. M. Renevier, V. C. Fox, D. G. Teer, J. Hampshire, Performance of low friction MoS₂/titanium composite coatings used in forming applications; *Materials and Design*, **21**(4), 2000, pp 337-343
151. N. M. Renevier, H. Oosterling, U. König, H. Dautzenberg, B. J. Kim, L. Geppert, F. G. M. Koopmans, J. Leopold, Performance and limitations of MoS₂/Ti composite coated inserts, *Surface and Coatings Technology*, **172** 2003, pp.13-23.
152. N. M. Renevier, N. Lobiondo, V. C. Fox, D. G. Teer, J. Hampshire, Performance of MoS₂/metal composite coatings used for dry machining and other industrial applications, *Surface and Coatings Technology*, **123**(1), 2000, pp 84-91

- 153.** V. Rigato, G. Maggioni, D. Boscarino, L. Sangaletti, L. Depero, V. C. Fox, D. Teer, C. Santini, A study of the structural and mechanical properties of Ti---MoS₂ coatings deposited by closed field unbalanced magnetron sputter ion plating, *Surface and Coatings Technology*, **116-119** 1999, pp.176-83.
- 154.** D. A. Lelonis, J. W. Tereshko, C. M. Andersen, Boron Nitride Powder—A High-Performance Alternative for Solid Lubrication, *GE Advanced Ceramics*, Pub. No. 81506 (9/03)
- 155.** D. A. Lelonis, Boron Nitride - A Review, *Ceramic Technology International*, 1994.
- 156.** R. Deacon, Lubrication by Lamellar Solids, *Proceedings of the. Royal Society*, **243A**, 1957, pp. 464.
- 157.** T. Allen, *Particle Size Measurement*, vol. 1, 5th edition, Chapman and Hall, New York, 1997, pp. 404-416
- 158.** C. H. Hager Jr., in: MS Thesis – Evaluation of Coating Processes for the Fretting Amelioration of Titanium Blade Disk Assemblies found in the High Temperature Compressor of Jet Turbine Engines, The Pennsylvania State University, University Park, PA, 2002.
- 159.** A.P. Alkimov, V.F. Kosarev, A.N. Papyrin, *Dokl. Akad. Nauk SSSR* 318 (1990) 1062–1065.

Appendix A

Optical and SEM Images of Powders

Figures A.1-A.5 show the optical images of the Ni coated BN powders. The powder particles were mounted in epoxy, polished, and observed under the optical microscope so as to study the structure of the cross-section of the coated powders.

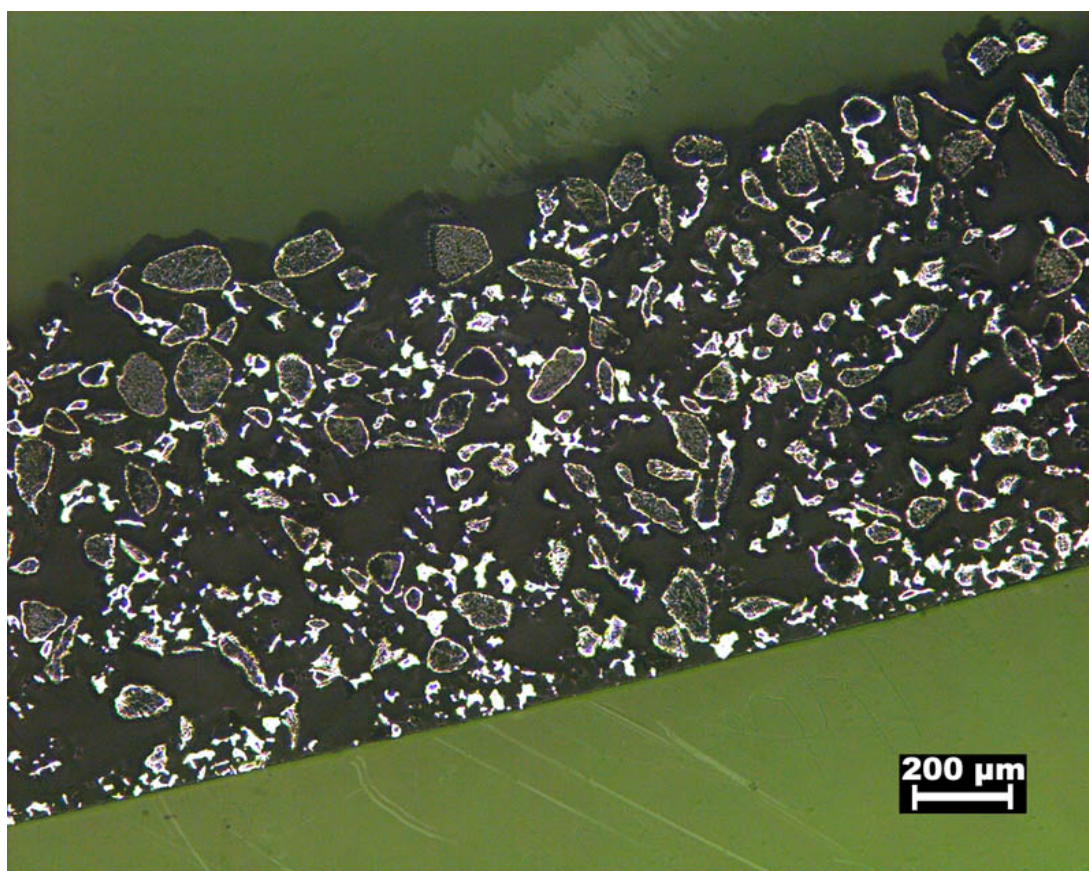


Figure A.1: Optical image of Ni coated BN powder

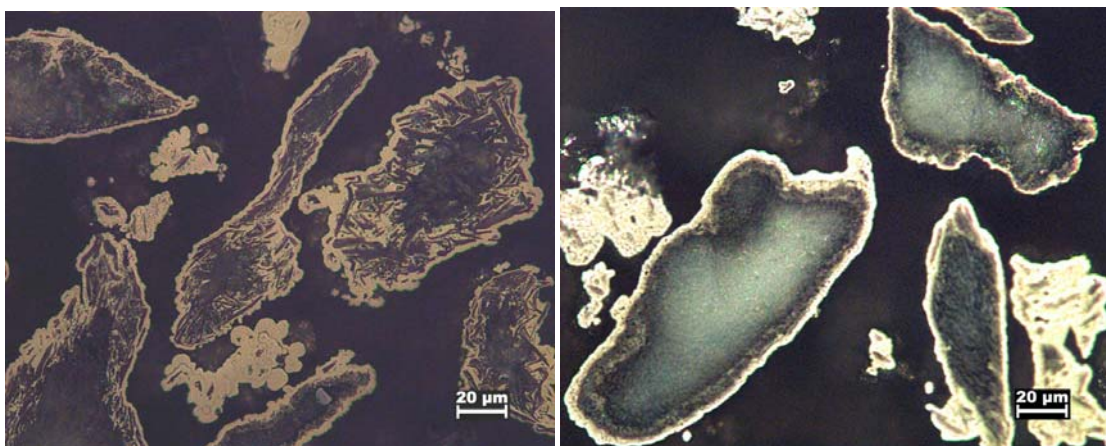


Figure A.2: Optical image of Ni coated BN powder

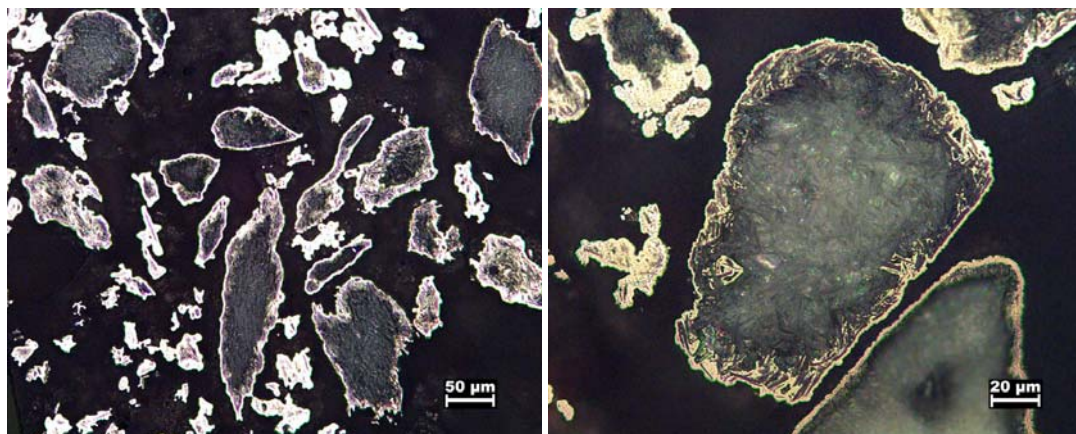


Figure A.3: Optical image of Ni coated BN powder

The particle size distribution and surface morphology of the Ni coated BN powders was studied under the SEM, as shown in Figures A.6-A.15

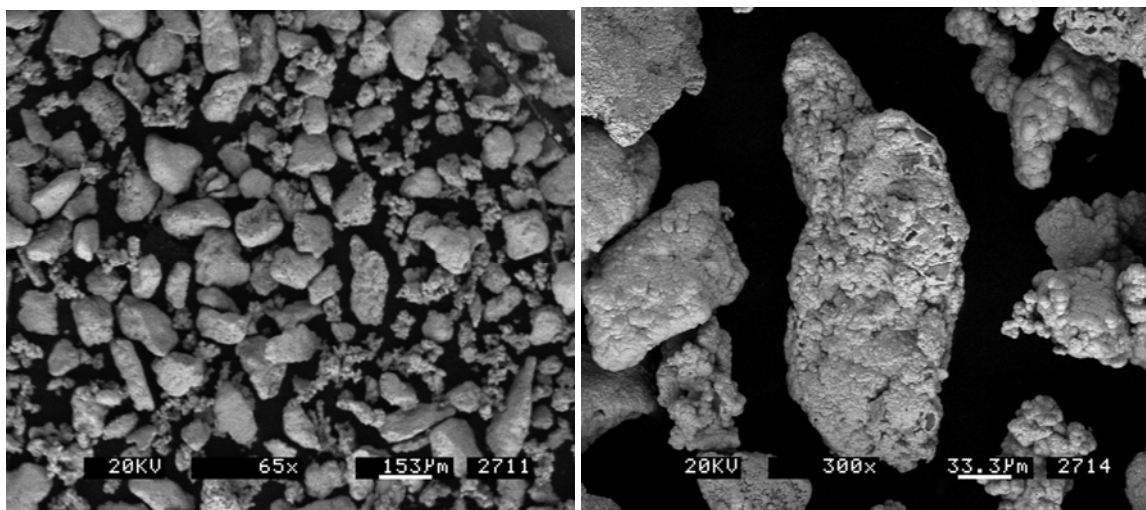


Figure A.4: SEM image of Ni coated BN powder

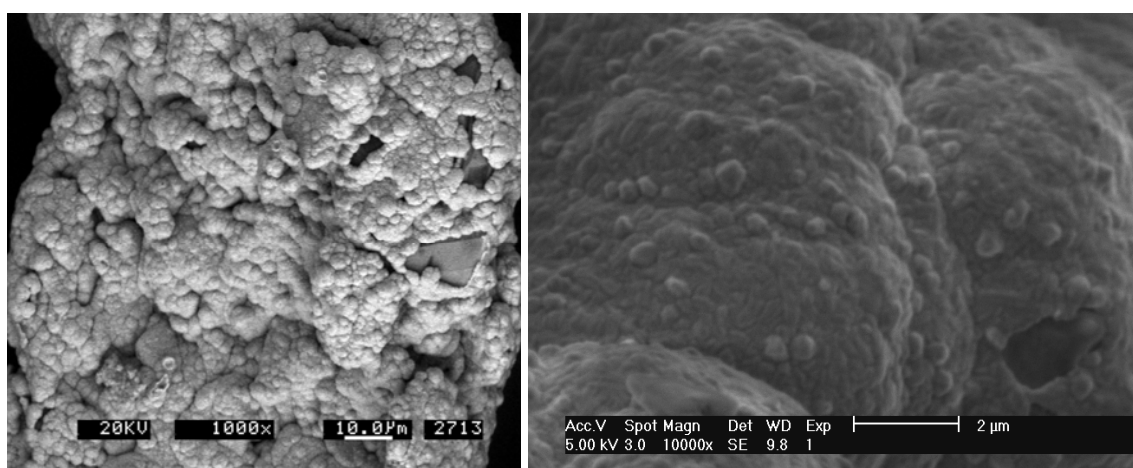


Figure A.5: SEM image of Ni coated BN powder

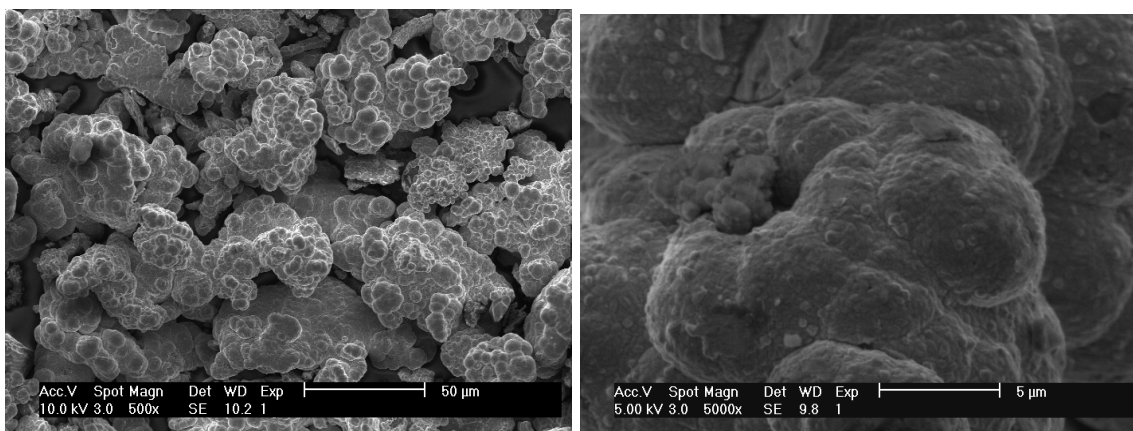


Figure A.6: SEM image of Ni coated BN powder

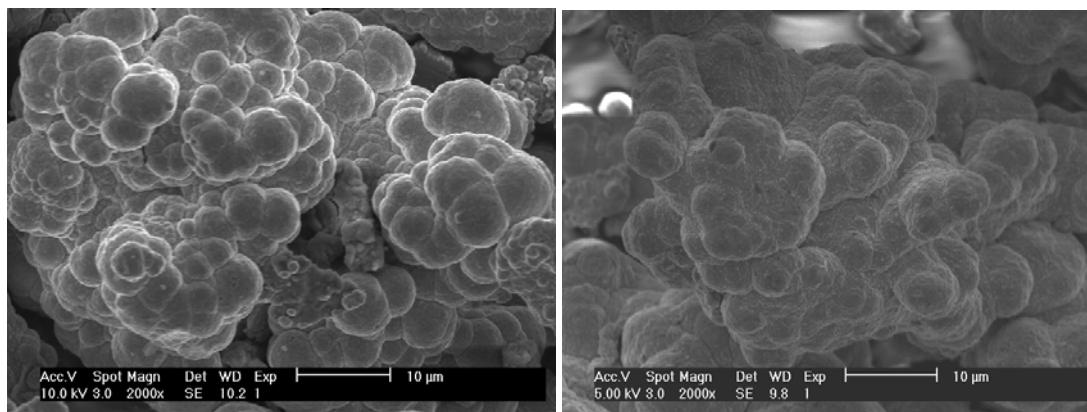


Figure A.7: SEM image of Ni coated BN powder

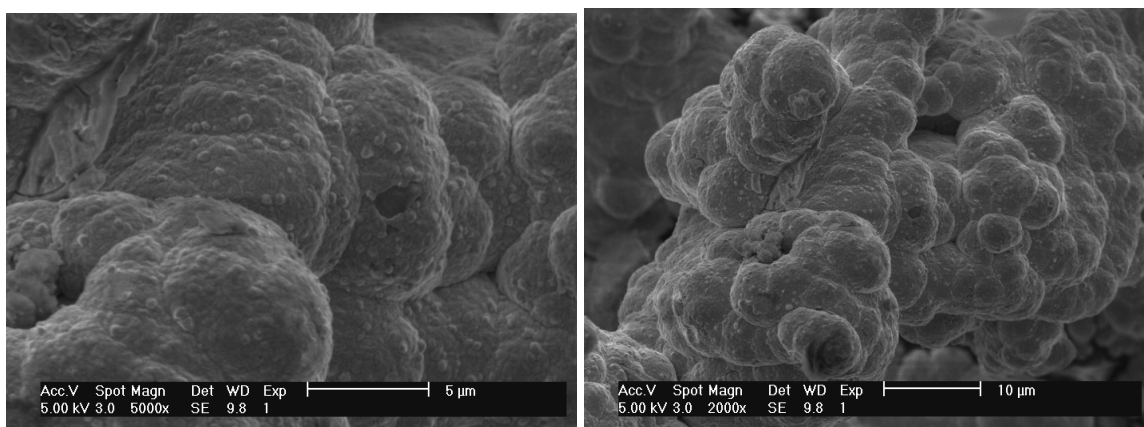


Figure A.8: SEM image of Ni coated BN powder

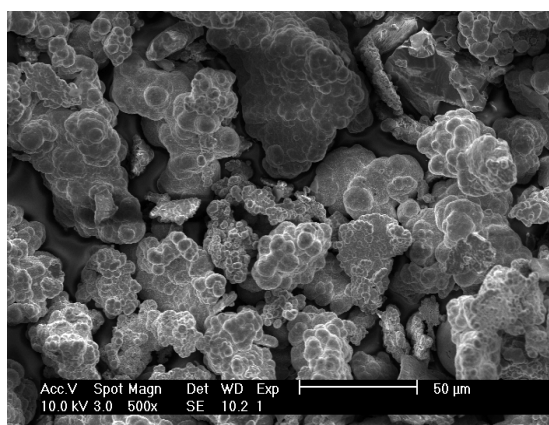


Figure A.9: SEM image of Ni coated BN powder

Figures A.17- A.19 show the SEM images of admixed Ni-BN powders.

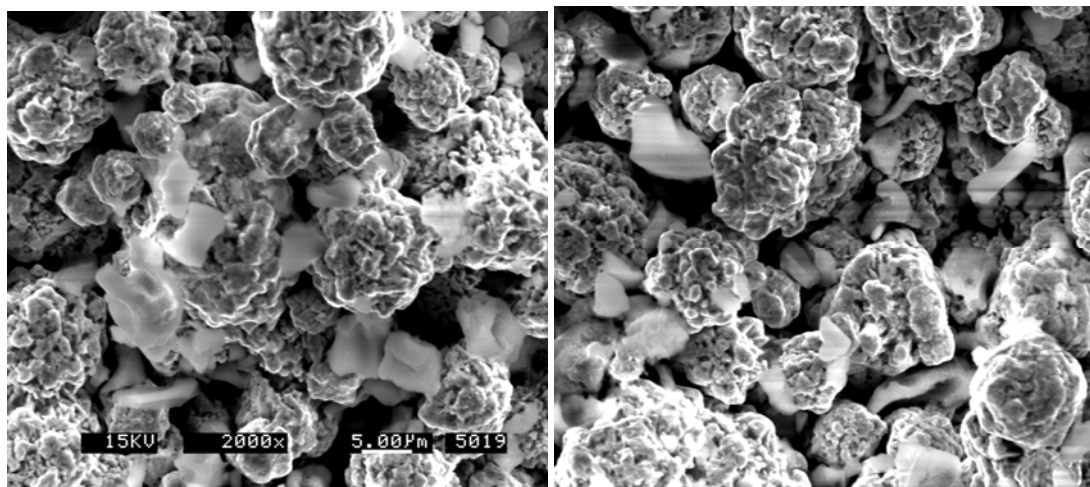


Figure A.10: SEM image of admixed Ni-BN powders

Figures A.19 –A.23 show the SEM images of admixed Ni-Ni coated BN powders.

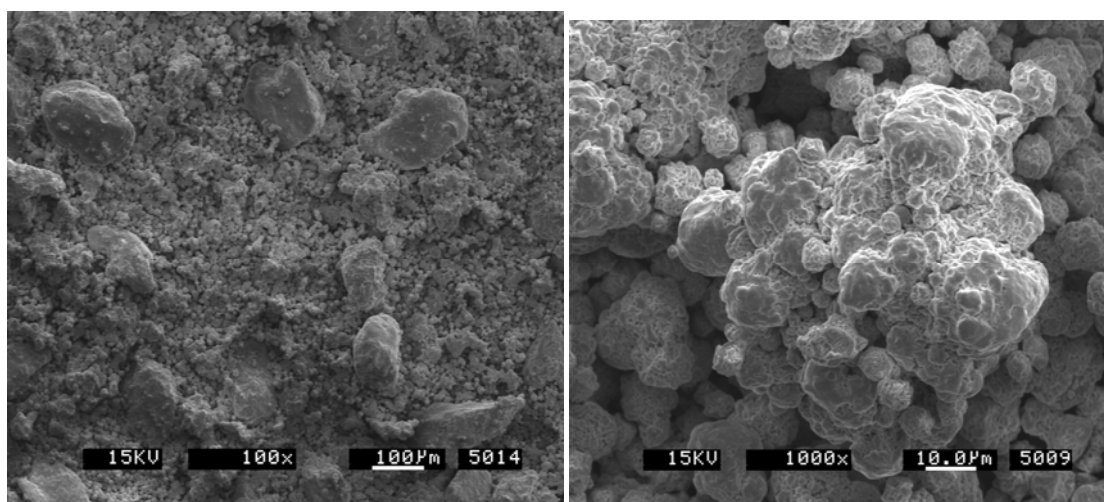


Figure A.11: SEM image of admixed Ni-Ni coated BN powders

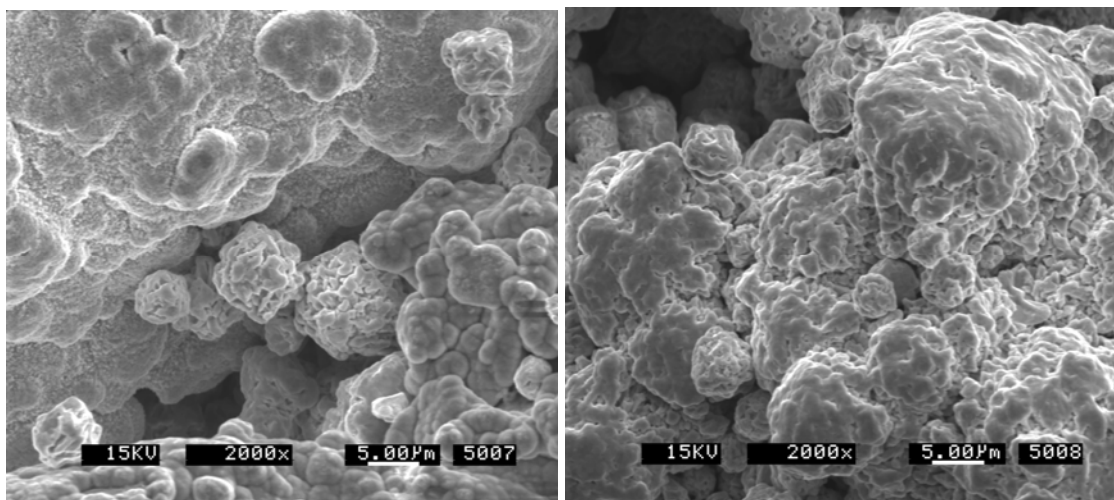


Figure A.12: SEM image of admixed Ni-Ni coated BN powders

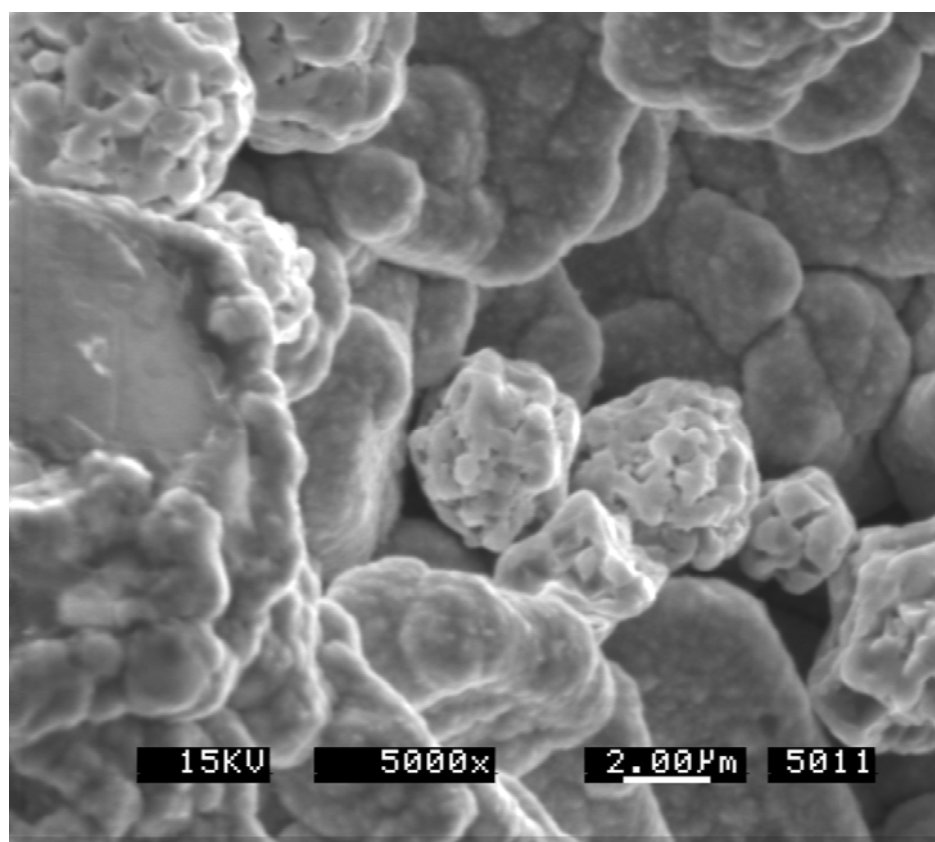


Figure A.13: SEM image of admixed Ni-Ni coated BN powders

Appendix B

Additional SEM images of Ni-MoS₂ and Ni-BN coatings

B.1 Optical images of pure Ni coating sprayed with helium



Figure B.1: Optical image of pure Ni coating

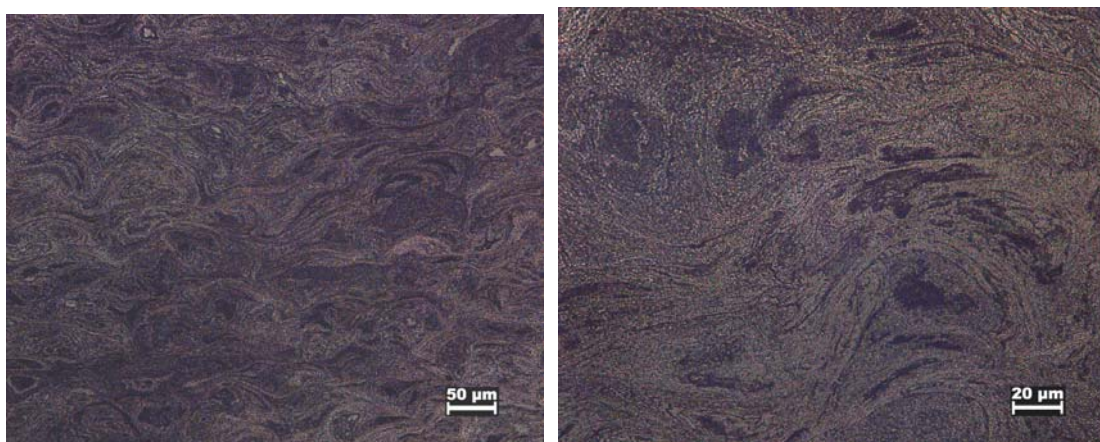


Figure B.2: Optical image of etched pure Ni coating

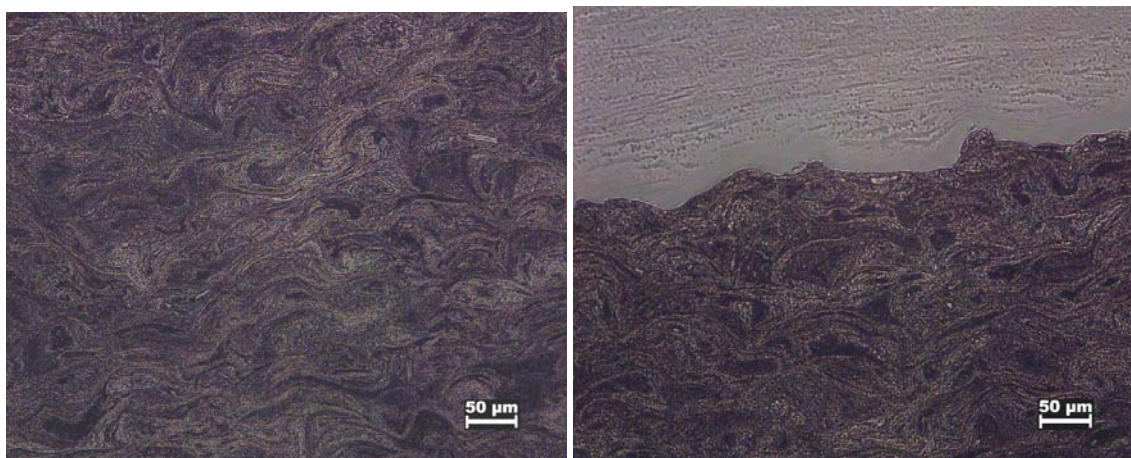


Figure B.3: Optical images of etched pure Ni coating

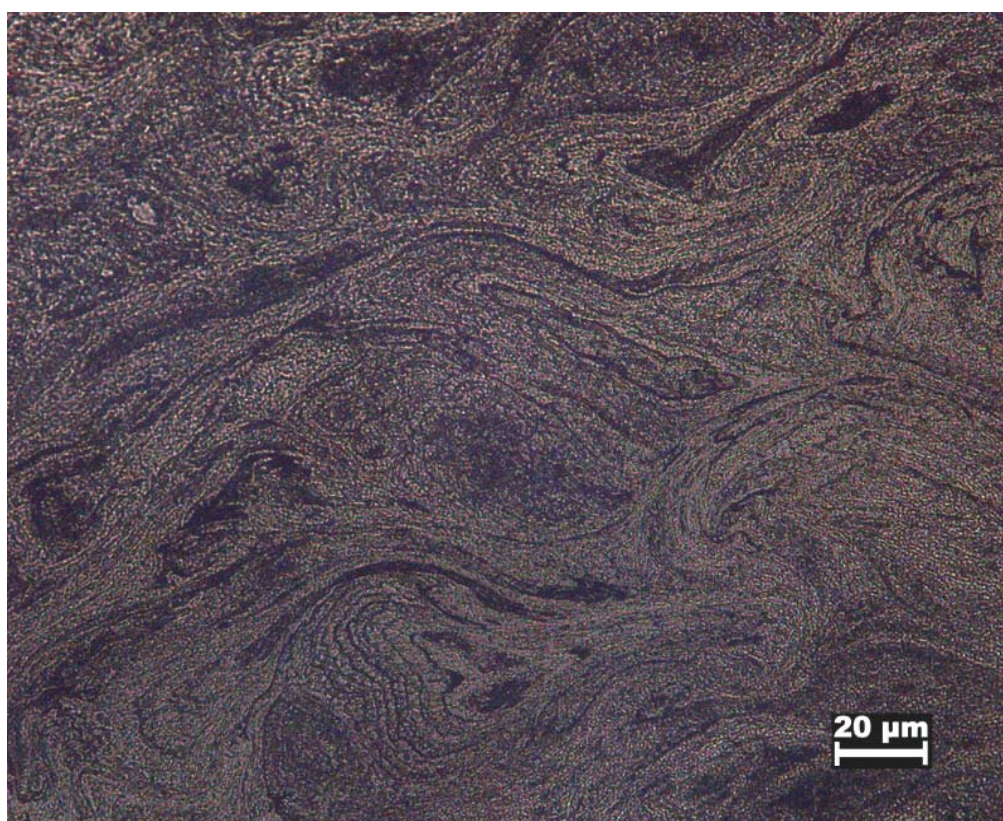


Figure B.4: Optical image of etched pure Ni coating

B.2 SEM images of (admixed) Ni-MoS₂ coatings sprayed with helium

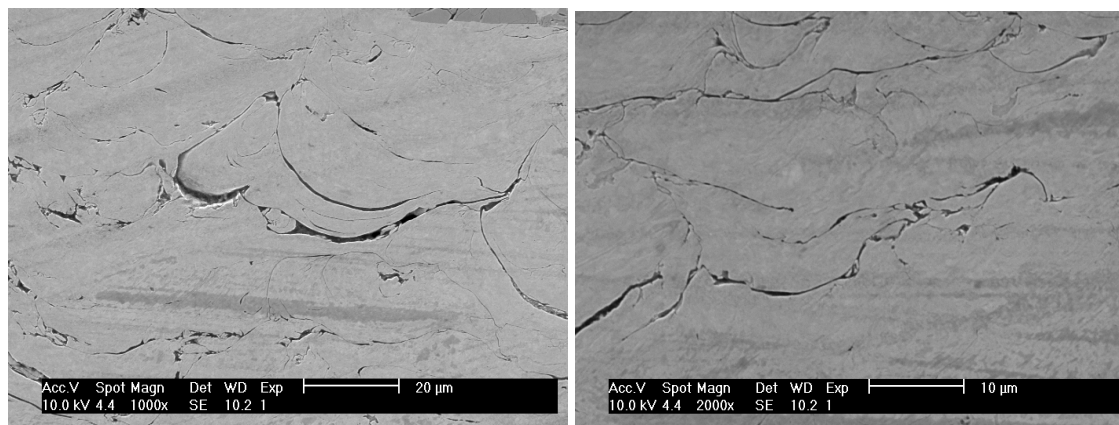


Figure B.5: SEM images of (admixed) Ni-MoS₂ coating

B.3 SEM images of (admixed) Ni-BN coatings sprayed with helium

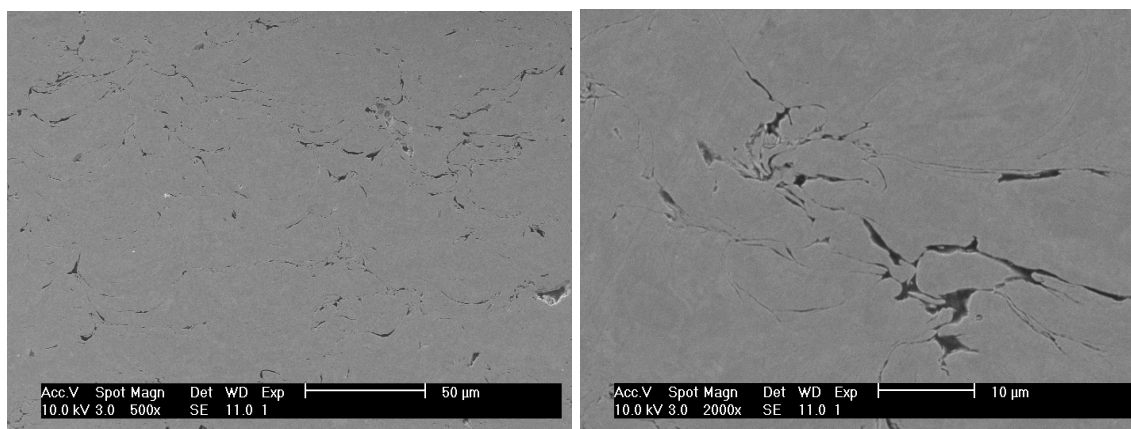


Figure B.6: SEM images of (admixed) Ni-BN coating

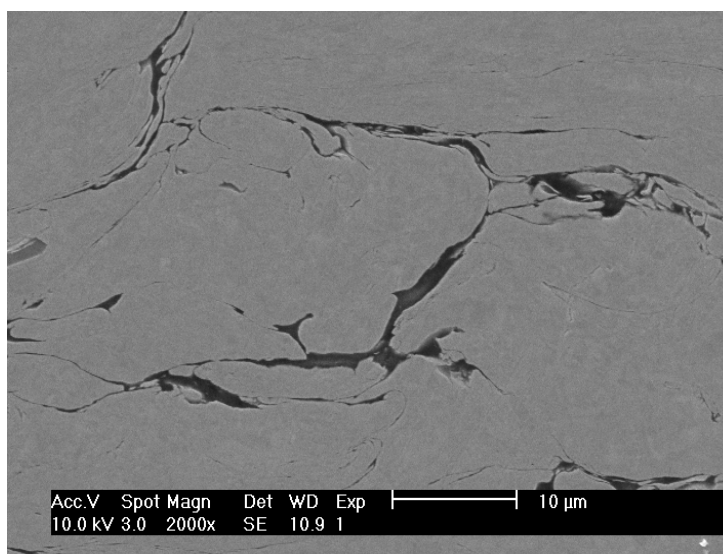


Figure B.7: SEM image of (admixed) Ni-BN coating

B.4 SEM images of (milled) Ni-MoS₂ coatings sprayed with helium

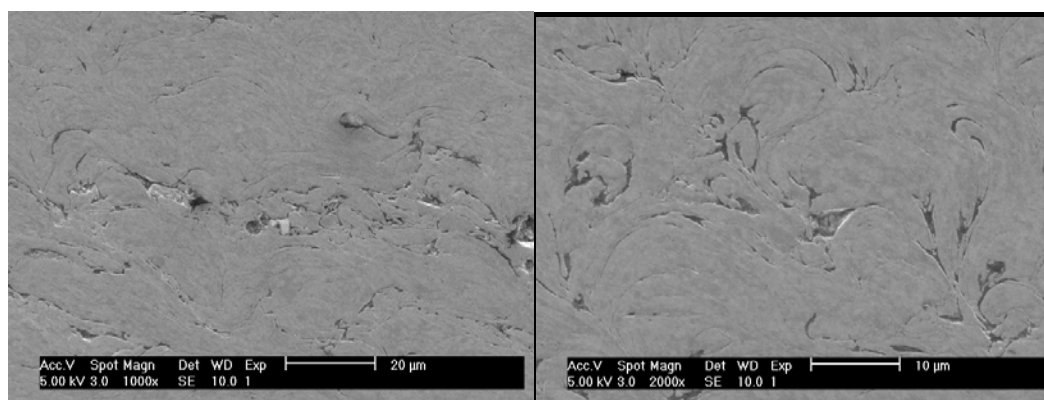


Figure B.8: SEM images of (milled) Ni-MoS₂ coating

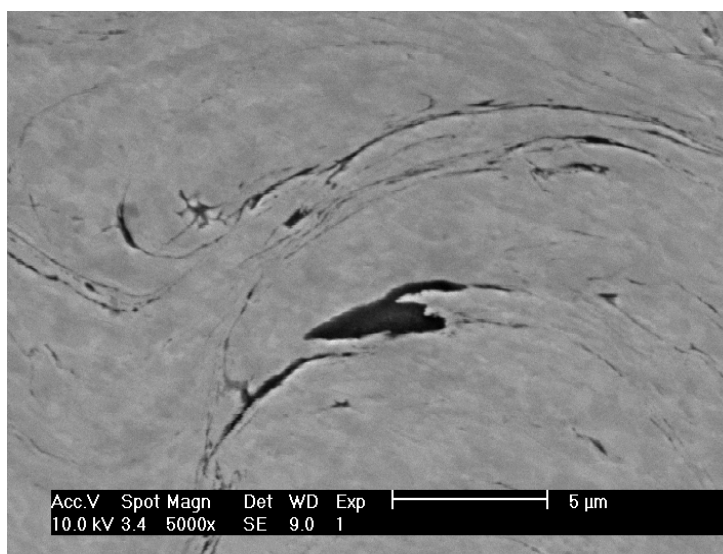


Figure B.9: SEM image of (milled) Ni-MoS₂ coating

B.5 SEM images of (milled) Ni-BN coatings sprayed with helium

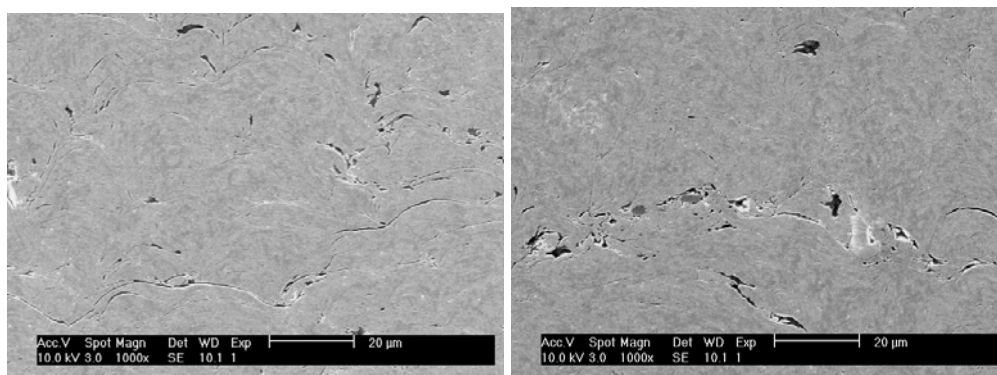


Figure B.10: SEM images of (milled) Ni-BN coating

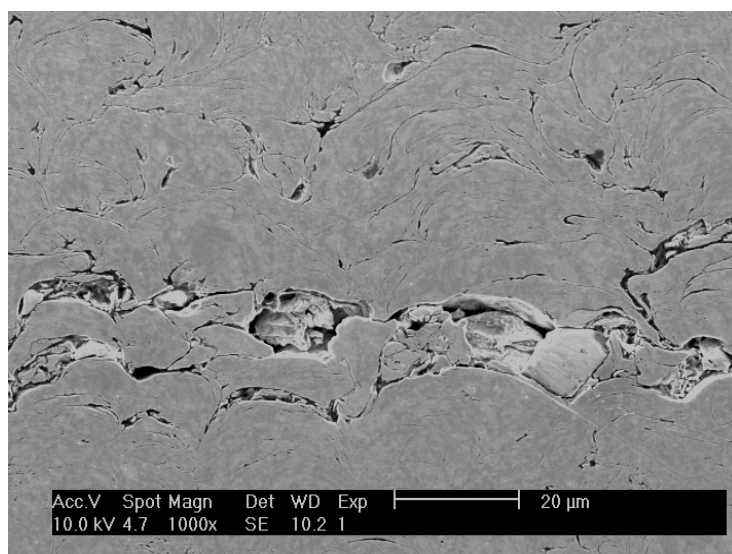


Figure B.11: SEM images of (milled) Ni-B N coating

B.6 Optical and SEM images of (admixed) Ni-Ni coated BN coatings sprayed with helium

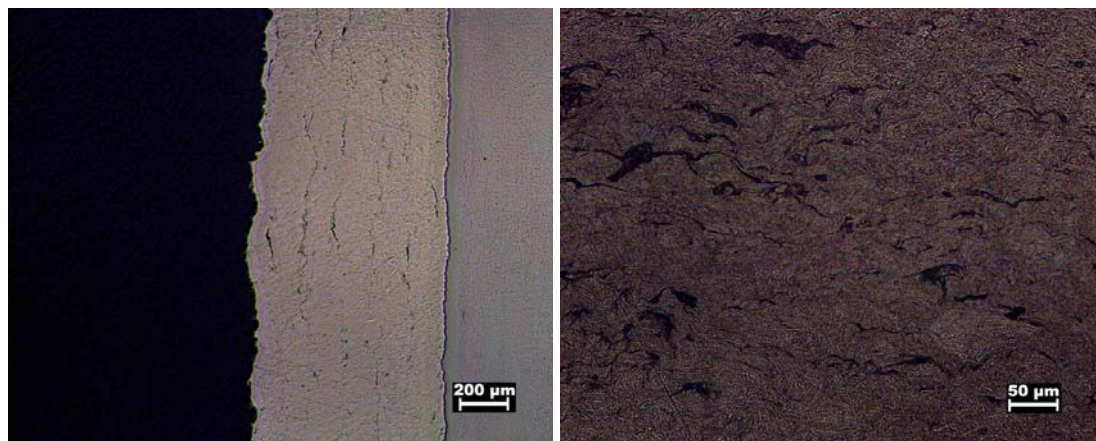


Figure B.12: Optical images of etched (admixed) Ni-Ni coated BN coating

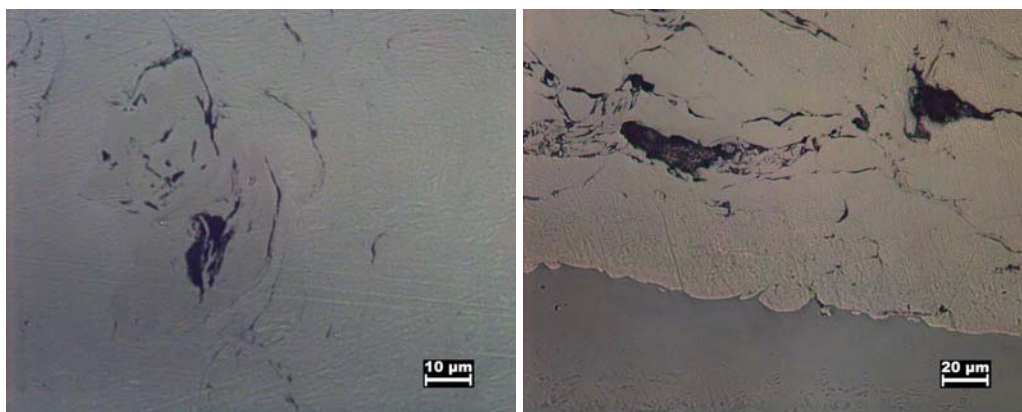


Figure B.13 Optical images of (admixed) Ni-Ni coated BN coating

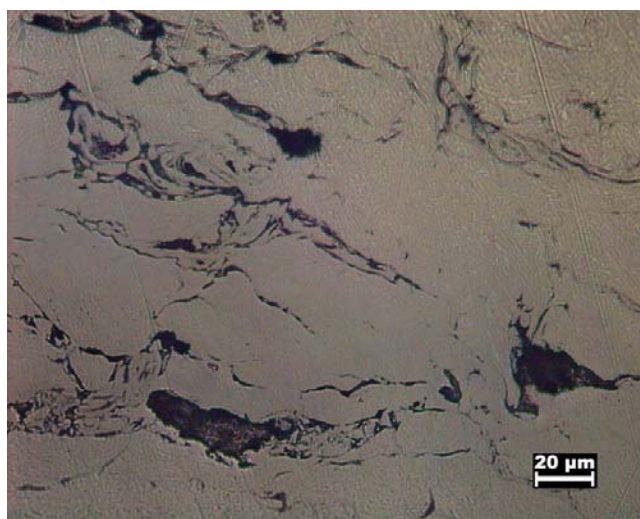


Figure B.14: Optical image of (admixed) Ni-Ni coated BN coating

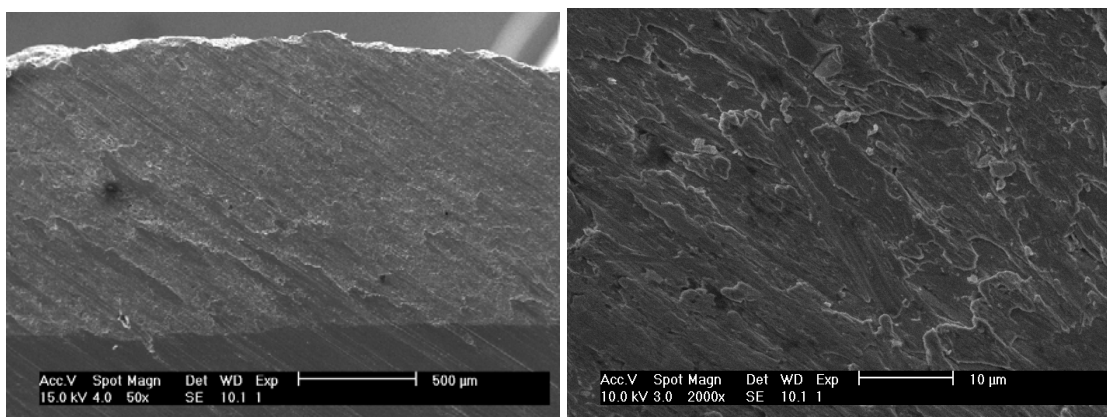


Figure B.15: SEM images of (admixed) Ni-Ni coated BN coating

;

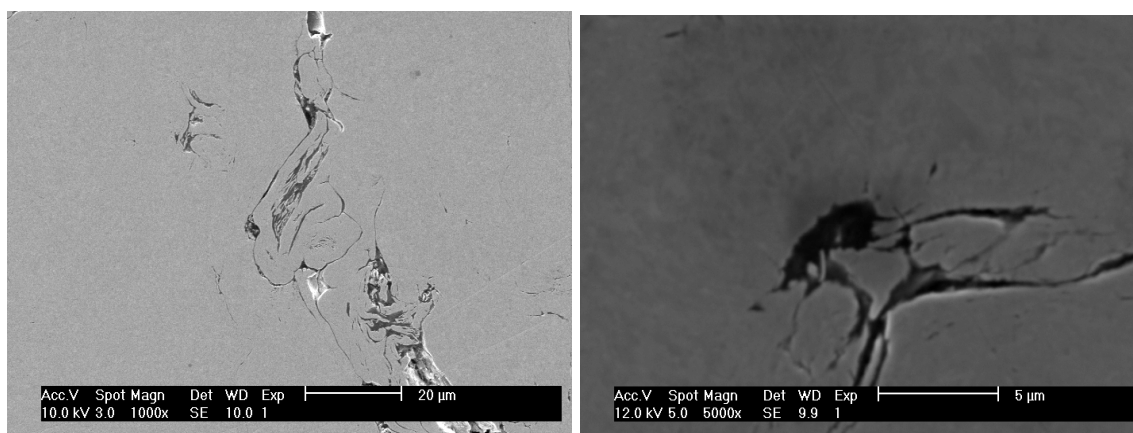


Figure B.16 SEM images of (admixed) Ni-Ni coated BN coating

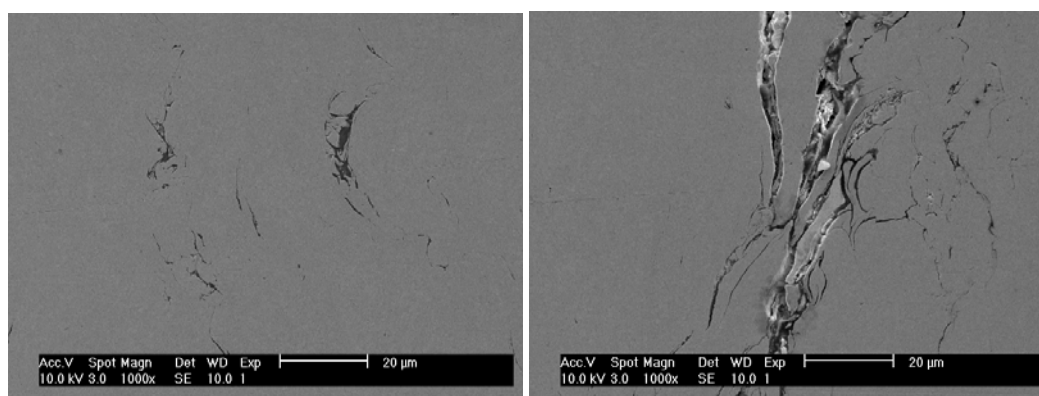


Figure B.17: SEM images of (admixed) Ni-Ni coated BN coating

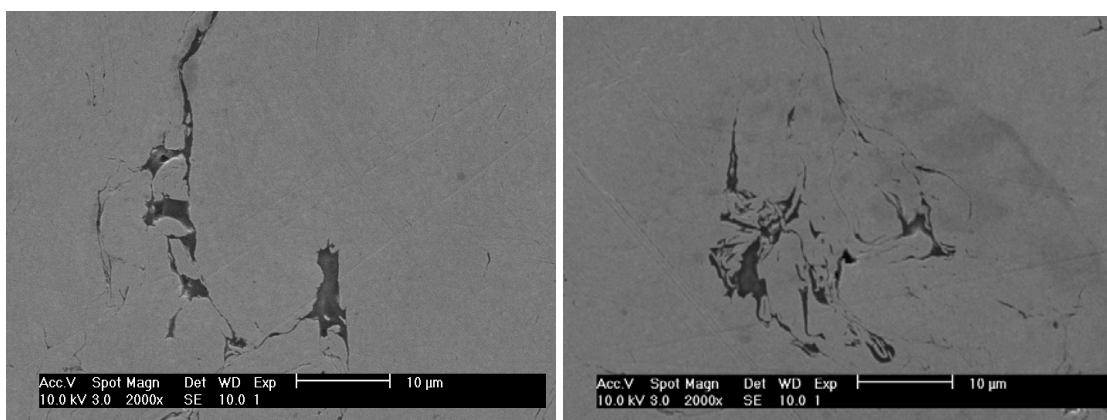


Figure B.18: SEM images of (admixed) Ni-Ni coated BN coating

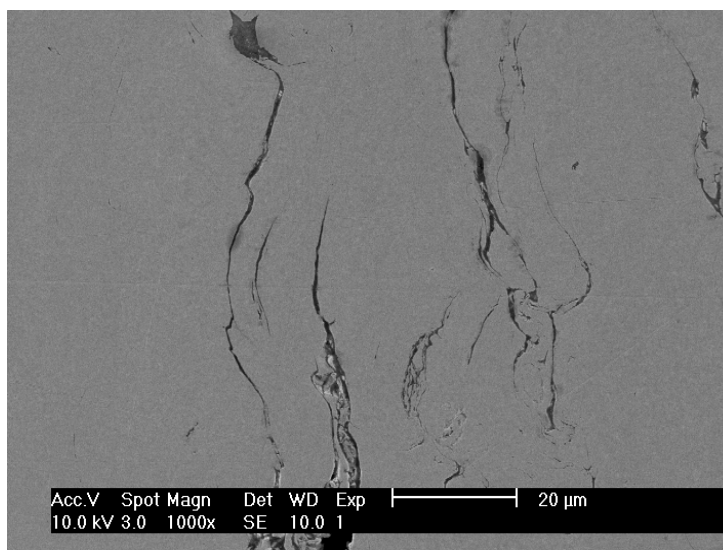


Figure B.19: SEM image of (admixed) Ni-Ni coated BN coating

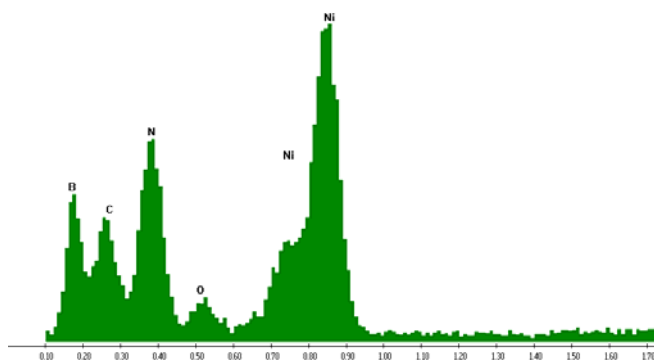


Figure B.20: EDX of a BN rich region in the (admixed) Ni-Ni coated BN coating

Appendix C

Effect of Particle Diameter and Process Parameters on Particle Velocity

Particle velocity and critical velocity plots for Ni particles of various sizes at a gas temperature of 500 °C and initial particle temperature of 27 °C have been plotted using a code developed at Sandia National Laboratory. The effects of process gas and gas pressure on particle velocity have been studied.

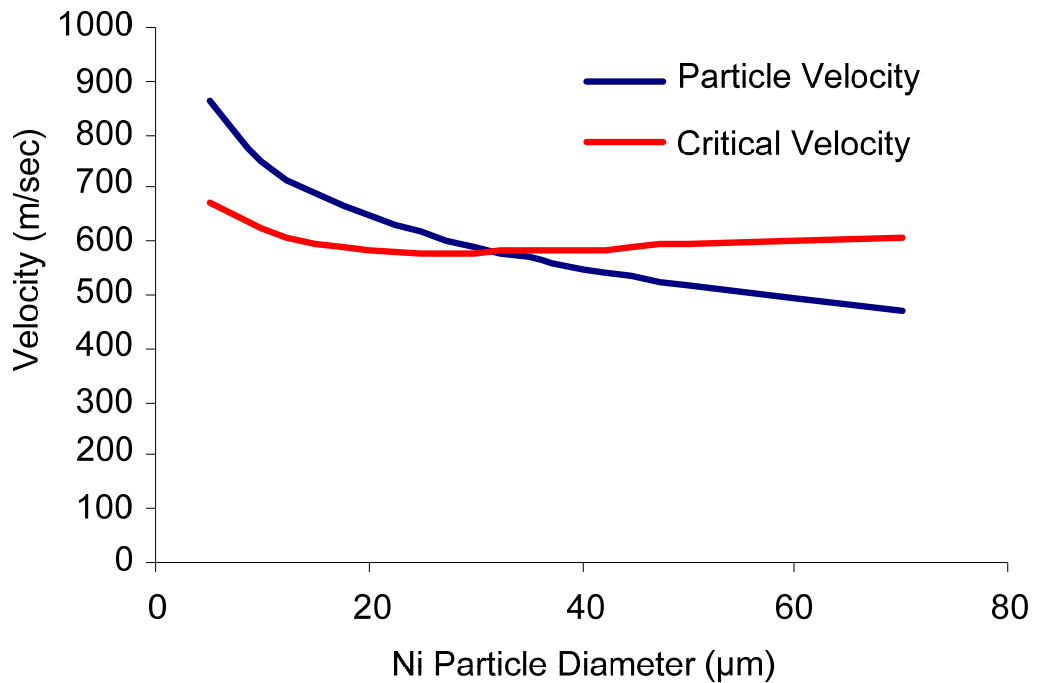


Figure C.1: Particle velocity and critical velocity of Ni as a function of particle diameter, using nitrogen gas at 2.1 MPa

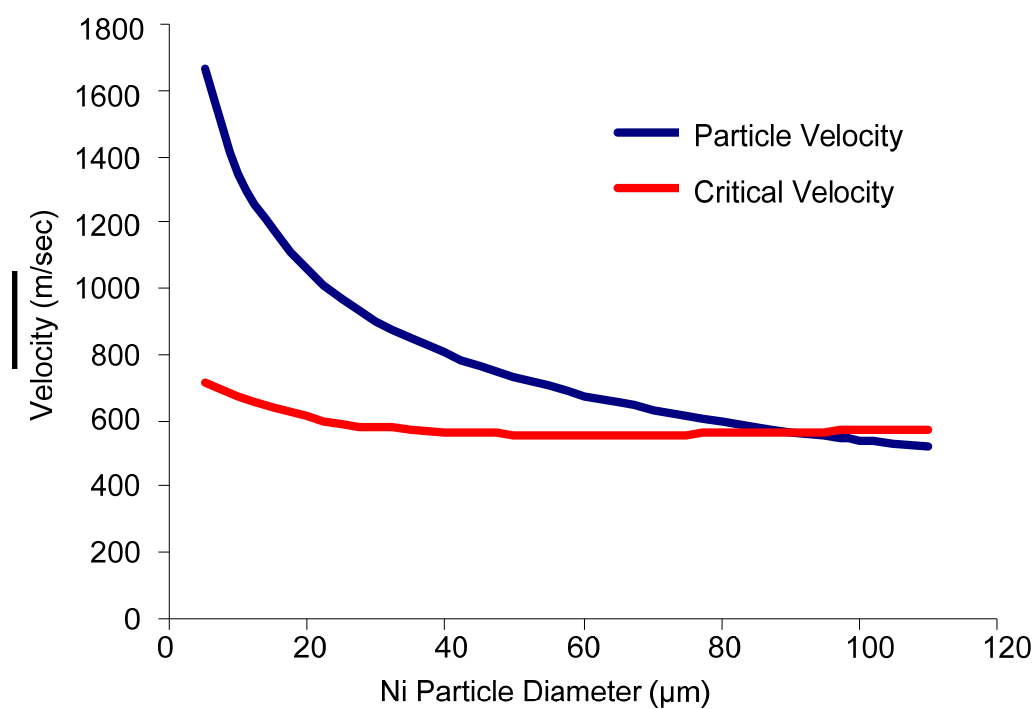


Figure C.2: Particle velocity and critical velocity of Ni as a function of particle diameter, using helium gas at 2.1 MPa

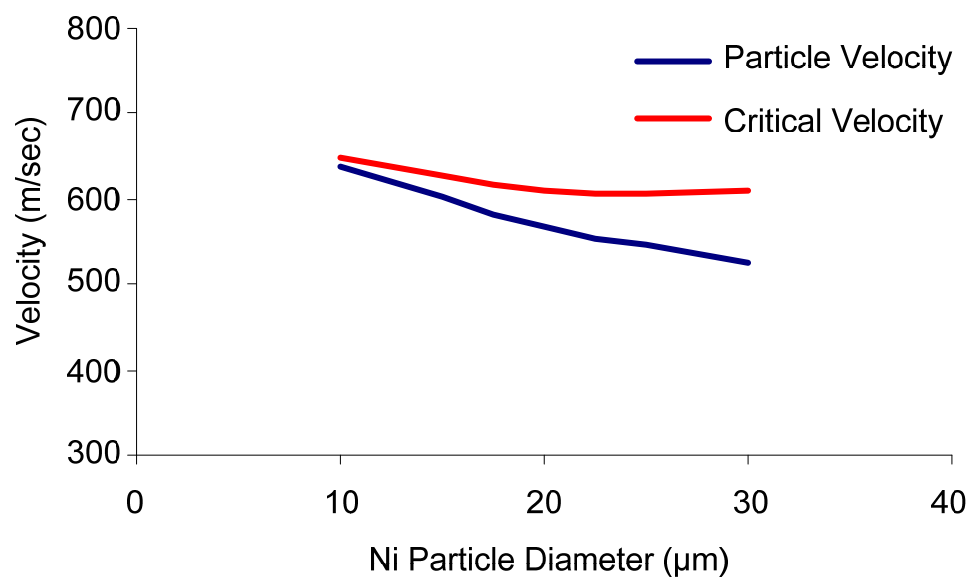


Figure C.3: Particle velocity and critical velocity of Ni as a function of particle diameter, using argon gas at 2.1 MPa

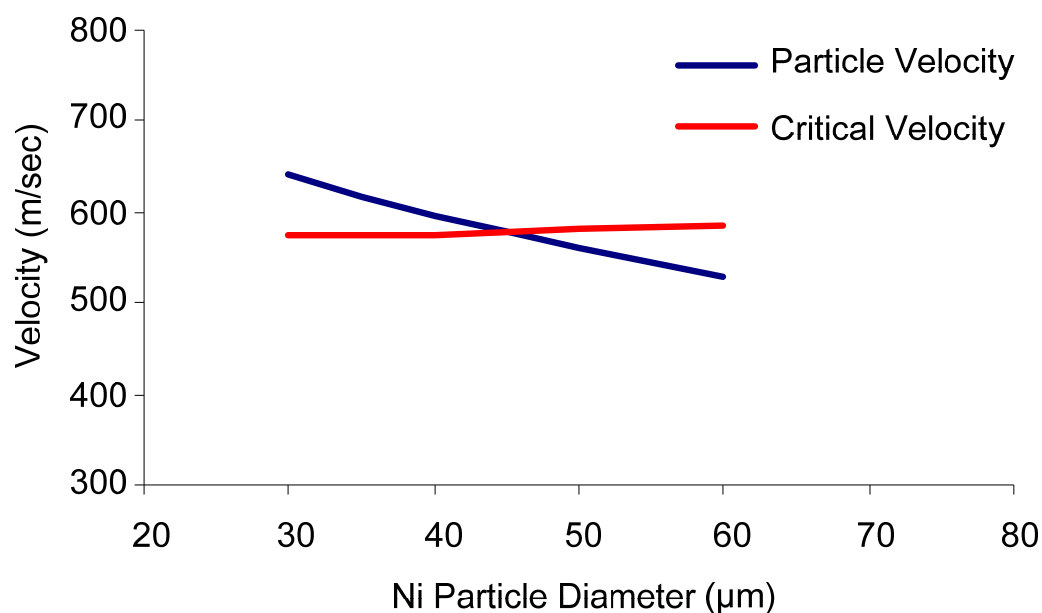


Figure C.4: Particle velocity and critical velocity of Ni as a function of particle diameter, using a mixture of 70% Nitrogen -30% Helium gas at 2.1 MPa

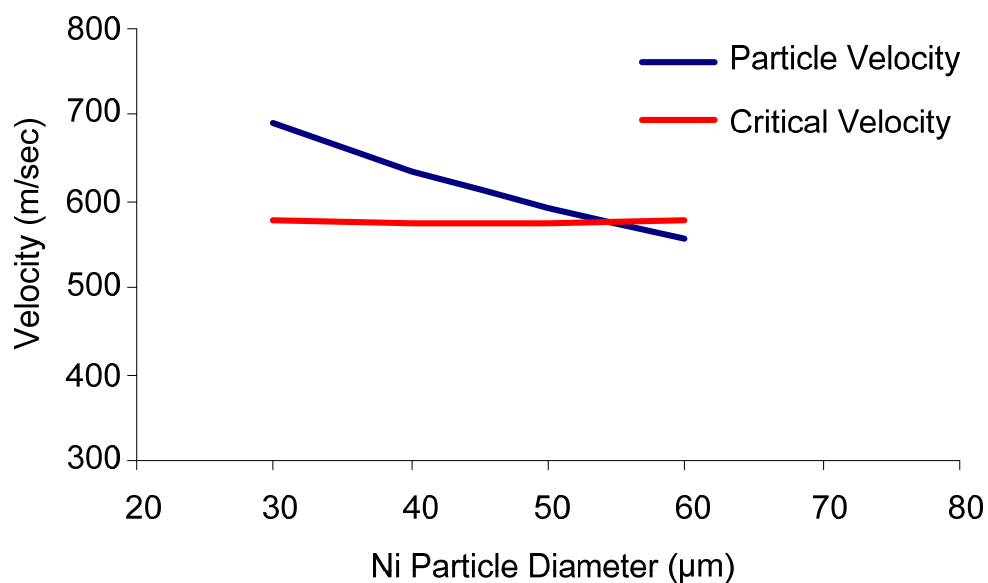


Figure C.5: Particle velocity and critical velocity of Ni as a function of particle diameter, using a mixture of 50% Nitrogen -50% Helium gas at 2.1 MPa

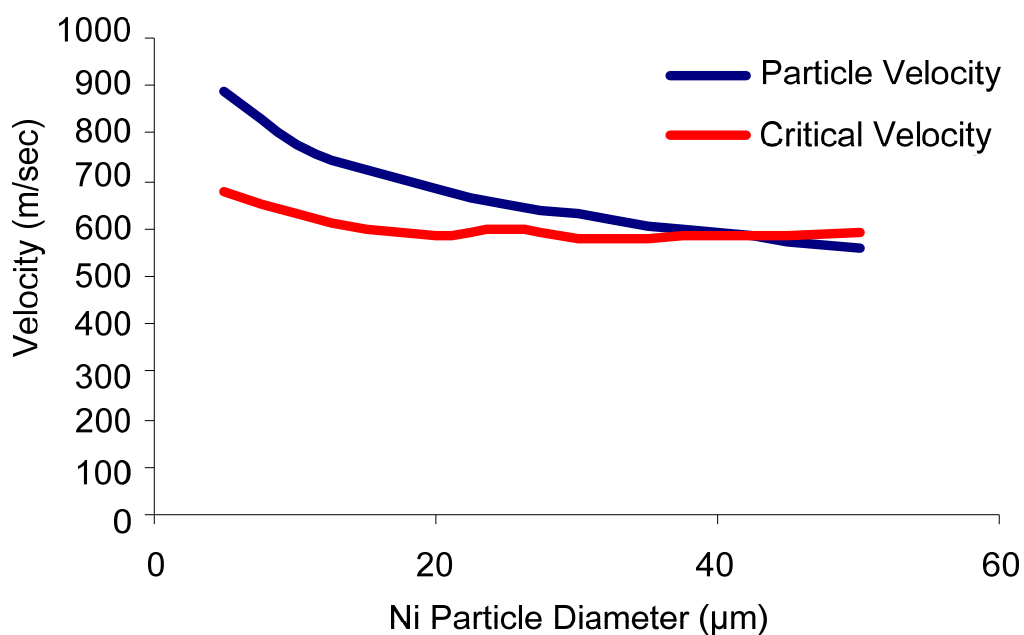


Figure C.6: Particle velocity and critical velocity of Ni as a function of particle diameter, using nitrogen gas at 3.45 MPa

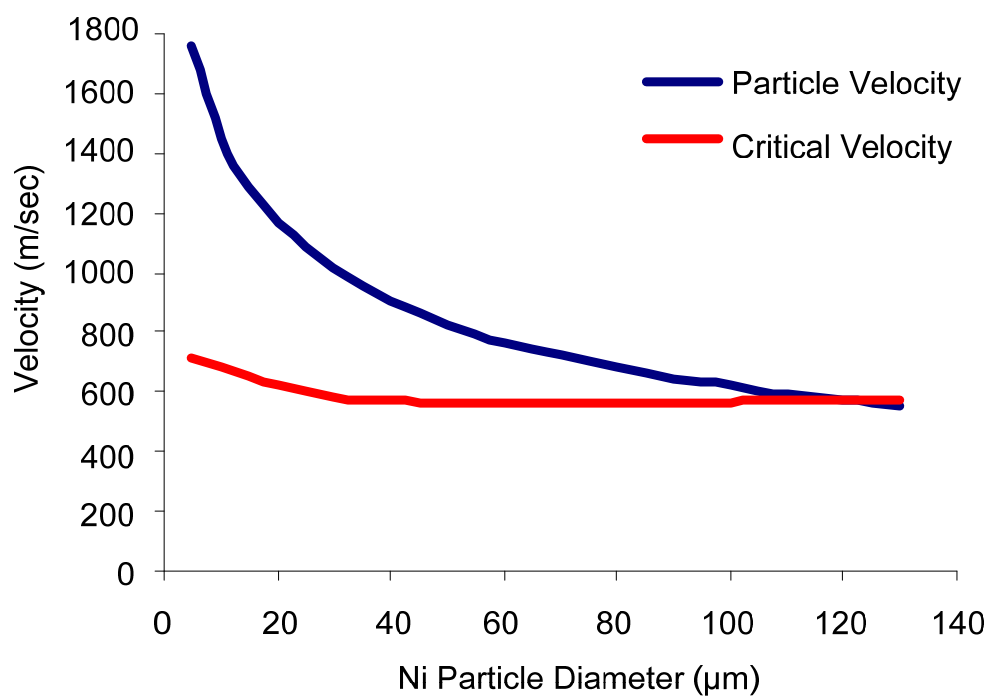


Figure C.7: Particle velocity and critical velocity of Ni as a function of particle diameter, using helium gas at 3.45 MPa

Appendix D

Non-Technical Abstract

Dovetail joints are used to attach Titanium turbine blades to Titanium disks. Despite close tolerances, there is still relative motion of between the mating parts in the joint. Such a situation leads to a material degradation phenomenon known as fretting wear. Several types of surface treatments and coatings have been investigated in the past to protect the dovetail joints from the harmful effects of fretting wear. Generally, this is accomplished by increasing the wear resistance or lubricity of the contacting surfaces. However, the lubricants typically lose their ability to reduce friction at the high temperatures and pressures encountered in the turbine engine.

In the current research, a low temperature coating method known as Cold Spray has been modified for the development of coatings which have a slippery component imbedded into them. During cold spray, powder particles are accelerated to very high velocity so that they deform and bond to the substrate surfaces. Due to the low temperatures and absence of other chemical reactions, thermally vulnerable materials can be deposited without significant material degradation. For the alloy component, Nickel has been selected due to its high hardness and wear resistance. Molybdenum-disulfide (MoS_2) and Boron Nitride (BN) have been employed as the lubricants because of their excellent solid lubricating properties. The developed coatings were examined for the distribution of lubricant and presence of porosity using microscopy. Furthermore, coatings with the most homogeneous lubricant distributions were analyzed for hardness,

bond-strength, and fretting wear. Based on the above analysis, it was concluded that cold spray process can be used for the development of Ni-BN composite coatings which possess better hardness and comparable bond strength relative to pure Ni coatings.

**Self-Lubricating Coatings for Elevated Temperature Applications using
a High-Velocity-Particle-Consolidation (HVPC) Process**

Part 2: Nano-Encapsulated-Particles for Improved Coatings

A.E. Segall, I. Smid, and J. Weyant
Engineering Science and Mechanics
The Pennsylvania State University
University Park, PA 16802

and

T.J. Eden
Applied Research Laboratory
The Pennsylvania State University
University Park, PA 16802

In Response to:

Program Research Development Broad Agency Announcement Number: 04-02-
MLK

Submitted to

AFRL/MLKN
Wright-Patterson AFB, OH 45433-7801

ABSTRACT

The development of wear-resistant self-lubricating coatings has been a major topic of interest in recent years. As such, the deposition of nickel coated hexagonal boron nitride (hBN) via high velocity particle consolidation (cold spray) was investigated as a possible self-lubricating coating for surfaces prone to fretting. Although hBN is a solid lubricant with a low coefficient of friction and is able to retain its lubricious properties in high temperatures and pressures, its brittle nature makes it a poor candidate for cold spray processes. Given this limitation, encapsulation of hBN particles with a ductile medium, such as nickel, allows for the particle deformation needed to create metallurgical bonds for cold spray coatings.

Using HVPC, nickel coatings ranging from 10-15 μ m were successfully deposited onto 10 μ m hBN powder through an electroless nickel deposition procedure. In addition, the composite powder was effectively deposited onto Ti-6Al-4V substrates through cold spray deposition. Incorporation of hBN particles within the coating have been characterized through microscopy (electron and optical), energy dispersive x-ray spectroscopy, micro hardness, and friction tests. Bond tests were also conducted on cold spray coatings to determine adhesion strength and self-lubricating properties. Results indicate that hBN has been uniformly distributed within the HVPC coatings resulting in a reduced friction coefficient.

TABLE OF CONTENTS

LIST OF FIGURES	viii
-----------------------	------

LIST OF TABLES	xiii
----------------------	------

MAIN BODY

Preface	xiii
---------------	------

Summary	xiv
---------------	-----

INTRODUCTION

Chapter 1 Introduction	1
------------------------------	---

1.1 Background.....	1
---------------------	---

1.2 Purpose of this study.....	2
--------------------------------	---

1.3 Thesis Outline.....	3
-------------------------	---

Chapter 2 Background	4
----------------------------	---

2.1 Fretting.....	4
-------------------	---

2.1.1 Introduction to Fretting Wear.....	4
--	---

2.1.2 Fretting in Ti-6Al-4V	7
-----------------------------------	---

2.2 Solid Lubrication	10
-----------------------------	----

2.2.1 Introduction to Solid Lubrication	10
---	----

2.2.2 Hexagonal Boron Nitride	11
-------------------------------------	----

2.3 High Velocity Particle Consolidation.....	13
---	----

2.3.1 Introduction to High Velocity Particle Consolidation.....	14
---	----

2.3.2 Cold Spray Process Parameters	15
---	----

2.3.3 Bonding of Particles to Substrate	18
---	----

2.3.4 Cold Spray Coatings Made With Ceramic Particles	20
---	----

2.4 Electroless Deposition	21
----------------------------------	----

2.4.1 Introduction to Electroless Nickel Deposition	21
---	----

2.4.2 Precursor Catalysts and Stabilizers	22
---	----

2.4.3 Reduction of Nickel.....	24
--------------------------------	----

2.4.4 Properties of Electroless Nickel Coating.....	25
---	----

METHODS, ASSUMPTIONS, & PROCEDURES

Chapter 3 Experimental Procedures.....	27
3.1 Basic Electroless Deposition Procedures.....	27
3.1.1 Introduction	27
3.1.2 Equipment.....	27
3.1.3 Equipment Cleaning Procedure	28
3.1.4 Powder Preparation	29
3.1.4.1 Milling	29
3.1.4.2 Nitric Acid Wash.....	29
3.1.5 Electroless Nickel Deposition	30
3.1.5.1 Tin Activation	30
3.1.5.2 Palladium Activation.....	31
3.1.5.3 Electroless Nickel Deposition	31
3.1.6 Characterization and Polishing Methods.....	32
3.2 Individual Experiments.....	33
3.2.1 Electroless Ni Deposition on 2-3 μm hBN	33
3.2.2 Electroless Ni Deposition on 2-3 μm hBN with Low pH.....	34
3.2.3 Electroless Ni Deposition on hBN Pellets.....	34
3.2.4 Electroless Ni Deposition on Admixed Ni hBN Pellets	35
3.2.5 Electroless Ni Deposition on 20-30 μm hBN	36
3.2.6 Cold Electroless Ni Deposition on 20-30 μm hBN	37
3.2.7 Ni coating 20-30 μm hBN without Pd Activation.....	37
3.2.8 Electroless Ni Deposition on Milled 20-30 μm hBN	37
3.2.9 Multiple Electroless Ni Depositions on Milled 20-30 μm hBN.....	38
3.2.10 Ni Deposition on Milled 20-30 μm hBN - Increased Solution to Powder Ratio	39
3.2.11 Large Ni Deposition on 20-30 μm hBN - Increased Solution to Powder Ratio	39
3.2.12 Ni Coating 20-30 μm hBN using Concentrated Electroless Solution	40
3.2.13 Up-scaled Ni coating 20-30 μm hBN using Concentrated Ni Solution	41
3.2.14 Up-scaled Ni coating 10 μm hBN with Concentrated Ni Solution	42
3.3 Preparation for Cold Spraying	43
3.4 Feedstock for Cold Spraying	44
3.5 Cold Spray Procedure	45
3.5.1 Cold Spray Equipment	45
3.5.2 Process Parameters	49
3.6 Characterization of Cold Spray Coatings	51
3.6.1 Mass, Thickness, Optical and SEM-EDS.....	51

3.6.2 Bond Testing	51
3.6.3 Friction Testing	52
3.6.4 Micro Hardness of Cold Spray Coatings.....	54

RESULTS AND DISCUSSION

Chapter 4 Results and Analysis	55
4.1 Electroless Nickel Deposition.....	55
4.1.1 Cleaning Flasks	55
4.1.2 Electroless Ni deposition on 2-3µm hBN.....	56
4.1.3 Electroless Ni deposition on 2-3 µm hBN with Low pH	58
4.1.4 Electroless Ni Deposition on hBN and Ni + hBN Pellets	60
4.1.5 Electroless Ni Deposition on 20-30 µm hBN.....	61
4.1.6 Cold Electroless Ni Deposition on 20-30 µm hBN	64
4.1.7 Ni coating 20-30 µm hBN without Pd activation.....	65
4.1.8 Electroless Ni Deposition on Milled 20 µm hBN	66
4.1.9 Multiple Electroless Ni Depositions on milled 20-30 µm hBN	67
4.1.10 Ni Deposition on Milled 20 µm hBN – Increased Solution to Powder Ratio	70
4.1.11 Large Ni Deposition on 20-30 µm hBN – Increased Solution to Powder Ratio	72
4.1.12 Concentrated Electroless Solution.....	73
4.1.13 Up-scaled Ni coating 20-30µm hBN using Concentrated Ni Solution	75
4.1.14 Up-scaled Ni coating 10µm hBN with concentrated Ni Solution	77
4.2 Powders for Cold Spray.....	79
4.2.1 Pure and Milled Nickel Powder	79
4.2.2 Nickel Coated hBN(20-30µm) admixed with Pure Nickel and 10µm hBN	82
4.3 Characterization of Cold Spray Coatings	84
4.3.1 Thick Nickel Coated 10µm hBN.....	85
4.3.2 Pure Nickel and Milled Nickel Coatings.....	94
4.3.3 30 vol% Ni coated hBN (20-30µm) admixed with Pure Ni	98
4.3.4 50 vol% Ni coated hBN (20-30µm) admixed with Pure Ni	99
4.3.5 Bond Testing	100
4.4 Friction Testing.....	104
4.5 Microhardness of Cold Spray Coatings.....	107

CONCLUSIONS

Chapter 5 Conclusion and Future Recommendation	109
5.1 Summary.....	109
5.2 Conclusions.....	110
5.3 Future Recommendations	113
Bibliography	114
Appendix A Images Ni coated hBN Powder	124
Appendix B Images of Cold Spray Coatings	126

LIST OF FIGURES

Figure 2-1: Evolution of damage as a function of the stabilized sliding condition [13].....	5
Figure 2-2: Scheme of a metallographic section of a fretting scar [14].....	6
Figure 2-3: Creation and evolution of the third body debris through the contact interface [14].....	7
Figure 2-4: (a) Image of actual dovetail joint and (b) illustration of a dovetail joint showing where cracking usually occurs [19].....	9
Figure 2-5: Comparison of coefficients of friction between solid lubricant powders [2]	12
Figure 2-6: Spray temperature versus spray velocity[50].....	14
Figure 2-7: Effect of particle size, powder material, and carrier gas on particle impact velocity [81].....	17
Figure 2-8: A two step catalyst coating process for electroless Ni deposition	23
Figure 2-9: Variation in Ni recovery and coating efficiency with respect to stabilizer amount[110]	24
Figure 2-10: Variation of Ni recovery and coating efficiencies with bath temperature [110].....	25
Figure 3-1: Cold spray system within the acoustic room	45
Figure 3-2: Cold spray system schematic	46
Figure 3-3: Data acquisition and control system	48
Figure 3-4: DeLaval type nozzle mounted on the robotic arm	49
Figure 3-5: Reciprocating test – schematic diagram [124].....	53
Figure 4-2: EDS scan of 2-3 μm hBN (a) before Ni deposition and (b) after being exposed to a Ni deposition.....	58
Figure 4-3: Rate of Ni deposition on pressed 2-3 μm hBN and 2-3 μm hBN/3-5 μm Ni pellets	61

Figure 4-4: (a) Optical image and (b) SEM image of Ni coated 20 μ m hBN cross section (1000x)	62
Figure 4-5: High magnification image of Ni nucleations on hBN at (a) 10,000x and (b) 50,000x	63
Figure 4-6: EDS scan of Ni agglomerate	64
Figure 4-7: Optical image of 20 μ m hBN after being exposed to a Ni deposition at a reduced temperature	65
Figure 4-8: Image showing the effect the Pd activation.....	66
Figure 4-9: Ni deposited on milled 20 μ m hBN	67
Figure 4-10: Milled 20 μ m hBN after being deposited with Ni for an extended period of time.....	68
Figure 4-11: Optical image of milled 20 μ m hBN coated with Ni twice.....	69
Figure 4-12: Optical image of milled 20 μ m hBN coated with Ni three times.....	70
Figure 4-13: Milled hBN which received a thick Ni coating during a deposition with an increased solution to powder ratio	71
Figure 4-14: Milled hBN which did not receive a thick Ni coating during the same increased solution to powder ratio deposition	72
Figure 4-15: Ni coating on hBN using 3g of powder and 4000 ml of electroless Ni solution	73
Figure 4-16: Ni deposited onto 20-30 μ m hBN using 500 ml of concentrated Ni solution and 1 g of 20-30 μ m hBN.	74
Figure 4-17: Ni coated hBN using 6g of 20-30 μ m hBN with 3000ml of concentrated Ni solution viewed at 500X magnification	76
4-18: Ni coated hBN using 6g of 20-30 μ m hBN with 3000ml of concentrated Ni solution viewed at 1000X magnification.....	76
Figure 4-19: Ni coated 10 μ m hBN using 0.1g of hBN with 3000 ml of concentrated Ni solution viewed at 100x.....	78
Figure 4-20: Ni coated 10 μ m hBN using 0.1g of hBN with 3000 ml of concentrated Ni solution viewed at 1000x.....	79

Figure 4-21: SEM image of pure 32 μ m electrolytic Ni supplied from Consolidated Astronautics	80
4-22: EDS scan of pure 32 μ m electrolytic Ni supplied from Consolidated Astronautics	80
Figure 4-23: Milled Ni powder used for cold spraying	81
Figure 4-24: EDS scan of milled Ni powder used for cold spraying.....	82
Figure 4-25: Ni coated hBN (20-30 μ m) admixed with pure Ni (50 vol%)	83
4-26: Ni Coated hBN (20-30 μ m) admixed with pure Ni (30 vol%).....	83
Figure 4-27: 10 μ m hBN fully coated with Ni.....	84
Figure 4-28: (a) Optical image and (b) SEM image of coatings consisting of Ni coated 10 μ m hBN sprayed with 500°C N ₂	86
Figure 4-29: EDS plot of the Ni coated 10 μ m hBN cold spray coating sprayed with N ₂	87
Figure 4-30: (a) Optical image and (b) SEM image of coatings consisting of Ni coated 10 μ m hBN sprayed with 188°C He and a 20 mm/sec traverse rate	89
Figure 4-31: EDS plot of Ni coated 10 μ m hBN cold spray coating sprayed with He at 188°C.....	90
Figure 4-32: (a) Optical image and (b) SEM image of coatings consisting of Ni coated 10 μ m hBN sprayed with 188°C He and a 50 mm/sec traverse rate	91
Figure 4-33: EDS plot of Ni coated 10 μ m hBN cold spray coating sprayed with He at 188°C with a 50 mm/sec traverse rate.....	92
Figure 4-34: (a) Optical image and (b) SEM image of coatings consisting of Ni coated 10 μ m hBN sprayed with 24°C He.....	93
Figure 4-35: EDS plot of Ni coated 10 μ m hBN cold spray coating sprayed with He at 24°C.....	94
Figure 4-37: (a) Optical and (b) SEM image of pure Ni cold spray coatings.....	95
Figure 4-38: EDS plot of the pure Ni cold spray coating	96
Figure 4-39: (a) Optical and (b) SEM image of milled Ni cold spray coating	97
Figure 4-40: EDS plot of the milled Ni cold spray coating	98

Figure 4-41: Optical images of 30 vol% Ni – hBN admixed with Ni and sprayed with (a) N ₂ and (b) He	99
Figure 4-42: Optical image of 50 vol% Ni – hBN admixed with Ni and sprayed with (a) N ₂ and (b) He	100
Figure 4-43: Fractured surface of HYSOL epoxy as a result of bond testing	102
Figure 4-44: Fractured surface of the pure Ni cold spray coating as a result of bond testing.....	102
Figure 4-45: Fractured surface of the milled Ni cold spray coating as a result of bond testing.....	103
Figure 4-46: Fractured surface of the thick Ni coated 10μm hBN sprayed with 500°C N ₂ cold spray coating as a result of bond testing.....	103
Figure 4-47: Fractured surface of the thick Ni coated 10μm hBN sprayed with 24°C He cold spray coating as a result of bond testing	104
Figure 4-48: (a) Substrate, (b) top view, and (c) bottom view of thick Ni coated 10μm hBN bond test coating that detached.....	104
Figure 4-49: Friction coefficient results for cold spray coatings.....	107
Figure A-1: Thin Ni coated 20-30μm hBN	124
Figure A-2: Thin Ni coated 20-30μm hBN	124
Figure A-3: As received 75μm Ni coated hBN from Federal Technologies Group (not used in this study).....	125
Figure A-4: Thick Ni coated 10μm hBN viewed at 100x.....	125
Figure A-5: Thick Ni coated 10μm hBN viewed at 500x.....	125
Figure B-1: Thick Ni coated hBN cold spray coating produced using 500°C N ₂ as a process gas	126
Figure B-2: Thick Ni coated hBN cold spray coating produced using 188°C He as a process gas and a 20 mm/sec traverse rate.....	126
Figure B-3: Thick Ni coated hBN cold spray coating produced using 188°C He as a process gas and a 50 mm/sec traverse rate.....	127
Figure B-4: Thick Ni coated hBN cold spray coating produced using 24°C He as a process gas	127

Figure B-5: Pure Ni cold spray coating using 500°C N₂ as a process gas 128

Figure B-6: Milled Ni cold spray coating using 500°C N₂ as a process gas..... 128

LIST OF TABLES

Table 3-1: Cold spray process parameters	50
Table 4-2: Thickness of cold spray coatings.....	85
Table 4-3: Adhesion strength of cold spray coatings.....	100
Table 4-4: Friction coefficient results for cold spray coatings	106
Table 4-5: Vickers hardness of cold spray coatings.....	108
Table 5-1: Friction coefficient and adhesion test results for cold spray coatings.....	112

PREFACE

This report represents the second component of research conducted over a number of years by a multiple graduate students and supervising faculty at the Pennsylvania State University. Accordingly, the main body of this report is the Masters thesis of Jens Weyant who studied the further development of and partial optimization of composite, self-lubricating coatings for the application to Ti dovetail joints commonly encountered in aircraft engines. As detailed in the thesis, the research has clearly established the foundation for a new system of self-lubricating coatings that has the potential for both reducing friction, as well as the relatively high costs of fretting damage and the schedule-based maintenance required to avoid catastrophic failures in the engine.

SUMMARY

Clearly, fretting and all associated wear is detrimental for the performance and fatigue life of turbine dovetail joints. However, because of the temperature limitations of most solid film lubricants (and the relatively high temperatures experienced by the dovetail joints), currently used coatings and MoS₂ lubricants do not adequately protect against fretting damage. On the other hand, traditional higher-temperature coating methods are not useful due to the just mentioned thermal vulnerability of solid lubricants. Given these important needs and significant difficulties, Ni-based self-lubricating coatings using hexagonal Boron Nitride (hBN) have been developed and further optimized using a lower temperature coating process commonly known as cold-spray or High Velocity Particle Consolidation (HVPC).

As detailed in Part 1 of this report, HVPC can indeed be used to develop self-lubricating coatings. However, the earlier research also indicated that increasing the thickness of any Ni coating on the lubricants would improve the overall coating qualities in order to facilitate plastic particle/substrate deformation to create metallurgical bonds; brittle materials such as hBN fracture upon impact with the substrate, thus severely inhibiting deposition. Since there are limits on the size of the particles that can be used to create such coatings, the best approach is to coat smaller lubricant particles with thicker Ni layers. Accordingly, the portion of the study detailed in this report (Part 2) investigated the use of electroless nickel deposition to encapsulate increasingly smaller hBN particles

in order to create a feedstock for HVPC capable of bonding to the substrate for self-lubricating coatings. Such a strategy was based on the fact that hBN is a solid lubricant which is able to retain its lubricity at high temperatures and pressures making it ideal for applications in dovetail joints.

As shown by the research, encapsulation of the hBN, through an electroless nickel process was able to provide the necessary ductile medium for bonding; for the first time, hBN has been uniformly incorporated into a nickel matrix using HVPC deposition. Tests showed that the presence of hBN distributed uniformly within the cold spray coatings reduced the coefficient of friction and increased the micro-hardness of the resulting HVPC coatings. However, a critical nickel thickness must be obtained before adequate particle-substrate bonding occurs. In addition, there is a window of acceptable velocities for reasonable bonding; particles traveling below the critical velocity do not adhere to the substrate while speeds above a maximum velocity tend to fracture excessively upon impact. Finally (and interestingly), coatings fabricated through a combination of fractured and intact particles showed an improved size distribution and uniformity of the hBN within the coating. Results also indicate that the coefficient of friction may be reduced even further if the size of the original core hBN particle is decreased. This should produce an even more homogenous distribution of hBN within the coating. Another benefit of using smaller core hBN particles, while maintaining particle size, would be that higher deposition velocities could be used before particle fracture occurs.

Chapter 1

Introduction

1.1 Background

The useful life of mating surfaces in motion can be increased by applying lubrication. In some cases, conventional methods of lubrication do not work because temperatures and/or pressures are too great. In recent years, the creation of wear-resistant self-lubricating coatings has been a major topic of interest, especially for applications in high performance machines where damages occur as a result of fretting. Application of lubricant coatings is one method used to prevent fretting

Lubricants are classified as being either as liquid (aqueous solutions and oils), semi solid (grease), or solid (graphite, molybdenum disulfide, hexagonal boron nitride). For high temperature and high pressure applications, liquid and semi solid lubricants fail unlike solid lubricants which are able to retain their lubricious properties in such environments [1,2].

Conventional methods of incorporating solid lubricants into self lubricating coatings include sputtering and physical vapor deposition. A disadvantage of these coatings is that they have low wear resistance and require constant replenishment [3,4].

High Velocity Particle Consolidation, or Cold Spray, is a relatively new high rate deposition method. Solid particles, usually 1-50 μm , are sprayed using helium (He) and/or nitrogen (N_2) as process gases. When particles impact the substrate they deform

and produce metallurgical bonds, which in turn create cold spray coatings [5]. To obtain the deformation needed for bonding, particle velocities are in the range of 300-1200 m/s [6].

1.2 Purpose of this study

The purpose of this study is to investigate the self lubricating properties of nickel – hexagonal boron nitride (hBN) composite coatings created through Cold Spray deposition. The correct combination of wear resistance and hBN lubricant properties provide for a damage resistant lubricant coating. By creating a coating with uniformly distributed hBN, lubricant properties can be observed throughout the life of the coating. Cold Spray has been adopted as the deposition method because of cost effectiveness, as well as minimal variation in feedstock and substrate microstructures due to the low temperatures used.

A major challenge of this project was to successfully form bonds between hBN particles and the substrate. Since hBN is a ceramic, it fractures upon impact instead of deforming and bonding when being cold sprayed. To provide the necessary ductile medium for cold spraying, an electroless nickel deposition procedure was explored. The goal was to deposit a thick enough nickel coating on hBN powder to allow for adhesion when cold spraying, while maintaining the lubricant properties of hBN.

1.3 Thesis Outline

A literature survey discussing fretting, solid lubrication, electroless nickel deposition, and cold spraying is presented in Chapter 2. Chapter 3 describes the experimental procedures used for the nickel and Cold Spray deposition, and chapter 4 reports and discusses experimental results. Chapter 5 places special emphasis on some of the mechanics involved with this project, and chapter 6 summarizes findings, discusses conclusions, and lists future recommendations.

Chapter 2

Background

2.1 Fretting

2.1.1 Introduction to Fretting Wear

Wear is defined as “damage to a solid surface generally involving the progressive loss of material due to relative motion between that surface and a contacting substance or surface” by the American Society of Testing and Materials (ASTM). Fretting wear usually occurs between vibrating surfaces of fixed mechanical joints, stacks of objects, and electrical connections [7]. Fretting is a damaging phenomenon caused by small scale oscillatory motions and is responsible for surface wear and crack propagation, a leading cause of device failure [8,9]. These small vibrations produce shearing between the crystal planes and produce displacements in the material surface. This results in wear, corrosion, and multi-site crack nucleation [10-12]. There are three basic wear regimes which are responsible for fretting damage: partial slip, partial and gross slip, and gross slip. When the oscillatory motions of the surfaces in contact are small in amplitude partial slip occurs. Partial slip is responsible for crack nucleation. When the oscillatory amplitude is sufficient to initiate gross slip, an increase in friction between the metallic surfaces often brings the surface displacement back into the partial slip regime. This combined effect results in an adhesion between the mating surfaces causing surface wear

and crack nucleation, and is the most detrimental to fatigue life. When gross slip regime is maintained the oscillatory amplitude is above a critical value, resulting in surface wear [13]. Figure 2–1 illustrates the fretting conditions associated with partial and gross slip.

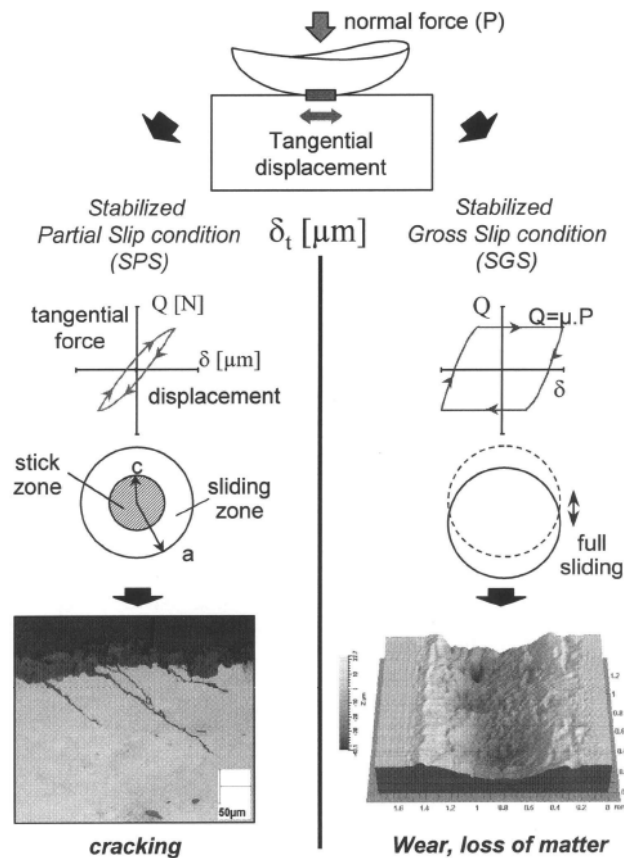


Figure 2–1: Evolution of damage as a function of the stabilized sliding condition [13]

The first stage of fretting wear begins with slip. In ductile metals, the slip bands created from surface displacements lead to crack formation and/or oxide debris. Research has shown that within the first few cycles of fretting on ductile materials, a layer is formed on the surface which differs from the bulk material. This change of surface is generally known as a tribologically transformed surface (TTS). Depending on the material and atmosphere, an oxide layer may be formed on the surface of the TTS,

and some instances there is a plastically deformed region directly below the TTS. Figure 2-2 shows an idealization of the TTS region just described.

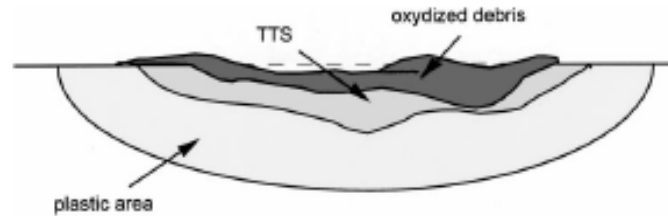


Figure 2-2: Scheme of a metallographic section of a fretting scar [14]

The formation of the TTS is the second step in the evolution of fretting wear. Once the TTS is formed, surface debris is created which may have a different structure than the bulk material. Due to the small stroke length of the vibrating surfaces, usually less than hundreds of micrometers, the particles remain between the two surfaces. The forming of debris is a phenomenon known as “third body behavior” and is illustrated in figure 2-3 [14]. The third bodies act as an abrasive and accelerate crack formation, increase oxidative wear, and increase fatigue [15].

Major methods used to increase a materials fretting resistance include inducing residual compressive stress, decreasing the coefficient of friction, increasing the surface hardness, altering surface chemistry, and increasing surface roughness [12].

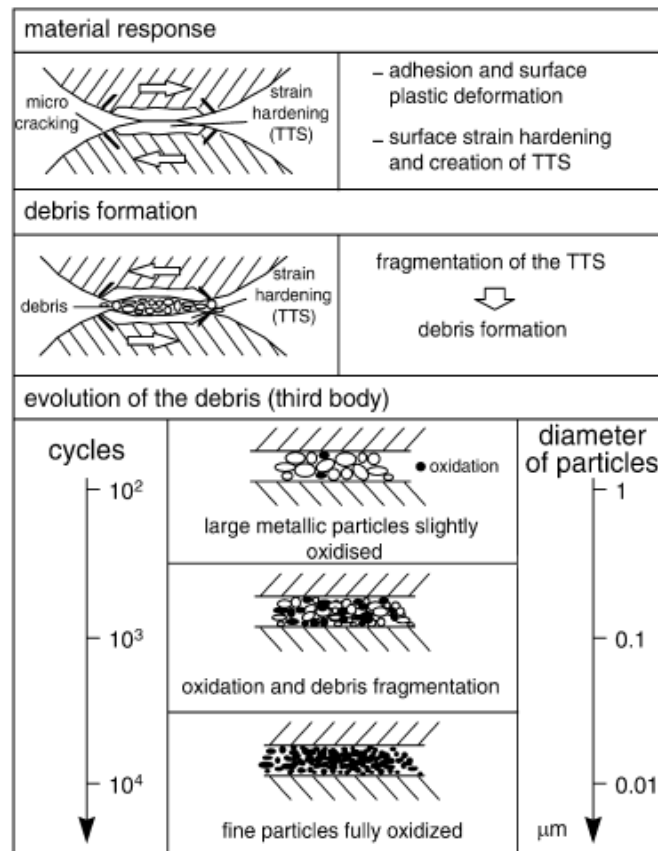


Figure 2-3: Creation and evolution of the third body debris through the contact interface [14]

2.1.2 Fretting in Ti-6Al-4V

Failures of dovetail joints in jet turbine engines are responsible for roughly one sixth of service mishaps. Fretting damage occurs because the joints are exposed to large centrifugal forces as well as tangential forces caused by blade vibrations. Reduction of fretting damage to the dovetail joint of jet turbine engines has been a highly studied topic for several years [16].

Different geometries of jet turbine dovetails show signs of fretting damage in various areas. Most often, fretting occurs on the flat-on-flat contact of the dovetail rather than on the large radii, as shown in figure 2-4. Studies show that fretting on flat-on-flat surfaces is less severe than cylindrical-on-flat surfaces [16]. Crack nucleation often occurs near the edge of the areas in contact which contain the highest stress levels [17-22]. Although areas of fretting may differ with dovetail geometry there is little difference in the lifetime of the joint [23].

Dovetail joints in jet turbine engines are often made from Ti-6Al-4V and other Ti alloys because Ti alloys have a lower density and a higher specific strength than other metals [24]. The reactive nature of Ti and its alloys make them susceptible to fretting damage, especially at elevated temperatures [25]. The coefficient of friction has been observed to increase rapidly within the first few fretting cycles due to the initiation of multiple crack nucleations, although only a few propagate [16, 26].

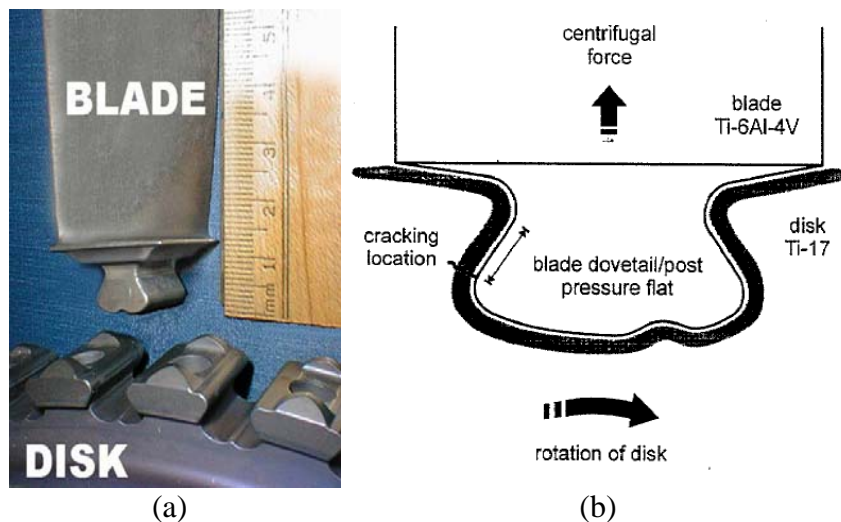


Figure 2-4: (a) Image of actual dovetail joint and (b) illustration of a dovetail joint showing where cracking usually occurs [19].

Four different mechanisms have been identified which improve fretting wear and fretting fatigue resistance in Ti alloys. Methods include inducing compressive residual stresses, decreasing the coefficient of friction, augmenting the hardness, and increasing the surface roughness [27]. Experiments comparing the effectiveness of fretting reduction methods conclude that inducing compressive stress via shot peening is one of the most effective [28,29]. Coatings such as TiCN, CrN+MoS₂, Cu-Al, and Ag+ with thicknesses ranging from 0.5 to 45 microns have previously been analyzed. The quality of the coatings was analyzed through friction, fretting fatigue, and a combination of friction and fretting fatigue testing. In the case of the CrN+MoS₂ coating, the coefficient of friction was greatly reduced due to a self lubricating effect. In this particular experiment the sample with the self lubricating coating did not display better fretting fatigue life than the original Ti-6Al-4V sample because the coating could not withstand the fretting load. On the other hand, the Cu-Al coating did improve fretting fatigue life of the titanium alloy. The Cu-Al coating consisted of many “hills” and “valleys”. Throughout the load cycles the “hills” produced third body particles that eventually filled in the “valleys”. The end result was a smoother surface with a lower coefficient of friction. This experiment demonstrates that by reducing the coefficient of friction, the fretting fatigue life will be extended provided that the coating has good wear resistance [30].

Experimental evidence of fretting wear in coatings made of two or more materials show a significant increase in friction. Such coatings were produced by physical vapor deposition and utilized Ti combined with Mo, NbN, or TaN. Ball on disc tests were used

to measure friction and sliding wear of the coatings. Results showed that friction of the coatings is initially low, but increased greatly with the contact surface area [31].

2.2 Solid Lubrication

2.2.1 Introduction to Solid Lubrication

Lubricants are often applied between surfaces in motion to prevent damage. Lubricants may be classified in three different categories including liquid, semi-solid, and solid lubricants. Liquid lubricants consist of aqueous solutions and viscous oils. Lubricants with a grease like consistency fall into the category of semi-solid lubricants. Other lubricants such as graphite, molybdenum disulfide (MoS_2), and hexagonal boron nitride (hBN) are considered solid lubricants. Solid lubricants may be used individually, as an additive to liquid lubricants, or along with resins or metals to make self lubricating coatings [1,2]. Conventional methods of making lubricant coating using solid lubricants include sputtering and physical vapor deposition. A disadvantage of conventional solid lubricating coatings is that they have a low wear resistance and require constant replenishment. Attempts of creating a self lubricating coating through sputtering and physical vapor deposition using MoS_2 in metal matrices show promise of friction reduction with improved wear resistance [32-39].

Solid lubricants are most suitable for high pressure and/or high temperature systems because their crystal structure allows the solid material to retain lubricity in such environments. Lubricants such as hBN and graphite have a hexagonal crystal structure

which forms covalent bonds between molecules making a lamellar crystal. These layers are held together by Van der Waals forces. Shearing is easy between the crystalline layers due to the weak Van der Waals forces [40-42].

2.2.2 Hexagonal Boron Nitride

There are two types of boron nitride: cubic and hexagonal. Cubic boron nitride is very hard, abrasive, and diamond like. Hexagonal boron nitride (hBN) is a white ceramic material that provides lubricious properties similar to other solid lubricants with some additional advantages; hBN is able to retain its lubricious properties in high temperatures and at high pressures. hBN is inert to most chemicals, making it environmentally friendly as well [43].

Hexagonal boron nitride has been proven to be an excellent lubricant. Plasma sprayed coatings made with hBN are currently in use in jet turbine engine seals [44]. They exhibit similar lubricious properties as graphite as well as the adherence properties of molybdenum disulfide. An experiment was conducted to compare the coefficient of friction, weld point, and scar diameter between several common solid lubricants including two different grades of graphite, molybdenum disulfide, antimony oxide, Teflon®, and hBN. Figure 2–5 shows the coefficients of friction of the different powders [2].

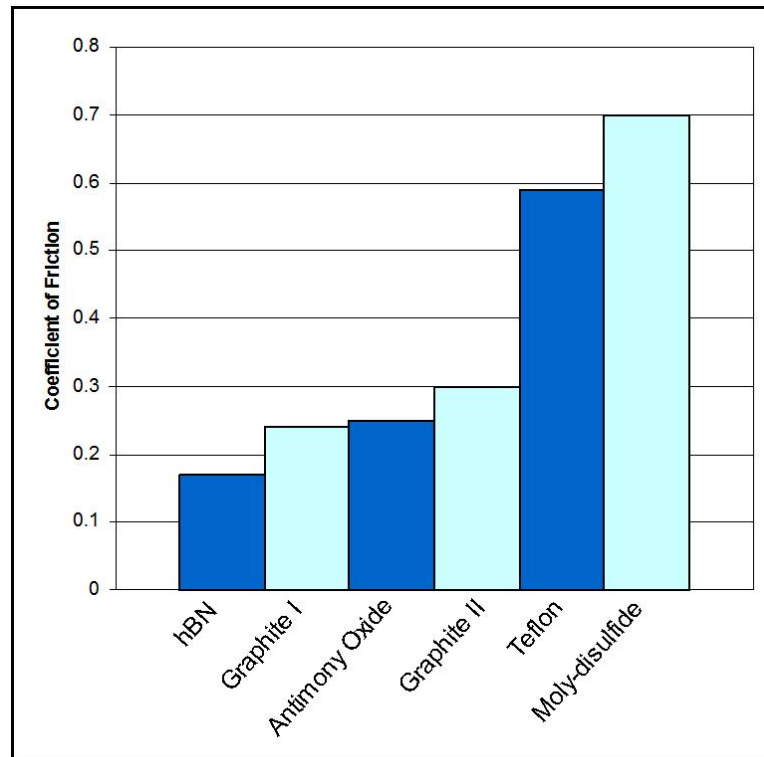


Figure 2–5: Comparison of coefficients of friction between solid lubricant powders [2]

It should be noted that hBN does not occur naturally. Common methods of producing hBN use combinations boric acid or boric oxide, urea or urea derivatives, and ammonia at temperatures ranging from 800°C to 2000°C [2].

2.3 High Velocity Particle Consolidation

2.3.1 Introduction to High Velocity Particle Consolidation

High Velocity Particle Consolidation, or Cold Spray, is a high rate deposition method. Solid particles (usually 1-50 μm) are sprayed with a process gas (helium (He), nitrogen (N_2), or a mixture of both), so that upon impact they plastically deform on the

substrate to produce a coating [5]. To obtain the deformation needed for bonding, particle velocities are in the range of 300-1200 m/s [6]. In the mid-1980s, experiments were conducted by several different groups which used tracer particles in supersonic wind tunnel tests. It was observed that at a critical velocity, particles bonded to the substrate surfaces rather than eroding the surface. Russian scientists from the Siberian Branch of the Institute of Theoretical and Applied Mechanics – Russian Academy of Science developed this occurrence into a deposition process. Successful depositions have since been done on various substrates using a variety of elemental powders, metal alloys, polymers, and composites [45-47]. Some of the most common materials deposited are ductile powders such as copper, aluminum, nickel, and nickel alloys [48].

Thermal spray processes such as plasma and arc spraying use high temperatures that melt the particles during deposition. This uses a significant amount of energy and is detrimental to heat sensitive coatings and substrates. Cold Spray is advantageous because it does not use temperatures above the softening or melting point of the material being deposited. The particles are further cooled during travel to the substrate ensuring that the particles are in the solid state when interacting with the substrate surface [49,50]. Figure 2-6 compares cold spray parameters with other thermal spray parameters.

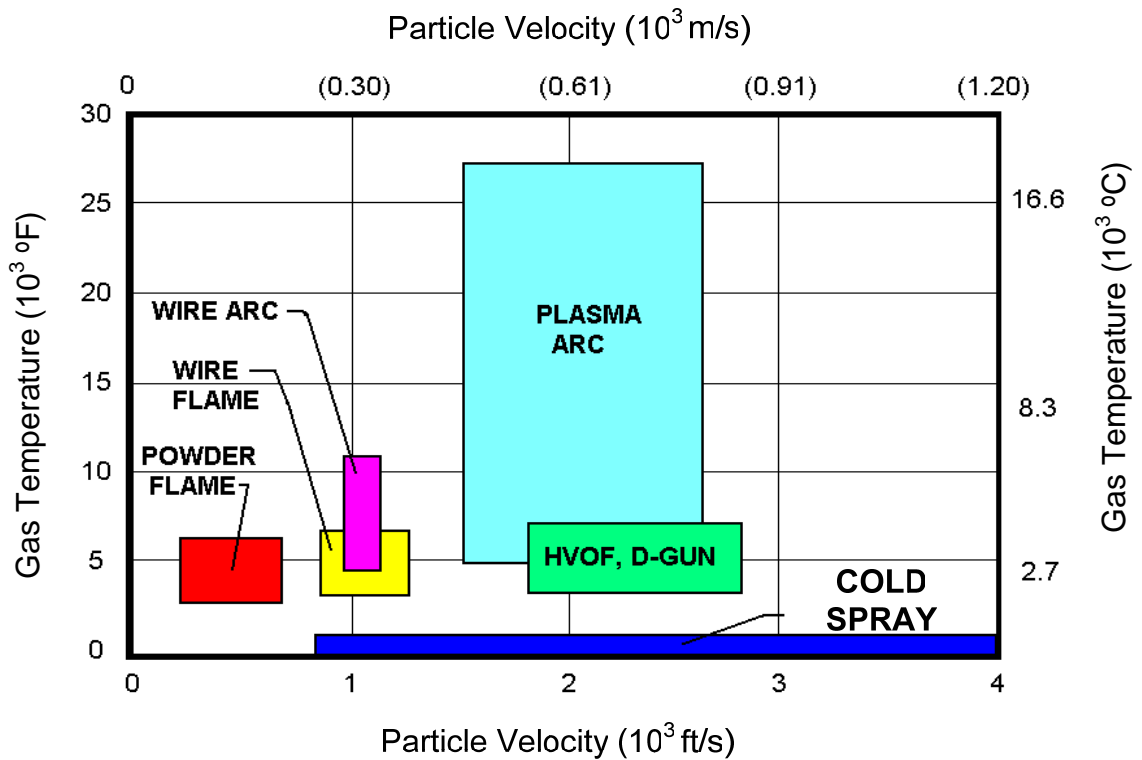


Figure 2-6: Spray temperature versus spray velocity[50]

Low temperature deposition induces minimal microstructural changes to the particles or the substrate. Experiments show that even powders on the nanoscale retain their microstructure after being cold sprayed [51-55]. Low temperatures also reduce in-flight oxidation resulting in higher quality coatings. Residual stresses are also lowered due to low differences in thermal energy between the particles and substrate [56]. Other ductile material such as Ni and solder which are conventionally electrochemically deposited can be cold sprayed eliminating the use of environmentally unsafe chemicals. Another advantage of cold spraying is that since deposited particles are in the solid phase, they impose potentially beneficial compressive stressing in the substrate through a peening effect [57-62].

2.3.2 Cold Spray Process Parameters

Cold spraying relies on a very specific set of parameters [64]. One of the most important parameters is the particle velocity. Particle velocities can fall into three regions. In the first region, particles are traveling at a velocity sufficiently high that immediately upon impact the particles adhere (v_{cr1}). Multiple experiments and models confirm that a critical velocity must be reached for particle-substrate bonding [65-70]. When the particle velocity decreases slightly below the critical velocity, the particles are traveling in the second possible region. Here the particles are still able to be deposited, but only after a certain amount of time known as the delay or induction time. The period needed for initial particles to roughen and clean the surface is known as the delay time. With the adhesion of the first particles comes a prompt adhesion of many more particles. The sudden continuous deposition is an “avalanche type process”. When the particle velocity is decreased further, the delay time increases. Due to the particles lacking sufficient kinetic energy to adhere immediately, the surface needs to be more aggressively treated, resulting in the longer delay time and less particle deformation [71]. The third possible region of particle velocity is when the particle is traveling too slowly to provide the needed kinetic energy to deform the particles on the substrate surface (v_{cr2}). Regardless of deposition time a coating will not be created [49,72]. When particles are traveling slower than v_{cr2} the substrate surface is eroded rather than coated. The ideal velocity is somewhere between v_{cr1} and v_{cr2} , and is known as the critical velocity.

High velocities of 300-1200 m/s are needed to create coatings. Usually increasing the inlet pressure of the process gas is the easiest method of increasing particle velocity. The

initial temperature of the process gas can also be raised to further increase particle velocity [73]. Higher gas pressure and temperatures results in increased particle velocity by reducing the gas density, in turn reducing drag. It has been shown that the particle density and temperature are the most important factors in reaching the critical velocity [65]. The type of nozzle used on the cold spray gun also affects the particle velocity. Typically converging/diverging or DeLaval nozzles are used. Acceleration of particles is hindered by friction along the straight section of the nozzle [74]. Particles are forced through the converging section of the nozzle and upon entrance into the divergence section of the nozzle, they accelerate rapidly due to gas expansion [58,75].

There are basically two different designs for cold spray nozzles, utilizing either circular or rectangular cross sections. Nozzles with circular cross sections are advantageous because they provide a more symmetric flow of particles with similar velocities. Nozzles with rectangular cross sections are also advantageous in some instances because they can provide a spray pattern with a very narrow depth and large width. This spray pattern can be used to coat large areas by positioning the spray nozzle so that the wide cross section is perpendicular to the direction of nozzle travel. Likewise, the rectangular nozzle can be used to coat thin lines by moving the thin cross section perpendicular to the substrate. To gain further velocity, the process gas may be changed and/or heated.

The density and heat transfer of the gas is another important factor to consider when cold spraying [58,76]. Stagnation regions close to the substrate may sometimes slow particle velocity considerably, especially when depositing nanoscale particles [77]. This must be compensated for in the nozzle design so that the particles have sufficient

kinetic energy when they reach the substrate [78]. Nozzle dimensions may vary for different powders in order to obtain maximum particle velocity and in turn increase deposition efficiency [23,79,80].

Another way to increase particle velocity is to use a mixture of He and N₂ or pure He as a process gas. Helium increases particle velocity because it has a higher specific heat and lower mass density which results in lower drag during deposition [66]. Previous experiments have been conducted using various process gases to show a relation to impact velocity versus powder size [81]. Results are plotted in Figure 2-7 .

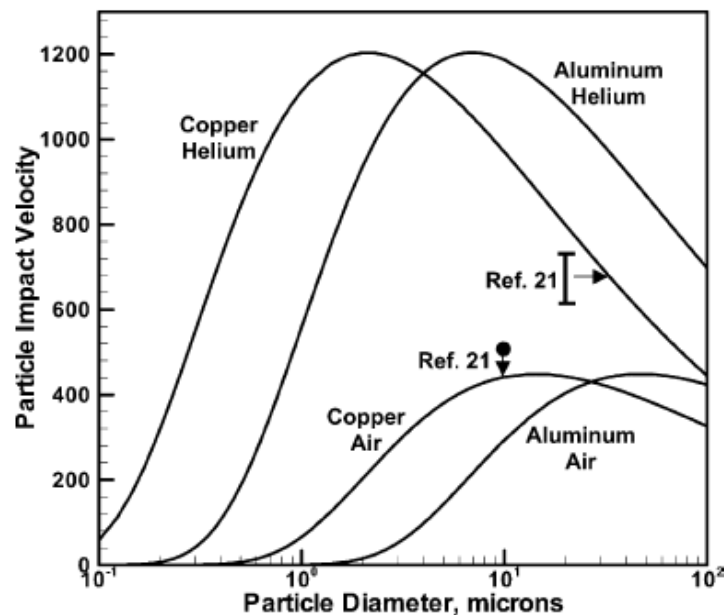


Figure 2-7: Effect of particle size, powder material, and carrier gas on particle impact velocity [81].

Particle size is another important parameter to consider when cold spraying. Powders which are too large may not be able to reach the critical velocity for particle-substrate adhesion. Powders which are too fine pose a threat of explosion and handling problems [66].

2.3.3 Bonding of Particles to Substrate

The physical process of particle deformation and bonding during cold spray is still not well understood. The leading theory of cold spray bonding proposes that during impact, the particles are in the solid state and endure plastic deformation allowing the inner part of the particle to come into intimate contact with the substrate surface [82]. This disrupts any oxide film on the particles which promotes bonding. Although any oxide film on the particles being deposited is disrupted during impaction, the final coating produced may contain oxides and pores affecting the bond strength of the coating [83]. Support of this theory comes from various models and experimental findings. Models showing particle deformation upon impact have been created and take into consideration strain hardening, strain rate hardening, thermal softening, heating due to friction, plastic limit, and viscous dissipation [84]. The ability to deposit a wide range of ductile materials and the inability to deposit brittle materials without being co-deposited with a ductile powder supports this theory. Other experiments confirm that a sufficient amount of kinetic energy is needed to create a coating [85,86]. Accelerating the particles to a material specific critical velocity is necessary to obtain the needed kinetic energy. Kinetic energy is responsible for particle-substrate bonding during cold spraying. The kinetic energy needed for particle bonding is significantly less than the energy needed to melt the particles suggesting that the bonding process takes place partially, if not completely in the particle's solid state. It can be observed that when the kinetic energy increases (i.e. particle velocity increases), the depth of impaction between the particles and substrates increases as well as the bond strength [58,67,92,121].

The microstructure of cold spray coatings is largely influenced by the microstructure of the powder being sprayed, the particle size, and the angle of spraying. Materials with a low dislocation density, such as Al, produce coatings with similar microstructures to that of the original powder. Materials with a high dislocation density, like Ni and Cu, are much more prone to recrystallization. Studies show that cold sprayed Ni coatings have grain refinement and more uniform local microstructures [87]. Although the bulk of the particles deposited show similar microstructure to that of the original powder, microstructural changes have been observed at the interfaces between particles [88,63,89]. Local microstructures of the cold spray coating are strongly dependant on local stresses caused by adiabatic heating after particle impaction. Local melting may be observed and is likely due to the high velocity of the particles [90,91]. Melting of particles upon impact does not significantly raise the temperature of the cold spray coating. Thermal spray methods which use partial or full particle melts create coatings with high residual stresses because the coating quickly solidifies upon impact, resulting in a significant shrinkage of the coating [92].

Properties of the substrate material also affect the bonding of cold spray coatings. Substrates which are too ductile do not support the necessary particle deformation; particle-substrate bonding does not rely on the deformation of the substrate, but instead relies on the deformation of the particle. The presence of thick oxide layers, as can be found on some Al substrates, prohibit metal to metal contact which in turn reduces bonding [93].

Cold spray coatings typically have low porosity of less than one percent in certain cases, but may have as much as five percent porosity [94]. Post deposition treatments are

available to improve coating properties. In particular, diode lasers have been used as a means of specific heat treatment to improve micro hardness, density, and particle bond strength of cold sprayed coatings [95].

To improve the adhesion of particles the substrate surface may be grit blasted. Grit blasting is not a suitable solution for many applications such as when the substrate has thin walls, already has a coating, or if parts are made from a brittle material. Since cold sprayed particles are in the solid state when reaching the surface they may act as a surface treatment that is less aggressive than grit blasting. Surface treating with cold sprayed particles eliminates the possibility of contamination due to sand blasting [49].

2.3.4 Cold Spray Coatings Made With Ceramic Particles

Coatings have been made which utilize only ceramic particles. Due to lack of deformation upon impact deposition efficiency was typically less than 10% and only thin coatings of 2-10 μ m could be achieved. Fracturing of the particles has been observed upon impact with the substrate [96]. More successful coatings have been created by admixing ceramic powders with ductile powders [97]. Another approach used to promote bonding of ceramic particles is to coat the powder with a metal in order to allow sufficient deformation upon impact with the substrate. Coating powder is typically done by electric plating, chemical plating, and vacuum methods [98].

2.4 Electroless Deposition

2.4.1 Introduction to Electroless Nickel Deposition

Metal deposition through chemical reduction techniques have been used since the 19th century. The electroless technique did not become popular until 1945 when Brenner discovered an efficient method of depositing nickel which used hypophosphite as a reducing agent. In 1946, Gutzeit, Gorbunova, and Nikiforova also investigated electroless nickel plating [99]. Today, nickel deposition is more convenient to use since the process is simpler than other electroless plating procedures for metals such as copper, cobalt, silver, and gold. The electroless procedure is commonly used for coatings on valves, medical implants, and electrical components, as well as for corrosion and wear applications [100,101].

Electroless plating does not use an external current source, but instead relies on chemical reactions within the solution. This allows substrates of almost any shape to be coated as long as it is submersed in the plating solution. Even powders can be uniformly coated providing the powder surface is catalytic [102]. In many cases, coatings cannot be formed on dielectrics unless it is first pretreated with a catalyst. Some advantages of electroless plating include uniformity in coating, formation of coatings with unique properties, coatings on non-conductive substrates, and the relative simplicity of the overall procedure. Electroless plating does not require sophisticated equipment; only an inert deposition tank is needed along with agitation devices, heaters, filters, and required chemicals. One disadvantage of electroless deposition is the relative high cost of

chemicals, especially for the reducing agent. A second disadvantage is that the coating thickness is limited by the amount of metallic ions in the solution [103,104].

In recent years there has been increased interest in using electroless deposition methods to create wear resistant coatings, many of which incorporate particle into metallic matrices. Particles imbedded in a metal matrix have been shown to have superior mechanical and friction properties. Powders pre-coated with metals prior to fabrication of wear resistant coatings were shown to be effective [105]. Previous studies to show that the incorporation of cubic-BN particles in a nickel matrix can produce a successful wear resistant coating [106]. Other studies show that electroless procedures can be used to coat non-conducting particles such as SiC, silica, diamond, alumina, carbon fibers, and graphite [98,107-110].

2.4.2 Precursor Catalysts and Stabilizers

Dielectrics require the use of catalyst coatings to activate deposition. A two step process which uses tin chloride (SnCl_2) and then palladium chloride (PdCl_2) is commonly used [104]. Figure 2-8 illustrates how this two step process would be applied to a non-conducting powder such as hBN. First tin (Sn) ions attach to the particle's surface during sensitization. The Sn ions then allow Pd ions to attach during the Pd activation. The Pd ions act as active sites for Ni deposition. The use of extra catalysts may become very complex, time consuming, and expensive [98].

The amount of catalyst needed depends on the stability of the solution. The more stable the solution the more catalyst is needed. Unstable solutions are not desirable

because they often result in unwanted deposition on equipment. The addition of stabilizers, such as sodium citrate slows the Ni deposition process which may result in a reduction of deposition efficiency [111]. Figure 2-9 plots the relation between deposition efficiency with respect to the amount of stabilizer used. As shown by the figure there is a delicate balance between stabilizers and catalysts.

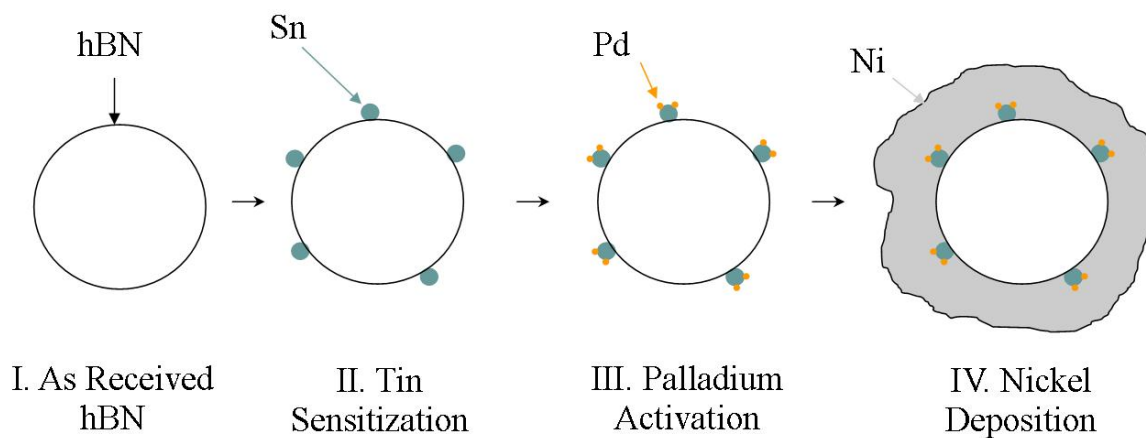


Figure 2-8: A two step catalyst coating process for electroless Ni deposition

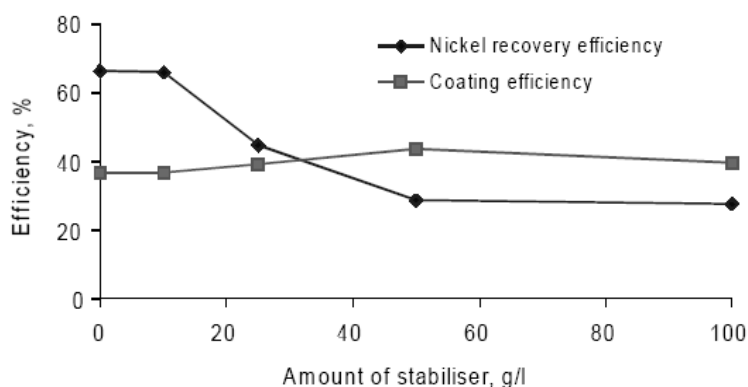


Figure 2-9: Variation in Ni recovery and coating efficiency with respect to stabilizer amount[111]

2.4.3 Reduction of Nickel

In the electroless Ni deposition process, Ni salts are reduced from an aqueous solution. The majority of reducing agents use hydrogen compounds. The most common reducing agents are sodium hypophosphite and borohydride; metallic ions are reduced when hydrogen atoms link with phosphorus. All reductions take place within the solution without the aid of an external powder source [112].

It has been found that the deposition rate of Ni increase with increasing hypophosphite concentration, pH, and temperature. Common operating temperatures are between 80-90°C without the aid of catalysts. Figure 2-10 shows a plot of deposition efficiency versus temperature of the solution. At a certain point, the deposition rate increases sharply, but at the expense of the usable Ni within the solution [111]. The deposition rate of Ni is also affected by the number of active sites on the substrate's surface. As Ni reduces onto the substrate more, active locations are produced, hence the electroless procedure is autocatalytic. The sites that result in Ni reduction also absorb hypophosphite and hydrogen ions, resulting in a phosphorous-nickel coating [99].

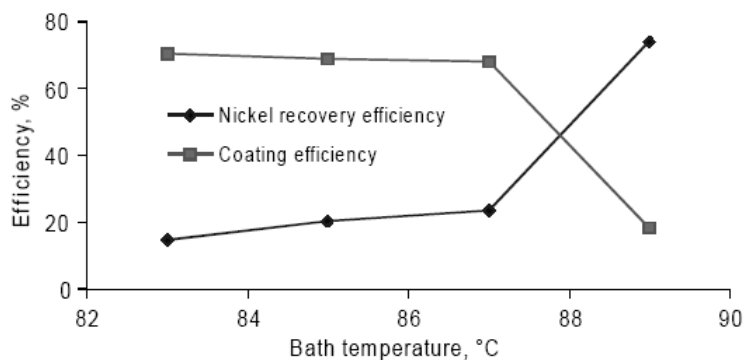


Figure 2-10: Variation of Ni recovery and coating efficiencies with bath temperature [111]

The deposition rate decreases if the concentration of reactive substances is not maintained. The solution life is the time span for which the deposition solution is useful. The solution can be used for a single plating, or it can be reused by replenishing the reactive components. Replenishing the solution reduces the overall amount of waste, but also introduces error into the deposition rate. Solution replenishment is usually reserved for large scale plating.

2.4.4 Properties of Electroless Nickel Coating

Nickel coatings produced through electroless processes have been observed to exhibit superior wear resistance. This is due to the incorporation of Ni-P alloy into the Ni coating. Further heat treatment using temperatures above 300°C have been shown to increase mechanical properties of the coating [111]. Coatings have been reported to be either crystalline, amorphous, or a mixture of both. Low phosphorous (1-5%P) content usually results in crystalline microstructures, medium phosphorous (6-9%) content results in mixed crystalline and amorphous microstructures, and high phosphorous (10-13%) content results in amorphous microstructure. The higher the phosphorous content the better corrosion resistance the coating has, but the hardness and wear resistance decrease [101].

Chapter 3

Experimental Procedures

3.1 Basic Electroless Deposition Procedures

3.1.1 Introduction

Many of the following experiments use the same basic procedure and equipment. Variables between experiments include equipment cleaning procedures, powder preparation methods, deposition time, solution temperature, powder size, powder material, solution to powder ratio, and solution concentration. For all electroless nickel deposition procedures used in this study, powders were measured to an experiment specific weight and exposed to a tin sensitization, palladium activation, and then the electroless nickel deposition.

3.1.2 Equipment

Glassware was used for all experiments. Depending on the experiment, a 500 ml beaker, 1 liter beaker, 500 ml Erlenmeyer flask, or a 4 liter Erlenmeyer flask was used as a vessel for deposition. Chemicals solutions were agitated/stirred using a 5510 Branson ultrasonic bath and/or a Barnant Mixer 10 series mechanical stirrer.

All chemicals and powder were measured separately by weighing the materials in an appropriate sized plastic weigh boat on a Mettler AE 200 electronic balance. Liquids

less than 200 ml were measured using a graduated cylinder, while liquids greater than 200 ml were measured by reading the graduations on the respective flask or beaker. The pH of Ni solutions were measured using paper EMD colorpHast pH indicator strips. Temperatures were measured with a digital thermometer and times were measured with a digital stop watch.

The powder was separated from solution by using a vacuum pump apparatus. Pall Supor® 0.2µm filter paper was used along with a glass frit. The pump for this system was a Welch 1405. Once the powder was separated from solution it was dried in a Lindberg Blue-M oven.

3.1.3 Equipment Cleaning Procedure

The flasks, beakers, and stirrers were cleaned using several different methods. Initial cleanings were done using soap with distilled water (dH₂O) followed by rinsing with acetone, dH₂O, followed by isopropanol, and again with dH₂O. Unfortunately, equipment cleaned with this procedure was found to be vulnerable to Ni deposition. To maximize the amount of Ni deposited on the desired material, a different cleaning procedure was adopted. New cleaning procedures were composed of two different standard cleaning methods. The first standard cleaning method, SC1, used a mixture of dH₂O, hydrogen peroxide, and ammonium hydroxide in a respective 5:1:1 ratio. Equipment to be cleaned was exposed to the SC1 and warmed between 70-80°C for 10 minutes. This removed organic contaminants. After the SC1 was used the flask was rinsed well with dH₂O before using the second standard clean, SC2. SC2 consists of

dH₂O, hydrogen peroxide, and hydrochloric acid in a respective 6:1:1 ratio, and is used to remove metallic contaminants. SC2 was also warmed to 70-80°C for 10 minutes. After SC2, the equipment was rinsed well with dH₂O. When using the standard cleaning methods no visible Ni was observed to be deposited on the equipment.

3.1.4 Powder Preparation

3.1.4.1 Milling

Hexagonal boron nitride and pure Ni powder were milled for certain experiments. A measured amount of powder was first placed into a polypropylene milling jar of appropriate size along with 4.75 mm diameter 440 C stainless steel milling balls in a 3:1 ball to powder ratio. Heptane was added along with the powder to assist particle fracture and to reduce oxidation. A model 4000 milling machine from Speed Selector Inc. was used. The powder was milled for 12 hours before being sieved to separate the powder from milling balls. The heptane was evaporated from the powder by placing powder/heptane mix into a 60°C oven until dry.

3.1.4.2 Nitric Acid Wash

To clean the surface of hBN powder, nitric acid was used. Powder was placed into a beaker containing nitric acid in 5:1 acid to powder ratio. The hBN remained in the nitric acid for 30 min before being diluted with distilled water (dH₂O). The powder was allowed to settle to the bottom of the flask so that the excess liquid could be removed.

This process was repeated two more times. The dilution was done to prevent damage to the vacuum filtration apparatus. After the acid was sufficiently diluted, the powder was vacuum filtered and vigorously rinsed with dH₂O, and then placed in an oven to dry.

3.1.5 Electroless Nickel Deposition

3.1.5.1 Tin Activation

For efficient use of lab time and to increase the accuracy of chemical composition 1000 ml of tin solution was prepared at a time in a polypropylene jar. By use of an electronic balance, 9.928g of stannous chloride dihydrate was measured and mixed with 500 ml of dH₂O. Next 40 ml of 3.0 M hydrochloric (HCl) acid or 120 ml of 1.0 M HCl acid was added. Distilled water was again added to dilute to 1000 ml of 0.044 M tin (II) chloride-0.12 M HCl solution.

For each experiment, tin (II) solution was warmed to roughly 25°C in a clean flask. Powder was added to the tin bath and agitated either by a mechanical stirrer, sonication, or a combination of both. Once the tin sensitization was complete the powder was vacuum filtered from the solution and dried. The time of Sn sensitization varied among experiments.

3.1.5.2 Palladium Activation

To produce 1000 ml of 5.6×10^{-4} M palladium solution dissolved in 0.12 M hydrochloric acid, 0.0993 g of palladium (II) chloride was weighed and placed into a

1000ml polypropylene jar. The addition of 500 ml of dH₂O followed by the measurement of 40 ml of 3.0M hydrochloric or 120 ml of 1.0 M HCl acid. Once the Pd was dissolved in the HCl solution more distilled water was added to make 1000 ml of solution.

Each palladium activation process used the 5.6×10^{-4} M PdCl₂ – 0.12 HCl solution. The solution was poured into a clean flask and warmed to 25°C. Powder was added to the warmed solution and agitated either by a mechanical stirrer, sonication, or a combination of both. After the Pd activation the powder was vacuum filtered, rinsed with distilled water, and dried. The time of Pd activation varied among experiments.

3.1.5.3 Electroless Nickel Deposition

Individual nickel baths were made for each experiment to ensure similarity between deposition trials. These baths consisted of 0.8 M nickel sulfate hexahydrate, 0.2 M sodium hypophosphite monohydrate, and 0.08M sodium citrate dihydrate. Parameters such as deposition time, temperature, pH, and method of agitation were varied to study the effects of each.

Most Ni deposition experiments used 315 ml of solution. To produce 315 ml of electroless nickel solution, 6.6237g of nickel sulfate hexahydrate, 6.6780 g of sodium hypophosphate monohydrate, and 7.4090 g of sodium citrate dihydrate were individually measured and placed into a clean 500 ml flask. dH₂O was added to make 315 ml of solution. The pH of the solution was increased by adding ammonium hydroxide. For different volumes and concentration of solution the ratio of chemicals remained constant.

Electroless plating solutions were agitated by use of a mechanical stirrer, sonic bath, or a combination of both.

3.1.6 Characterization and Polishing Methods

To characterize the Ni coatings produced in this study, optical microscopy, scanning electron microscopy (SEM) was used, as well as energy dispersive x-ray spectroscopy (EDS). The effectiveness of the nickel deposition could be determined by comparing samples before and after the nickel deposition.

For optical characterization powder samples were cold mounted in a 3.81cm (1.5 inch) epoxy puck, ground, and polished so that a cross section of the powder could be viewed. Plane grinding was done by hand using 800, 1200, and 2400 grit silicon carbide sand paper using light pressure and water. Polishing was done using a Struers Rotopol 22 auto polisher. First, 9, 6, and 3 micron diamond suspension was used on separate MD-DAC polishing cloths for 3 minutes. Blue alcohol based lubricant and force was applied automatically by setting the machines lubricant controls to 7 and the force to 30 N. The next polishing was done using 1 micron alumina with distilled water on a MD-CHEM cloth. Epoxy samples were polished for 5 min 30 sec using 30 N of force. The cloth was kept very well lubricated and was rinsed with water for the last minute of polishing. Finally OP-A (0.04 μm alumina) was used for 3 minutes with 25 N of force. Water was used to rinse the cloth during the last minute.

To obtain higher resolution images, powder samples were mounted on SEM stubs using double sided copper tape and then viewed in a Philips SEM with EDS capability.

EDS was used to determine elements present in the powder samples. Powder mounted in epoxy could not be viewed in the SEM because it is an insulator and produced poor resolution images. Coating polished epoxy samples with a conductive material has not been investigated because the coating used to enhance magnification would obstruct the view of the particle cross sections.

3.2 Individual Experiments

3.2.1 Electroless Ni Deposition on 2-3 μm hBN

Once it was determined that the electroless nickel method worked an experiment was conducted to determine if the same method would work on hexagonal boron nitride (hBN). A sample of hBN was obtained from laboratory overstock; in this case, the 99.9% pure 2-3 μm hBN was manufactured by Atlantic Equipment Engineers. This experiment used 3.232 g of the hBN along with flasks cleaned with soap and water. This powder was subject to 8 min of Sn sensitization using 200 ml of solution in an ultrasonic bath followed by 8 min of Pd activation in 200 ml of solution in an ultrasonic bath. The average temperatures of the baths were respectively 26.4°C and 26.9°C. After the powder had dried, it was placed into nickel deposition bath with a pH of 9.0 and sonicated for 30 min. The hBN powder stayed in suspension so a mechanical stirrer was not used. Once the nickel deposition was complete, the powder samples were mounted in epoxy and viewed using an optical microscope. Some powder was also mounted onto an SEM stub and characterized using the SEM and EDS.

3.2.2 Electroless Ni Deposition on 2-3 μm hBN with Low pH

An electroless nickel deposition procedure was followed as above, where 3.237 g of hBN was exposed to Sn and Pd baths as before with respective average temperatures of 25.1°C and 26.4°C. Ammonium hydroxide was omitted from the nickel solution to keep it at 6.5 pH. The hBN powder was added to the 27.2°C Ni bath and sonicated. The powder was removed from the solution via vacuum filtration after 30 min to keep deposition time similar to the original Ni deposition on 2-3 μm hBN, even though it was obvious the Ni deposition was not complete.

This experiment with a low pH Ni solution was repeated to determine how a complete deposition would compare to previous experiments. Here, 3.220g of hBN was measured and exposed to Sn and Pd baths as before. A Ni solution was prepared without adding ammonium hydroxide. The solution had an initial pH of 6.5 and temperature of 25°C. The solution was sonicated for 80 min before the reaction stopped.

3.2.3 Electroless Ni Deposition on hBN Pellets

Due to the small size of the hBN powder used in previous experiments the deposited Ni thicknesses could not be determined by optically viewing a cross section. To increase the size of the sample, 2-3 μm hBN powder was hand pressed into 0.65 cm tall, 1.27 cm diameter pellets. The pellets did not hold together well so there was no sonication or mechanical stirring used during this deposition procedure. All flasks used in this experiment were cleaned with SC1 and SC2, and all solutions were at room temperature (approximately, 22.5°C). Five pellets were carefully placed in the same 200

ml of tin solution. The pellets sat in the solution untouched for 10 min and then were carefully removed from the solution and placed in an oven to dry. Once dry, the pellets were placed into 200 ml of Pd solution. The pellets sat untouched for 10 min before being removed, rinsed, and placed in an oven to dry overnight. A 315 ml nickel solution was prepared with a pH of 9. The Ni solution was evenly divided into five 100 ml beakers, one pellet placed into each of the beakers. A pellet was removed from the Ni solution at 15 min, another at 30 min, 45 min, 90 min, and the last at 270 min. The pellets were individually mounted in epoxy and polished such that a cross section of the nickel coated surface could be viewed using an optical microscope. Thicknesses of the nickel coatings were measured at 50 different locations with the optical microscope. The thicknesses were then averaged and plotted.

3.2.4 Electroless Ni Deposition on Admixed Ni hBN Pellets

To study how the presence of Ni already in solution affects the nickel deposition process, 5.2184g of 2-3 micron hBN powder was mixed with 1.3048g of 3-5 micron nickel powder. Three pellets were hand pressed similarly to the pellets from the previous experiment. The pellets were tin sensitized and Pd activated for 10 min each at room temperature without any agitation. Flasks were cleaned with SC1 and SC2. The pellets were then placed into 3 separate clean beakers of 24.1°C Ni solution. One of the pellets was removed from the solution at 15 min, another at 30 min, and the final at 45 min. The pellets were rinsed, dried, mounted in epoxy, and then polished so that the thickness of

the deposited nickel could be viewed with an optical microscope. Measurements of the Ni thickness were taken at 50 different locations on each pellet, averaged, and plotted.

3.2.5 Electroless Ni Deposition on 20-30 μ m hBN

hBN with an average size of 20-30 μ m was purchased from Momentive Performance Materials. Flasks were cleaned with SC1 and SC2 before tin sensitizing 3.2405g of hBN in 200ml of solution that averaged 30.1°C, for 12 minutes. After being filtered and dried the powder was then Pd activated in 200 ml of solution for 12 minutes. The solution had an average temperature of 36.2°C and was prepared with a pH of 10. The powder was added to the initially 28.5°C nickel bath and sonicated for a total of 2 hrs and 45 min. Some of the powder was mounted and polished in epoxy and some was mounted on an SEM stud with Cu tape. The powder was characterized optically as well as with an SEM and EDS.

3.2.6 Cold Electroless Ni Deposition on 20-30 μ m hBN

Initially, three flasks were cleaned with SC1 and SC2. Then, 3.239g of 20-30 μ m hBN was Sn sensitized and Pd activated as before. Ice was added to the water of the ultrasonic bath before the flask containing the Ni solution was placed in the water. The flask sat in the water until the solution temperature equalized to the sonic bath temperature, 11.7°C. Once the powder was added to the solution, it was sonicated for 180 min before remaining un-agitated overnight. The next morning, the solution was

sonicated for another 180 min, bringing the total deposition time to 20 hours and 45 minutes. It was then vacuum filtered, rinsed, and prepared for optical characterization.

3.2.7 Ni coating 20-30 μm hBN without Pd Activation

As usual, equipment for this experiment was cleaned with SC1 and SC2. Next, 3.306g of hBN was measured and Sn sensitized at 36.1°C. It was then vacuum filtered and dried while a Ni solution was prepared with a pH of 10. It was warmed to 28.5°C before the dry Sn sensitized hBN was added. The hBN powder was sonicated in the Ni solution for 3 hours before being vacuum filtered, rinsed, and dried.

3.2.8 Electroless Ni Deposition on Milled 20-30 μm hBN

Approximately 10g of hBN was measured and milled using the parameters previously stated. After milling, the hBN was washed in nitric acid to remove any heptane residue. A 3.24g amount of milled powder was measured and placed into 200 ml of 25°C SnCl_2 solution. The powder was sonicated for 12 min before being vacuum filtered and dried. Once dry the powder was sonicated in 200 ml at 25°C, PdCl_2 solution for 12 min and then vacuum filtered, rinsed, and dried. While the powder was drying 315 ml of 10 pH Ni solution was prepared. The dry powder was placed into the Ni solution and sonicated for 90 min to ensure complete deposition. It was then rinsed with dH_2O and dried before being cold mounted in epoxy.

3.2.9 Multiple Electroless Ni Depositions on Milled 20-30 μm hBN

The previous experiment was repeated with no limit placed on the deposition time. Here, the Ni deposition was left undisturbed until there were no visible signs of the reaction taking place. After the powder had been rinsed, filtered and dried, roughly half of the powder was saved for characterization. The other half of the once Ni coated-milled powder was exposed to another Ni deposition using the same procedure as before. In this experiment the powder was exposed to 100 ml of SnCl_2 , 100 ml PdCl_2 , and 160 ml of Ni solution following the same deposition time and temperature as before. After the second coating, a small amount of the powder was saved for optical characterization. The remaining amount of powder was exposed to a third Ni deposition. A sample of the triple coated powder was also mounted in epoxy and polished.

3.2.10 Ni Deposition on Milled 20-30 μm hBN - Increased Solution to Powder Ratio

Partial Ni coatings were found when using the milled hBN powder, so the previous experiment was repeated using larger amounts of solution for longer deposition times. From the previously milled hBN powder, 1g was measured and placed into 300ml of 25°C SnCl_2 and sonicated for 1 hour. The powder was then vacuum filtered and dried. Next, the hBN powder was sonicated in a 25°C PdCl_2 bath for 1hour, vacuum filtered, rinsed and dried. 500 ml of 10 pH Ni solution was prepared and warmed to an initial temperature of 25°C. Then, 1g of tin / palladium coated powder was added to the Ni solution and sonicated for 3 hours. Next, the powder was vacuum filtered, rinsed, and

dried. A small sample of the powder was mounted in epoxy and polished for characterization.

3.2.11 Large Ni Deposition on 20-30 μm hBN - Increased Solution to Powder Ratio

In efforts to increase the amount of Ni deposited, the amount of Ni solution used per deposition trial was increased. In this experiment, 3g of as received 20-30 μm hBN was measured. The powder was tin coated, through sonication in 200 ml of SnCl_2 solution for one hour. Once tin activated, the powder was vacuum filtered, and dried in an oven. The dry powder was sonicated in 200 ml of PdCl_2 for one hour, vacuum filtered from the solution, rinsed with dH_2O , and dried. While the powder was drying, 1500 ml of Ni solution was prepared in a 4000 ml flask using the same ratios of chemicals as previous experiments. The pH of the solution was raised to 10. With the Sn sensitized-Pd activated hBN added the solution was sonicated and stirred mechanically until the nickel deposition process was complete. The powder was then vacuum filtered, rinsed, and dried. A small sample of the powder was mounted in epoxy for optical characterization.

3.2.12 Ni Coating 20-30 μm hBN using Concentrated Electroless Solution

The limiting factor when up-scaling is the size of container used. To help with this problem, an experiment was conducted using the recipe from the increased solution to powder ratio experiment, where the concentration of the Ni solution was doubled. For this deposition, 1g of hBN was measured using a digital balance and sonicated for one

hour in 50 ml SnCl_2 . The powder was vacuum filtered and dried before being sonicated in 50 ml of PdCl_2 solution. The powder was separated from the Pd solution through vacuum filtration while being rinsed with dH_2O , and then dried in an oven. Meanwhile, the concentrated Ni solution was being prepared. For this solution, 21.0514g of nickel (II) sulfate hexahydrate, 21.1487g of sodium citrate, and 23.5279g of sodium hypophosphite were measured and placed into a flask. dH_2O was added along with ammonium hydroxide to create 500ml of solution which had a pH of 10. Pre Sn - Pd coated hBN was added to the concentrated Ni solution. The Ni solution containing the powder was sonicated and mechanically stirred until the Ni deposition had ceased. It was then removed from the used Ni solution through vacuum filtration while being rinsed with dH_2O , and dried in an oven. Once dry a small sample of powder was mounted in epoxy for optical characterization.

3.2.13 Up-scaled Ni coating 20-30 μm hBN using Concentrated Ni Solution

The procedure using the concentrated Ni solution produced the best single deposition coating, so it was chosen to create large amounts of powder needed for Cold Spraying. To begin, 6g of hBN was measured on a digital balance and subjected to a Sn sensitization which used 400 ml of solution and was sonicated for 1 hour. It was then vacuum filtered and dried. Once dry, the powder was Pd activated using 400 ml of PdCl_2 solution and 1 hour of sonication. The powder was vacuum filtered, rinsed with dH_2O , and dried. Three liters of concentrated Ni solution was prepared by using 126.401g of nickel (II) sulfate hexahydrate, 126.892 g of sodium hypophosphite monohydrate, and

141.167g of sodium citrate dihydrate. Solution volume was raised to 3 liters by adding dH₂O. Roughly 60 ml of ammonium hydroxide was added to the solution to raise the pH to 10. The dry Sn and Pd activated powder was weighed again before being added to the Ni solution. After being weighed the powder was added to the Ni solution and stirred with a mechanical stirrer for at least 8 hours. Once the reaction completed, the powder was removed from the solution, rinsed with dH₂O, and dried. Dry nickel coated hBN powder weight was recorded. The Ni coated hBN was in large, hard agglomerates after being dried for the final time, so it was deagglomerated through use of mortar and pestle. A sample of the finely ground powder was mounted in epoxy for optical characterization.

3.2.14 Up-scaled Ni coating 10µm hBN with Concentrated Ni Solution

The powder produced from the previous experiment produced acceptable Ni coatings on the hBN particles for admixing with pure Ni powder. Since the objective of the Ni deposition process, was to deposit a sufficiently thick Ni coating so that the powder may be sprayed without admixing with Ni another procedure was developed. Here, 3.06 g of 10µm hBN was Sn sensitized through sonication in 200 ml of SnCl₂ solution for one hour at 25°C. The powder was then vacuum filtered and dried before being Pd activated by sonication in 200 ml of PdCl₂ solution for one hour at 25°C. This amount of prepared hBN provides enough powder for multiple experiments. It also reduces variables between experiments since all the powder was prepared similarly.

The first electroless Ni deposition using the prepared hBN powder consisted of 0.5g hBN in 3000 ml of concentrated Ni solution. The electroless Ni solution contained

126.3g of nickel (II) sulfate hexahydrate, 126.8 g of sodium hypophosphite monohydrate, and 141.1g of sodium citrate dihydrate with dH₂O in a clean 4 liter flask. The pH was raised to 10 by adding 60 ml of ammonium hydroxide. The powder and solution were mechanically stirred and sonicated until the deposition was complete. A portion of the powder was mounted in epoxy for optical characterization.

To obtain yet a thicker Ni coating on the 10 μ m hBN, the amount of powder for 3000 ml of concentrated Ni solution was reduced by a factor of ten. This experiment uses 0.05g of prepared 10 μ m hBN in 3000 ml of concentrated Ni solution. The concentrated Ni solution was prepared by adding 126.3g of nickel (II) sulfate hexahydrate, 126.82 g of sodium hypophosphite monohydrate, and 141.18g of sodium citrate dihydrate with dH₂O in a clean 4 liter flask. The pH was raised to 10 by adding 60 ml of ammonium hydroxide. A small 0.05g amount of the prepped hBN powder was added to the electroless Ni solution. The solution and powder were stirred mechanically on a hot plate until the reaction was complete. The average temperature of the solution was 30.2°C. Once the powder was dry it was prepared for further characterization.

The experiment was repeated using twice as much hBN, where 3000 ml of concentrated Ni solution was prepared by adding 126.3g of nickel (II) sulfate hexahydrate, 126.8 g of sodium hypophosphite monohydrate, and 141.1g of sodium citrate dihydrate with dH₂O in a clean 4 liter flask and warmed to 32.8°C. The pH was raised to 10 by adding ammonium hydroxide. 0.1 g of the already prepared hBN was added to the solution and mechanically stirred until the reaction was complete. After the deposition was complete, the powder was rinsed with dH₂O, vacuum filtered and

dried. A small portion of the Ni coated hBN was mounted in epoxy for optical characterization.

3.3 Preparation for Cold Spraying

The substrates used for cold spray depositions consisted of 2"x 2" x 0.25" Ti-6Al-4V blocks cut from 6"x6"x0.25" feedstock and 1" diameter Ti-6Al-4V bond test cylinders. The surfaces were surface ground using a MSC 612 surface grinder to remove contaminants and to provide a planar deposition surface. Within 24 hours of the Cold Spraying experiments, the substrates were grit blasted with Trin Blast 16 which consists of 16 grit Al_2O_3 to increase surface roughness. After grit blasting, each substrate was rinsed with ethyl alcohol and scrubbed with a hard plastic bristle brush followed by a 30 minutes sonication in ethyl alcohol. After the substrates were placed into the specimen holder, they were rinsed one more time with alcohol, brushed, and dried with high pressure air. Powders used for cold spraying were dried at least 24 hours in a 65°C oven prior to spraying to remove any moisture in the powder, in effort to increase uniformity of powder flow.

3.4 Feedstock for Cold Spraying

Pure nickel (32 μm electrolytic from Consolidated Astronautics) was selected to be used as the baseline powder. A 200g portion of pure nickel was separated and milled for 8 hours using 4.75mm 440 stainless steel balls in heptane to determine the effects of work hardening on cold spray deposition. Nickel coated hBN from experiments 3.2.13 and

3.2.14 were used to make the feedstock powders. Since the nickel coating on the 20-30 μ m hBN was rather thin, it was admixed with pure 32 μ m nickel to create 30vol % and 50 vol% feedstocks. The volumes of the powders were measured using a Quanta Chrome Dual Auto Tapper. The 50 vol% powder sample used 90ml of 32 μ m pure nickel powder mixed with 90ml of the nickel coated 20-30 μ m hBN. The 30 vol% mixture was prepared using 120ml of pure nickel powder and 60ml of nickel coated 20-30 μ m hBN. Both powder samples were mixed with a WAB Turbula mixer for 1 hour. Thick nickel coated 10 μ m hBN was prepared for cold spraying by itself. All powders were placed in an oven at 65°C for a minimum of 24 hours before spraying.

3.5 Cold Spray Procedure

3.5.1 Cold Spray Equipment

All cold spray coatings were produced using a system built by ARL at Penn State. Cold spraying was conducted inside an acoustic room supplied by Industrial Acoustics Company, equipped with a Sulzer Mecto Spray Hood and dust collection system. The cold spray gun was mounted on an ABB, IRB 2400 robot arm supported from a sliding track fixed to acoustic room ceiling. Figure 3-1 is an image of the robotic arm controlling the nozzle movement while spraying. Figure 3-2 illustrates the cold spray system configuration.

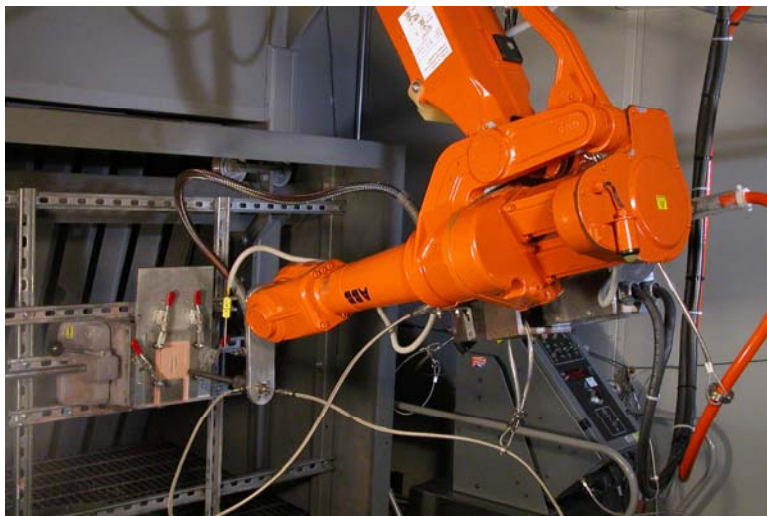


Figure 3-1: Cold spray system within the spray chamber

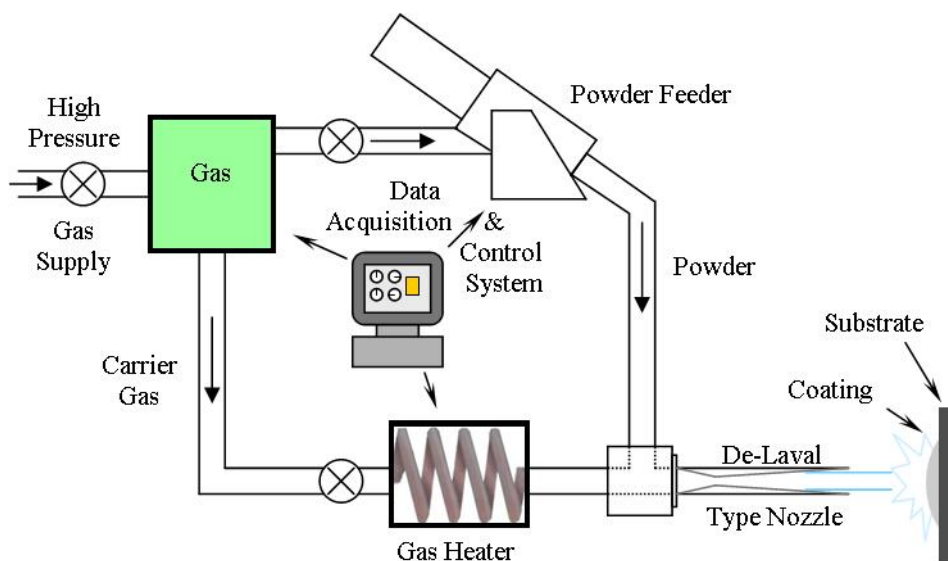


Figure 3-2: Cold spray system schematic

N_2 and He were used as the high pressure gas supply for various depositions. N_2 was supplied from a 6000 gallon Air Liquide Nitrogen tank at 1.24 MPa (180 psi). A Bauer Compressor KWB10 was used to increase the N_2 gas pressure to approximately

3.447 MPa (500 psi) inside a secondary 400 gallon tank. High pressure He was supplied from 24 – 16” bottles at a pressure of 16.55 MPa (2400 psi).

The gas control module consisted of a powder coated Hoffman enclosure with inlets for He and N₂, and exits for the main gas and process gas where the gas supply was split to the powder feeder and gas heater. The module contained a system of solenoid valves, N₂ actuated regulating valves, flow meters, pressure transducers, and other electronics. Gas diverted to the powder feeder was used to carry the powder to the pre-chamber of the nozzle. Gas diverted to the heater was heated to so that critical powder velocity could be obtained.

Power for the gas heater was supplied by a Miller Gold Star 652 CC-DC Welding power source that utilized a 40 KW heating coil powered by 480V-63Amp. Gas temperatures as high as 500°C for N₂ and 200 °C for He were used. To reduce He consumption, the cold spray system was first preheated using N₂ as a process gas. Once the system reached the experiment specific temperature (within 5-7 minutes) the carrier gas supply was switched to He. Gas temperature was maintained by an Omega Temperature controller.

The powder feeder consisted of a 1264 High Pressure/High Volume powder feeder mounted on a Praxair 1280 digital scale. Powder was stored in a hopper consisting of a large air tight pressure vessel. The flow of powder was controlled setting the RPM of powder feeder to a specific rate. Gas diverted to the powder feeder supplied up to 500 psi back pressure to endure even powder flow. A set temperature heater covered the powder hopper to increase flow-ability of the powder.

The gas control module, gas heater, and powder feeder were all controlled by a PXI-1000B computer using LabView software. The computer displayed and monitored analog and digital outputs and was to control the pressure of the gas pressure, powder flow, and gas temperature through a feedback loop.. The data acquisition system and control system were located outside the acoustic room. Figure 3-3 is an image of the data acquisition control system.



Figure 3-3: Data acquisition and control system

Powder was moved from the powder feeder to the nozzle pre-chamber by the carrier gas where it was accelerated in the supersonic De-Laval type nozzle by the heated gas. The nozzle was made from sintered tungsten carbide to minimize wear and plugging and had a 7.75mm inlet, a 3.05mm throat, and a 7.14mm exit. The substrates were secured in front of the De-Laval type nozzle so that the substrate face was perpendicular to the flow of particles.

3.5.2 Process Parameters

Several different powders were sprayed for this experiment. Each powder was first sprayed onto 2" x 2" x 1/4" Ti-6Al-4V substrates and then 1" diameter bond test slugs. Three separate coatings were created on each of the square substrates by passing the nozzle over the substrate 3, 6, and 9. Each pass was a rectangular loop which consisted of an upward stroke, a 2mm step to the left, a downward stroke, and 2mm step to the right.

Powders include 32 μ m pure nickel powder (electrolytic), milled 32 μ m pure nickel powder (electrolytic), thick (15 μ m) electroless nickel coated 10 μ m hBN, and thin (2-3 μ m) electroless nickel coated 2-3 μ m hBN admixed with pure nickel to make mixtures with 30 vol % and 50 vol % ratios. Powders were first sprayed with N₂ to create a preliminary coating. If the coating was not produced with N₂ the process gas was switched to He and the powder was sprayed again. The thick nickel coated 10 μ m hBN was of most interest so it was sprayed multiple times with changes in parameters such as process gas, gas temperature, and traverse rate. Table -1 lists the parameters used for each powder along with the initial surface roughness of the substrates.

The number of passes for bond slugs varied. The coating thickness per pass was calculated from coatings made on the square substrate and used to create coatings greater than 635 μ m thick on the bond slugs.

Table 3-1: Cold spray process parameters

Powder	Gas Type	Gas Temp (°C)	Traverse Rate (mm/sec)	Substrate Roughness (μm) (Ave of 4)
Ni(15μm) - hBN (10μm)	N ₂	500	20	>6.3
Ni(15μm) - hBN (10μm)	He	188	20	>5.97
Ni(15μm) - hBN (10μm)	He	24	20	~5.79
Ni(15μm) - hBN (10μm)	He	188	50	~5.59
Pure Nickel	N ₂	500	20	~5.74
Milled Nickel	N ₂	500	20	~5.36
50 vol% Ni(2-3μm) coated hBN (20-30μm) admixed with Pure Ni	N ₂	500	20	>6.1
50 vol% Ni(2-3μm) coated hBN (20-30μm) admixed with Pure Ni	He	189	20	>6.07
30 vol% Ni(2-3μm) coated hBN (20-30μm) admixed with Pure Ni	N ₂	500	20	>6.27
30 vol% Ni(2-3μm) coated hBN (20-30μm) admixed with Pure Ni	He	189	20	>6.05
30 vol% Ni(2-3μm) coated hBN (20-30μm) admixed with Pure Ni	He	183	50	>6.10

3.6 Characterization of Cold Spray Coatings

3.6.1 Mass, Thickness, Optical and SEM-EDS

The thickness of the cold spray coatings was measured by using digital calipers. The mass of the substrate before and after cold spraying was also recorded to determine the mass of powder which has adhered/imbedded to the substrate. An edge of each the square substrate was removed using a diamond blade and a Struers cut off saw to expose a full width cross section of the coatings. The cut edge was then polished by using 1200 grit and 2400 grit sand paper followed by 3μm diamond solution, 1 μm diamond solution,

and either 0.04 alumina or 0.25 diamond solution. Slivers of coating and substrate were cut and mounted in epoxy and polished with the same procedure. The polished cross sections were viewed with a Nikon Epishot 300 optical microscope and then with a Philips XL30 SEM with EDS capabilities. EDS was done to determine the presence of hBN in the coating.

3.6.2 Bond Testing

The ASTM C633-01 standard test procedure was followed to determine the adhesion strength of the cold spray coatings to the bond slugs. The bond slugs consisted of Ti-6Al-4V cylinders, which were roughly 5 cm tall and 2.54 cm in diameter. Powder was deposited onto one of the prepared bond slug surfaces via cold spray as previously explained. The cold spray coating was surface ground until flat and/or coating thickness of 500 μ m was reached. The total length of the bond slug and coating was measured at four different locations, averaged, and compared to the initial bond slug length to determine the thickness of the coating.

Bond slugs with flat coatings were glued to similar uncoated slugs using roughly 1 cc of E-214HP HYSOL. The adjoining bond slugs were air dried for 20 min before being cured at 150°C for two hours. The surface of the second bond slug was prepared by using a lathe to remove coatings from previous experiments.

The firmly glued bond slugs were placed in a MTS® Q-Test /100 tensile tester and an increasing load was applied at 635 μ m/min (0.025 in/min). The maximum load was recorded and used to calculate the adhesion strength through using Eq. 1 where P_{\max}

is the maximum load, A is the cross sectional area of the bond slug, and S_t is adhesion strength.

$$S_t = \frac{P_{\max}}{A} \quad 1$$

Cold spray coatings subject to bond testing include pure Ni sprayed with 500°C N₂, milled Ni sprayed with 500°C N₂, thick Ni coated 10µm hBN sprayed with 500°C N₂, and thick Ni coated 10µm hBN sprayed with 24°C He. A baseline test using only the adhesive was also conducted.

3.6.3 Friction Testing

Cold spray samples which have been identified as having an acceptable thickness were subjected to friction testing using ATSM standard G-133 for Linearly Reciprocating Ball-on-Flat Sinding Wear as a reference. Samples of cold spray coatings were cut from the bulk substrate to dimensions necessary to fit within the friction machine specimen holder. The samples were then cleaned using a standard procedure defined in the ASTM G-133 procedure. The coatings did not receive any further treatment besides the cleaning. A Plint High Frequency Friction Machine was used to determine the coefficient of friction of the cold spray coatings. A force transducer measured the friction force and the output was read through an oscilloscope. Input to the oscilloscope was coupled to a WavBook data acquisition system where it was viewed with WavView software. Figure 3-4 is a schematic of the reciprocating test machine.

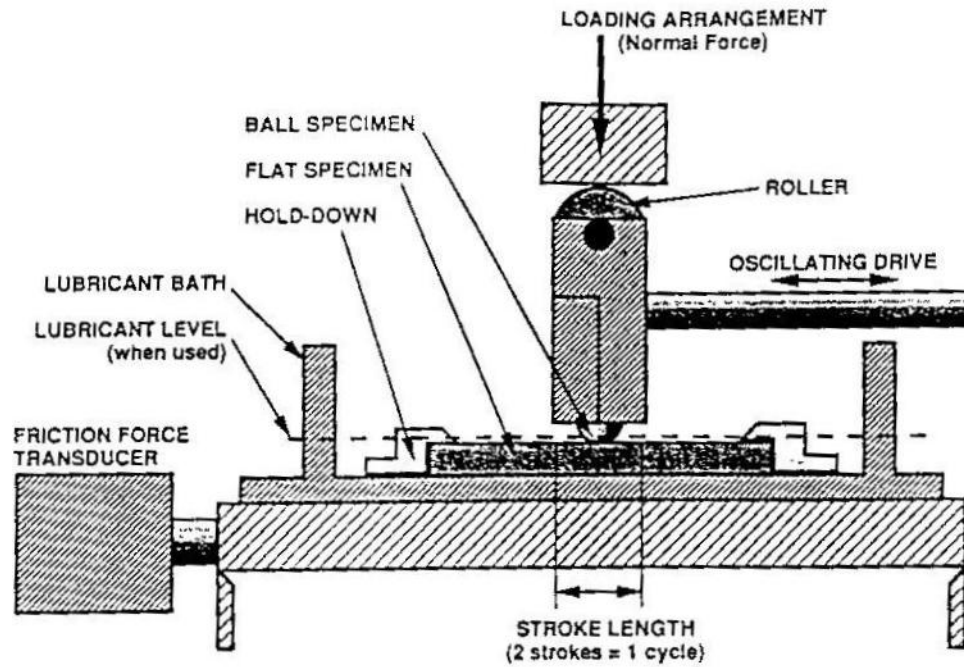


Figure 3-4: Reciprocating test – schematic diagram [124]

Friction tests were conducted by using a spherical-on-flat test geometry. A stainless steel ball was placed in contact with the section of the cold spray coating. The ball was moved tangentially to the coating surface with 30N normal force, 5 mm stroke length, at 5 Hz. Between tests, the stainless steel ball orientation was changed to provide similar contact geometry between tests. The ball was cleaned with standard lab cleaner between tests that were conducted the same day to provide similar conditions. The room temperature was 23.2°C and the humidity was 49%, according to the national weather service. Friction force versus time data was then plotted. The average force for one stroke was calculated and used to determine the coefficient (μ) of friction by dividing the friction force (F_f) by the normal force (F_N) as shown in Eq. 2.

$$\mu = \frac{F_f}{F_N}$$

2

3.6.4 Micro Hardness of Cold Spray Coatings

Micro hardness measurements were taken on cold spray coatings which were greater than 200µm thick. Cross sections of the coating were mounted in epoxy and polished following the same procedures as discussed earlier. MPIF standard 51 was followed and a Leco hardness testing machine coupled with a Leco video line micrometer VL-101 was used to take the measurements. A 300g gram load was applied to a Vickers diamond pyramid indenter for a 10 sec duration. The diagonal distances of the indentation were measured and used to calculate the Vickers hardness of the material. The Vickers hardness value was calculated by dividing the applied load by the measured area of indentation. Eq. 3 shows the relationship used to calculate the Vickers hardness (HV), where P is the applied load in grams and d^2 is the mean of the diagonal distances measured.

$$HV = \frac{1854.4P}{d^2} \quad 3$$

Chapter 4

Results and Analysis

4.1 Electroless Nickel Deposition

4.1.1 Cleaning Flasks

Glassware used for Ni depositions on 2-3 μ m hBN (experiment 3.2.1) was cleaned with soap and distilled water followed by rinsing with acetone and distilled water. This simple cleaning resulted in some Ni being deposited on the glassware as shown in figure 4–1(a). Standard cleans 1 and 2 were used to clean equipment before and after Sn sensitization, and after Pd activation for all experiments after and including Ni deposition on hBN pellets (experiment 3.2.3). When using SC1 and SC2 on the flask there was no visible Ni deposition on the glassware as shown in figure 4–1(b).

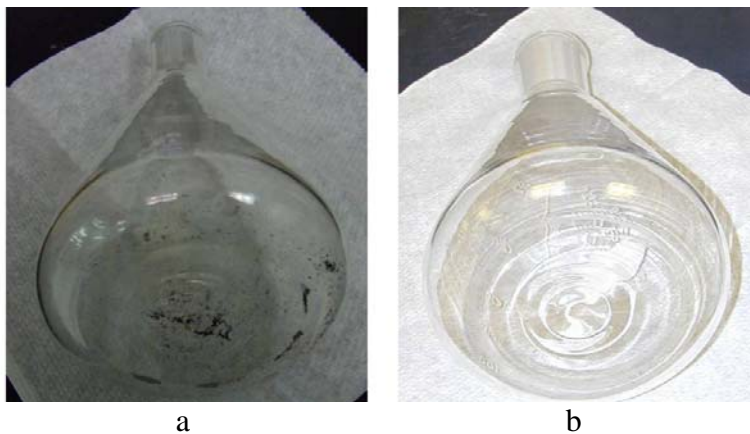


Figure 4–1: (a) Flask cleaned with soap and distilled water followed by rinsing with acetone and distilled water, (b) Flask after Ni deposition being cleaned with SC1 and SC2 between deposition steps.

4.1.2 Electroless Ni deposition on 2-3 μ m hBN

The hBN used in this experiment is smaller than desired for cold spray application, but was readily available. The smaller powder size and the lubricious properties of hBN made powder handling much more difficult. Due to the smaller powder size, i.e. greater surface area, the mass of powder used was reduced to half of the powder weight used in the Cu experiment in an attempt to keep the surface area to solution ratio similar. The original hBN was white and remained white after being exposed to the Sn bath, but turned an almond color after the Pd bath. It took significantly longer to filter the hBN after the Sn and Pd baths than the Cu powder. When the hBN was placed into the Ni bath it initially turned the bath from clear to milky green. After 5 minutes, the solution began to bubble aggressively, so much that foam consisting of solution and powder began coming out of the top of the flask. The foam was mixed back into the solution by swirling the flask by hand. At 10 minutes 5 cm of foam had been produced and was again mixed back into the solution. Roughly 5 cm of foam was mixed back into the solution every five minutes for the remaining time of the 30 min deposition.

Optical microscopy was used to characterize the Ni coated hBN, but beside the obvious color change of the powder, there was no measurable Ni thickness. Energy dispersive x-ray spectroscopy was used to determine what caused the color change of the hBN. Figure 4–2 compares EDS scans of the Ni coated hBN before and after the electroless procedure. Elements present in the post deposition scan results of the Sn sensitization and Ni deposition. The amount of Pd on the powder was minimal and therefore not detected through EDS. Phosphorous was present in the coating because it

co-deposited with Ni as a result of using sodium hypophosphite as a reducing agent. The high oxygen content is most likely due to the adhesive used since the presence of Cu is also observed. It was concluded from this experiment that Ni can be deposited on hBN, but further investigation is needed to determine the quality, thickness, and rate of Ni deposition.

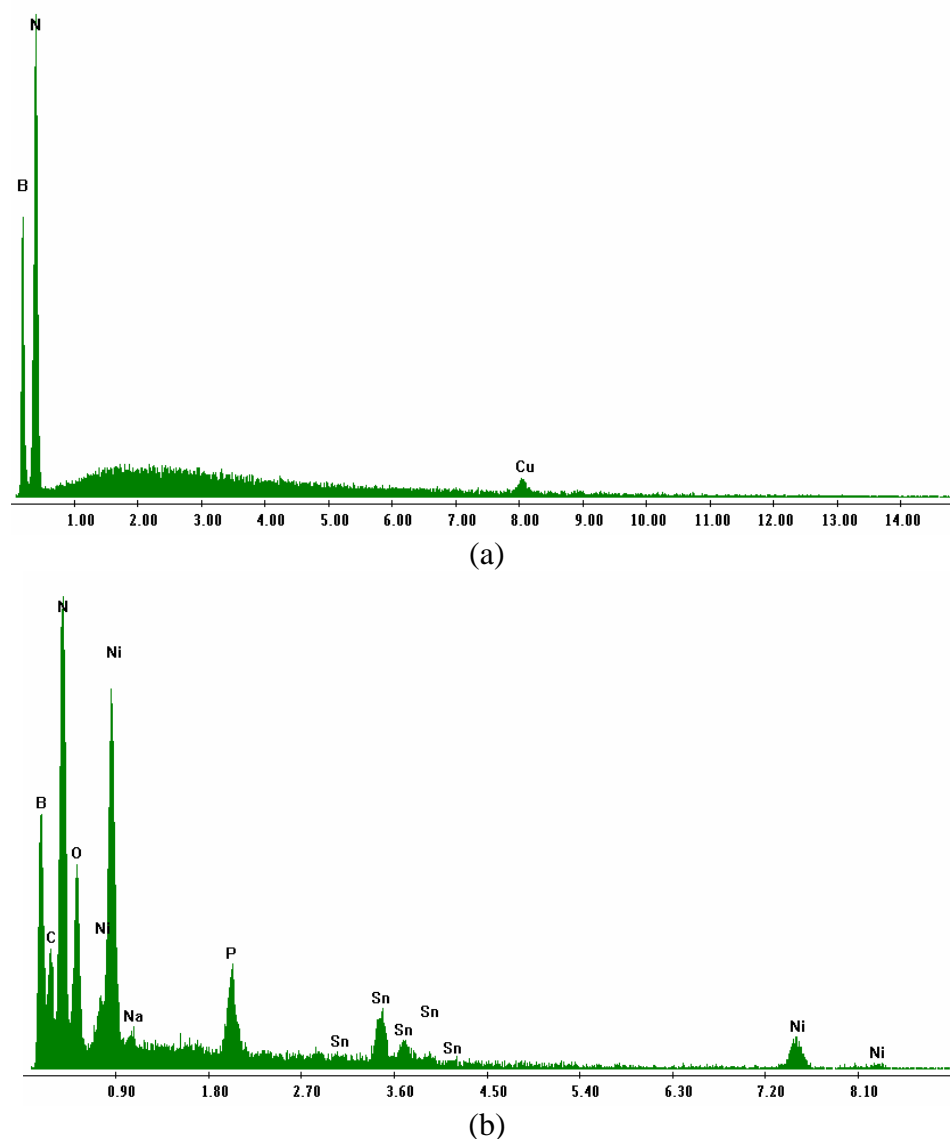


Figure 4-2: EDS scan of 2-3 μm hBN (a) before Ni deposition and (b) after being exposed to a Ni deposition

4.1.3 Electroless Ni deposition on 2-3 μm hBN with Low pH

An experiment was conducted to study how the pH of the electroless Ni solution effected the reaction. A sample of 2-3 μm hBN was Sn sensitized and Pd activated as in the previous Ni coating hBN experiment. The Ni solution did not have any ammonium hydroxide added so the pH remained at 6.5. After the hBN powder had been added to the Ni bath, no reaction seemed to be taking place. After 5 minutes, there was the slightest sign of Ni deposition because the once green solution now showing hints of grey. By 10 minutes, the solution was bubbling fast enough to build up 5 cm of foam which was swirled back into the solution by hand. At 15 minutes, the foam had risen to the top of the flask and was also mixed back into the solution. The Ni solution produced roughly 5 cm of foam at 20 min, 25 min, and 30 min. The powder was removed from the reaction after 30 min so that the time of deposition did not differ from the previous experiment.

Another experiment was conducted using 2-3 μm hBN and a Ni bath with 6.5 pH. In this deposition procedure, the hBN remained in the solution until there was no sign of bubbling. Just as the previous experiment, the solution remained calm for the first 5 min and eventually produced 5 cm of foam after 10 min. The flask was full of foam at 15 min and had 5 cm at 20 min. The foam production was checked every 5 min until foaming stopped. After 80 min the solution had stopped bubbling.

Assuming the bubbling of the solution is related to the deposition of Ni, it can be concluded that a decrease in pH will increase the time until Ni begins being deposited. At 5 min there was 10 cm of foam produced by the 9.0 pH Ni bath, whereas with Ni bath with 6.5 pH needed 15 min to produce the same amount of foam.

4.1.4 Electroless Ni Deposition on hBN and Ni + hBN Pellets

This experiment was conducted to study the rate Ni deposition. The Ni deposition reaction appeared to proceed much slower than previous experiments; this may be caused by the lack of sonication during the deposition procedure. After some time, bubbles formed on the surface of the pellets at an increasing rate. This observation was made for both hBN pellets and Ni + hBN pellets.

Plots shown in figure 4–3 of Ni thickness versus time show that once Ni is deposited, it was more favorable for more Ni to deposit. This confirms that the electroless Ni deposition is an autocatalytic reaction. There was slightly more Ni deposited on the Ni + hBN pellet than the pure hBN pellet. This difference was considered negligible because the thickness of Ni on each sample was not exactly uniform. The plot also shows that the presence of Ni does not effect the autocatalytic reaction of Sn sensitized and Pd activated hBN.

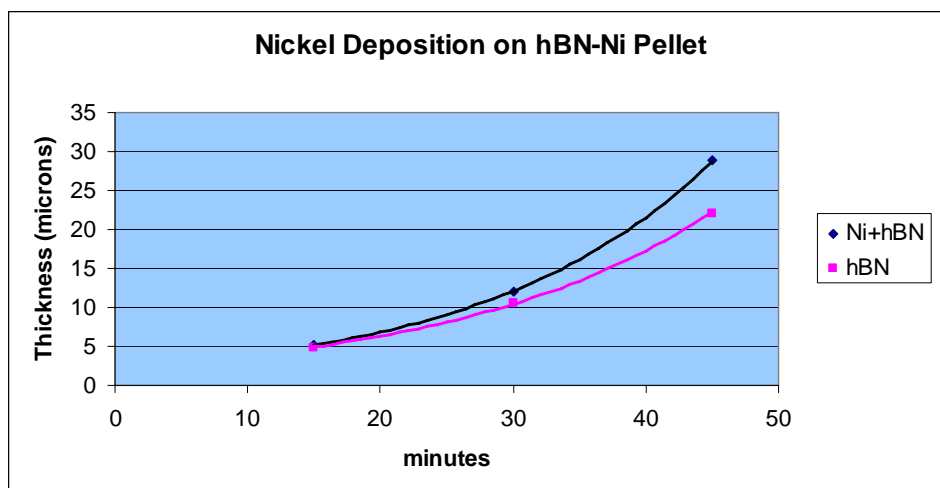
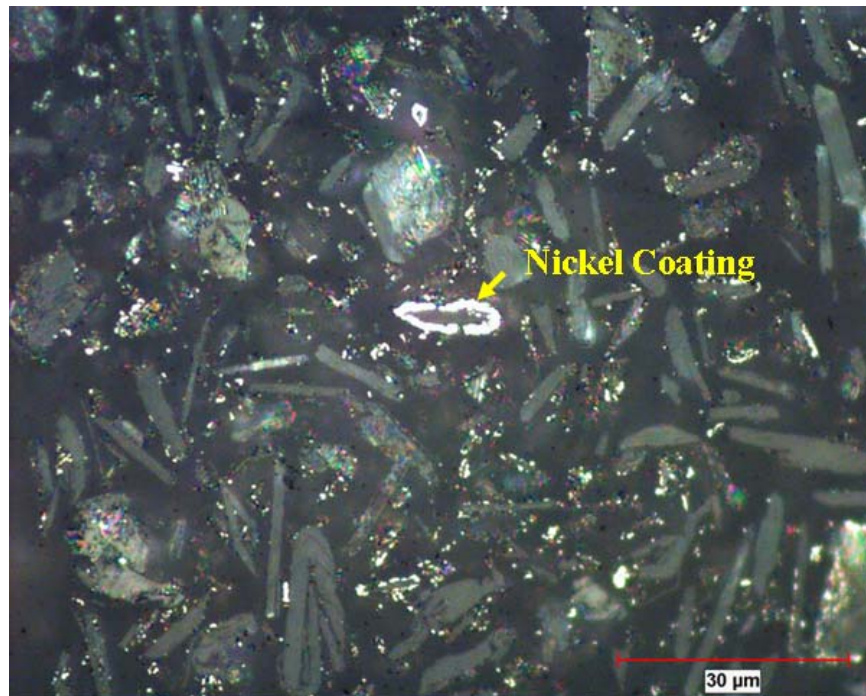


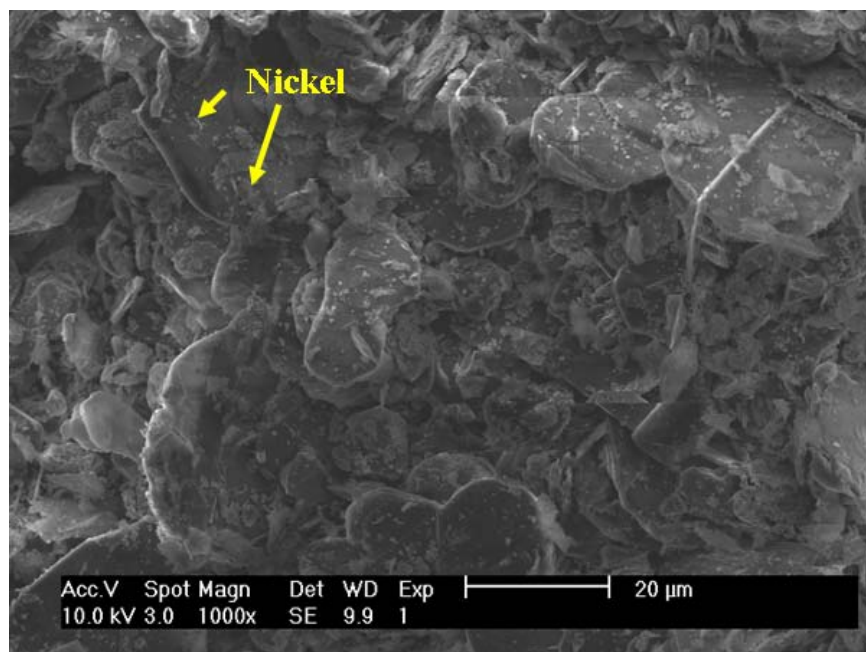
Figure 4–3: Rate of Ni deposition on pressed 2-3 μ m hBN and 2-3 μ m hBN/3-5 μ m Ni pellets

4.1.5 Electroless Ni Deposition on 20-30 μm hBN

A second experiment using 20 μm hBN was performed to determine how Ni would deposit on 20-30 μm hBN powder. Through optical characterization, it was found that Ni was deposited onto the hBN. Some of the hBN particles were completely coated with Ni while other hBN particles only had small Ni nucleations scattered across the particle surface as shown by optical and SEM images in figure 4-4. The powder was further characterized with a SEM and EDS. The lighter areas show the deposited Ni on the darker hBN. To confirm that the lighter areas actually were Ni, SEM images shown in figures 4-5 were taken at 10,000x and 50,000x and the EDS scan in figure 4-6 identifies the elemental composition of nucleations to be Ni. A possible reason for the Ni clumps may be that the reaction is taking place too quickly. Slowing the deposition process may promote more even Ni deposition on the powders surface.

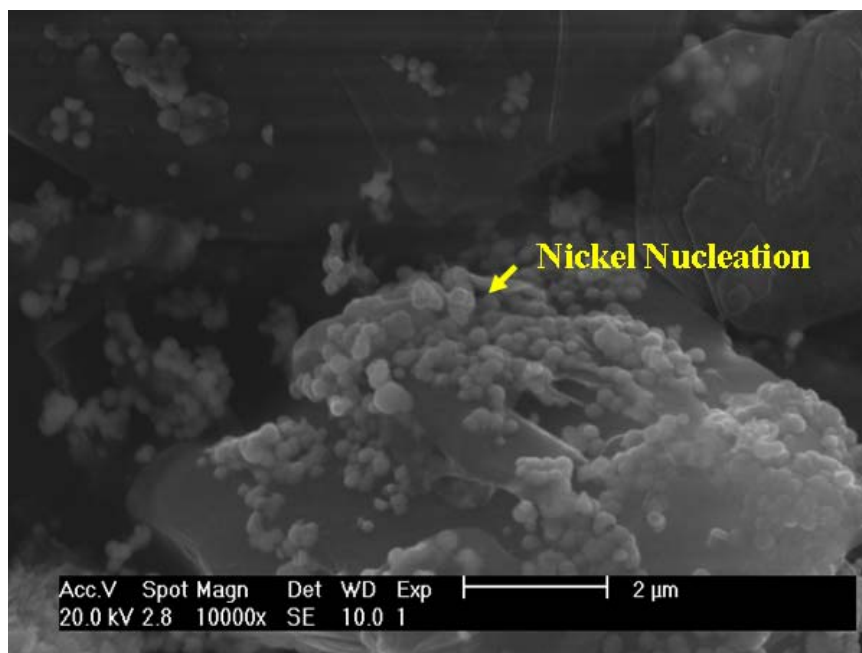


(a)

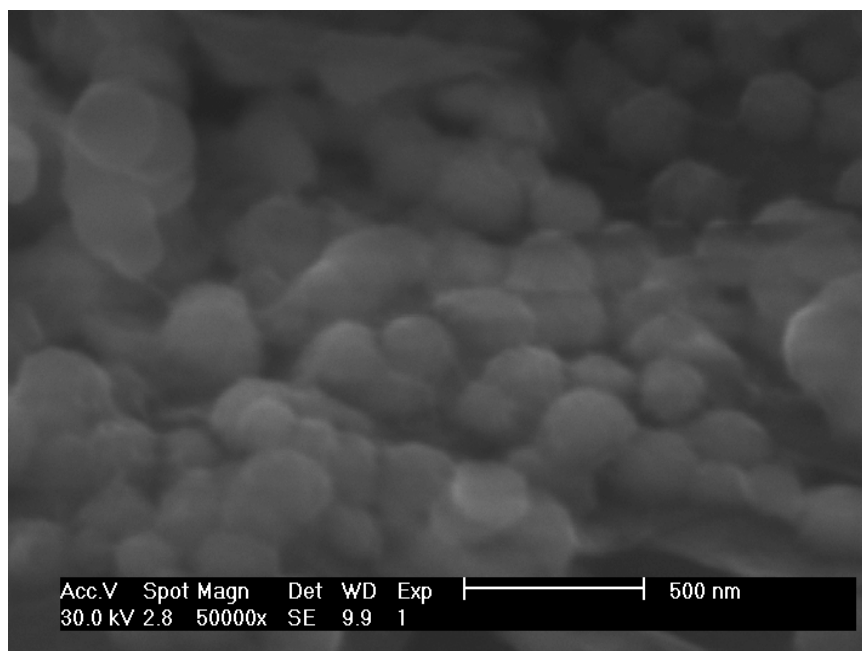


(b)

Figure 4–4: (a) Optical image and (b) SEM image of Ni coated 20 μm hBN cross section (1000x)



(a)



(b)

Figure 4–5: High magnification image of Ni nucleations on hBN at (a) 10,000x and (b) 50,000x

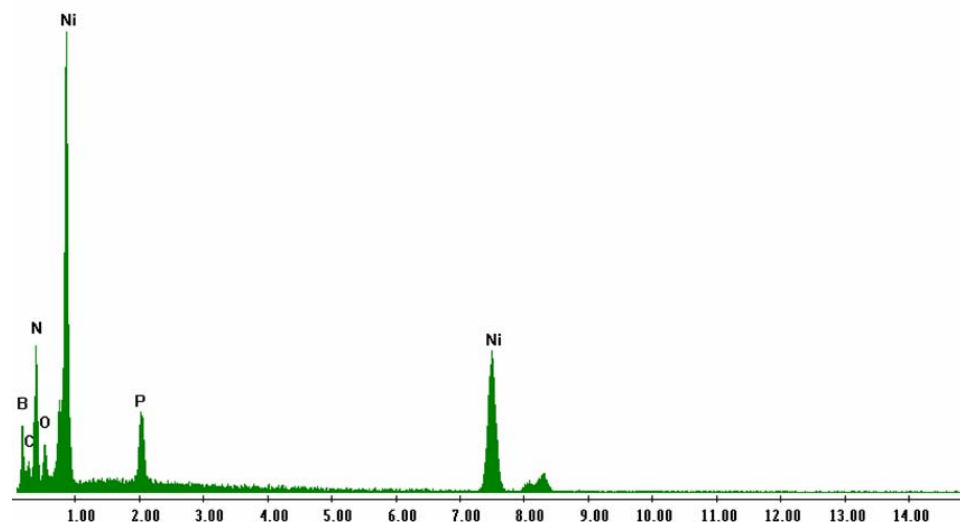


Figure 4–6: EDS scan of Ni agglomerate

4.1.6 Cold Electroless Ni Deposition on 20-30 μm hBN

Literature suggests using temperatures of 80-90°C for electroless Ni deposition on surfaces which do not contain catalyst coatings. Since this procedure does utilize catalyst coatings, and previous experiments show that Ni prefers to nucleate on specific sites, it was thought that by reducing the temperature during Ni deposition the Ni would be deposited more uniformly. Just such an experiment using 20-30 μm hBN was conducted with ice water in the ultrasonic bath. While the Ni solution was at a reduced temperature of 8°C no Ni was deposited. After 17 hours, the ice had melted and the temperature of the Ni solution had warmed to 21.7°C. Once warmed, the Ni deposited similarly to the first experiment using 20-30 μm hBN powder. Figure 4–7 is an optical image of a cross

section of 20-30 μm hBN after being exposed to the reduced temperature Ni deposition. This image shows a similar color change to the powder as seen in previous Ni deposition experiments. Although the Ni is still not uniformly deposited on the hBN, a threshold temperature of roughly 21.5°C has been identified.

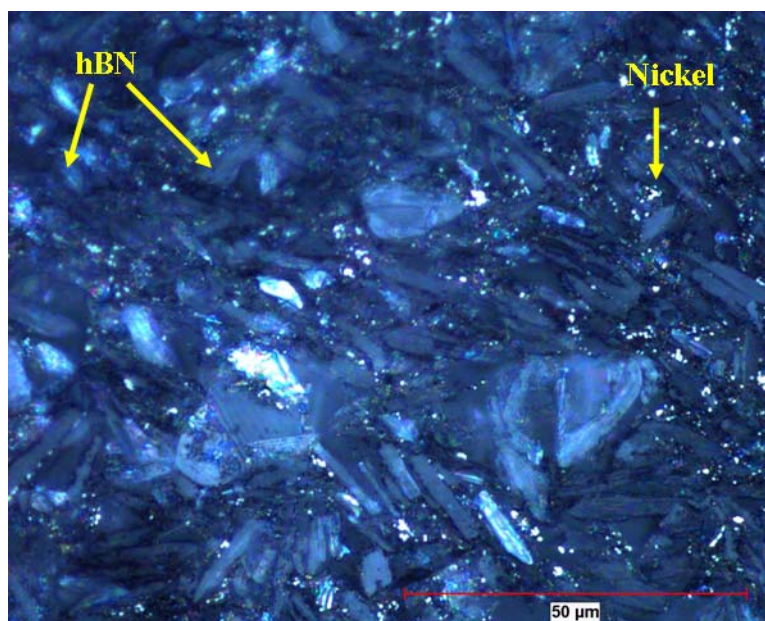


Figure 4–7: Optical image of 20 μm hBN after being exposed to a Ni deposition at a reduced temperature

4.1.7 Ni coating 20-30 μm hBN without Pd activation

Another experiment was conducted to determine if the Pd activation was necessary. Figure 4–8 shows the difference between the received hBN powder, the hBN powder being exposed to the Ni deposition procedure without Pd activation, and hBN powder being exposed to the Ni deposition procedure with Pd activation. It was concluded that the Pd activation is necessary for Ni deposition.

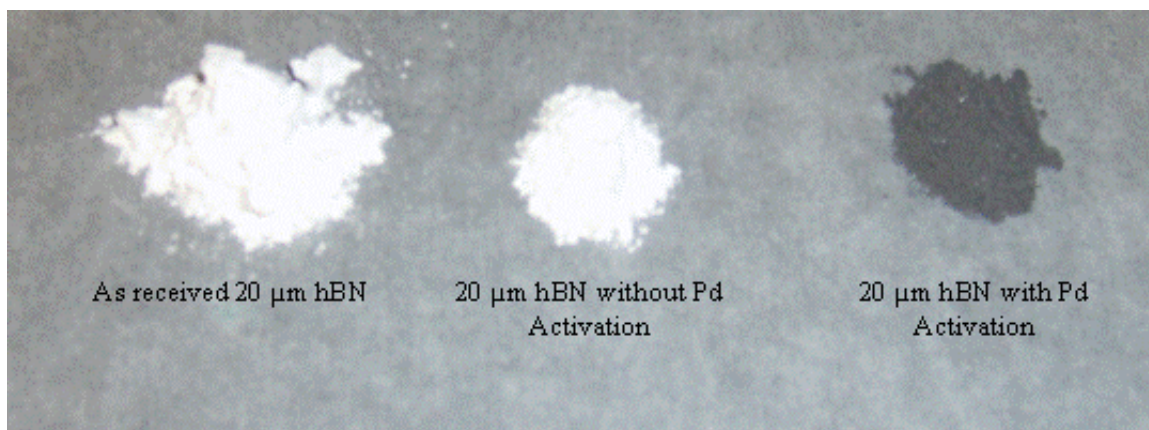


Figure 4–8: Image showing the effect the Pd activation

4.1.8 Electroless Ni Deposition on Milled 20 µm hBN

It was difficult to obtain an optimal milling speed because of the lubricity of the hBN. When the speed was too slow the milling balls tended to remain on the bottom of the polypropylene jar. When the speed increased the centrifugal forces were sufficient to keep the milling balls on the jar wall. Both of these conditions provide insufficient collisions of milling balls to fracture the hBN particles. Thus, there was a very narrow range of speeds acceptable for milling.

The Ni deposition procedure used for the first experiment with 20-30 µm hBN was followed for this experiment. The Ni deposition reaction appeared to take place just as before. Optical characterization was used to determine the quality of Ni coating on the milled hBN. Figure 4–9 shows several hBN particles which received a Ni coating. Although the Ni coating is not uniform for the entire hBN powder, the particles that did

receive the Ni coating were covered rather uniformly. While this experiment produced the best Ni coating on hBN, but it is still insufficient for cold spraying.

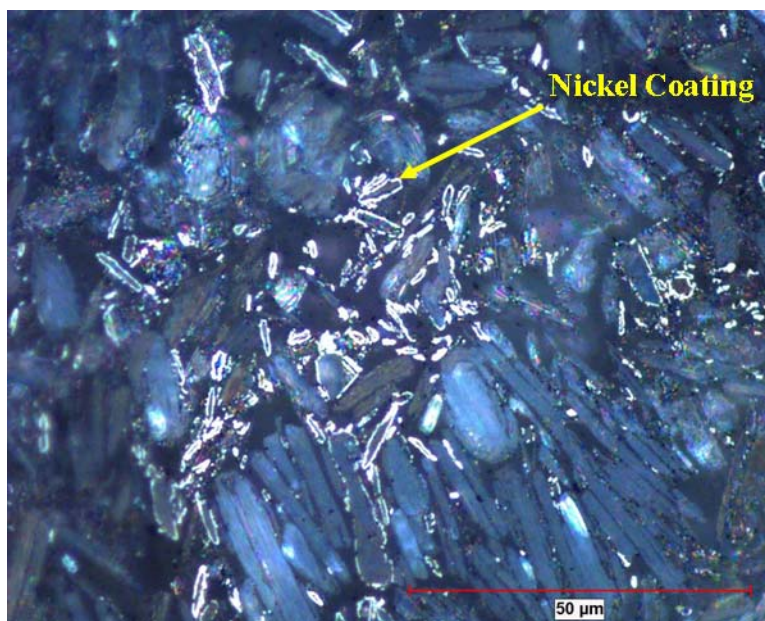


Figure 4–9: Ni deposited on milled 20µm hBN

4.1.9 Multiple Electroless Ni Depositions on milled 20-30 µm hBN

Another experiment was conducted using the milled hBN. This time, the hBN powder remained in the solution for an extended period of time to ensure all Ni was reduced from the electroless solution. After remaining in the solution overnight, the powder was prepared for optical characterization. Figure 4–10 shows a cross section of the Ni coated milled 20-30 µm hBN. There was more Ni deposited and the coating was more uniform on this powder than in previous experiments.

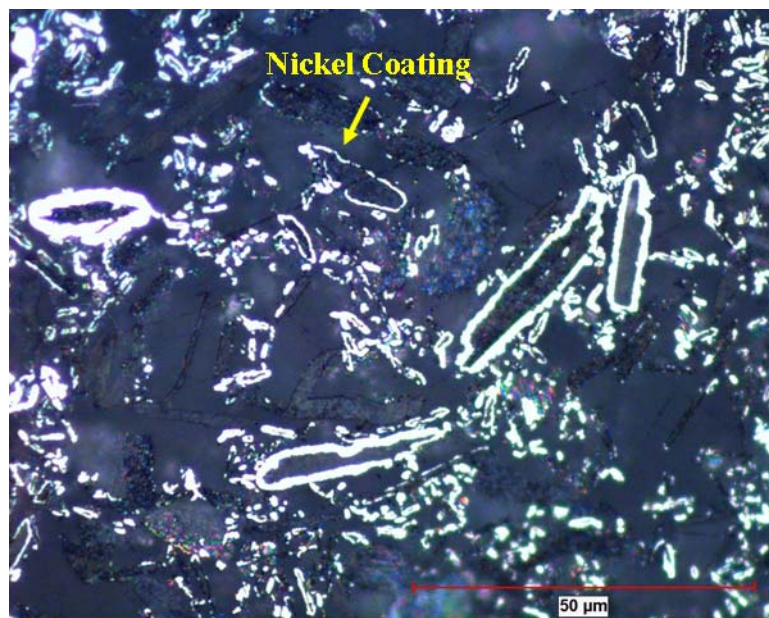


Figure 4–10: Milled 20 μm hBN after being deposited with Ni for an extended period of time

Powder that was not used for characterization was exposed to a Ni deposition for the second time to determine the effectiveness of multiple coatings on hBN. With less than half of the initial amount of powder remaining proportional amounts of SnCl_2 , PdCl_2 , and Ni solution were prepared. Since once coated powder was agglomerated, it was sonicated in 25 ml of dH_2O until broken apart. The water and powder was then poured into the SnCl_2 solution and sonicated for the same amount of time as in the initial coating. The powder was also placed in the PdCl_2 for the same amount of time as in the initial coating. When the newly prepared and once Ni coated powder was placed into the Ni solution the deposition reaction appeared to take place more rapidly. After 90 min the reaction had stopped completely and the powder was sitting on the bottom of the flask. Some of the powder was kept for optical characterization while the rest was used for a third Ni coating experiment. The proportions of chemicals used were proportional to the

amount of powder kept. When applying the third Ni coating, it was obvious that after 35 minutes that the Ni deposition reaction was complete.

Figure 4–11 shows the second Ni coating. Only powder that was coated with Ni during the first deposition was coated with Ni a second time; the first coating appeared broken and very porous. In contrast, the second Ni coating was more uniform and complete. While the Ni thickness seemed to increase, the Ni coating as a whole was not uniform and therefore unacceptable for cold spraying. Figure 4–12 shows an optical cross section for the triple Ni coated hBN powder. As shown in the figure, there is no distinct evidence of the three separate Ni coatings. Only a small percentage of the hBN powder is coated with Ni and it appears to be the same particles which were coated during the initial Ni deposition. In figure 4–12, a distinct transition between two coatings can be seen, although it cannot be determined which coatings they are.

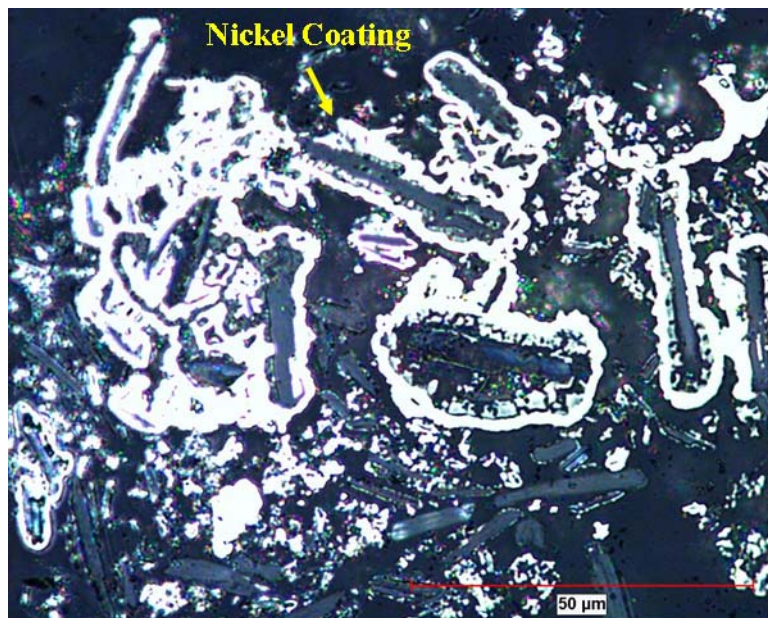


Figure 4–11: Optical image of milled 20 μm hBN coated with Ni twice

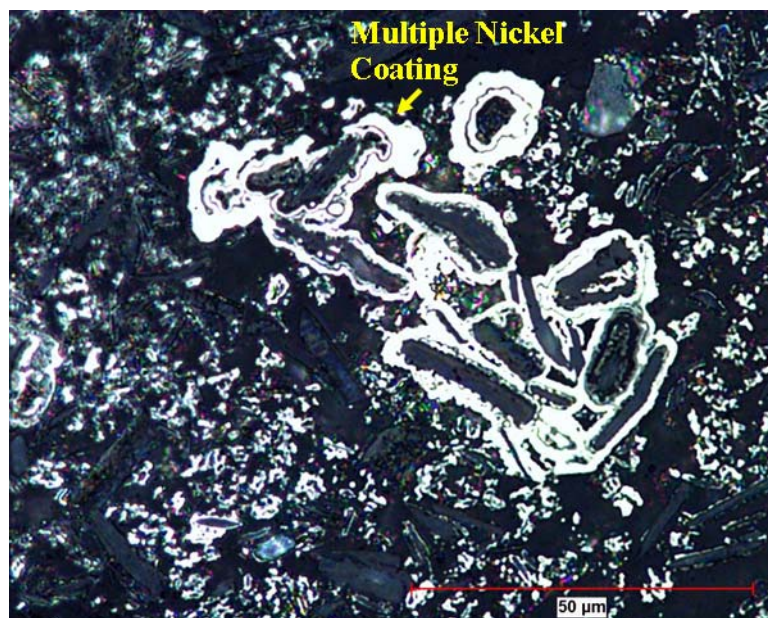


Figure 4–12: Optical image of milled 20 μm hBN coated with Ni three times

4.1.10 Ni Deposition on Milled 20 μm hBN – Increased Solution to Powder Ratio

The Ni deposition on the milled 20 μm hBN seemed to work well for the initial coating, whereas multiple coatings did not seem to help the uniformity of the coatings. The next experiment which used an increased solution-to-powder ratio was conducted in efforts to deposit more Ni during the first coating. Here, 3g of hBN was prepared for use in 1500 ml of Ni solution. Although sonication and mechanical stirring was used to agitate the solution and the flask was cleaned with SC1 and SC2, Ni was deposited into one area of the flask which trapped some hBN particles; Ni then preferentially deposited on this area creating an agglomerate on the order of millimeters. Figure 4–13 shows a cross section of Ni coated hBN which was stuck to the flask during the electroless

deposition procedure. In this particular area a thick coating of Ni was deposited onto the hBN. Figure 4–14 shows other hBN particles from the same deposition which were not uniformly coated with Ni.

It is plausible that the standard solutions were contaminated and did not clean the flasks properly. If metallic ions were still present on the glass surface from previous depositions after cleaning, then Ni from the solution would be apt to deposit onto the flask. In this case, while Ni was being deposited onto the flask, hBN particles became trapped resulting in the thick coating of Ni. As can be seen in figure 4–13, the Ni coatings of different hBN particles are connected, thus forming large Ni-hBN agglomerates.

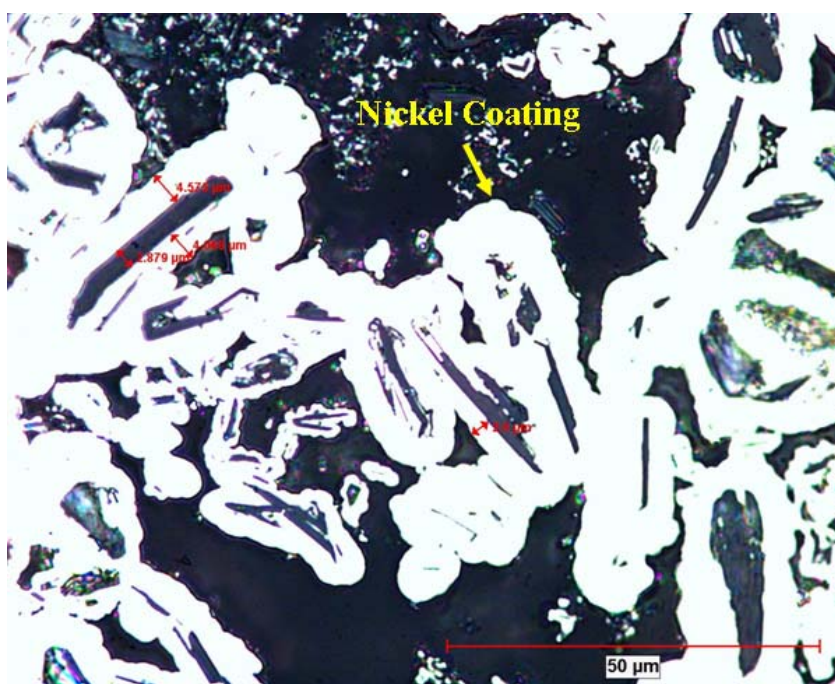


Figure 4–13: Milled hBN which received a thick Ni coating during a deposition with an increased solution to powder ratio

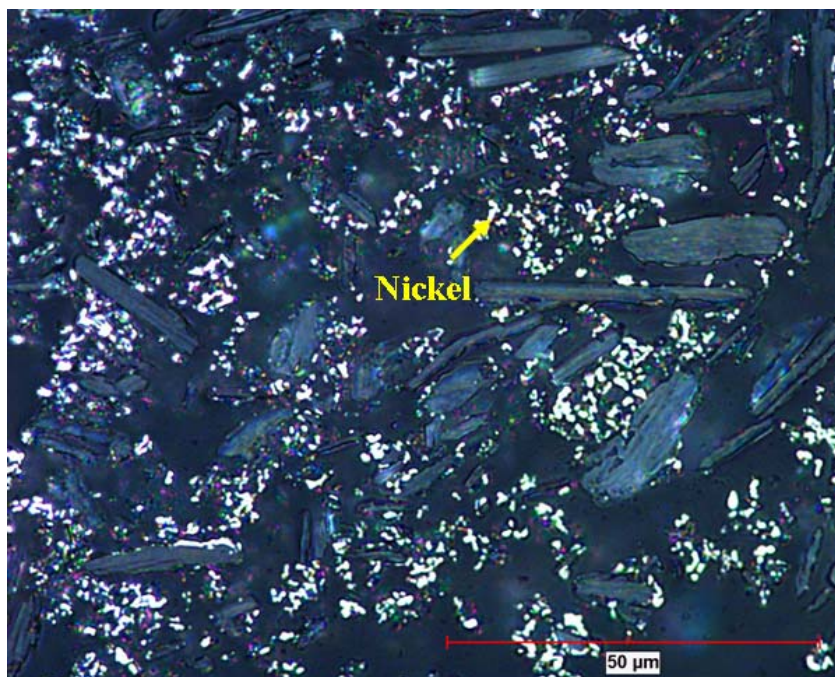


Figure 4–14: Milled hBN which did not receive a thick Ni coating during the same increased solution to powder ratio deposition

4.1.11 Large Ni Deposition on 20-30 μm hBN – Increased Solution to Powder Ratio

Although the Ni was not deposited uniformly on the hBN in the previous experiment, it was shown that thick layers can be deposited. This experiment is a replication of the previous experiment in an upscale version. To help eliminate any contamination and unwanted Ni deposition on the equipment, new batches of standard cleaning solution were prepared and used. In this case, 4000ml of Ni solution was prepared and a proportional amount of activated and sensitized hBN was added to the solution. Within 1 minute the solution began to turn grey and by 3 minutes the solution was foaming. At 3 minutes 10 seconds the solution was foaming so vigorously that it

began bubbling over the top of the flask. At 6 minutes, this subsided; figure 4–15 shows an optical image of some hBN particles which received a Ni coating.



Figure 4–15: Ni coating on hBN using 3g of powder and 4000 ml of electroless Ni solution

There are two major concerns with this experiment. Most importantly there is still insufficient Ni deposited uniformly onto the hBN. Secondly, there was a significant amount of solution and powder lost due to the overflow during the reaction. Obviously further adjustments to the deposition procedure need to be made.

4.1.12 Concentrated Electroless Solution

In this experiment an electroless solution was prepared having twice the chemicals per amount of distilled water (dH_2O). To further increase the ratio of solution to powder, the amount of Sn sensitized and Pd activated hBN was decreased to 1g for

500 ml of concentrated Ni solution. Once the powder was added to the solution, it was mechanically stirred in a sonic bath until it appeared that the reaction was complete. The deposition took place for 6 hours and there was some Ni deposited onto the flask. Figure 4-16 shows an optical cross section of the Ni deposited onto the hBN from the concentrated solution. The bright areas show the Ni surrounding the darker hBN particles. The very darkest particles that can be seen are Ni coated hBN particles that are not in the cross section plane of view since they are deeper in the transparent epoxy mount. In this deposition, the Ni thickness has not been significantly increased from previous experiments, but overall uniformity of the coatings was improved. Virtually every hBN particle was coated with Ni.

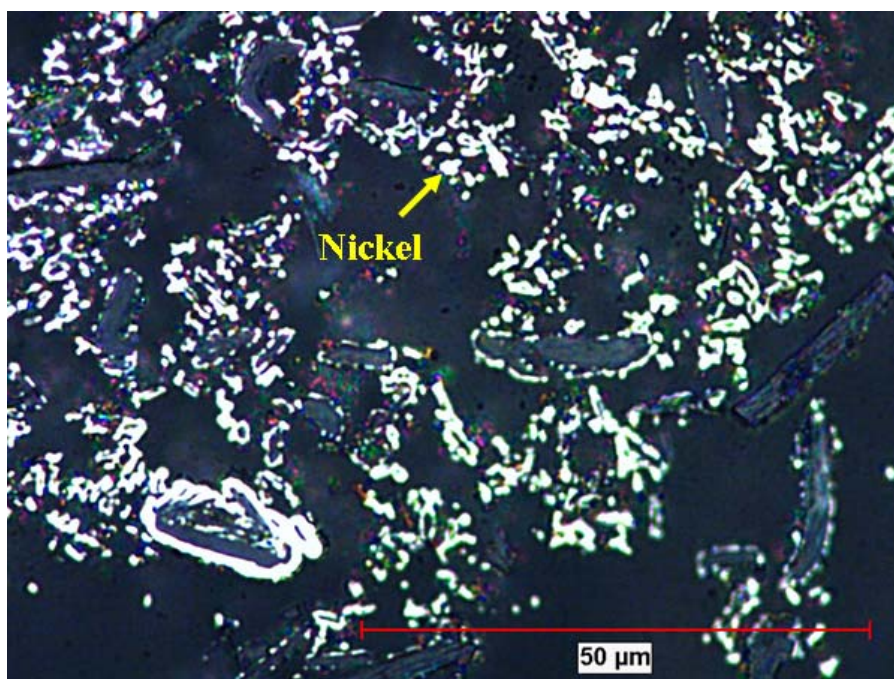


Figure 4-16: Ni deposited onto 20-30 μ m hBN using 500 ml of concentrated Ni solution and 1 g of 20-30 μ m hBN.

4.1.13 Up-scaled Ni coating 20-30 μ m hBN using Concentrated Ni Solution

The previous experiments showed some promising results, so they were repeated at a larger scale. Here, 6g of Sn sensitized and Pd activated hBN was used with 3000ml of concentrated Ni solution. The prepped hBN powder was added to the solution and observed for the first hour. Initially, there were no signs of Ni deposition. The powder was left in the flask, after 12 hours it was fully Ni coated.

Figure 4-17 shows an optical cross section of the powder at 500x magnification. The bright areas show the Ni surrounding the darker hBN particles. There is a significant Ni coating on the hBN particles. In fact, most of the hBN powder was completely surrounded in an envelope while only a few hBN particles received partial Ni coatings. Figure Figure 4-18 shows and optical cross section at 1000x magnification and a better view of some partially coated hBN particles.

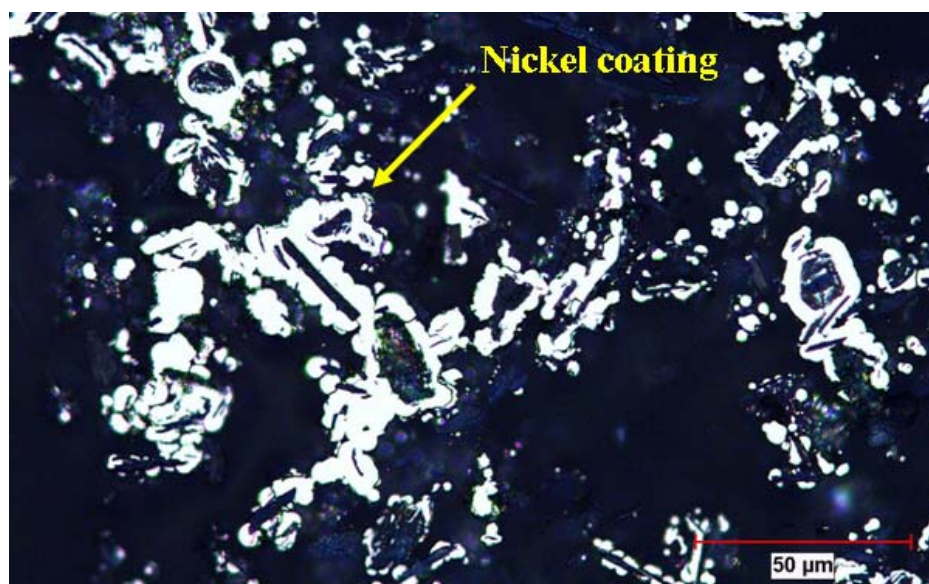


Figure 4-17: Ni coated hBN using 6g of 20-30 μ m hBN with 3000ml of concentrated Ni solution viewed at 500X magnification

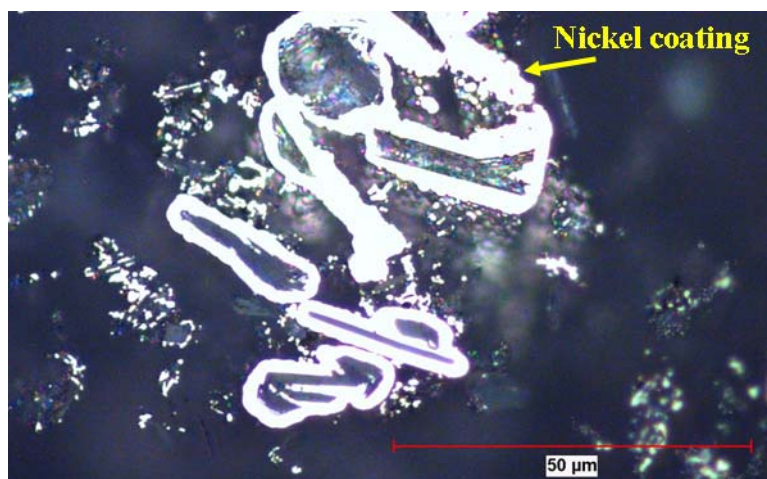


Figure 4-18: Ni coated hBN using 6g of 20-30μm hBN with 3000ml of concentrated Ni solution viewed at 1000X magnification

Ni coated hBN from this experiment was deemed acceptable for cold spraying when being admixed with pure Ni powder. Therefore, his electroless deposition procedure was repeated multiple times to produce sufficient powder for cold spray testing.

4.1.14 Up-scaled Ni coating 10μm hBN with concentrated Ni Solution

In efforts to deposit as thick a Ni coating as possible, only 0.05g of Sn sensitized - Pd activated hBN was used for the preliminary deposition using 10 μm hBN. Initial observations of the Ni deposition were similar to previous experiments in that after a short while, the solution slowly began to bubble before turning grey, and the bubbling energetically. When the deposition had appeared to stop, the powder settled, and was observed to be large flakes of Ni.

The experiment was repeated using 0.1g of the already sensitized-activated hBN. While being stirred, the reaction proceeded the same as in previous experiments. When complete, the stirrer was turned off and the solution sat undisturbed until all the powder settled to the bottom. This time, a considerable amount of powder (~25g) was produced. After being removed from the solution and dried, the powder was optically characterized.

Figure 4-19 shows a cross section of the Ni coated 10 μ m hBN powder viewed at 100x magnification. The bright areas show the Ni surrounding the darker hBN particles. Some of the darkest spots show particle pullout as a result of polishing. Clearly, a substantial amount of Ni has been deposited onto the 10 μ m hBN; some of the particles do not show an hBN core. This may be due to an off center cross section of the particle, or Ni being deposited into the solution rather than onto the hBN. From previous experiments, there is no evidence of Ni depositing into the solution alone. Therefore it is most likely that particles that do not show an hBN center are off-center cross-sections. Figure 4-20 shows a 1000x magnification of an individual particle. The core of the particle is comprised of not one, but several hBN particles. From a previous experiment, it has been observed that the Ni deposition can entrap multiple hBN particles to form agglomerates in sizes ranging in the millimeter range. A similar event would explain the multi-core center of the particle.

This procedure produced the thickest Ni coatings thus far. Given the success of this experiment, it was repeated to create sufficient Ni coated hBN for cold spraying.

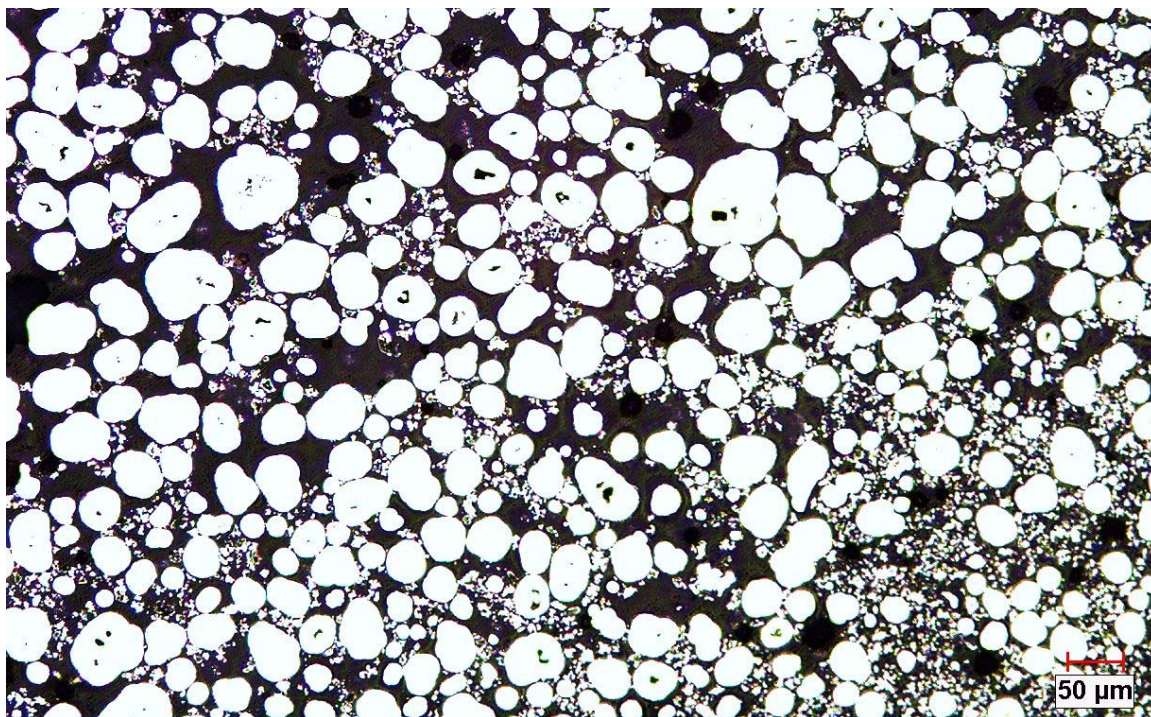


Figure 4-19: Ni coated 10μm hBN using 0.1g of hBN with 3000 ml of concentrated Ni solution viewed at 100x

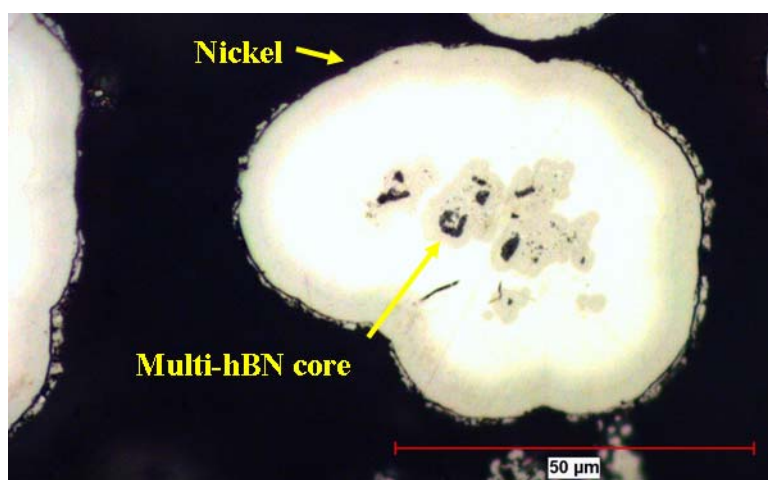


Figure 4-20: Ni coated 10μm hBN using 0.1g of hBN with 3000 ml of concentrated Ni solution viewed at 1000x

4.2 Powders for Cold Spray

4.2.1 Pure and Milled Nickel Powder

Figure 4-21 shows an SEM image of the pure 32 μ m electrolytic Ni used for cold spraying. Figure 4-22 is an EDS scan showing elements present. As can be seen in the figures, the powder is pure Ni. The high carbon content is due to the adhesive used to secure the powder and is shown by the darkest areas in the SEM image. The oxygen content may be due to Ni oxide and the organic adhesive used to mount the powder.

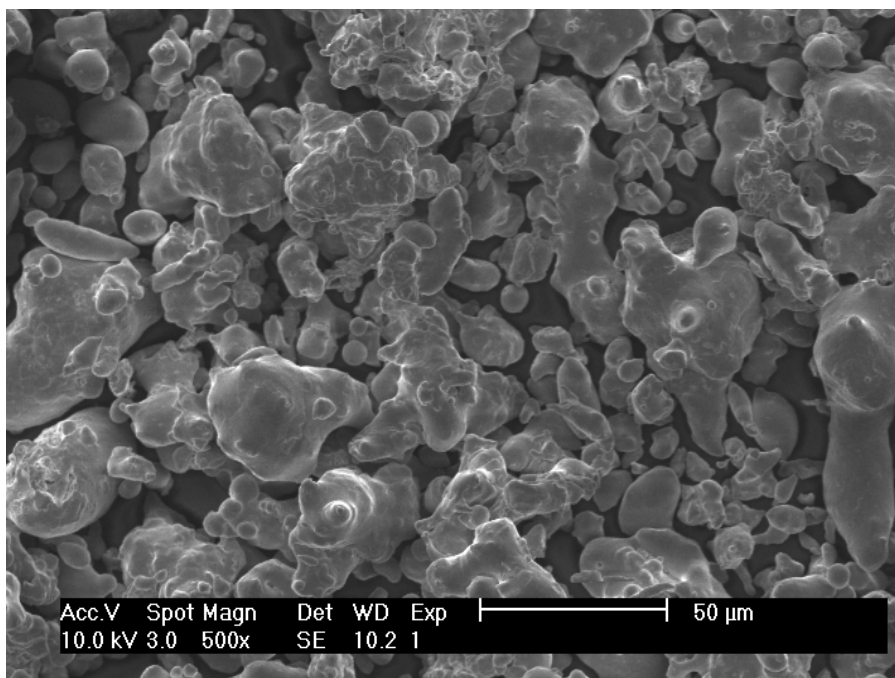


Figure 4-21: SEM image of pure 32 μ m electrolytic Ni supplied from Consolidated Astronautics

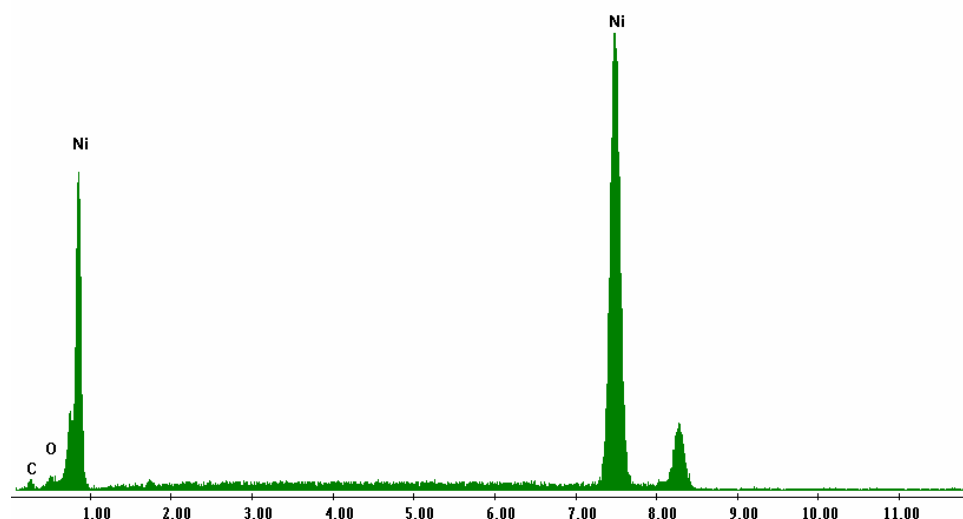


Figure 4-22: EDS scan of pure 32μm electrolytic Ni supplied from Consolidated Astronautics

Figure 4-23 shows an SEM image of the milled 32μm electrolytic Ni used for cold spraying. Figure 4-24 shows an EDS scan and the elements present. As can be seen in the figure the powder is pure Ni. The content of carbon and oxygen in the milled powder is found to be slightly higher than in the pure Ni powder, which most likely due to more of the adhesive being exposed during the EDS scan.

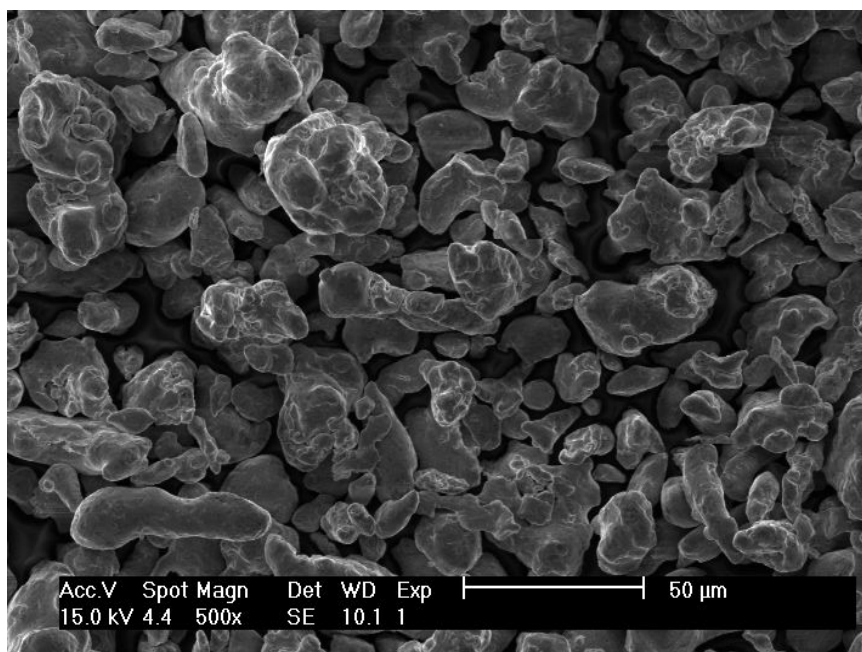


Figure 4-23: Milled Ni powder used for cold spraying

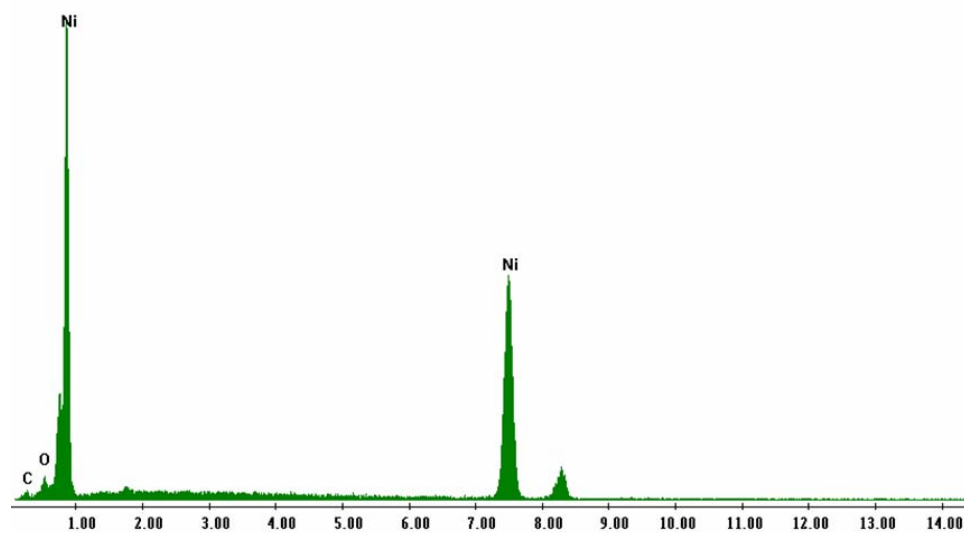


Figure 4-24: EDS scan of milled Ni powder used for cold spraying

4.2.2 Nickel Coated hBN(20-30 μ m) admixed with Pure Nickel and 10 μ m hBN

Figure 4-25 shows an SEM image of Ni coated hBN(20-30 μ m) admixed with pure Ni powder creating a blend with 50 vol% Ni-hBN powder. The larger, smoother, particles are pure Ni and the smaller particles are hBN with electroless Ni deposits. Some of the hBN particles only have Ni nucleation sites, meaning that the particle is not completely coated. Similarly, figure Figure 4-26 shows an SEM image of Ni coated hBN(20-30 μ m) admixed with pure Ni powder making a 30 vol% blend. The pure Ni particles can clearly be identified as the smoother and larger particles, whereas the Ni coated hBN can be identified as the smaller and more jagged particles. As can be seen in both images some of the hBN particles only have Ni nucleation sites.

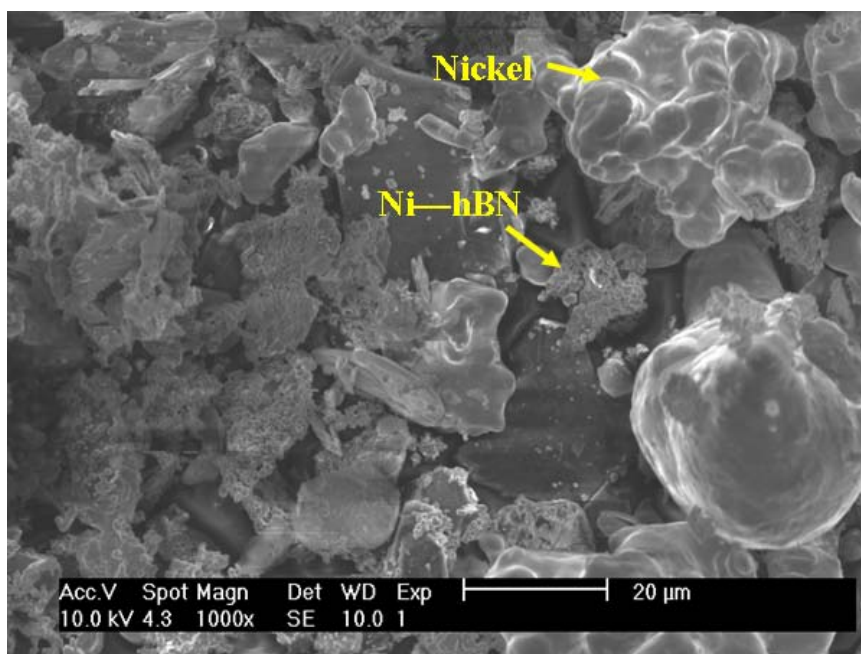


Figure 4-25: Ni coated hBN (20-30 μ m) admixed with pure Ni (50 vol%)

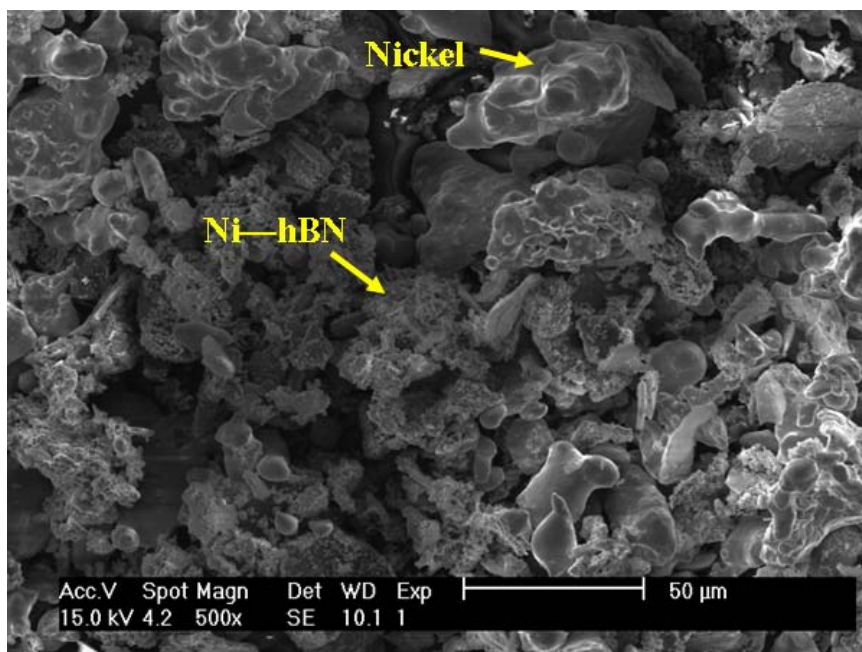


Figure 4-26: Ni Coated hBN (20-30µm) admixed with pure Ni (30 vol%)

Figure 4-27 is an SEM image of thick Ni coated 10 µm hBN which was the product of the electroless procedure followed in procedure 3.2.14. Unlike Ni coated hBN from previous experiments, this powder is fully coated with Ni. The SEM imaging shows that there was no exposed hBN visible. Although the coatings are not entirely uniform, the hBN seems to be completely coated.

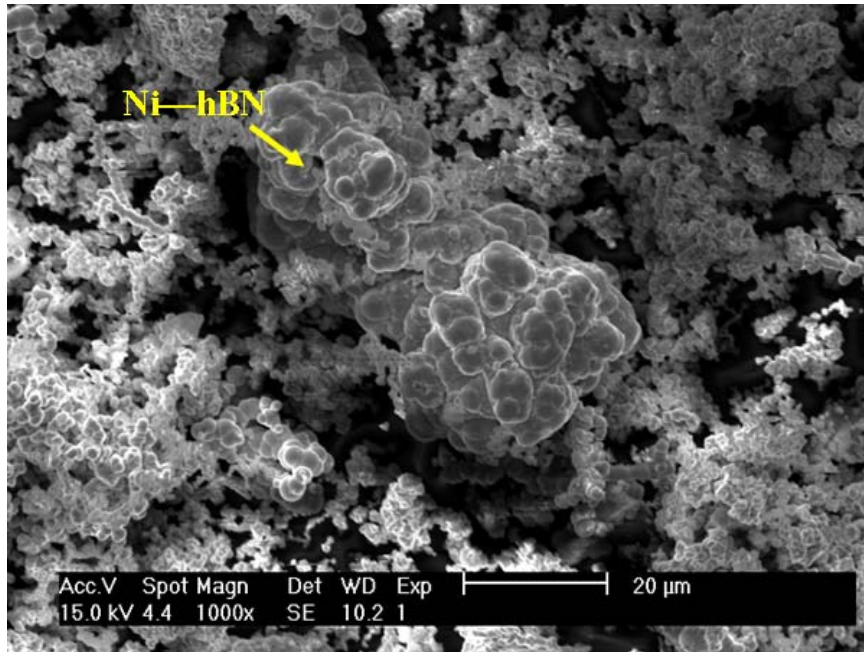


Figure 4-27: 10μm hBN fully coated with Ni

4.3 Characterization of Cold Spray Coatings

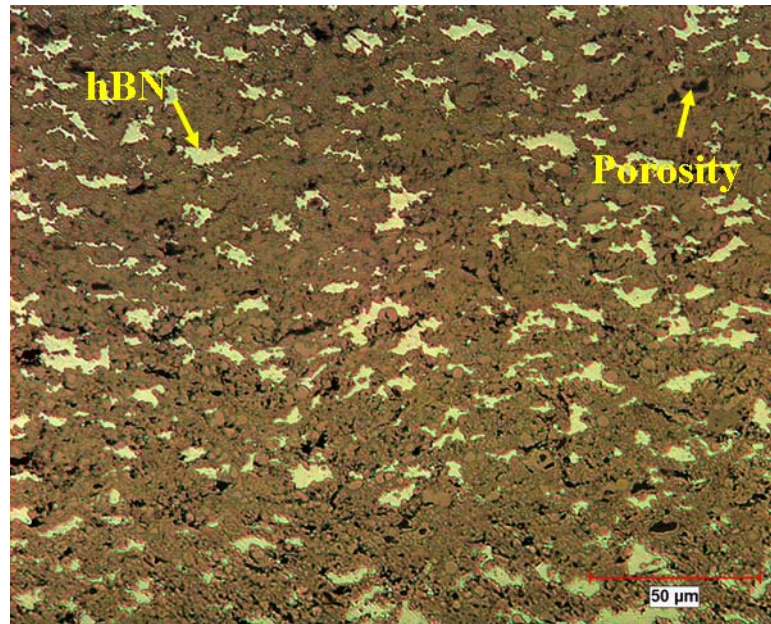
The cold spray coating thickness and the post spray mass of the substrate was measured immediately after processing; table -2 lists the coating thickness and mass gain of the substrates. In contrast, cold spray deposition using the thin Ni coated hBN produced insignificant coatings, so only optical imaging was used for further characterization. Cold spray depositions using pure Ni, milled Ni, and thick Ni coated hBN did produce coating and were further analyzed optically, with SEM,

Table 4-2: Thickness of cold spray coatings

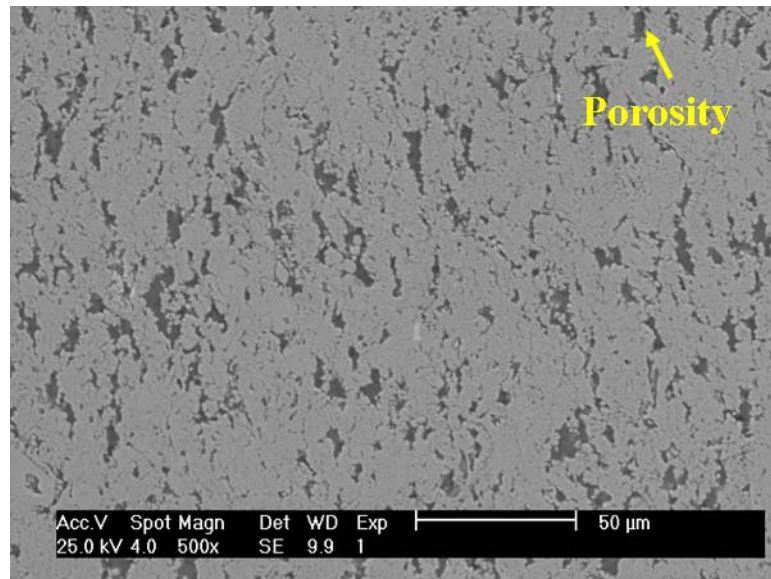
Powder	Gas Type	Gas Temp (°C)	Traverse Rate (mm/sec)	9 pass thickness (μm)	6 pass thickness (μm)	3 pass thickness (μm)	Wt. Gain (g)
Ni - hBN (10μm)	N ₂	500	20	755	643	280	2.1922
Ni - hBN (10μm)	He	188	20	0	5	25	0.2552
Ni - hBN (10μm)	He	24	20	280	165	94	0.9417
Ni - hBN (10μm)	He	188	50	0	0	0	0.2293
Pure Ni	N ₂	500	20	540	279	107	2.1077
Milled Ni	N ₂	500	20	404	285	107	1.4959
50 vol% Ni-hBN (20-30μm) : Pure Ni	N ₂	500	20	64	0	10	0.0032
50 vol% Ni-hBN (20-30μm) : Pure Ni	He	189	20	102	142	43	0.0000
30 vol% Ni-hBN (20-30μm) : Pure Ni	N ₂	500	20	5	45	0	0.0264
30 vol% Ni-hBN (20-30μm) : Pure Ni	He	183	20	94	262	160	0.4213

4.3.1 Thick Nickel Coated 10μm hBN

The Ni coated 10μm hBN was first sprayed with N₂ since there was a limited supply of He available. N₂ was used at 500°C and resulted in uniform coatings which increased in thickness with the number of passes. Successful cold spray coatings suggest that Ni coatings on the hBN particles are thick enough to provide the necessary ductile medium for particle-substrate adhesion. Since satisfactory coatings were produced, it was decided to continue with other powders. Figure 4-28 displays optical and SEM images showing polished cross sections of the cold spray coatings. An EDS scan was taken of the full SEM image and is shown in figure 4-29.



(a)



(b)

Figure 4-28: (a) Optical image and (b) SEM image of coatings consisting of Ni coated 10 μm hBN sprayed with 500°C N₂

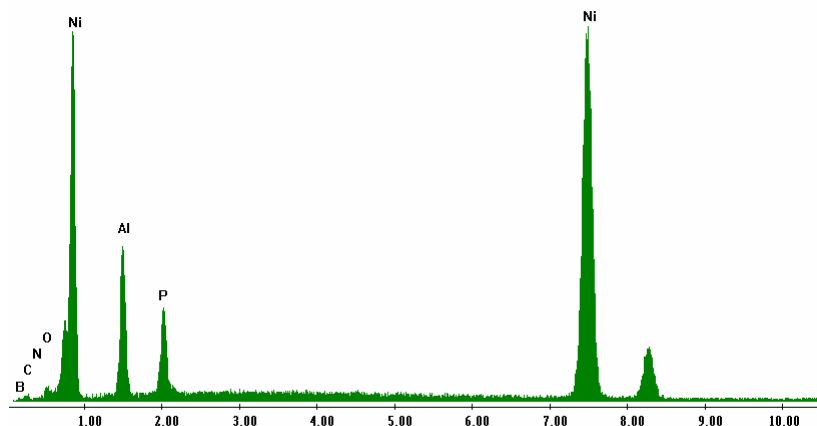


Figure 4-29: EDS plot of the Ni coated 10 μ m hBN cold spray coating sprayed with N₂

The presence of boron (B) and nitrogen (N) confirms that hBN has been incorporated into the cold spray coating and that the lighter colored areas in the optical and SEM images are hBN particles. Voids in the coatings caused by porosity and hBN removal allow alumina particles to become imbedded, resulting in the high aluminum and oxygen content shown.

Helium was used as the process gas for subsequent sprays of Ni coated 10 μ m hBN. Initially the maximum process temperature of 200°C was set for He. The nozzle temperature showed little signs of increasing after 188°C, so this it was decided to continue spraying at 188°C. These parameters resulted in negligible coatings thicknesses despite the weight gain of the substrates. Figure 4-30 shows optical and SEM images of the cold spray coating. Imaging shows that a thin coating was produced, but unlike the coatings produced with N₂, there is not a uniform distribution of hBN particles. The optical image shows some hBN imbedding within the coating. An EDS scan was taken to determine the presence of hBN. Results are plotted in figure 4-31 which show no

presence of hBN. It is possible that the He provided a sufficient velocity that the entire particle shattered upon impact, releasing the inner hBN particles. Only hBN particles entrapped by incoming Ni-hBN particle remain in the coating resulting in negligible amount of hBN incorporated into the coating.

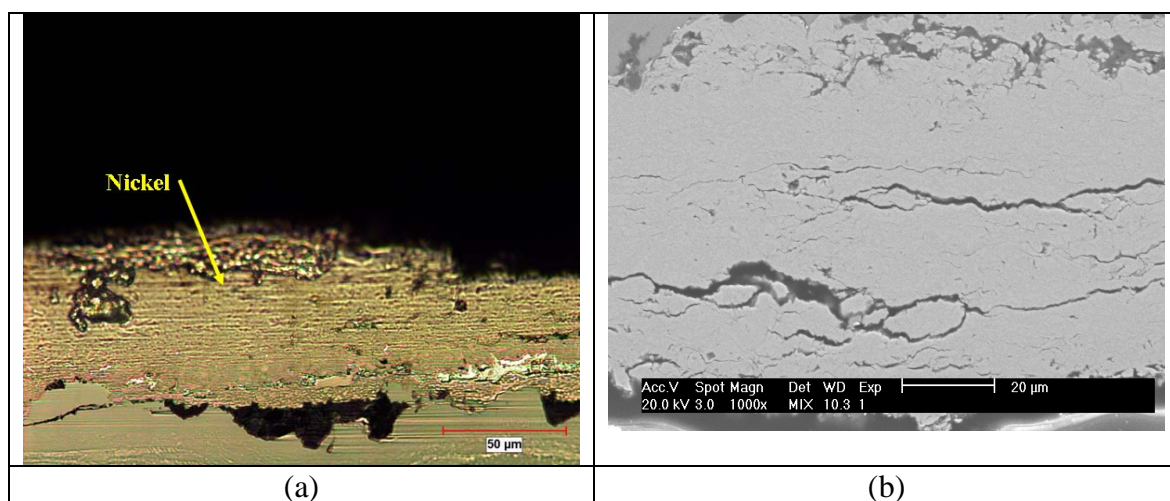


Figure 4-30: (a) Optical image and (b) SEM image of coatings consisting of Ni coated 10µm hBN sprayed with 188°C He and a 20 mm/sec traverse rate

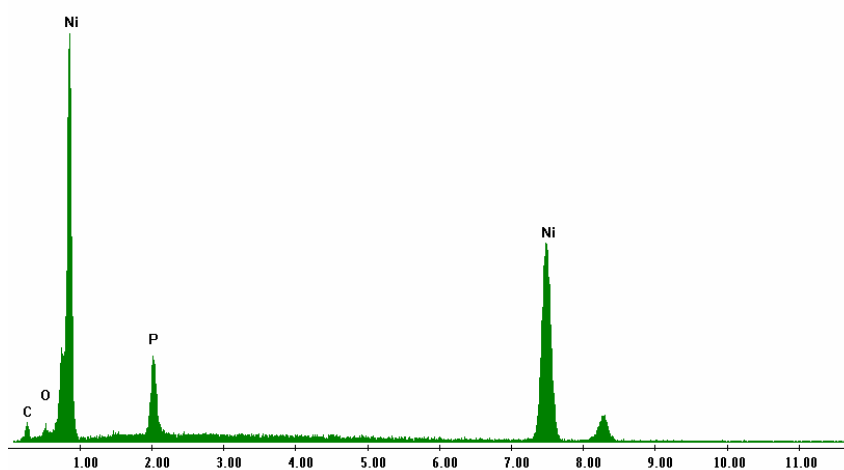


Figure 4-31: EDS plot of Ni coated 10µm hBN cold spray coating sprayed with He at 188°C

The next deposition trial used the same thick Ni coated 10 μ m hBN powder with 188°C He as a process gas. In an effort to decrease any self-grit-blasting effects, the traverse rate of the nozzle was increased from 20mm/sec to 50 mm/sec. This decreased the time particle flow was in contact with coatings deposited from preceding passes. Figure 4-32 shows optical and SEM images of the cold spray coating, neither of which show evidence of hBN particles imbedded within the cold spray coating. Figure 4-33 displays an EDS scan of the SEM image shown in figure 4-32. There are no peaks associated with boron to nitrogen which confirms the lack of hBN within the coating. The increased traverse rate decreased the likelihood of entrapping shattered hBN particles resulting in less hBN incorporation into the coating.

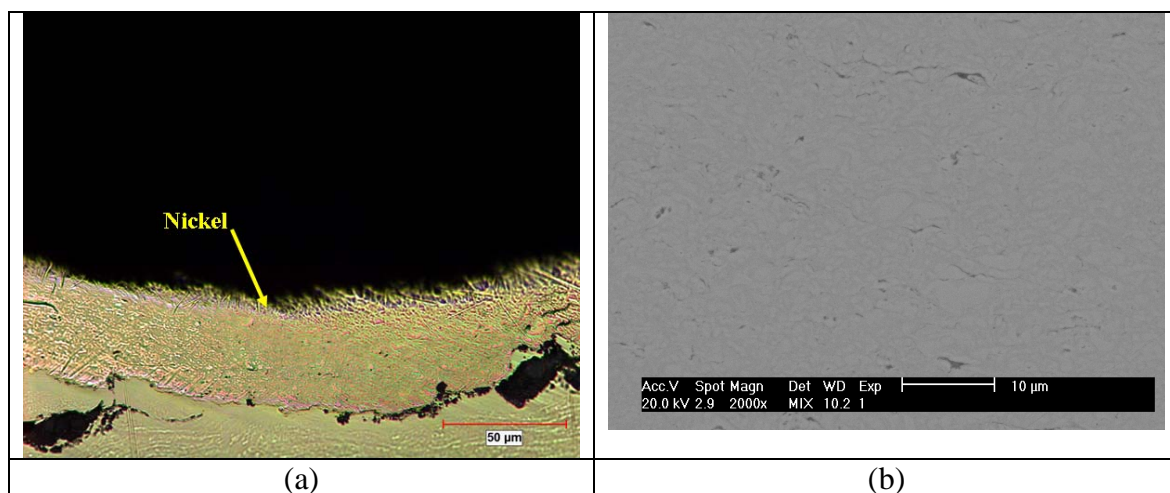


Figure 4-32: (a) Optical image and (b) SEM image of coatings consisting of Ni coated 10 μ m hBN sprayed with 188°C He and a 50 mm/sec traverse rate

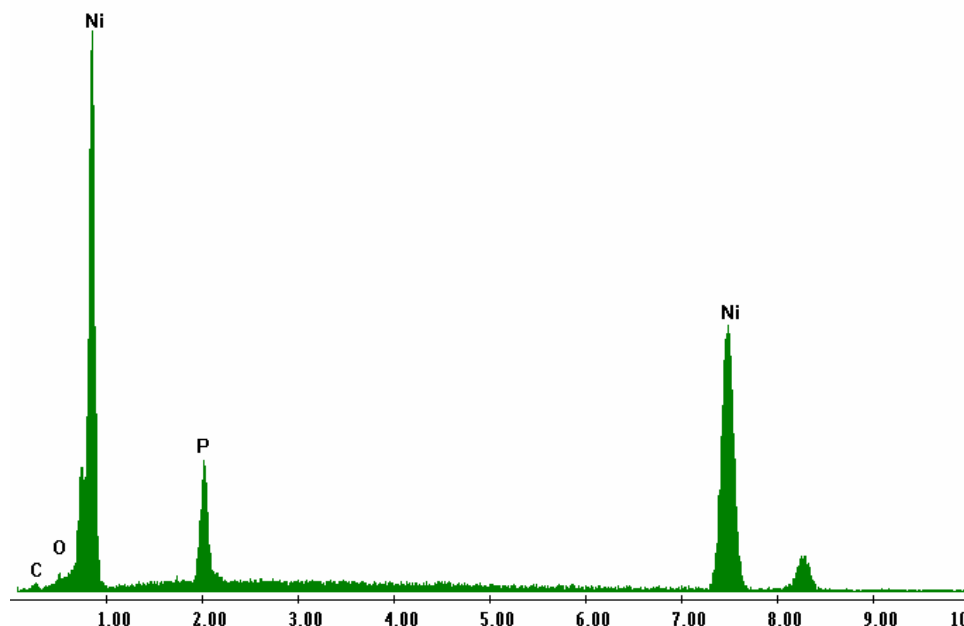
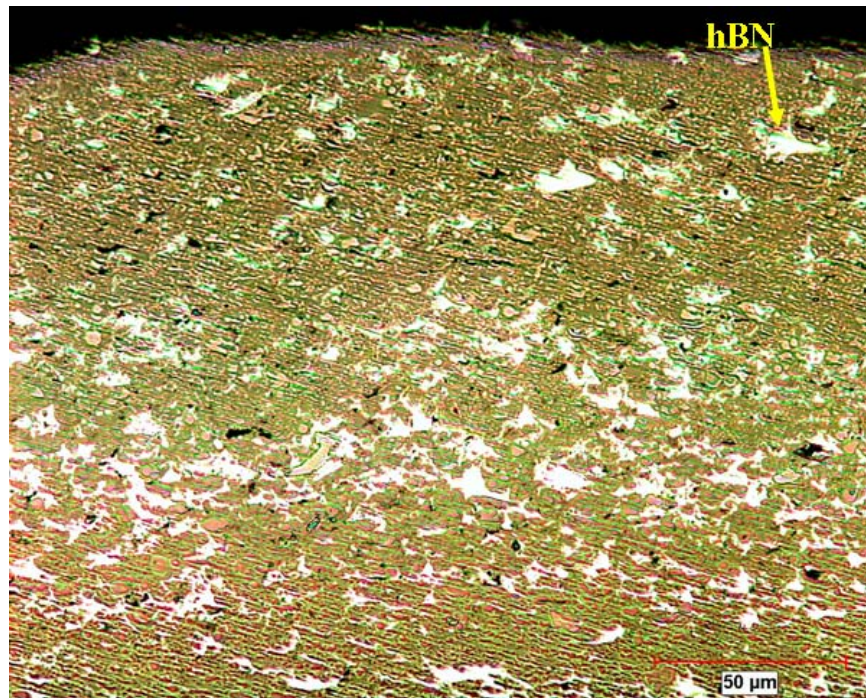
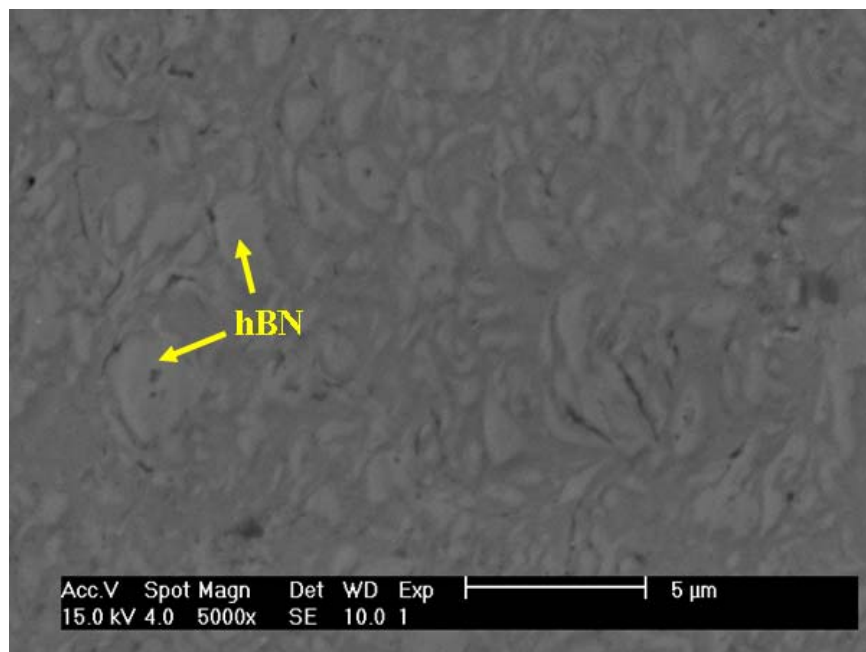


Figure 4-33: EDS plot of Ni coated 10 μ m hBN cold spray coating sprayed with He at 188°C with a 50 mm/sec traverse rate

The temperature of the He was reduced to 24°C for the next deposition of Ni coated hBN in order to reduce the velocity of the particles in hopes of keeping them intact during deformation. After 9 passes, of the cold spray coating was 180 μ m thick. Figure 4-34 shows optical and SEM images of the cold spray coatings produced. The optical image shows similar distribution of the hBN as compared to the coating produced with 500°C N₂. The SEM image shows small hBN particles, much less than 10 μ m, incorporated into the coating. The use of He may have increased the velocity of the particles enough to result in the shattering of some Ni-hBN particles upon impact. The debris was then trapped within the coating. Figure 4-35 is an EDS plot of the SEM image shown in figure 4-34 confirming that the lighter colored areas are in fact hBN particles.



(a)



(b)

Figure 4-34: (a) Optical image and (b) SEM image of coatings consisting of Ni coated 10μm hBN sprayed with 24°C He

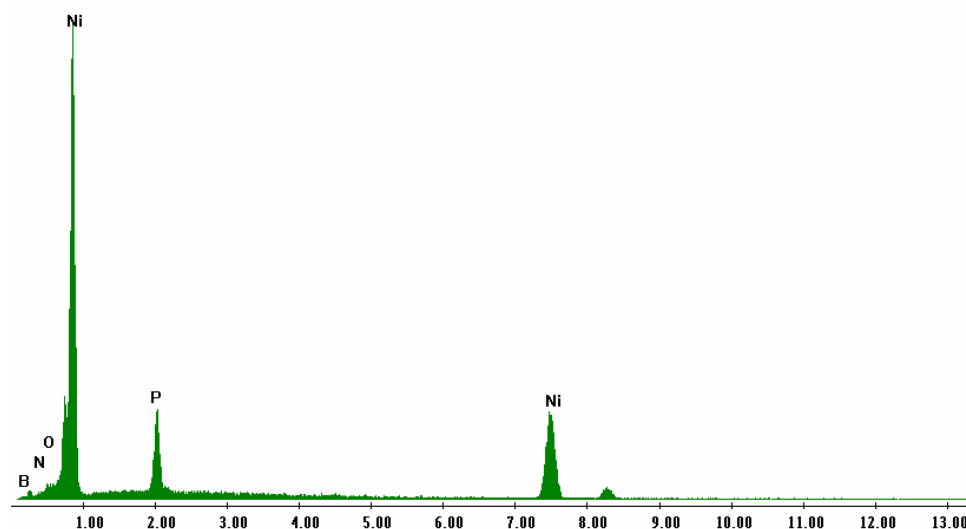
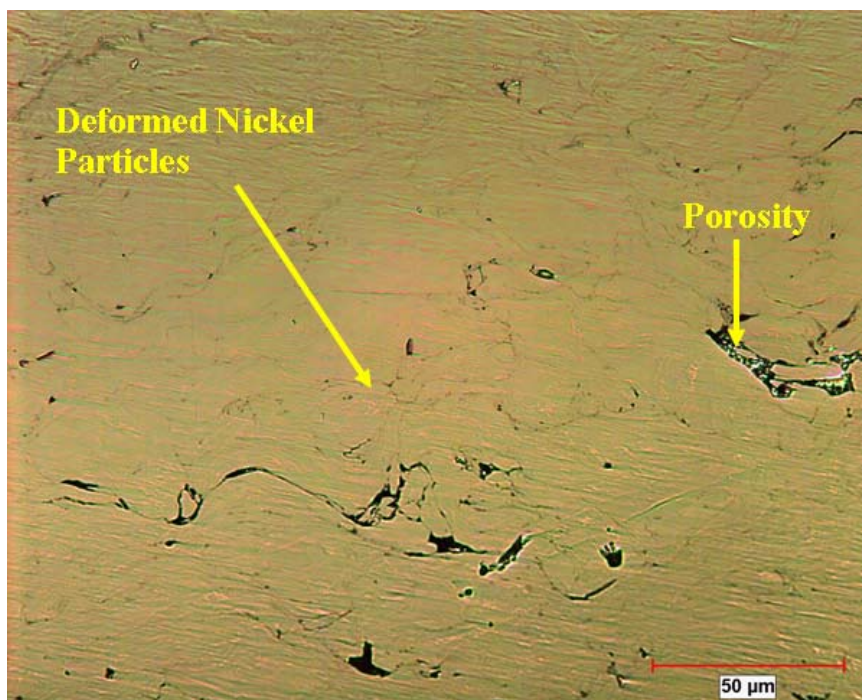


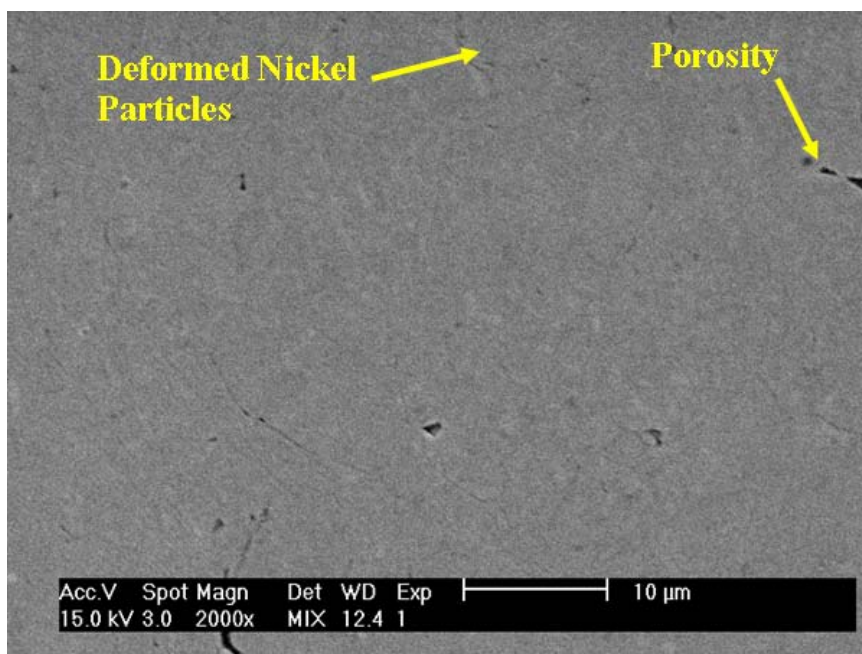
Figure 4-35: EDS plot of Ni coated 10 μ m hBN cold spray coating sprayed with He at 24°C

4.3.2 Pure Nickel and Milled Nickel Coatings

Pure Ni powder was sprayed with N₂ at 500°C. Again, coatings were produced, but the thicknesses were slightly less when compared to the thick Ni coated 10 μ m hBN. Figure 4-36 shows optical and SEM images of polished cross sections of the pure Ni cold spray coatings. Figure 4-39 shows an EDS scan of the coating shown in figure 4-37 (b). The EDS scan shows no signs of contamination caused by grit blasting or polishing.



(a)



(b)

Figure 4-386: (a) Optical and (b) SEM image of pure Ni cold spray coatings

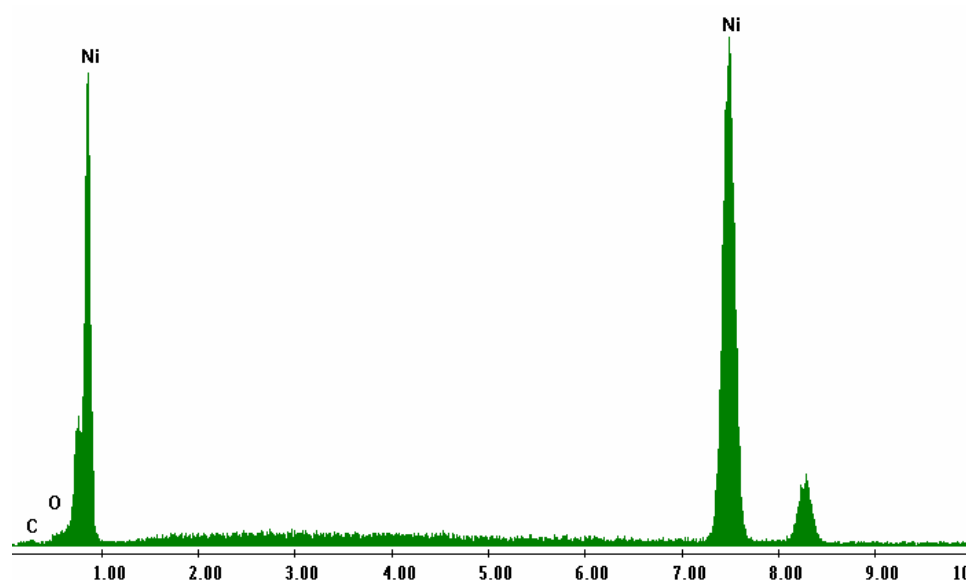
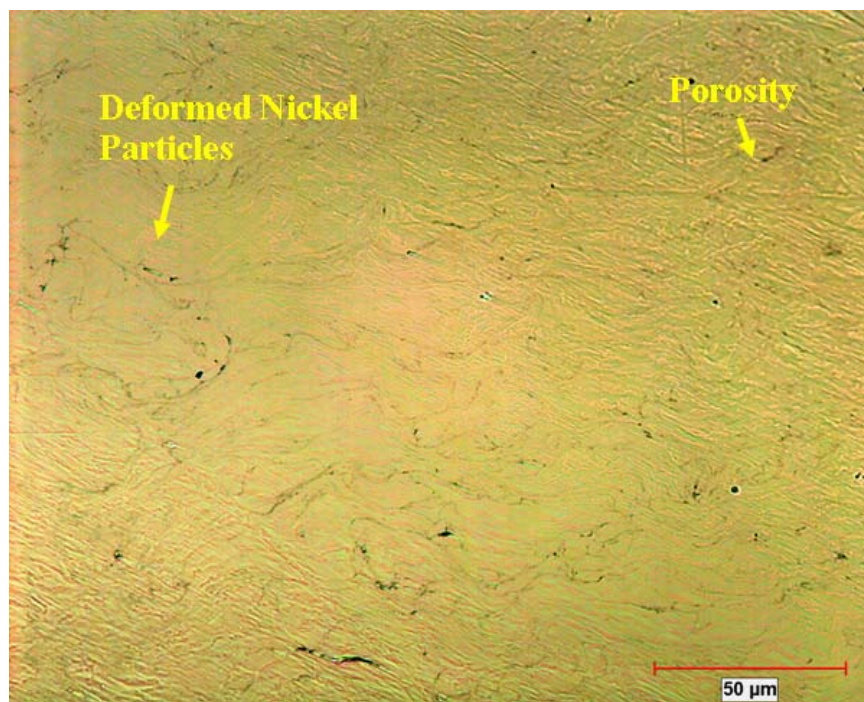
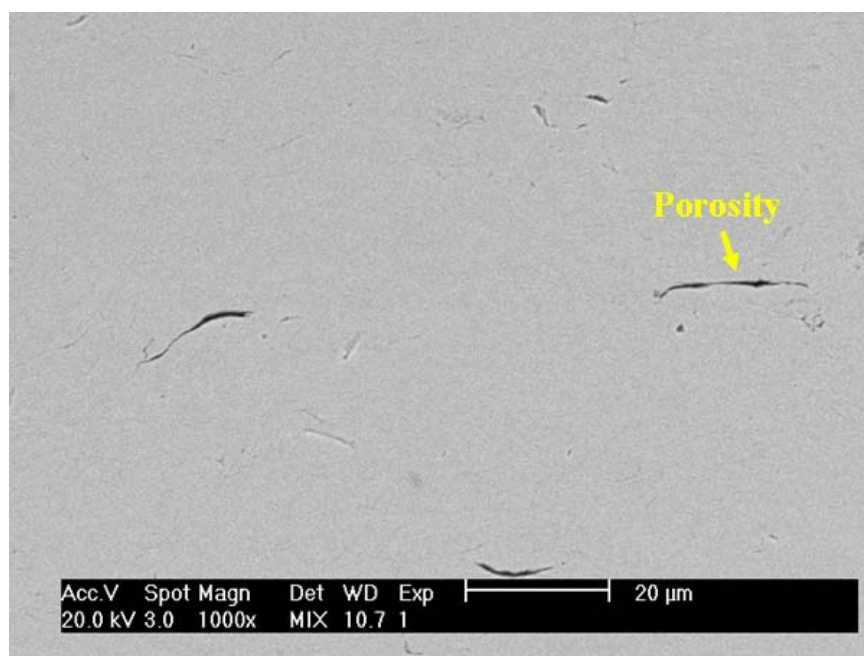


Figure 4-397: EDS plot of the pure Ni cold spray coating

Spraying of milled Ni powder at 500°C produced similar coatings to the pure Ni powder with the exception of the 9 pass procedure. Unlike the pure Ni powder coatings, the milled Ni powder showed very little increase in coating thickness from the 6 pass coating. This may be due to the work hardening of powder as a result of milling. Figure 4- shows optical and SEM images of polished cross sections of the cold spray coating produced by using milled Ni powder and N₂ as a process gas. Deformed particles can be distinguished by black outlines. Larger black areas show porosity within the coating. Figure 4-39 is an EDS plot which confirms that the coating is Ni and that insignificant contamination has been introduced.



(a)



(b)

Figure 4-38: (a) Optical and (b) SEM image of milled Ni cold spray coating

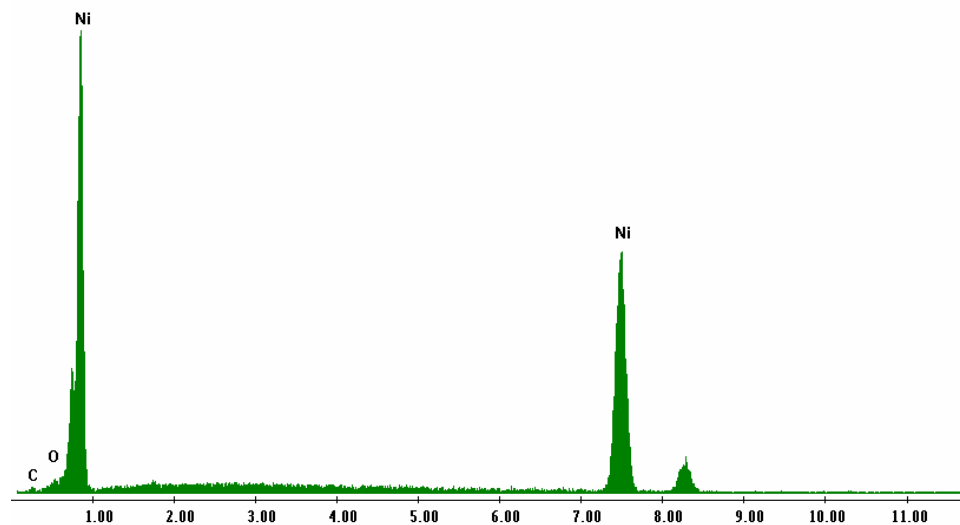


Figure 4-39: EDS plot of the milled Ni cold spray coating

4.3.3 30 vol% Ni coated hBN (20-30 μ m) admixed with Pure Ni

The 30 vol % mixture of thin Ni coated 20-30 μ m hBN was the next powder to be sprayed. Figure 4- shows results from the first attempt to create a coating used N₂ as a process gas, and the second using He as a process gas. The use of He resulted in a trivial coating thickness less than 75 μ m thick with no signs of 20-30 μ m hBN. Optical imaging provided sufficient characterization and no further investigation of the coating was necessary.

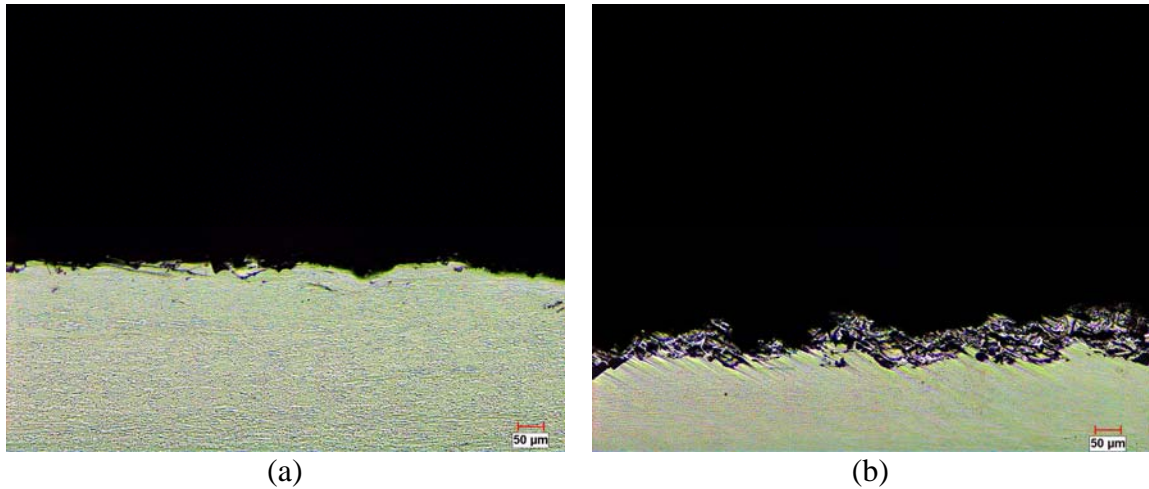


Figure 4-40: Optical images of 30 vol% Ni – hBN admixed with Ni and sprayed with (a) N_2 and (b) He

4.3.4 50 vol% Ni coated hBN (20-30 μ m) admixed with Pure Ni

Thin Ni coated hBN admixed with 50 vol% of pure Ni was sprayed next. As before, N_2 was the first process gas to be used followed by He. Figure 4-40 show optical cross sections of polished coatings. As can be seen in the figures there is insignificant particle deposition on the Ti-6Al-4V substrate. This is a result of even less ductile media (Ni) present, in relation to the 30 vol% Ni-hBN, to aid Ni-hBN particle adhesion than in the previous deposition.

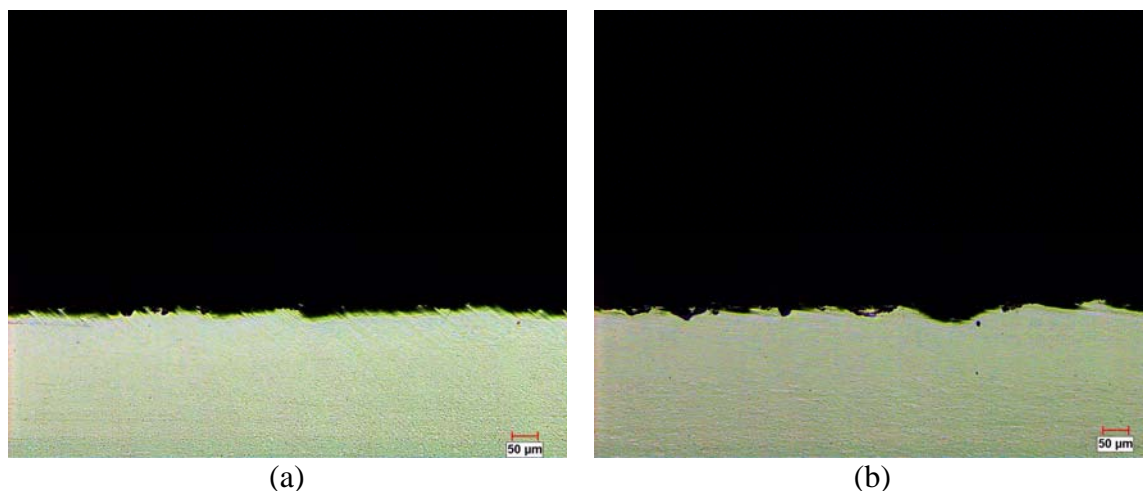


Figure 4-401: Optical image of 50 vol% Ni – hBN admixed with Ni and sprayed with (a) N₂ and (b) He

4.3.5 Bond Testing

Bond testing was performed on cold spray coatings at least 500µm thick to determine the adhesion strength to Ti-6Al-4V and cohesion within the coatings. Table -3 lists the results of the bond tests.

Table 4-3: Adhesion strength of cold spray coatings

Coating	Type of Failure	Bond Strength (MPa)
HYSOL Epoxy	Cohesive	53.8
Pure Ni	At Epoxy	27.1
Milled Ni	Cohesive	37.7
Thick Ni coated 10µm hBN Sprayed with 500°C N ₂	Adhesive	0.53
Thick Ni coated 10µm hBN Sprayed with 24°C He	Adhesive	2.9

The HYSOL epoxy was tested first to determine the adhesion strength of the epoxy. Fracture of the epoxy occurred at 53.79 MPa and is shown in figure 4-41.

Fracture of the pure Ni and milled Ni coatings occurred at 27.1 MPa and 37.7 MPa, respectively. In the case of the pure Ni coating, fracture occurred between the coating and epoxy interface as shown in figure 4-42. This is unexpected since the pure epoxy was able to withstand 53.8 MPa. As for the milled Ni, fracture occurred within the cold spray coating. Figure 4-43 shows some of the milled Ni coating on both bond slugs. Cold sprayed coating of the thick Ni coated 10 μ m hBN sprayed with 500°C N₂ and 24°C He had respective bond strengths of 0.53 MPa and 2.9 MPa. For both coatings, fracture occurred between the cold spray coating and substrate as shown in figure 4-44 and figure 4-45.

It should be noted that an additional bond slug was spray coated with thick Ni coated 10 μ m hBN using 500°C N₂. The number of passes was increased in an effort to create a sample with a thicker coating. Initially the coating looked as if it had successfully bonded to the substrate, so the coating thickness was measured and found to be 1.23mm. Within minutes of measuring the coating detached from the substrate. Figure 4-46 shows the substrate along with top and bottom views of the detached coating. The substrate shows almost no evidence of the cold spray coating indicating that the detachment occurred solely at the coating-substrate interface. This may be due to increased residual stress within the thicker coating. Similar stress within the other thick Ni coated 10 μ m hBN cold spray coatings may have caused the low bond strengths.



Figure 4-41: Fractured surface of HYSOL epoxy as a result of bond testing



Figure 4-42: Fractured surface of the pure Ni cold spray coating as a result of bond testing



Figure 4-43: Fractured surface of the milled Ni cold spray coating as a result of bond testing



Figure 4-44: Fractured surface of the thick Ni coated 10μm hBN sprayed with 500°C N₂ cold spray coating as a result of bond testing



Figure 4-45: Fractured surface of the thick Ni coated 10 μ m hBN sprayed with 24°C He cold spray coating as a result of bond testing

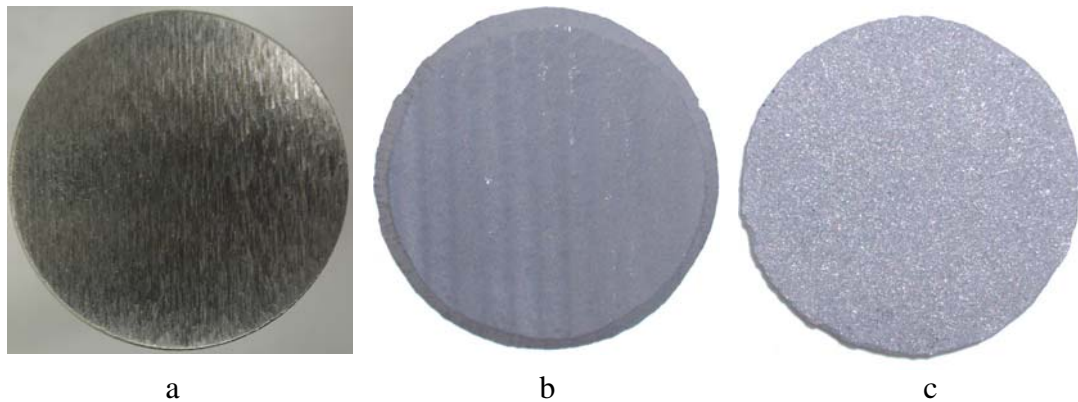


Figure 4-46: (a) Substrate, (b) top view, and (c) bottom view of thick Ni coated 10 μ m hBN bond test coating that detached

4.4 Friction Testing

Friction tests were conducted on a surface ground Ti-6Al-4V substrate (baseline) with a roughness of 106 μ m, on the pure Ni and milled Ni cold spray coatings, and on cold spray coatings made with thick Ni coated 10 μ m hBN sprayed with N₂ at 500°C, and He at 24°C. The surfaces of the cold spray coatings were not ground flat to avoid contamination and to keep the coatings as thick as possible. To avoid false readings the ball bearing was allowed to reciprocate until it wore a smooth track into the surface (within 15 sec). Other coatings were determined to have insufficient coating thickness and were not tested for friction.

Figure 4- displays the friction coefficients of the cold spray coatings. The Ti-6Al-4V sample was tested as the experimental control. The coefficient of friction (COF) of the thick Ni-coated hBN sprayed with 24°C He cold spray coating performed the best with a COF roughly half that of the Ti-6Al-4V. The thick Ni-coated hBN sprayed with 500°C N₂ produced the next lowest COF. The friction coefficient for the pure Ni cold spray coating was only slightly higher Ti-6Al-4V while the COF for the milled Ni sample was almost double.

When comparing the friction coefficients of the pure Ni and the coatings containing hBN, it is obvious that the presence of hBN within the coating is responsible for the reduced COF. The COF for the milled Ni coating is surprisingly high. It may be possible that the milling work hardened the particles and/or increased the amounts of Ni.

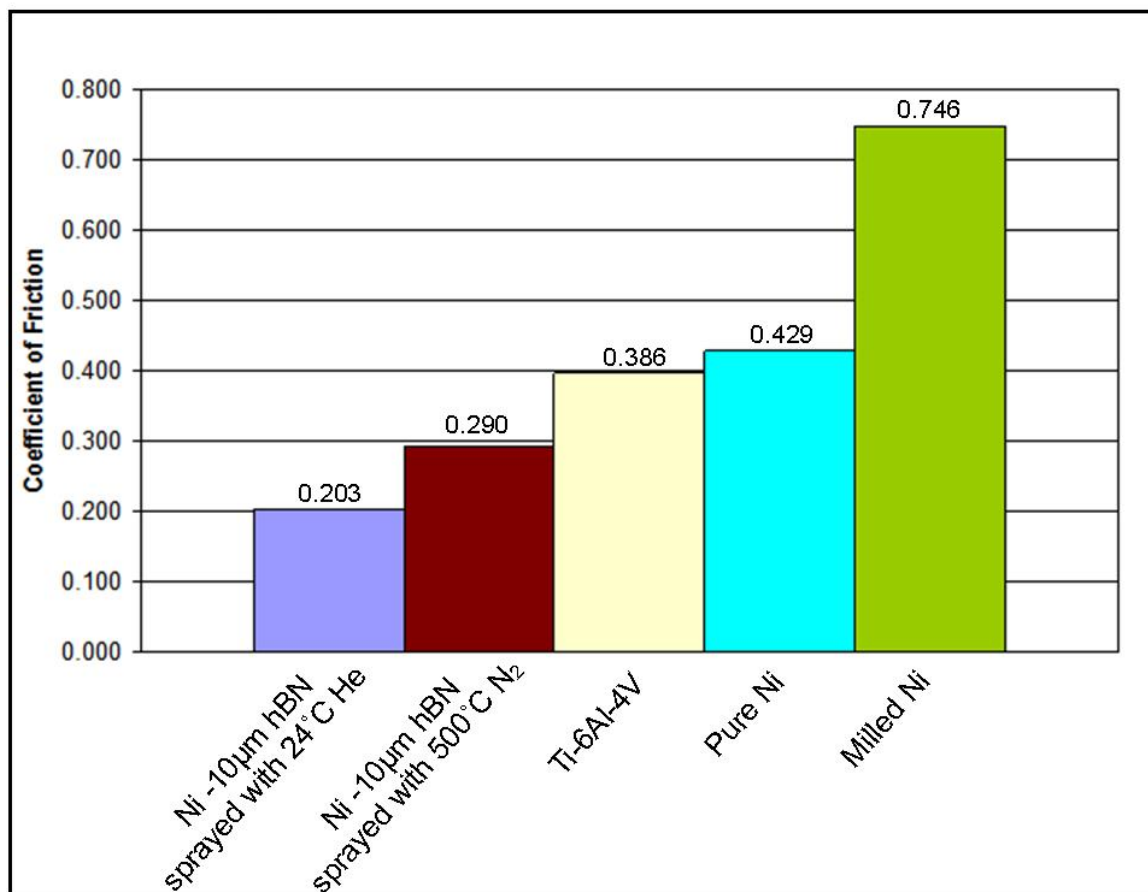


Figure 4-48: Friction coefficient results for cold spray coatings

4.5 Microhardness of Cold Spray Coatings

Table 4–4 lists the result of Vickers hardness (HV) testing which used a 300g applied load. The Ti-6Al-4V had an HV value of 365, and the pure Ni and milled Ni coatings had values of 253 and 250, respectively. The similarity among the Ni coatings is a result of the plastic deformation the particles endured during impact with the

substrate. Even though the milled Ni powder would have initially been work hardened more than the un-milled Ni powder, the end result is similar HV values.

The cold spray coating which incorporated hBN by using 500°C N₂ as a process gas had a slightly higher HV of 303. This suggests that the uniform distribution of intact hBN particles increased the hardness of the coating. The Ni-hBN coating which used 24°C He as a process gas had the highest HV value of 308. Even though the soft-lubricant particles would have a lower HV value on their own, distribution within a Ni matrix results in a coating with an overall higher HV value. This is due to the ceramic hBN particles preventing plastic deformation of Ni during the indentation. The coating which contained intact hBN only had a Vickers hardness value closer to the values of the Ni coatings. The incorporation of intact and shattered hBN within the coating produced by 24°C He is responsible of the higher HV value.

Table 4–4: Vickers hardness of cold spray coatings

Powder	Gas Type	Gas Temp (°C)	Traverse Rate (mm/sec)	Count	Standard Deviation	HV (300gf)
Ti-6Al-4V				5	22.81	365
Ni - hBN (10µm)	N ₂	500	20	10	20.3	303
Ni - hBN (10µm)	He	24	20	15	51.9	308
Pure Ni	N ₂	500	20	10	33.1	253
Milled Ni	N ₂	500	20	6	30.8	250

Chapter 5

Mechanics of Cold Spray Coatings

5.1 Work Hardening Background

Time independent deformations are classified as being either elastic or plastic. Objects, such as springs that are able to return to their initial state after a displacement are said to be elastic. Hooke's law explains that the force (F) required to cause the object to deform is equal to the displacement (x) multiplied by a proportionality constant (k), shown in Equation 4 [125]. Elastic deformation of a material is a reversible process, where upon removal of loading the material returns to its original state. The stress (σ) and strain (ϵ) are linearly related, and can be used to define a proportional constant known as the modulus of elasticity (E), as shown in equation 5.

$$F = kx \quad 4$$

$$E = \frac{\sigma}{\epsilon} \quad 5$$

Permanent deformation occurs beyond the elastic limit, where the stress-strain relation is no longer linear. This is where plastic deformation occurs. Elastic deformation ends once the material reaches its yield strength. When a load is applied beyond yielding, work hardening (strain hardening) occurs and increases the elastic limit of the material. Upon removal of the load, the material will relax following a line with the same slope as the elastic modulus. The elastic limit can be increased through work hardening until it

reaches the ultimate strength. Figure 5-1 illustrates the stress strain relation of ductile materials and identifies the proportional limit, yield point, work hardening region, and ultimate strength [126].

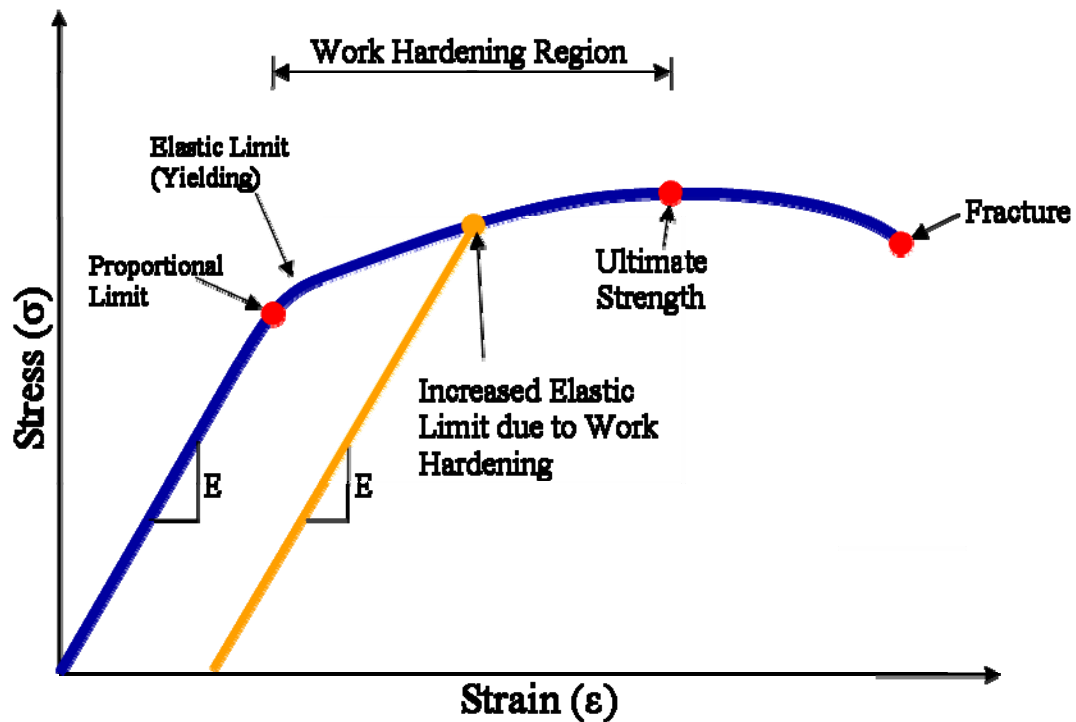


Figure 5-1: Engineering Stress strain diagram

It should be noted that work hardening is a result of dislocation formation within the crystal structure of the material. As deformation of the material increases, so does the number of dislocations. The accumulation of dislocations prevents movement within the crystal structure, causing an overall strengthening of the material, hence work hardening. However, a work hardened material becomes more brittle as it reaches the maximum allowed plastic deformation. Once the material can no longer deform, it fails [126].

Archard's equation describes the relation of wear resistance and hardness, shown in Equation 6. The volume (V) of material removed is usually inversely proportional to

the material hardness (H), and linearly proportional to the normal load (L) and sliding distance (S). A dimensionless constant (K) is known as the wear coefficient, which depends on other mechanical properties including the elastic modulus [127].

$$V = K \frac{LS}{H} \quad 6$$

Lubricant coatings typically have a low hardness, but effectively reduce wear due to the reduced coefficient of friction. As previously mentioned, wear resistant properties of the electroless Ni encapsulation are determined by the percent of phosphorous within the coating.

5.2 Work Hardening of Coatings

Milled and un-milled nickel powder has been examined in this study to determine the effect of work hardening on cold spray deposition. During milling, collisions between the stainless steel balls and powder cause plastic deformation of the powder, resulting in work hardening. Milling increased the elastic limit of the Ni powder to some value below the ultimate strength.

As previously mentioned the Cold Spray process relies on plastic deformation of particles to produce coatings. During deposition, the milled and un-milled particles experienced notably more plastic deformation than by milling alone. It may be speculated that the extreme deformation observed from particles colliding with the substrate significantly work hardened the Ni, and increased the elastic limit to a value at or near the ultimate strength. Some of the kinetic energy used to deform the particles is

transformed to thermal energy, which results in a softening of the material. It has been observed that the softening effect may overtake the work hardening, consequentially softening the coating [65].

The similarity between the sprayed milled Ni and un-milled Ni Vicker's hardness shown in table 5.1 can be explained by the initial deformation upon impact, which increased the hardness past any effect due to milling. Simultaneously, heating due to the extreme deformation softened the particles. The milled Ni powders were sprayed at an elevated temperature, which may have alleviated stresses within the particles, bringing them to a state more similar to that of the un-milled Ni powder. The combination of further heating and plastic deformation upon impact resulted in the milled and un-milled Ni powder converging to a similar hardness value.

Table 5.1: Vickers hardness of Ni and milled Ni coatings

Powder	Gas Type	Gas Temp (°C)	Count	Standard Deviation	HV (300gf)
Pure Ni	N ₂	500	10	33.1	253
Milled Ni	N ₂	500	6	30.8	250

5.3 Effect of Process Gas Temperature on Composite Powders

Successful bonding has been shown to occur only after a certain critical velocity has been reached, which depends on the temperature and thermomechanical properties of the sprayed material and substrate [65]. The initial temperature of the gases and the composite powders used had a significant effect on coating bonding.

Hexagonal boron nitride has been proven to retain its lubricious properties at high temperatures, as explained in the literature survey. This is due to the chemical and thermal resistance, in turn resulting in a relatively low coefficient of thermal expansion (CTE). On the other hand, Ni has a relatively high coefficient of thermal expansion. Coatings produced using the thick Ni coated hBN at 500°C N₂ were observed to have a high amount of porosity when viewing a polished cross section. Exposure to the 500°C N₂ may have resulted in separation of the Ni shell and hBN core particle. Bonds between the Ni encapsulation were broken as a result of the separation, resulting in the high percentage of particle pullout during polishing. If the separation of the coating occurred, hBN particle removal would also occur during friction testing, resulting in a friction coefficient closer to that of pure Ni; as observed.

Coatings produced using 24°C He exhibited less porosity when a polished cross section was optically viewed. The decreased porosity was a result of increased kinetic energy, which allow for further particle deformation. In addition, the low temperature gas may have aided bonding between the Ni coating and hBN particles, due to decreased thermal expansion during deposition. This increased adherence of hBN within the coating, resulting in decreased particle pullout and decreased coefficient of friction.

Chapter 6

Conclusion and Future Recommendation

6.1 Summary

This study investigated the use of electroless nickel deposition to encapsulate hexagonal boron nitride (hBN) in order to create a feedstock for Cold Spray capable of bonding to the substrate for self lubricating coating applications. hBN is a solid lubricant which is able to retain its lubricity at high temperatures and pressures making it ideal for applications in high performance machines. Since dovetail joints in jet engines are prone to fretting, the application of hBN based self lubricating coatings within the joint may significantly increase the service life of the engine by providing resistance to fretting.

The Cold Spray deposition process relies on the plastic deformation of particles onto the substrate to create metallurgical bonds. Brittle materials such as hBN fracture upon impact with the substrate instead of deforming plastically, thus inhibiting deposition. Encapsulation of the hBN, through an electroless nickel process provides the necessary ductile medium for bonding.

For the first time, hBN has been uniformly incorporated into a nickel matrix using Cold Spray deposition. The presence of hBN distributed uniformly within the cold spray coatings reduced the coefficient of friction and increased the hardness of the cold spray coatings.

6.2 Conclusions

The present work demonstrates that an appropriate balance of nickel thickness and uniformity on hBN powder, along with particle velocity resulted in particle-substrate bonding with homogeneous distribution of hBN within the cold spray coating. Based on the results from this work, the following can be concluded:

- Electroless nickel deposition can be performed on hBN with the use of catalyst coatings (SnCl_2 , PdCl_2), and that the coating process is autocatalytic. Increasing the amount of reactive chemicals within the electroless solution results in increased coating thickness and uniformity.
- A critical nickel thickness must be obtained before particle-substrate bonding occurs. Thinly coated particles fracture upon impact instead of plastically deforming.
- Work hardening of nickel powder by milling is insignificant when compared to the work hardening produced by plastic deformation upon impact with the substrate.
- Elevated process gas temperatures may separate the nickel encapsulation from hBN particles due to the difference in thermal expansion coefficients.

Detachment from the hBN reduces coating bonding and allows for easier hBN particle pullout, increasing the friction coefficient of the Cold Spray coating to a value closer to pure nickel.

- Sufficient coating thickness allows hBN particles to be incorporated into a nickel matrix via cold spray deposition. Incorporation of hBN reduces the coefficient of

friction of the overall coating, when compared to the Ti-6Al-4V substrate and pure nickel coatings.

- There is a window of acceptable velocities which result in bonding. Particles traveling below the critical velocity do not adhere to the substrate, and particles traveling above a maximum velocity fracture excessively upon impact.
- Coatings fabricated through a combination of fractured and intact particles showed increased size distribution and uniformity of hBN within the coating. Increased uniformity of hBN results in decreased friction coefficients and increased micro-hardness.

6.3 Future Recommendations

The nickel coated 10 μ m hBN sprayed with 24°C helium produced the best friction results due to the incorporation of shattered particles within the coating. The coefficient of friction may be reduced even further if the size of the original core hBN particle is decreased. This should result in an even more homogenous distribution of hBN within the coating. Another benefit of using smaller core hBN particles, while maintaining particle size, would be that higher deposition velocities could be used before particles fracture.

Further exploration of bonding as a function of nickel thickness is needed. Thicker nickel coatings would allow for more particle deformation upon impact, which may in turn improve adhesion properties of the coating. The number of bond tests conducted should be increased to obtain a more statistically valid result.

Variations to the electroless deposition parameters may improve wear resistant properties of the coatings. The reducing agent, sodium hypophosphite, incorporates phosphorous atoms into the nickel coating. The percent of phosphorous within the coating affects the wear resistance and corrosion resistance of the coatings. Further investigation could produce a nickel coating which displays maximum wear resistance.

Heat treatments conducted prior to cold spraying on the electroless nickel coated hBN feedstock may increase mechanical properties of the nickel coating. Likewise, post Cold Spray heat treatments could also be conducted to increase the mechanical properties of the nickel coating and to reduce residual stresses within the coating. This may improve wear resistance and adhesion properties.

Bibliography

1. Z.R. Zhou, L. Vincent, Lubrication in fretting - a review, *Wear*, 1999, **225-229**, p. 962-967
2. D.A. Lelonis, J.W. Tereshko, C.M. Anderson, Boron nitride - a high-performance alternative for solid lubrication, G.E. Company Ed., 2003. Pub. No. 81506
3. Y.W. Bae, W.Y. Lee, T.M. Besmann, C.S. Yust, P.J. Blau, Preparation and friction characteristics of self lubricating TiN-MoS₂ composite coatings, *Material Science and Engineering*, 1996, **A209** p. 372-376
4. N.M. Renevier, J. Hampshire, V.C. Fox, J. Witts, T. Allen, D.G. Teer, Advantages of using self-lubricating, hard, wear resistant MoS₂-based coatings, *Surface & Coatings Technology*, 2001, **142-144**, p. 67-77
5. R.S. Lima, A. Kucuk, C.C. Berndt, J. Karthikeyan, C.M. Kay, J. Lindemann, Deposition efficiency, mechanical properties and coating roughness in cold-sprayed titanium, *Journal of Materials Science Letters*, 2002, **21**, p. 1687-1689
6. A.E. Segall, A.N. Papyrin, J.C. Conway Jr., D. Shapiro, A cold-gas spray coating process for enhancing titanium, *Journal of Metals*, 1998, **50**(9), p. 52-54
7. P.J. Blau, Fifty years of research on the wear of metals, *Tribology International*, 1997, **30**(5), p. 321-331
8. S. Fourvy, K. Elleuch, G. Simeon, Prediction of crack nucleation under partial slip and fretting conditions, *Journal of Strain Analysis*, 2002, **37**, p. 549-564.
9. O. Jin, S. Mall, Shear force effects on fretting fatigue behavior of Ti-6Al-4V, *Metallurgical and Material Transactions*, 2004, **35A**, p. 131
10. M. P. Szolwinski, T. N. Farris, Mechanics of fretting fatigue crack formation, *Wear*, 1996, **198**, p. 93-107
11. J.C. Newman Jr., The merging of fatigue and fracture mechanics concepts: a historical perspective, *Progress in Aerospace Sciences*, 1998, **34**, p. 347-390
12. Y. Fu, J. Wei, A. Batchelor, Some consideration on the mitigation of fretting damage by the application of surface-modification technologies, *Materials Processing Technology*, 2000, **99**, p. 231-245

13. S.Fouvry, P. Dou, Ph. Perruchaut, A quantitative approach to Ti-6Al-4V fretting damage: friction, wear and crack nucleation, *Wear*, 2004, p 916-929.
14. E. Sauger, S. Fouvry., L. Ponsonnet, Ph. Kapsa, J.M. Martin, L. Vincent, Tribologically transformed structure in fretting, *Wear*, 2000, **245** p 39-52
15. C.H. Hager Jr., J.H. Sanders, S. Sharma, Characterization of mixed and grass slip fretting wear regimes in Ti6Al4V interfaces at room temperature, *Wear*, 2004 p 167-180.
16. J.M. Wallace, R.W. Neu, Fretting fatigue crack nucleation in Ti-6Al-4V, *Fatigue Fracture Engineering Material Structure*, 2002, **26**, p. 199-214
17. M. Ciavarella, G. Demelio, A review of analytical aspects of fretting fatigue, with extensions to damage parameters, and application to dovetail joints, *International Journal of Solids and Structures*, 2001, p 1791-1811.
18. A. L. Hutson, T. Nicholas, P. Goodman, Fretting Fatigue of Ti-6Al-4V under flat-on-flat contact, *International Journal of Fatigue*, 1999, **21**,p. 663-669
19. R.A. Antoniou, T. C. Radtke. (1997). Mechanisms of fretting-fatigue of titanium alloys, *Material Science and Engineering*, 1997, **A237** p. 229-240
20. W.A. Glaeser, B.H. Lawless, Behavior of alloy Ti-6Al-4V, *Wear*, 2001, **250**, p. 621-630
21. P.J. Golden, A.F. Grandt Jr. Fracture mechanics based fretting fatigue lif predictions in Ti-6Al-4V, *Engineering Fracture Mechanics*, Fracture mechanics based, **71**,p. 2229-2243
22. P.A. McVeigh, G. Harish, T.N. Farris, M.P. Szolwinski, Modeling interfacial conditions in nominally flat contacts for application to fretting of turbine engine components, *International Journal of Fatigue*, 1999, **21**, p. S157-S165
23. P.J. Golden, T. Nicholas, The effect of angle on dovetail fretting experiments in Ti-6Al-4V, *Fatigue Fracture Engineering Material Structure* 2005, **28**, p. 1169-1175
24. The Pennsylvania State University, Lecture 18: Titanium, *NMAT380*
25. C.H. Hager, J.H. Sanders, S. Sharma, Effect of high temperature on the characterization of fretting wear regimes at Ti6Al4V interfaces, *Wear*, 2006, **260**, p. 493-508
26. B.P. Conner, A.L. Hutson, L. Chambon, Observations of fretting fatigue micro-damage of Ti-6Al-4V, *Wear*, 2003, **255**, p. 259-268

27. Y. Fu, N.L. Loh, A.W. Batchelor, D. Liu, X. Zhu, J. He, K. Xu, Improvement in fretting wear and fatigue resistance of Ti-6Al-4V by application of several surface treatments and coatings, *Surface & Coatings Technology*, 1998, **106**, p. 193-197
28. L. Xue, A.K. Koul, M. Bibby, W. Wallace, M. Islam, A survey of surface treatments to improve the fretting fatigue resistance on Ti-6Al-4V, *Surface Treatment Effects II*, 1995, p. 265-272
29. C. Ruiz, K.C. Chen, Life assessment of dovetail joints between blades and discs in aero-engines, *IMEchE conference publications*, 1986, **1**, p. 187-194
30. Ren, Weiju, Shankar Mall, Jeffery H. Sanders, Shashi K. Sharma, Evaluation of coatings on Ti-6Al-4V substrates under fretting fatigue, *Surface and Coatings Technology*, 2005, p 177-188
31. O.W. U. Wiklund, M. Larsson, S. Hogmark, Evaluation of new multilayer physical vapour deposition coatings in sliding contact, *Wear*, 1999, **236** p. 88-95
32. V.C. Fox, N. Renevier, D.G. Teer, J. Hampshire, V. Rigato, The structure of tribologically improved MoS₂-metal composite coatings and the industrial applications, *Surface & Coatings Technology*, 1999, **116**(119), p. 492-497
33. M.R. Hilton, G. Jayaram, L.D. Marks, Microstructure on cosputter-deposited metal- and oxide-MoS₂ solid lubricant thin films, *Journal of Materials Research*, 1997, **13**(4), p. 1022-1032
34. J.R. Lince, M.R. Hilton, Metal incorporation in sputter-deposited MoS₂ films studied by extended x-ray absorption, *Journal of Materials Research*, 1996, **10**(8), p. 2091
35. T.L. Mogne, C. Donnet, J.M. Martin, A. Tonck, N. Millard-Pinard, Nature of super-lubricating MoS₂ physical vapor deposition coatings, *American Vacuum Society*, 1994, **12**(4), p. 1998-2004
36. M.B. Peterson, R.L. Johnson, Friction and wear investigation of molybdenum disulfide, N.A.C.A. Aeronautics Ed., Lewis Flight Propulsion Laboratory, 1953.
37. N.M. Renevier, V.C. Fox, D.G. Teer, J. Hampshire, Coating characteristics and tribological properties of sputter-deposited MoS₂ metal composite coatings deposited by closed field unbalanced magnetron sputter ion plating, *Surface & Coatings Technology*, 2000, **127**, p. 24-37
38. N.M. Renevier, N. Lobiondo, V.C. Fox, D.G. Teer, J. Hampshire, Performance of MoS₂/metal composite coatings used for dry machining and other industrial applications, *Surface & Coatings Technology*, 2000, **123**, p. 84-91

39. M.C. Simmons, A. Savan, H. Van Swygenhoven, E. Pfluger, S. Mikhailov, Structural, morphological, chemical and tribological investigations of sputter deposited MoS_x / metal multilayer coatings, *Surface & Coatings Technology*, 1998, **108-109**, p. 340-344
40. Y. Kimura, T. Wakabayashi, K. Okada, T. Wada, H. Nishikawa, Boron nitride as a lubricant additive, *Wear*, 1999 p 199-206
41. M. Chhowalla, G.A. Amaratunga, Thin films of fullerene-like MoS_2 nanoparticles with ultra-low friction and wear, *Nature*, 2000, **407**, p. 164-167
42. M. Chhowalla, G.A. Amaratunga, Thin films of fullerene-like MoS_2 nanoparticles with ultra-low friction and wear, *Nature*, 2000, **407**, p. 164-167
43. N. Ooi, V. Rajan, J. Gottlieb, Y. Catherine, J.B. Adams, Structural properties of hexagonal boron nitride, *Modeling and Simulation in Material Science and Engineering*, 2006 p 515-535
44. G.A. Sileo, J.W. Appleby, S.T. Narsavage, F.X. Alent, C.G. Davis, Plasma sprayed abradable seals for gas turbine engines, U.S. Patent, United Technologies, 1996
45. R.C. Dykhuizen, M.F. Smith, Gas Dynamic Principles of Cold Spray, *Journal of Thermal Spray Technology*, 1998 p 205-212
46. S.V. Klinkov, V.F. Kosarev, M. Rein, Cold Spray deposition: significance of particle impact phenomena, *Aerospace Science and Technology*, 2005, **9**, p. 582-591
47. J. Vlcek, D.P. Jonke, M. Enghart, Potential application of cold spray coatings in the aircraft and space industry, *Dünnschicht*, 2005, **96**(3), p. 684-699
48. L. Ajdelsztajn, A. Zuniga, B. Jodoin, E.J. Lavernia, Cold gas dynamic spraying of a high temperature alloy, *Surface and Coating Technology*, 2005 p 2110-2116
49. A. Papyrin, V. Kosarev, S. Klinkov, A. Alkhimov, V. Fomin. Cold Spray Technology. Khristianovich Institute of Theoretical and Applied Mechanics of Russian Academy of Science in Novosibirsk, Russia. Elsevier, 2007
50. K. Sakaki, Cold spray process - overview and application trends, *Material Science Forums*, 2004, **449-452**, p. 1305-1308
51. L. Ajdelsztan, B. Jodoin, G.E. Kim, and J. M. Schoenung, Cold spray deposition of nanocrystalline aluminum alloys, *Metallurgical and Material Transactions*, 2005, **36A** p. 657-666

52. H.J. Kim, C. H. Lee, S. Y. Hwang, Superhard nan0 WC-12%Co coating by cold spray deposition, *Material Science and Engineering*, 2005, **391**, p. 243-248
53. H.J. Kim, C. H. Lee, S. Y. Hwang, Fabrication of WC-Co coatings by cold spray deposition, *Surface & Coatings Technology*, 2005, **191**, p. 335-340
54. R.C. McCune, W.T. Donlon, O.O Popoola, E.L. Cartwright, Characterization of copper layers produced by cold gas-dynamic spraying, *Journal of Thermal Spray Technology*, 2000, **9**(1)
55. V. Shukla, G.S. Elliot, B.H. Kear, Hyperkinetic deposition of nanopowders by supersonic rectangular jet impingement, *Scripta Materialia*, 2001, **44**, p. 2179-2182
56. T. Van Steenkiste, D.W. Gorkiewicz, Analysis of tantalum coatings produced by the kinetic spray process, *Journal of Thermal Spray Technology*, 2004, **13**(2), p. 265
57. J. German, Splat Science, *Euromaterials*, 2001, **8**(4), p. 11
58. M. Grujicic, C. Tong, W.S. DeRosset, D. Helfritch, Flow analysis and nozzle-^[1]shape optimization for the cold-gas dynamic-spray process, *Proc. Instn. Engrs Vol. 217*, 2003 p 1603-1613
59. S.B. Kang, H.K. Kang, K. Euh, Processing and microstructures of tungsten/copper composites produced by plasma spray and cold spray, *Material Science Forums*, 2005, **475-479**, p. 945-948
60. H. K. Kang, S.B. Kang, Tungsten/copper composite deposits produced by a cold spray, *Scripta Materialia*, 2003, **49**, p. 1169-1174
61. H. Kreye, T. Stoltehoff, Cold spraying-a study of process and coating characteristics, *1st International Thermal Spray Conference*, C.C. Berndt Ed., 2000
62. H. Lee, S. Mall, Stress relation and fretting fatigue behavior of titanium alloys, *Air Force Institute of Technology*.
63. R.S. Lima, J. Karthikeyan, C.M. Kay, J. Lindemann, C.C. Berndt, Microstructural characteristics of cold-sprayed nanostructured WC-Co coatings, *Thin Solid Films*, 2002, **416**, p. 126-135
64. M.F. Smith, J.E. Brockmann, R.C. Dykhuizen, D.L. Gilmore, R.A. Neiser, T.J. Roemer, Cold spray direct fabrication - high rate, solid state, material consolidation, *Materials Research Society Symposia Proceedings*, 1999, **542**, p. 65-76

65. H. Assadi, F. Gartner, T. Stoltenhoff, H. Kreye, Bonding mechanism in cold gas spray, *Acta Materialia*, 2003, **51** p. 4379-4394
66. T.L. K. Balani, A. Agarwal, J. Karthikeyan, N. Munroe, Effect of carrier gases on microstructural and electrochemical behavior of cold-sprayed 1100 aluminum coating, *Surface & Coatings Technology*, 2004, **195** p. 272-279
67. M. Grujic, J.R. Saylor, D.E. Beasley, W.S. DeRosset, D. Helfrich, Computational analysis of the interfacial bonding between feed-powder particles and the substrate in the cold gas dynamic-spray process, *Applied Surface Science*, 2003, **219**, p. 211-227
68. T.H. Van Steenkiste, J.R. Smith, R.E. Teets et. al., Kinetic spray coatings, *Surface & Coatings Technology*, 1999, **111**, p. 62-71
69. T. Stoltenhoff, H. Kreye, and H.J. Richter, An analysis of the cold spray process and its coatings, *Journal of Thermal Spray Technology*, 2002, **11**(4), p. 542-550
70. A.O. Tokarev, Structure of aluminum powder coatings prepared by cold gas-dynamic spraying, *Metal Science and Heat Treatment*, 1996, **38**(3-4), p. 136-139
71. L. Zhao, K. Bobzin, D. He, J. Zwick, F. Ernst, E. Lugscheider, Deposition of aluminum alloy Al12Si by cold spraying, *Advanced Engineering Materials*, 2006, **8**(4), p. 264-267
72. N. N. Koronkina, S.V. Panin, A.P. Alkhimov, Investigation of Plastic Deformation Development at mesoscale level in composition with cold-sprayed coatings, *Modern Technique and Technologies*, 2001, p. 71-73
73. C.J. Li, W.Y. Li, Deposited characteristics of titanium coating in cold spray, *Surface & Coatings Technology*, 2003, **167**, p. 278-283
74. T.C. Jen, L. Li, Q. Chen, W. Cui, X. Zhang, The acceleration on micro-nano particles in supersonic De-Laval-Type nozzle, *American Society of Mechanical Engineers, Heat Transfer Division*, 2003, **374**(3), p. 281-5673
75. T.C. Jen, L. Li, W. Cui, Q. Chen, X. Zhang, Effects of shock waves on the particles acceleration for cold gas dynamic spray, *ASME International Mechanical Engineering Congress and Exposition*, 2004.
76. V.F. Kosarev, S.V. Klinkov, A.P. Alkhimov, A.N. Papyrin, On some aspects of gas dynamics of the cold spray process, *Journal of Thermal Spray Technology*, 2002, **12**(2), p. 265-281

77. V. Shukla, G.S. Elliot, B.H. Kear, Nanopowder deposition by supersonic rectangular jet impingement, *Journal of Thermal Spray Technology*, 2000, **9**(3), p. 394-398
78. B. Jodoin, Cold spray nozzle mach number limitation, *Journal of Thermal Spray Technology*, 2002, **11**(4), p. 496-507
79. K. Sakaki, Y. Shimizu, Effect of the increase in the entrance convergent section length of the gun nozzle on the high-velocity oxygen fuel and cold spray process, *Journal of Thermal Spray Technology*, 2001, **10**(3), p. 487-496
80. A. Alkhimov, V. Kosarev, S. Klinkov, The features of cold spray nozzle design, *Journal of Thermal Spray Technology*, 2001, **10**(2), p. 375-381
81. M. Grujic, C.L. Zhao, C. Tong, W.S. DeRosset, D. Helfrich, Analysis of the impact velocity of powder particles in the cold-gas dynamic-spray process, *Material Science and Engineering*, 2004, **A368**, p. 222-230
82. J. Vlcek, L. Gimeno, H. Huber, E. Lugscheider, A systematic approach to material eligibility for the cold-spray process, *Journal of Thermal Spray Technology*, **14**(1), p. 125-133
83. S. Barradas, R. Mollins, M. Jeandin, M. Arrigoni, M. Boustie, C. Bolis, L. Berthe, M. Ducos, Application of laser shock adhesion testing to the study of the interlamellar strength and coating-substrate adhesion in cold-sprayed copper coating of aluminum, *Surface & Coatings Technology*, 2005, 197 p. 18-27
84. G. Aggarwal, P. Walia, A. E. Segall, I. Smid, Development of Self Lubricating Coatings for Ti-6Al-4V Dovetails using a High-Velocity-Particle-Consolidation (HVPC) Process, *Engineering Science and Mechanics – The Pennsylvania State University*
85. A.V. Bolesta, V.M. Fomin M.R. Sharafutdinov, B.P. Tolochko, Investigation of interface boundary occurring during cold gas-dynamic spraying of metallic particles, *Nuclear Instruments and Methods in Physics Research*, 2001, **A 470** p. 249-252
86. R. Morgan, P. Fox, J. Pattison, C. Sutcliffe, W. O'Neill, Analysis of cold gas dynamically sprayed aluminum deposits, *Material Letters*, 2004, **58**, p. 1317-1320
87. C. Borchers, F. Gärtner, T. Stoltenhoff, Borchers, H. Kreye, Microstructural bonding of cold sprayed face centered cubic metals, *Journal of Applied Physics*, 2004, **96**(8), p. 4287-4292
88. C.J. Li, W.Y. Li, Y.Y. Wang, Formation of metastable phases in cold-sprayed soft metallic deposits, *Surface & Coatings Technology*, 2005, **198**, p. 469-473

89. T.H. Van Steenkiste, J.R. Smith, R.E. Teets, Aluminum coatings via kinetic spray with relatively large powder particles, *Surface & Coatings Technology*, 2002, **154**, p. 237-252
90. C. Borchers, F. Gärtner, T. Stoltenhoff, Borchers, H. Kreye, H. Assadi, Deformation microstructure of cold gas sprayed coatings, *Materials Research Society Symposium*, M.R. Society Ed., 2001
91. M. Gruijic, C.L. Zhao, W.S. DeRosset, D. Helfritch, Adiabatic shear instability based mechanism for particles/substrate bonding in the cold-gas dynamic-spray process, *Materials and Design*, 2004, **25**, p. 681-688
92. L. Ajdelsztan, G.E. Kim, J.M. Schoenung, Cold spray deposition of nanocrystalline aluminum alloys, *Metallurgical and Material Transactions*, 2005, **36A**, p. 657-666
93. D. Zhang, P.H. Shipway, D.G. McCartney, Cold gas dynamic spraying of aluminum: the role of substrate characteristics in deposition formation, *Journal of Thermal Spray Technology*, 2004, **14**(1), p. 109-116
94. T. Van Steenkiste, J.R. Smith, Evaluation of coatings produced via kinetic and cold spray processes, *Journal of Thermal Spray Technology*, 2003, **13**(2), p. 274-282
95. J. Morimoto, T. Onoda, Y. Sasaki, N. Abe, Improvement of solid cold sprayed TiO₂-Zn coating with direct diode laser, *Vacuum*, 2004, **73**, p. 527-532
96. H.Y. Lee, Y.H. Yu, Y.C. Lee, Y.P. Hong, K.H. Ko, Interfacial studies between cold sprayed WO₃, Y₂O₃ films and Si substrates, *Applied Surface Science*, 2004, **227**, p. 224-249
97. H.Y. Lee, Y.H. Yu, Y.C. Lee, Y.P. Hong, K.H. Ko, Thin film coatings of WO₃ by cold gas dynamic spray: a technical note, *Journal of Thermal Spray Technology*, 2005, **14**(2)
98. X. Gong, X. Li, The study of Ni coating on the surface of MoS₂ powder, *State Hunan Nonferrous Metals*, 2000, **16**, p. 28- 30
99. A. Malecki, A. Micek-Ilnicka, Electroless nickel plating from acid bath, *Surface and Coatings Technology*, 2000, **123**, p. 72-77
100. N. Takano, N. Hosoda, T. Yamada, T. Osaka, Mechanism of the chemical deposition of nickel on silicon wafers in aqueous solution, *Journal of the Electrochemical Society*, 1999, **146**(4), p. 1407-1411

101. R. Taheri, I.N.A Oguocha, S. Yannacopoulos, The tribological characteristics of electroless NiP coatings, *Wear*, 2001, **249**, p. 386-396
102. C.A. Leon, R.A.L. Drew, Preparation of nickel-coated powders as precursors to reinforce MMCs, *Journal of Materials Science*, 200, **35**, p. 4763-4768
103. C. Lin, I. Smid, Encapsulation of tungsten carbide particles with nickel, C.I.S.P Ed., The Pennsylvania State University, 2006
104. J. Gao, F. Tang, J. Ren, Electroless nickel deposition on amino-functionalized silica spheres, *Surface and Coatings Technology*, 2005, **200**, 2249-2252
105. L. Xibin, L. Rutie, G. Xuebing, Study of Ni-Cr high temperature solid self lubricating materials added with Ni coated MoS₂ Powder, *Rare Metal Materials and Engineering*, 2003, **32(10)**, p. 783-786
106. N.K. Shrestha, K. Sakurada, M. Masuko, T. Saji, Composite coatings of nickel and ceramic particles prepared in two steps, *Surface and Coatings Technology*, 2001, **140**, p. 175-181
107. R. Zhang, L. Gao, J. Guo, Temperature-sensitivity of coating on copper on sub-micron silicon carbide particles by electroless deposition in a rotation flask, *Surface and Coatings Technology*, 2003, **166**, p. 67-71
108. S. Ramesh, Y. Koltypin, R. Prozorov, A. Gedanken, Sonochemical deposition and characterization of nanophasic amorphous nickel on silica microspheres, *Chem. Mater.*, 1997, **9(2)**, p. 546-551
109. C.Y. Huang, W.W Mo, M.L Roan, The influence of heat treatment on electroless-nickel coated fibre (ENCF) on the mechanical properties and EMI shielding of ENCF reinforced ABS polymeric composites, *Surface and Coating Technology*, 2004, **184**, p. 123-132
110. Z. Shi, X. Wang, Z. Ding, The study of electroless deposition of nickel on graphite fiber, *Applied Surface Science*, 1999, **140**, p. 106-110
111. J.T.W. Jappes, B. Ramamoorthi, R.K. Nair, Effect of process parameters on efficiency and performance of electroless nickel-phosphorous deposits, *IE Journal*, 2004, **85**, p. 53-58
112. G. G. Zusmanovich, Effect of heat treatment on the hardness of nickel-phosphorus coatings, *Metallurg*, 1960, **4**, p. 48-50
113. C.D. Lykins, S. Mall, V. Jain, A shear stress based parameter for fretting fatigue crack initiation, *Fatigue Fract Engng Mater Struct*, 2001 p 461-473.

114. M. Pushpavanam, S.R. Natarajan, Nickel-boron nitride electro-composites, *Metal Finishing*, 1995 p 97-99
115. D.G. Teer, New solid lubricant coatings, *Wear*, 2001 p 1068-1074
116. R.W. Lynch, H.G. Drickamer, Effect of high pressure on the lattice parameters of diamond, graphite, and hexagonal boron nitride, *The Journal of Chemical Physics*, 1966 p 181-184
117. P. Walia, "Development of Ni-based self-lubricating composite coatings for Ti-6Al-4V dovetail joints using the cold spray process," The Pennsylvania State University
118. T. Schmidt, F. Gaertner, H. Keye, New Development in Cold Spray Based on Higher Gas and Particle Temperatures, *Journal of Thermal Spray Technology*, 2006 p 488-494
119. D.L. Gilmore, R.C. Dykhuizen, R.A. Neiser, T.J. Roemer, M.F. Smith, Particle Velocity and Deposition Efficiency in Cold Spray Process, *Journal of Thermal Spray Technology*, 1999 p 576-582
120. J. Karthikeyan, Cold Spray Technology: International Status and USA Efforts, *ASB Industries, Inc*, 2004 p 1-14
121. R.C. Dyhuzien, M.F. Smith, D.L. Gilmore, R.A. Neiser, X. Jiang, S. Sampath, Impact of high velocity cold spray particles, *ASM International*, 1999, **8**, p. 559-564
122. H. Proudhon, S. Fouvry, G.R. Yantio, Determination and prediction of the fretting crack initiation: introduction of the (P, Q, N) representation and definition of a variable process volume, *Laboratoire de Tribologie et de dynamique des systèmes, UMR*, 2005.
123. R.L. Fusaro, How to evaluate solid lubricant films using a pin-on-disk tribometer, NASA Ed., Lewis Research Center, 1986
124. ASTM Standard G 133, Standard Test Method for Linearly Reciprocating Ball-on-Flat Sliding Wear, *Annual Book of ASTM Standards*, 1995, **3(01)**, p.521-527
125. Young, Hugh D., and Roger A. Freedman. University Physics. 10th ed. New York: Addison Wesley Longman, 2000.
126. Dowling, Norman J. Mechanical Behavior of Materials - Engineering Methods for Deformation, Fracture, and Fatigue. 3rd ed. Upper Saddle River: Pearson Prentice Hall, 1993.

127. L. Wang, Y. Gao, Q. Xue, A comparative study on the tribological behavior of nanocrystalline nickel and cobalt coatings correlated with grain size and phase structure, *Materials Chemistry and Physics*, 2005, **10(14)**, p. 96-103

Appendix A

Optical Images Ni coated hBN Powder

Figure A-1 through Figure A-4 Figure A-5 show optical images of various Ni coated hBN powders to provide a better representation of the particles size distribution. Cross sections were viewed by mounting the powder in epoxy and polishing by procedures discussed earlier.

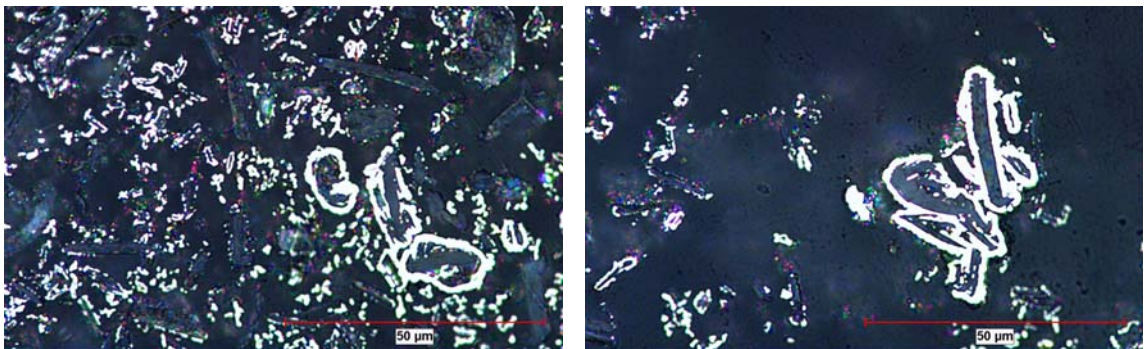


Figure A-1: Thin Ni coated 20-30µm hBN

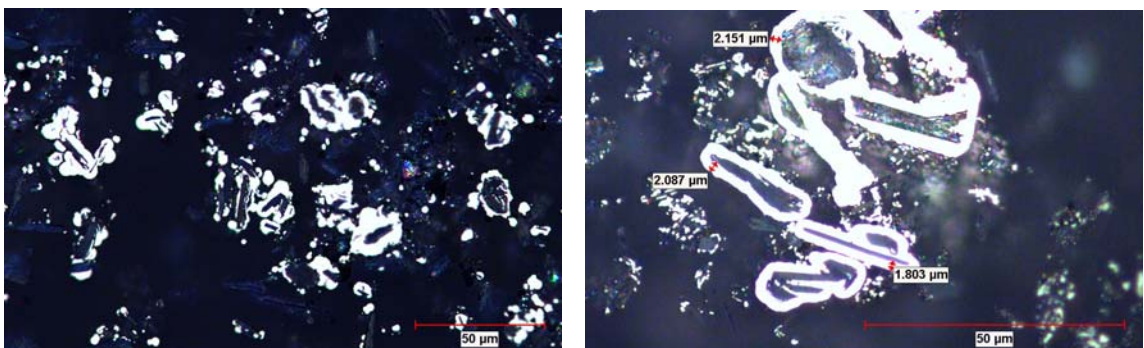


Figure A-2: Thin Ni coated 20-30µm hBN

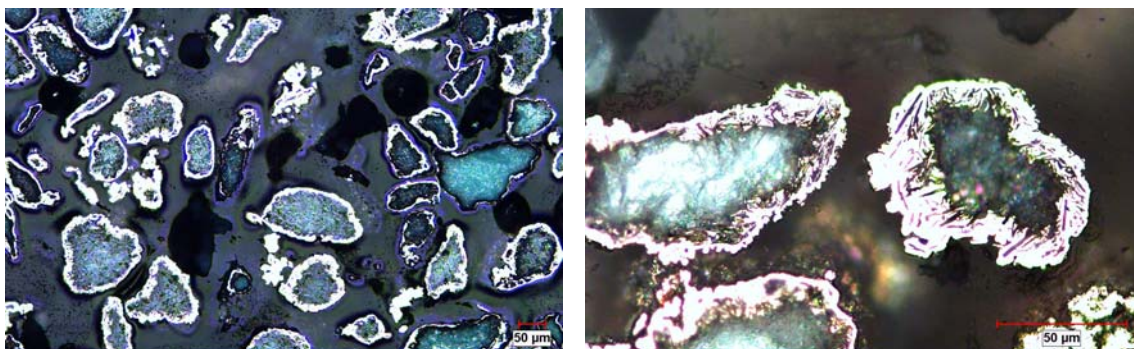


Figure A-3: As Received 75µm Ni coated hBN from Federal Technologies Group (not used in this study)

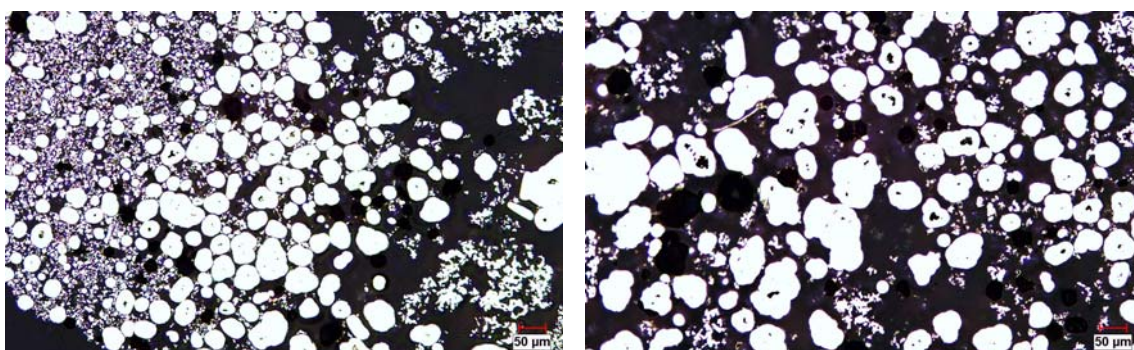


Figure A-4: Thick Ni coated 10µm hBN viewed at 100x

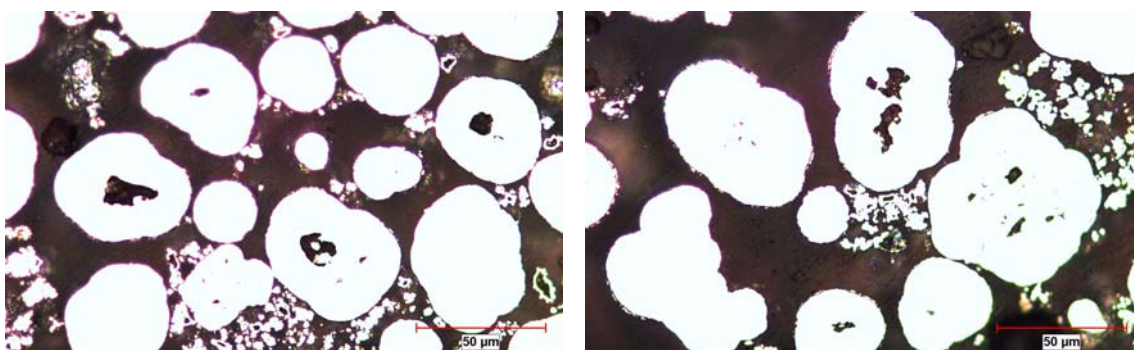


Figure A-5: Thick Ni coated 10µm hBN viewed at 500x

Appendix B

Images of Cold Spray Coatings

This section provides additional optical images of coatings produced via cold spray. Figure A-1 - A-6 show cross sections of the cold spray coatings.

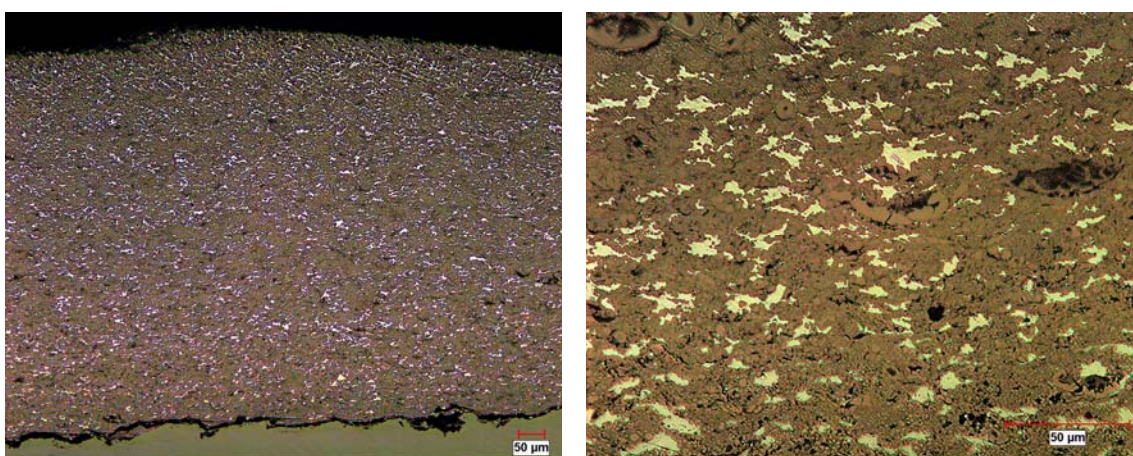


Figure A-1: Thick Ni coated hBN cold spray coating produced using 500°C N₂ as a process gas

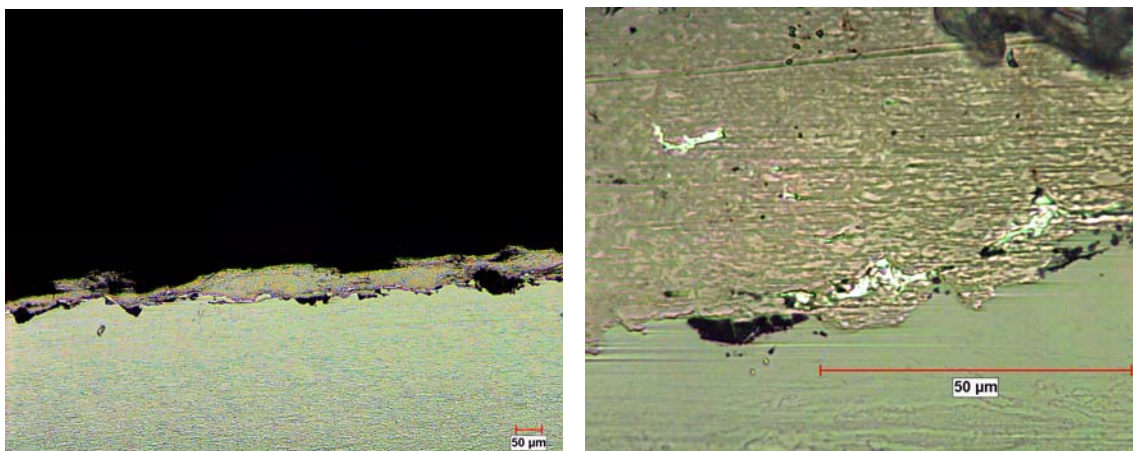


Figure A-2: Thick Ni coated hBN cold spray coating produced using 188°C He as a process gas and a 20 mm/sec traverse rate

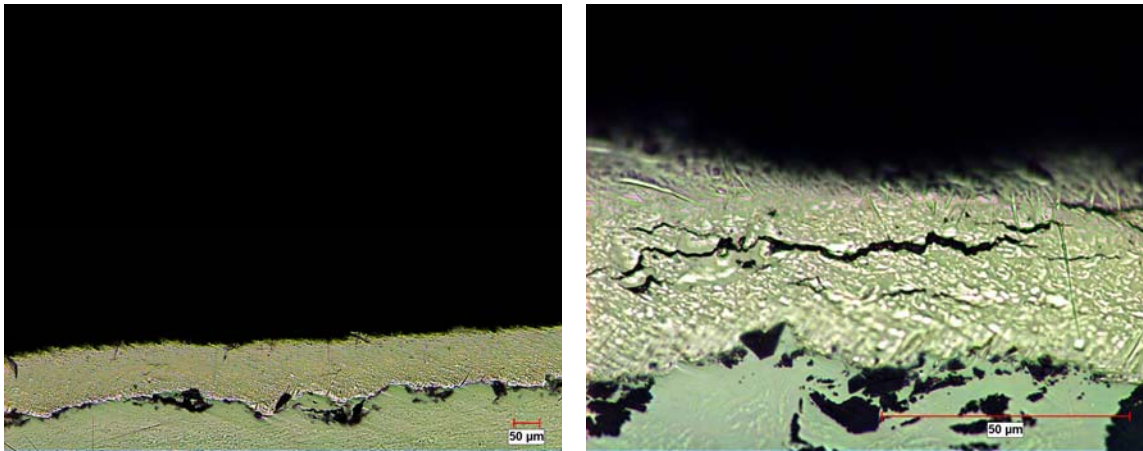


Figure A-3: Thick Ni coated hBN cold spray coating produced using 188°C He as a process gas and a 50 mm/sec traverse rate

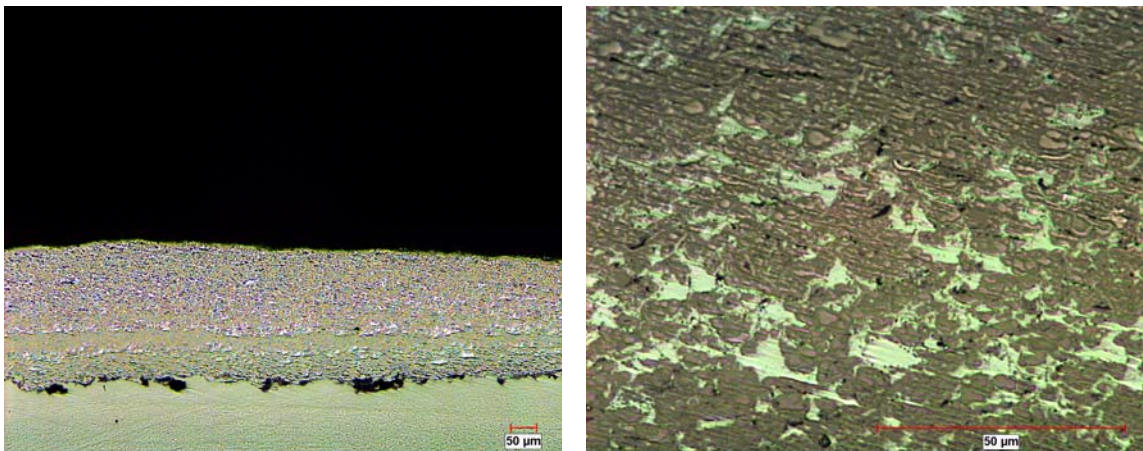


Figure A-4: Thick Ni coated hBN cold spray coating produced using 24°C He as a process gas

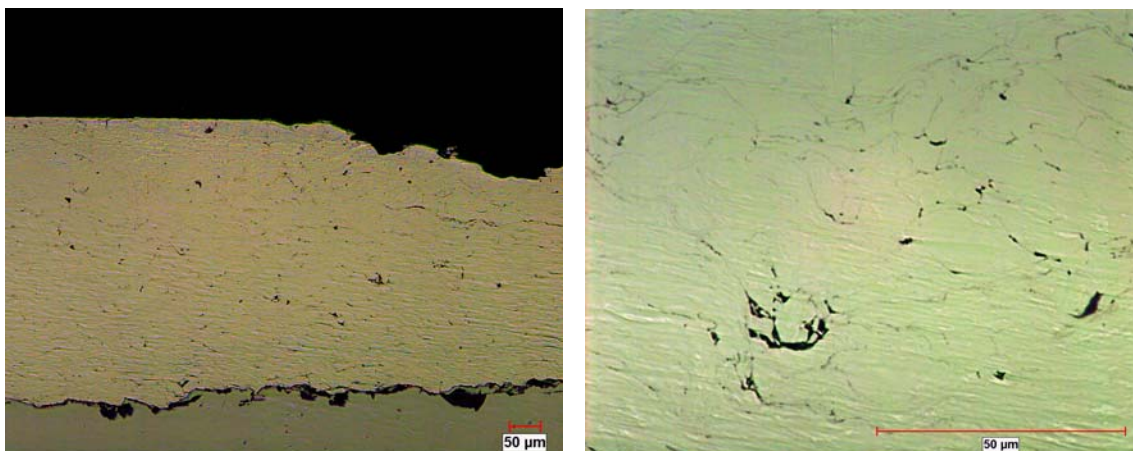


Figure A-5: Pure Ni cold spray coating using 500°C N₂ as a process gas

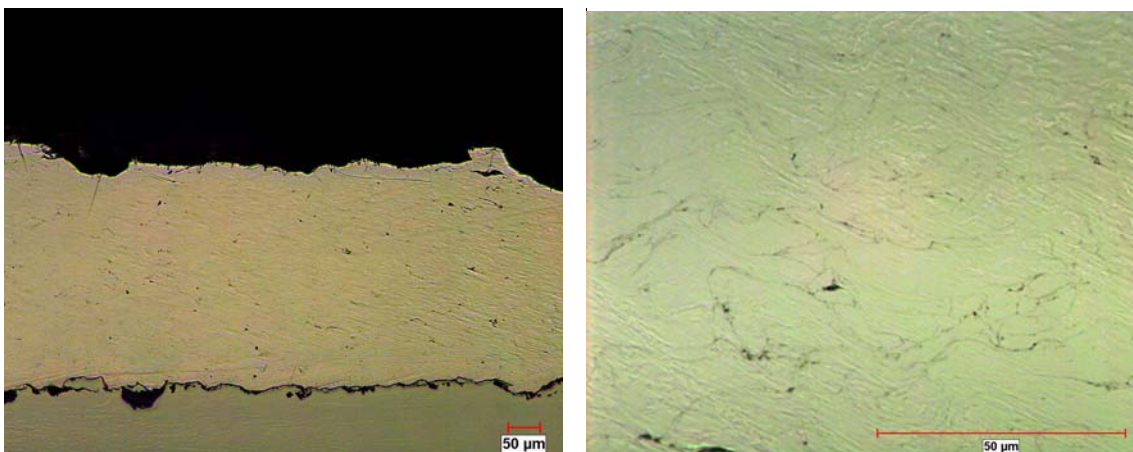


Figure A-6: Milled Ni cold spray coating using 500°C N₂ as a process gas

Appendix C

Calculations of Friction Coefficients

Ti-6Al-4V				Ni coated 10µm hBN sprayed with 500°C N2			
Test Number	Coefficient of Friction		Deviation from Average	Test Number	Coefficient of Friction		Deviation from Average
1	0.284		-0.112	1	0.369		0.078
2	0.386		-0.010	2	0.309		0.019
3	0.401		0.005	3	0.288		-0.002
4	0.451		-0.009	4	0.224		-0.039
5	0.460		0.063	5	0.262		-0.028
Average	0.396	Standard Deviation	0.063	Average	0.290	Standard Deviation	0.046

Pure Ni				Ni coated 10µm hBN sprayed with 24°C He			
Test Number	Coefficient of Friction		Deviation from Average	Test Number	Coefficient of Friction		Deviation from Average
1	0.687		0.259	1	0.235		0.032
2	0.401		-0.027	2	0.209		0.005
3	0.369		-0.060	3	0.178		-0.025
4	0.395		0.104	4	0.196		-0.002
5	0.291		-0.138	5	0.198		-0.005
Average	0.429	Standard Deviation	0.156	Average	0.203	Standard Deviation	0.021

Milled Ni			
Test Number	Coefficient of Friction		Deviation from Average
1	0.771		0.025
2	0.685		-0.062
3	0.678		-0.068
4	0.801		0.004
5	0.797		0.050
Average	0.746	Standard Deviation	0.053

Appendix D

Non-technical Abstract

Fretting occurs when two surfaces rub against each other in small amplitude oscillatory motions. The cyclic stressing of the surfaces in contact results in surface erosion and particle break offs, also known as fretting wear. The debris produced from fretting wear continues to damage the surfaces in contact until fractures occur. Common methods of fretting prevention include application of hard and/or lubricant coatings. Hexagonal boron nitride (hBN) is being investigated as a possible lubricant for the dovetail joints in gas turbine engines, an interface which is especially prone to fretting wear.

High velocity particle consolidation (Cold Spray) has been used to deposit the hBN coating. With this method particles are accelerated to 300-1000 m/s using gas temperatures of 0-700°C. The expansion of gas through the nozzle reduces the temperature of deposited particles, minimizing heat transfer to the substrate. Cold spray works best with ductile powders because successful deposition relies on impaction and particle deformation. hBN is not ductile, so a ductile medium is needed to allow for hBN deposition.

Nickel has been electrolessly deposited onto hBN particles to provide the necessary ductile medium for cold spraying. In the electroless process, nickel is reduced from a solution onto a substrate without the use of an external current source; i.e. the entire nickel deposition occurs within the solution. This procedure used a mixture of chemicals (nickel sulfate and sodium citrate) along with a reducing agent (sodium hypophosphite) to create a water based solution. The hBN powder is pretreated with catalyst coatings of tin chloride and palladium chloride. When pretreated hBN powder is added to the electroless solution the catalysts on the powder's surface caused nickel ions to be reduced resulting in a uniform coating on the powder.

Nickel coatings as thick as 15 microns have successfully been deposited onto hBN powder. The nickel encapsulated hBN powder was used to create self-lubricating coatings through Cold Spray. Friction and bond tests were performed to determine the coating quality. Incorporation of hBN within the coating reduced the coefficient of friction of the coating.